CISM International Centre for Mechanical Sciences 608
Courses and Lectures

Laurent Ponson *Editor*

Mechanics and Physics of Fracture

Multiscale Modeling of the Failure Behavior of Solids

International Centre for Mechanical Sciences

Springer

CISM International Centre for Mechanical Sciences

Courses and Lectures

Volume 608

For more than 40 years the book series edited by CISM, “International Centre for Mechanical Sciences: Courses and Lectures”, has presented groundbreaking developments in mechanics and computational engineering methods. It covers such fields as solid and fluid mechanics, mechanics of materials, micro- and nanomechanics, biomechanics, and mechatronics. The papers are written by international authorities in the field. The books are at graduate level but may include some introductory material.

Laurent Ponson
Editor

Mechanics and Physics of Fracture

Multiscale Modeling of the Failure Behavior of Solids

Springer

Editor
Laurent Ponson
Institut Jean Le Rond d'Alembert
Sorbonne Université, CNRS
Paris, France

ISSN 0254-1971 ISSN 2309-3706 (electronic)
CISM International Centre for Mechanical Sciences
ISBN 978-3-031-18339-3 ISBN 978-3-031-18340-9 (eBook)
https://doi.org/10.1007/978-3-031-18340-9

This Springer imprint is published by the registered company Springer Nature Switzerland AG
The registered company address is: Gewerbestrasse 11, 6330 Cham, Switzerland

Preface

The four chapters in this book are based on the material provided during an Autumn School which took place at the *Centre International des Sciences Mécaniques—International Center for Solid Mechanics (CISM)* in Udine, Italy. The general theme and title of this school was

Mechanics and physics of fracture:
multiscale modeling of the failure behavior of solids

The school was intended for both Ph.D. students and confirmed researchers, and its objective was to provide a comprehensive understanding of the macroscopic failure behavior of solids from the description of the microscopic failure processes and their coupling with the microstructure. Several fundamental questions were addressed:

- The relation between the microstructural features of materials and their fracture properties and crack trajectories.
- The role of damage mechanisms and non-linear deformations near the crack tip on the failure behavior of solids.
- Finally, the role of dynamic inertial effects during fast fracture was more briefly evoked.

The courses provided a pedagogical overview of recently developed concepts and tools, that permit to perform the transition from small scales to large ones in fracture problems, thus introducing basic rules for the rational design of tough solids.

The chapters in this book reproduce and extend the contents of four of the six courses delivered. Their titles, authors, and summarized contents are as follows:

Chapter 1 **: Introduction to Fracture Mechanics** *by Prof. K. Ravi-Chandar, University of Austin*

This introductory chapter presents a unified continuum treatment of modern-day fracture mechanics. Particular attention is directed toward instabilities taking place during the slow and fast propagation of cracks. The concepts introduced serve as a basis for the more advanced topics addressed in subsequent chapters.

Outline:

1.1 Introduction to quasi-static fracture mechanics
1.2 Dynamic fracture and instabilities
1.3 Fracture paths and instabilities during slow fracture

Chapter 2**: Perturbations of Cracks** *by Prof. J.B. Leblond, Sorbonne Université (formerly Université Pierre et Marie Curie)*

This chapter, of theoretical character, is devoted to the description of various methods of analysis of geometric perturbations of cracks in linear elastic media, in both 2D and 3D. Important applications to the prediction of crack paths are presented.

Outline:

2.1 2D crack perturbations in e:mixed-mode I+II
2.2 3D coplanar crack perturbations
2.3 3D out-of-plane crack perturbations

Chapter 3**: Fracture Mechanics of Heterogeneous Materials** *by Dr. L. Ponson, CNRS—Sorbonne Université*

This chapter explores the basic mechanisms underlying crack propagation in brittle heterogeneous materials and introduces tools that allow for the prediction of their effective failure properties from their microscale features. The second part of this chapter explores two fascinating features of the failure behavior of disordered materials, namely, the intermittent dynamics of cracks and the roughening processes leading to the complex structure of fracture surfaces.

Outline:

3.1 Effective toughness of heterogeneous solids
3.2 Failure of disordered materials: intermittent crack dynamics and depinning transition
3.3 Roughening mechanisms and applications to statistical fractography

Chapter 4**: Toughening Mechanisms in Biological Materials: Experiments, Modeling and Bio-inspiration** *by Prof. F. Barthelat, University of Colorado Boulder*

This chapter is devoted to fracture of biological materials. After a presentation of relevant experimental techniques, explanations of their extraordinary fracture performances will be discussed, with references to their specific architecture based on mineralized tissues, fibrous tissues, natural elastomers, and gels. Finally, an overview of bio-inspired materials is given.

Outline:

4.1 Experimental tools for fracture mechanics and application to biological materials
4.2 Why biological materials are so tough
4.3 Toughness of bio-inspired materials

Globally, the response to the courses given during the autumn school was excellent: participants obviously appreciated their instructiveness and enjoyed them, from both the theoretical and practical points of view. We hope that the present book will

encounter the same success, and that its readers will find, in reading its chapters, the same pleasure as their authors took in writing them.

Paris, France Laurent Ponson

Contents

Introduction to Mechanics of Fracture

Krishnaswamy Ravi-Chandar

Abstract This chapter covers the basic theory of linear elastic fracture mechanics. First, the global or energy based approach to fracture modeling is described. This is followed by a discussion of the local approach, based on stress intensity factors. Aspects of mixed mode fracture are then described followed by an overview of dynamic fracture. Finally, the use of a phase field model to simulate fracture is briefly summarized.

1 Introduction

The development of the theory of fracture and the mechanics associated with its implementation has had a significant impact in the analysis and design of reliable and durable structures. Structural failure could occur through one of three modes: *buckling*, *plastic collapse*, and *fracture*. Failure by buckling has been studied since the days of Euler, who considered the buckling of simple beams. The **buckling** critical load for a simply-supported beam is $P_{cr} = \pi^2 B/L^2$, where L is the length of the beam, $B = EI$ is the bending rigidity of the beam, E is the modulus of elasticity of the beam, and I is the second moment of the cross-sectional area of the beam. This mode of failure is governed by the interaction between the geometry of the structure and the stiffness properties of the material/structure, and is not influenced at all by the strength of the material. Once the possibility for this type of failure is identified, it can be prevented quite easily through proper structural design that avoids the bifurcations that trigger such buckling modes. When buckling failures are eliminated, the resulting structures could be subjected to greater stress levels, such that they approach the yield strength of the material; when the nonlinearities associated with plastic deformation are triggered, the creation of plastic hinges, shear bands, and other localized deformation modes can convert stable structures to

K. Ravi-Chandar (✉)
Center for Mechanics of Solids, Structures and Materials, Department of Aerospace Engineering and Engineering Mechanics, The University of Texas at Austin, Austin, TX 78712-0235, USA
e-mail: ravi@utexas.edu

L. Ponson (ed.), *Mechanics and Physics of Fracture*, CISM International Centre for Mechanical Sciences 608,
https://doi.org/10.1007/978-3-031-18340-9_1

Table 1 Timeline of major events in the area of structural reliability

Year	Event	Remarks
1800–1850	Boilers in steam boats explode Railroad car axles break	Fatigue studies of Wohler
1901		Charpy impact test developed
1911		ASME boiler and pressure vessel codes developed
1919	Boston molasses tank	 The Boston Daily Globe EXTRA MOLASSES TANK EXPLOSION INJURES 50 AND KILLS 11 Death and Devastation In Wake of North End Disaster
1920	*Griffith's theory of fracture*	
1940s	Liberty ships crack at port Charpy energy requirement for structures adopted	
1950s	Comet airplane, Minuteman and Polaris missile failures Irwin's fracture criterion: toughness K_{IC} ASTM Fracture Committee formed	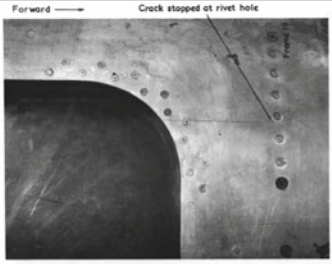 FIG. 35. Crack stopped at rivet hole in frame, 6,901 cycles. First starboard window.
1960s	F111, C5A airplane failures Nuclear pressure vessels and pipes Paris Law for fatigue crack growth	
1970s	J-based nonlinear fracture theory and dynamic fracture theory developed	US Air Force adopts fracture criterion: KIC

(continued)

Table 1 (continued)

Year	Event	Remarks
1980s	Aloha Airline Multi-site-damage	

mechanisms and triggger the failure mode called **plastic collapse**. Such localization is typically the result of overstressing the structural components, and, in principle, could be overcome through proper redesign to decrease the stress or through selection of alternate materials with higher strength. Even when the failure modes of buckling and collapse of structures are circumvented through proper design, structural failures are still possible, but now driven by yet another mode of failure—that of **fracture**.

Fracture is the process of breakage of atomic bonds and the creation of new surfaces from a volume. This mode of failure brings a fundamentally different perspective to the problem of reliability and durability—that of intrinsic defects in the material. Throughout the industrial age, repeated catastrophic failures that resulted in significant loss of life and property that were the result of fracture, occurred in numerous, seemingly diverse, applications; a short listing of some of these failures is provided in Table 1. A fundamentally different perspective is needed to provide the framework for including the process of fracture in the analysis of structural reliability. Griffith (1921) provided such a framework for the analysis of structures susceptible to failure by fracture.

2 An Overview of the Griffith Theory of Fracture

2.1 How Strong is a Solid?—An Atomistic Point of View

We begin with an elementary consideration of the theoretical strength of an idealized, perfect solid, represented by a regular periodic array of atoms, bonded to each other in a cubic lattice with spacing a_0. The interatomic interaction is represented by an interaction energy represented in the upper part of Fig. 1.

At equilibrium the force is zero, and the slope indicates the elastic modulus of the lattice; with decreasing separation distance, a large compressive force develops rapidly, and with increasing separation distance, the force increases initially, but

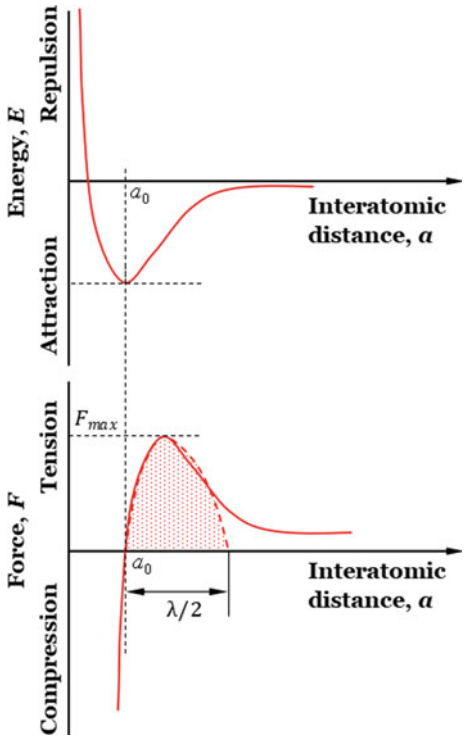

Fig. 1 Interatomic interaction; **a** energy versus separation distance. **b** Force versus separation distance

reaches a maximum, corresponding to the maximum strength of the interatomic bonding. When pulled beyond this distance, the pull force overcomes the attractive force between two atoms and the force drops off to zero gradually, severing the atomic bond. It is this peak force that corresponds to the theoretical strength of this material. In order to get an estimate of this strength in terms of the other parameters, we represent the force versus interatomic distance curve in terms of the stress and strain as

$$\sigma = \sigma_{\max} \sin\left(\frac{2\pi a_0}{\lambda}\varepsilon\right) \tag{1}$$

where $\sigma = F / a_0^2$, $\varepsilon = (a - a_0)/a_0$ and $\sigma_{\max}$ is the theoretical strength of the solid; this curve is shown by the dashed line in Fig. 1. We may obtain an estimate of the theoretical strength in terms of the modulus of elasticity if we consider that $E = \left.\frac{d\sigma}{d\varepsilon}\right|_{\varepsilon=0}$

$$\sigma_{\max} = \frac{E}{\pi}\frac{\lambda}{2a_0} \tag{2}$$

An order of magnitude estimate of theoretical strength may be obtained by setting $\lambda = 2a_0$, resulting in $\sigma_{\max}/E \sim \pi^{-1}$. Better estimates may be obtained by considering a more appropriate function for the interatomic force interactions, but the results

Table 2 Typical values of the modulus of elasticity and macroscopic strength

Material	Modulus GPa	Strength GPa	Strength/Modulus
Steels	200	0.10–2	0.0005–0.01
Glass	70	0.17	0.0025
Carbon fibers	400	4	0.01
Glass fibers	70	11	0.16

are similar with the ratio of σ_{max}/E varying from 0.1 to 0.25 (see Tetelman and McEvily 1967). However, the strength of most common materials is in this range only in perfectly crystalline solids. A list of material properties of a selected number of materials is given in Table 2; clearly, the strength of most materials is orders of magnitude below the theoretical strength.

The strength can also be estimated in terms of the surface energy. The area under the stress-strain curve, shown as the shaded region in Fig. 1, is the work done on the solid at the point when atomic separation is completed; since the solid is unstressed at this point, this work must now be equated to the surface energy of the newly created surfaces. Thus,

$$2\gamma = \int_{a_0}^{a_0+\lambda/2} \sigma_{\max} \sin\left(\frac{2\pi[a-a_0]}{\lambda}\right) da = \frac{\lambda\sigma_{\max}}{\pi} \tag{3}$$

where γ is the surface energy per unit area, and the factor two on the left hand side accounts for the fact that two surfaces are created by fracture. Eliminating λ between Eqs. (2) and (3), we get an estimate of the theoretical strength as

$$\sigma_{\max} = \sqrt{\frac{E\gamma}{a_0}} \tag{4}$$

One can get another estimate the theoretical strength by considering that for most materials, $E \sim 10^9 - 10^{11}$ Pa, $\gamma \sim 1$ J/m^2, and $a_0 \sim 1^\circ A$; this estimate yields $\sigma_{max} \sim$3–30 GPa, quite high in comparison to measured strengths of materials, as can be seen from Table 2, even considering the fact that a rather low estimate of the surface energy is used.

2.2 *How Strong is a Solid?—The Role of Defects*

Griffith (1921) identified clearly that most materials contained flaws or defects at scales from the atomic to the microscopic, and that these defects must play a signifi-

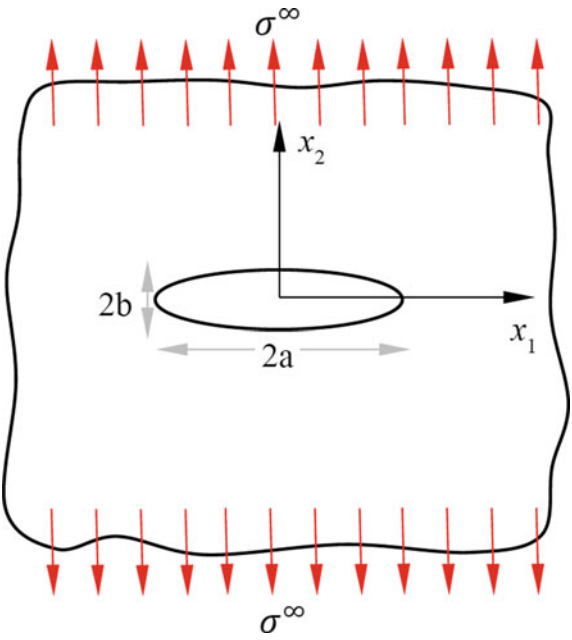

Fig. 2 Plate with an elliptical hole, loaded under uniform stress

cant role in lowering the actual strength. An estimate of the stress concentration due to a defect can be obtained by considering the linear-elastic solution to the problem of an infinite plate loaded uniformly with a normal stress σ^∞, containing an elliptical hole as illustrated in Fig. 2. The normal stress at the point (a, 0) was determined by Inglis (1913) to be

$$\sigma_{22}(a,0) = \sigma^\infty \left(1 + 2\frac{a}{b}\right) \tag{5}$$

For a narrow elliptical defect that looks like a crack, the ratio of a/b could be quite large and the local stress near the edge of the elliptical hole could be orders of magnitude greater than the far-field stress; this enhanced stress at the edge of the elliptical hole could provide a possible explanation for the lower observed macroscopic strength. However, it is not adequate, because the stress enhancement near the edge does not depend on the absolute size of the elliptical hole, a feature that appears counterintuitive—one expects a small defect to be less significant than a larger defect. Griffith overcame this dilemma by suggesting that while the defect length a could be of arbitrary size, the height b is limited by the atomic lattice spacing. Replacing b in favor of the curvature of the ellipse $\rho(a,0) = b^2/a$, and ignoring the first term in Eq. (5) relative to the second, we get

$$\sigma_{22}(a,0) = 2\sigma^\infty \sqrt{a/\rho} \tag{6}$$

In going from an elliptical hole to a crack, we take the limit of $b \to 0$, but limit the curvature at the crack tip to $\rho \to \rho_0$, a constant that depends on the interatomic separation. As a result, we now have dependence of the stress concentration at the tip of the flaw on the flaw size, a. Next, if we examine the limit that as the macroscopic stress $\sigma^\infty \to \sigma_f$, the far-field uniform stress at failure (the macroscopic strength), and, the elevated stress at the crack tip tends to, $\sigma_{22}(a, 0) \to \sigma_{\max}$, the theoretical strength we get

$$\sigma_f \sqrt{a} = \frac{1}{2} \sigma_{\max} \sqrt{\rho_0} \tag{7}$$

Noting that the right hand side contains only material properties, Eq. (7) provides an estimate of the macroscopic strength and its dependence on the flaw size.

Considering $\rho_0 \sim 10^{-10}$ m and the defect to be $a \sim 10^{-6}$ m, we get an estimate of $\sigma_f \sim 0.005\, \sigma_{\max}$. This estimate is in the range of strengths listed in Table 2. The idea that flaws of the size of a micron could influence the macroscopic strength significantly and provide a square-root dependence on the flaw size is rather well supported by this estimate. Griffith proceeded to confirm the estimate in Eq. (7) through two sets of experiments on glass. In the first set of experiments, he prepared thin-walled cylinders with diameters 0.59 in to 0.74 in and wall thickness of 0.02 in and thin-walled spheres with diameters 1.49 in to 2 in and wall thickness of 0.01 in. Defects were generated in these specimens by scribing with a glass-cutter's diamond or a hard steel edge, and annealed by heating to 450 C for one hour. The bursting pressure of the cylinders and spheres were measured in order to determine the macroscopic strength with cracks of different length a. Griffith found that $\sigma_f \sqrt{a} = 0.263$ MPa$\sqrt{\text{m}}$ from both the cylinders and spheres, confirming the scaling estimate shown in Eq. (7). Griffith went further; arguing that a fibrous material with a single line of molecules should exhibit the theoretical strength, Griffith fabricated fibers of different diameters and tested their strength in uniaxial tension; these tests were meticulous in that they explored various factors that could influence the results—such as the temperature to which the glass was heated before making the fibers, the age of the fibers, etc.—and eventually extracted the strength of freshly fabricated fibers. Fibers with diameters in the range of 3.3 μ to 1 mm were tested to determine the relationship between the fiber diameter and macroscopic strength; Griffith's tabulated results are plotted in Fig. 3. While Griffith suggested extrapolating the curve to estimate the theoretical strength, it is more important that the trend in the macroscopic strength follows the predictions of Eq. (7), clearly illustrating the role of defects in dictating the macroscopic strength of materials. This brings us to the next and most important aspect of Griffith's theory of rupture.

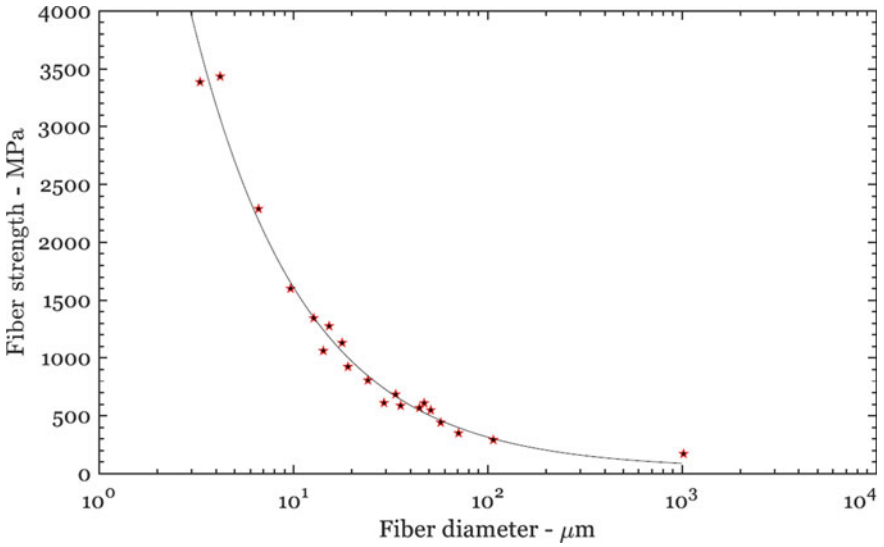

Fig. 3 Dependence of the strength of glass fibers on the fiber diameter. Symbols indicate measured data taken from Griffith (1921), while the solid line is a trend line through this data

2.3 How Strong is a Solid?—Energy Balance and Continuum Aspects

Once it is accepted that flaws or defects that are intrinsic to the material govern its macroscopic load-carrying capability, the question that arises naturally concerns how one might incorporate this within the framework of continuum mechanics. Griffith formulated his theory of rupture by augmenting the theorem of minimum potential energy. Quoting from Griffith,

…the problem of the rupture of elastic solids has been attacked from a new standpoint. According to the well-known 'theorem of minimum energy', the equilibrium state of an elastic solid body, deformed by specified surface forces, is such that the potential energy of the whole system is a minimum. The new criterion of rupture is obtained by adding to this theorem the statement that, the equilibrium position, if equilibrium is possible, must be one in which rupture of the solid has occurred, if the system can pass from the unbroken to the broken condition by a process involving a continuous decrease in potential energy. In order, however, to apply this extended theorem to the problem of finding the breaking loads of real solids, it is necessary to take account of the increase in potential energy which occurs in the formation of new surfaces in the interior of such solids. …A.A. Griffith (1921).

This is a singularly spectacular accomplishment in the theory of rupture or fracture in that this has provided a way in which conversion of energy from bulk to

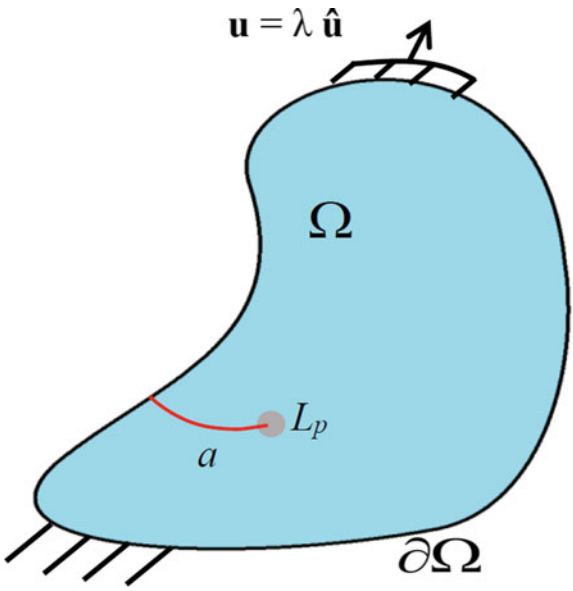

Fig. 4 Linear elastic body with a crack of length a

surface can now be addressed in a consistent manner. In fact, over the past century, this approach has been applied extensively to problems of fracture and adhesion. We will develop the machinery necessary for application of this augmented potential energy theorem in a very general setting within linear elastic behavior.

Consider a linearly elastic body occupying the region Ω of unit thickness, bounded by $\partial\Omega$, containing a crack of length a as indicated in Fig. 4. In a purely mechanical setting, the potential energy Π is written as

$$\Pi = -W_{\partial\Omega} + U_{\Omega} \tag{8}$$

where $W_{\partial\Omega}$ is the work done by the external forces on the body and U_{Ω} is the strain energy stored in the body. According to Griffith's theory, the total energy of the system must now be augmented to include the surface energy: thus, the total energy E is

$$E = -W_{\partial\Omega} + U_{\Omega} + 2\gamma a \tag{9}$$

where the last term corresponds to the surface energy γ over a crack of length a, with the factor two indicating that there are two units of area created per unit extension of crack length. The system is in thermodynamic equilibrium when

$$\frac{\partial E}{\partial a} = \frac{\partial \Pi}{\partial a} + 2\gamma = 0 \Rightarrow -\frac{\partial \Pi}{\partial a} = 2\gamma \tag{10}$$

Furthermore, this equilibrium configuration is stable if

$$\frac{\partial^2 E}{\partial^2 a} > 0 \tag{11}$$

It is common practice in the theory of fracture to define

$$G = -\frac{\partial \Pi}{\partial a} \tag{12}$$

as the *energy release rate*, and corresponds to the decrease in the potential energy of the system per unit crack extension. With this notation the criterion for fracture, based on the theorem of potential energy is stated succinctly as

$$G = 2\gamma \tag{13}$$

Before proceeding to develop this theory of rupture further, we make a number of observations regarding the theory of fracture.

Remark 1 The energy release rate is typically a function of the overall geometry of the body, the load applied, and the crack length. The specific functional form will be determined through solution of a boundary value problem within the linearized theory of elasticity. Subsequently, Eq. (13) can be used to determine the equilibrium crack length, provided the surface energy is known.

Remark 2 No details of the material failure process have been discussed in formulating the fracture criterion; the only restriction is that the material exhibits linearly elastic behavior up to the point of rupture. This is a severe restriction that requires further consideration. Typically, the failure process can be cleavage, intergranuar/transgranular fracture (polycrystalline materials), cavitation (ductile metals, polymers), disentanglement of macromolecules (polymers), microcracking (glasses, ceramics), fiber breakage (composites), etc. Extension of the Griffith theory to account for some of these effects, and not just surface energy as in the original formulation, was first triggered by suggestions of Orowan (1948) to include energy associated with inelastic processes preceding material separation into the energy balance equation. Specifically, for ductile materials, Orowan suggested considering a zone of plastically deforming material that would consume an additional amount of energy γ_p per unit area of crack extension.

Extension of this idea to other materials is achieved in an analogous manner. In general, consider a volume defined by a characteristic length L_p at the tip of the crack as illustrated in Fig. 4; nonlinear deformation as well as damage processes are assumed to be confined to this volume in the vicinity of the crack tip, labeled

the *fracture process zone* and the external regions are subjected to linear elastic deformations. Furthermore, this length L_p is assumed to be small in comparison to other characteristic dimensions of the body containing the crack: $L_p << a$. This idea is commonly referred to as "small scale yielding", but more appropriately this should be identified as *small scale process zone*. Under such circumstances, the fracture criterion is still assumed to be given by the Griffith theory in Eq. (13), with the exception that γ is replaced by $\gamma + \gamma_p \equiv \Gamma$, where Γ is now denoted as the *fracture energy* per unit area and Eq. (13) may be rewritten as

$$G = 2\Gamma \tag{14}$$

In most cases, $\gamma_p >> \gamma$ and the latter could be ignored in estimating Γ. Furthermore, the fracture process is assumed to be self-similar in that each increment of crack extension is identical, dissipating the same amount of energy.

Remark 3 There is no size scale indicated in the formulation other than the restriction that the fracture process zone should be small: $L_p << a$. Thus the fracture criterion in Eq. (14) applies at scales ranging from the atomic—in length scales of a few tens of nanometers—to the geological—in earthquake fault problems dealing with length scales of a few hundred kilometers, with the only restriction being $L_p << a$.

Remark 4 The surface energy, γ, is typically on the order of a few J/m^2. However, when plastic deformation or other mechanisms are invoked inside the fracture process zone, the resulting fracture energy, Γ, could be several orders of magnitude greater, with the fracture energy being on the order of 10 J/m^2 for glasses and ceramics, about 100 to 1000 J J/m^2 for polymers, and to 100 kJ/m^2 for ductile metals. Γ may be determined through calibration experiments as described later.

Remark 5 Γ may be a function of the temperature and the strain-rate, resulting from changes in the development of the failure mechanisms within the fracture process zone.

Remark 6 If the equilibrium in Eq. (14) corresponds to a minimum energy configuration, the crack will stay in stable equilibrium at the calculated length; on the other hand, if the equilibrium corresponds to a maximum unstable crack extension will occur, and the energy balance expression in Eq. (9) has to be augmented with appropriate kinetic energy terms.

The continuum formulation discussed above, based on the theorem of minimum energy principle, provides a framework for the determination of the equilibrium and stability conditions of cracks in solids, enabling assessment of criticality of structures containing cracks. Application of this framework requires two essential ingredients: first, one needs a procedure for the calculation of the energy release rate. Second, an appropriate calibration of the fracture energy must be obtained for each material. We discuss these in the following section.

2.4 Calculation of the Energy Release Rate

The energy release rate for a linear elastic structure containing a crack can be derived from elementary mechanics as discussed here. Consider a cracked body of unit thickness as shown in Fig. 5. A load P (per unit thickness) is applied to the body through a compliant spring loading system, with a compliance C_M. The specimen contains a crack of length a, has a compliance that depends on the crack length, denoted by $C(a)$ and sustains a displacement between the load points Δ_{sp}. The total displacement between the loading points, Δ_T, is considered to be fixed:

$$\Delta_T = \Delta_M + \Delta_{sp} = [C_M + C(a)]\, P = \text{const} \tag{15}$$

We now consider the calculation of the potential energy change of the system at fixed overall displacement; in this condition, the additional work of external forces at the boundary is $dW_{\partial\Omega} = 0$. The strain energy is

$$U_\Omega = \frac{1}{2} C_M P^2 + \frac{1}{2} C(a) P^2 \tag{16}$$

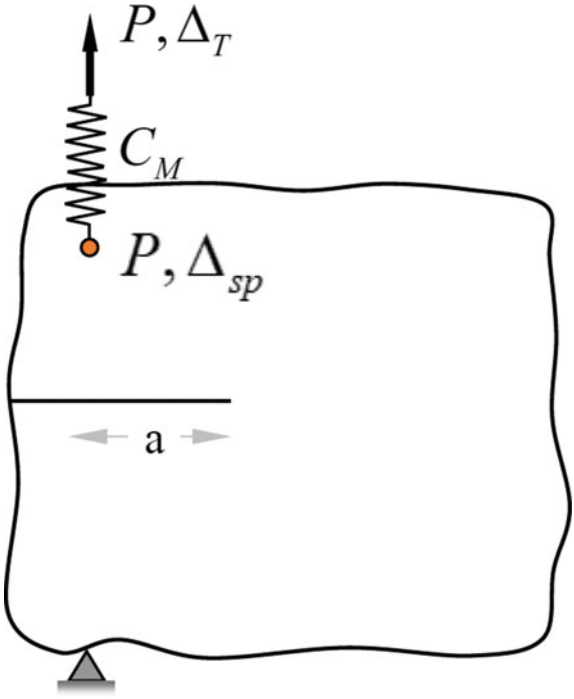

Fig. 5 Sketch of a cracked specimen loaded through a compliant loading machine

The first term corresponds to the strain energy stored in the loading machine, and the second term is the elastic strain energy in the specimen. Note that P can be eliminated between Eqs. (15) and (16) to obtain the strain energy in terms of the displacements as well. Next, the energy release rate G can be determined using

$$d\Delta_T = 0 = C'(a)Pda + [C(a) + C_M]\,dP$$
$$dU_\Omega = \frac{1}{2}P^2\,C'(a)da + [C(a) + C_M]\,P\,dP$$

and eliminating dP to get:

$$G = -\frac{d\Pi}{da} = -\frac{dU_\Omega}{da} = \frac{1}{2}P^2\,C'(a) = \frac{1}{2}C'(a)C^{-2}\Delta_{sp}^2 \tag{17}$$

where the prime stands for differentiation with respect to the argument. It is important to note that the energy release rate is independent of the loading machine compliance, and hence the equilibrium crack length depends only on the specimen compliance and the load. However, the machine compliance will influence the stability of the equilibrium condition; if we impose the condition in Eq. (11), the equilibrium will be stable if

$$E"(a) > 0 \Rightarrow 2\left[C'(a)\right]^2 > C"(a)\,[C_M + C(a)] \tag{18}$$

with a dependence on the machine compliance. Depending on the specimen and loading conditions, it is possible to trigger stable, unstable, and stick-slip type responses in the crack extension. We have now reduced the problem of evaluation of the energy release rate to the calculation of the specimen compliance, $C(a)$, which we will illustrate with a few very simple examples.

Example 1 Obreimoff's experiment on cantilever beam specimens.

The first example we consider is an experiment performed by Obreimoff (1930) on mica with the aim of providing a method for determining the fracture energy. Consider inserting a wedge of height Δ into a thick slab of mica in order to separate a layer of mica of height d from a large block as shown in Fig. 6; at equilibrium, the wedge exerts a force P on the layer that has separated over a length a.

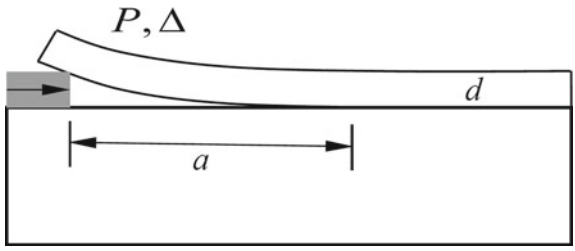

Fig. 6 Wedge driven into a mica sheet to cleave a layer of thickness d

Considering the layer of the mica to be a beam of unit width, the compliance of the system can be calculated from elementary mechanics. Bernoulli-Euler beam theory indicates that the wedge height and the force are related by the cantilever beam deflection formula:

$$\Delta = \frac{Pa^3}{3EI} \tag{19}$$

where E is the modulus of elasticity and $I = d^3/12$ is the second moment of the crosssection of the layer, per unit width of the layer. Then the compliance of the specimen can be expressed as

$$C(a) = \frac{4a^3}{Ed^3}; \quad C'(a) = \frac{12a^2}{Ed^3}; \quad C''(a) = \frac{24a}{Ed^3} \tag{20}$$

The energy release rate is then obtained by substitution into Eq. (17) either in terms of the force P or in terms of the wedge height Δ as:

$$G = \frac{6a^2P^2}{Ed^3} = \frac{3Ed^3\Delta^2}{8a^4} \tag{21}$$

The equilibrium crack length can be obtained by setting this equal to the fracture energy, 2Γ; rearranging, we determine the equilibrium crack length in terms of the wedge height:

$$a = \left(\frac{3Ed^3\Delta^2}{16\Gamma}\right)^{\frac{1}{4}} \tag{22}$$

If the equilibrium crack length is measured for given layer thickness and wedge height, Eq. (22) can be used to determine the fracture energy, Γ, as demonstrated by Obreimoff's experiments.[1] It is a straightforward exercise to find that under prescribed wedge height Δ, the crack length is stable at the length given by Eq. (22). In Obreimoff's original experiments, he also retracted the wedge and showed that healing can occur with lower fracture energy when tested in ambient air. Furthermore, he demonstrated that the fracture energy was significantly greater when tested under a vacuum environment to prevent contamination.

Example 2 Double-cantilever beam specimen.

Another very popular geometry of a body with a crack that has been used extensively as a means for determining the fracture energy experimentally is the double-cantilever-beam (DCB) configuration illustrated in Fig. 7. The main difference from the Obreimoff experiment is the use of two cantilevers that are symmetrically disposed with respect to the horizontal. In addition, we will consider that the loading

[1] Obreimoff considered a bending moment applied at the tip of the separated layer of mica. It is interesting to note that although Obriemoff published his results ten years after Griffith, in the same journal, he makes no reference to Griffith!

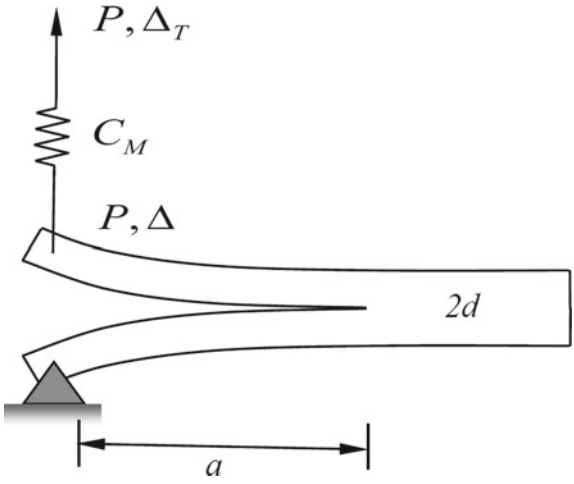

Fig. 7 Double cantilever beam (DCB) specimen configuration

is applied through a compliant machine so that the machine compliance effects on equilibrium and stability can be explored. The compliance in Eq. (20) is multiplied by two to account for the presence of two beams:

$$C(a) = \frac{8a^3}{Ed^3}; \quad C'(a) = \frac{24a^2}{Ed^3}; \quad C''(a) = \frac{48a}{Ed^3} \tag{23}$$

Calculating the energy release rate and substituting into the fracture criterion yields the equilibrium crack length

$$a = \left(\frac{3Ed^3\Delta^2}{32\Gamma}\right)^{\frac{1}{4}} = \left(\frac{E\Gamma d^3}{6P^2}\right)^{\frac{1}{2}} \tag{24}$$

in terms of either the wedge height or the load. If the stability condition in Eq.(18) is evaluated, we find that the equilibrium is stable if

$$\frac{a}{d} > \left(\frac{C_M E}{16}\right)^{\frac{1}{3}} \tag{25}$$

If the load is kept fixed, corresponding to $C_M \to \infty$, the equilibrium is unstable; on the other hand, for a fixed displacement on the cantilever, corresponding to $C_M \to 0$ the crack is always stable. In practice, since the compliance of the loading machine is unlikely to be zero, there is a minimum initial crack length given by Eq. (25) beyond which the equilibrium is stable.

Example 3 Semi-infinite strip specimen.

Next, we consider the semi-infinite strip configuration of unit thickness as illustrated in Fig. 8. The width of the strip is large in relation to the height $2h$. The material is

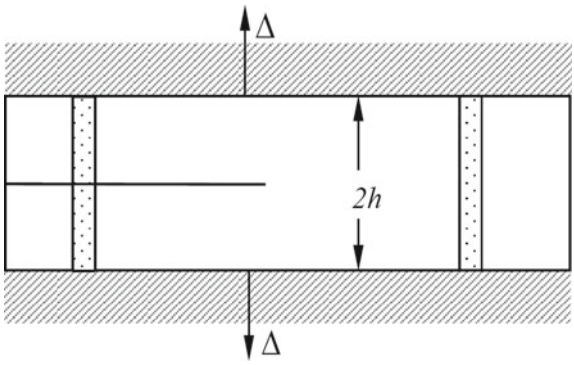

Fig. 8 Semi-infinite strip specimen

considered to obey Hooke's law. The specimen is held by a rigid support along the upper and lower boundaries of the strip, and displaced symmetrically in the vertical direction by an amount Δ such that the crack located along the line of symmetry grows at a steady-state along the horizontal direction. The energy release rate corresponding to this can be estimated quite easily through a simple argument. Far to the right side from the tip of the crack, the stress and strain state in the strip are uniform, and are given by

$$\begin{cases} \varepsilon_{11} = [\sigma_{11} - \nu\sigma_{22}]/E = 0 \\ \varepsilon_{22} = [\sigma_{22} - \nu\sigma_{11}]/E = \Delta/h \end{cases} \tag{26}$$

At steady-state, for an extension of the crack by an amount Δa, a vertical strip of width Δa far ahead of the crack that is uniformly stretched can be thought of as being cracked and transported into an unstressed, broken strip far behind the crack tip as illustrated by the shaded strips in Fig. 8. The elastic energy released from this vertical strip as the crack extends by an amount Δa is calculated to be

$$\Delta U_\Omega = \frac{1}{2}\sigma_{22}\varepsilon_{22}(2h\Delta a) = \frac{E(\Delta/h)^2}{2(1-\nu^2)}(2h\Delta a) \tag{27}$$

At fixed displacement Δ, the energy release rate is

$$G = -\frac{\Delta U_\Omega}{\Delta a} = \frac{E\Delta^2}{(1-\nu^2)h} \tag{28}$$

This enables the determination of the fracture energy under a fixed grip condition; this specimen geometry has been used extensively in the characterization of polymers, solid-propellants, rubbers, soft-materials and numerous other materials. It is easy to show that the crack extension is neutrally stable in this geometry.

Example 4 Peeling of an adhesively bonded tape.

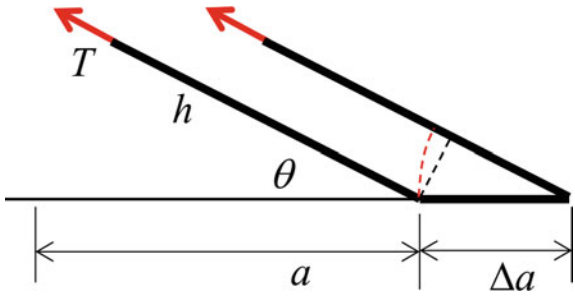

Fig. 9 Geometry of peeling of a tape at an angle θ

The problem of peeling of an adhesively bonded tape from rigid substrate has received a lot of attention. We consider the most elementary formulation of the problem presented by Kendall (1971, 1975). Consider a tape of unit width, inextensible and flexible, and adhered to a rigid substrate. A portion of the tape of length a is debonded and lifted to an angle θ and a tension T (per unit width) is applied as indicated in Fig. 9. The energy release rate is estimated as follows: since the tape is inextensible and flexible, there is no strain energy in the system; therefore one has to calculate only the change in the work done by the applied forces. If we consider peeling by an increment, Δa, at fixed tension, the geometry of the tape changes as illustrated by the red dashed line in Fig. 9. As a result, the point of load application must move by an amount $(1 - \cos\theta)\Delta a$ and the additional work done by the external force is: $\Delta W_{\partial\Omega} = (1 - \cos\theta)\Delta a$. Therefore the energy release rate is obtained as

$$G = \frac{\Delta W_{\partial\Omega}}{\Delta a} = T(1 - \cos\,\theta) \tag{29}$$

At steady peeling, this energy release rate must be equated to the adhesive energy for peeling the tape from the substrate, denoted by γ_A; thus the peel force necessary is

$$T = \gamma_A(1 - \cos\theta)^{-1} \tag{30}$$

Clearly, the force necessary to peel is the smallest at γ_A when $\theta = \pi$, bending the tape back on itself. On the other hand, when $\theta \to 0,\ T \to \infty$, implying that horizontal peeling is not possible. This is a consequence of the assumption of inextensibility; for an inextensible tape pulled horizontally, the applied tension can do no additional work with increase of Δa and hence the adhesion cannot be overcome. In order to remove this peculiarity, we need to consider the case of an elastically extensible tape, still flexible. Now, in addition to the work done by the external force, the elastic energy change in the tape must be estimated; this requires special care not only in the elastic elongation of the tape, but the additional work done by the external force due to this elongation. First, the newly peeled length Δa acquires elastic energy from the tension

$$\Delta U_\Omega = \frac{T^2\Delta a}{2Eh} \tag{31}$$

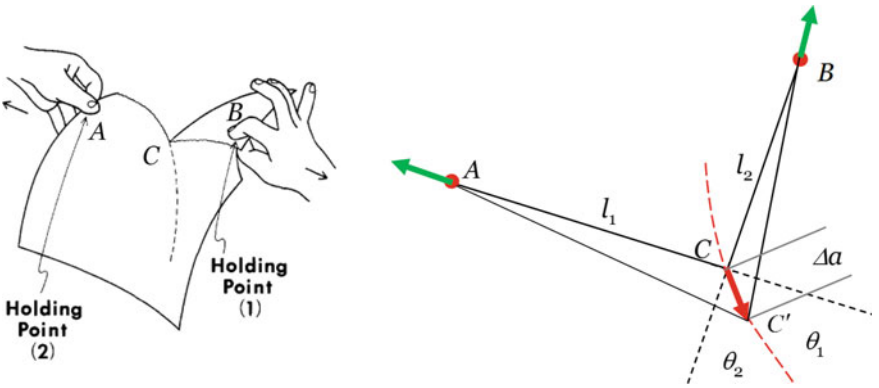

Fig. 10 **a** Tearing of paper (reproduced from O'Keefe 1994, and marked). **b** Geometry of the tear mapped on to the flat undeformed configuration of the paper

Next, the tension moves through the distance estimated for the inextensible tape, plus an additional amount due to the elongation of the tape segment Δa; thus,

$$\Delta W_{\partial\Omega} = T(1-\cos\theta)\Delta a + T\left(\frac{T\,\Delta a}{hE}\right) \tag{32}$$

The energy release rate is then calculated as

$$G = \frac{\Delta W_{\partial\Omega}}{\Delta a} - \frac{\Delta U_{\Omega}}{\Delta a} = T(1-\cos\theta)\Delta a + \frac{T^2}{2hE} \tag{33}$$

Equating this to the adhesive energy of the tape, results in a nonlinear equation for the peel force at equilibrium:

$$T(1-\cos\theta) + \frac{T^2}{2hE} = \gamma_A \tag{34}$$

Comparing Eqs. (34) and (30), it is apparent that the force required for peeling is lower for the elastic tape in comparison to the inextensible tape. In particular, the force required for horizontal peeling is found to be $T = \sqrt{2hE\gamma_A}$. It is also possible to consider the effects of nonzero bending stiffness (Roman 2013) and plasticity in estimating the force necessary for peeling (Kim and Aravas 1988; Kinloch et al. 1994, Wei and Hutchinson 1998). There is a large literature on various additional aspects of this problem.

Example 5 Tearing of paper.

In the next example, we consider another problem in which the body is inextensible and flexible so that only the work of external forces exchanges energy with the fracture energy. This problem was addressed by O'Keefe (1994) and Roman (2013).

Consider a thin sheet of paper that is inextensible and flexible. The sheet is first torn from one edge to some interior point to introduce a precrack, with its tip at C as illustrated in Fig. 10a. Subsequently, it is held at two points A and B on either side of the torn edge and torn further by pulling apart with a force T. Calculation of the energy release rate follows a very simple logic: static equilibrium implies that the forces at A and B must be equal and opposite to each other; in addition, the sheet will bend and twist in such a manner that the crack tip C will be along the line connecting A and B, as illustrated in Fig. 10a. The latter requirement can be demonstrated through a simple idea; first, consider that the line connecting A and B does not either pass through the crack tip C or intersect the crack line. Then the line of action of the force does not influence the crack tip at all; in this condition the paper will not tear from the crack. Next, consider the line connecting A and B to intersect the crack line, away from the tip; upon application of a force, the sheet will bend and twist with little resistance until the line connecting A and B passes through the crack tip and exhibit greater resistance! Hence the condition that the line $\overrightarrow{AB}$ must pass through C. It is easy to argue that this system of forces could be drawn in the flat reference state of the sheet since the sheet is inextensible and has zero bending stiffness; this is illustrated in Fig. 10b. Let us denote $\overrightarrow{AC} = l_1$ and $\overrightarrow{BC} = l_2$. The continued path of the crack is shown by the red dashed line in the figure, subtending an angle θ_1 and θ_2 with the prolongations of the lines $\overrightarrow{AC}$ and $\overrightarrow{BC}$, respectively. When the crack extends an amount Δa from C to C' along a dashed line, the forces at A and B move through a distance $dl_1 = \Delta a \cos\theta_1$ and $dl_2 = \Delta a \cos\theta_2$, respectively, and do additional work. The energy release rate is then obtained as:

$$G = -\frac{\Delta \Pi}{\Delta a} = \frac{\Delta W_{\partial R}}{\Delta a} = T(\cos\,\theta_1 + \cos\,\theta_2) \tag{35}$$

Applying the fracture criterion results in

$$T = (\cos\,\theta_1 + \cos\,\theta_2) = 2\Gamma \tag{36}$$

Here, we need an additional consideration in order to determine the direction of crack extension; it is postulated that *the crack will choose that direction along which the energy release rate is a maximum* since this will result in the smallest force at which the energy criterion is satisfied. For this problem, this is equivalent to maximizing the energy release rate keeping the total angle $\theta_1 + \theta_2$ constant. This yields $\theta_1 = \theta_2 = \theta$, implying that the crack will follow the direction that bisects the angle ACB, yielding a hyperbolic crack path with A and B as the foci. Imposing the fracture criterion in Eq. (14), we get the force necessary to tear the paper as a function of position:

$$T = \Gamma \sec\,\theta \tag{37}$$

The bisector ACB is $\theta = \pi/2$ when the crack tip lies on the major axis of the hyperbola and decreases to zero as the crack tip grows far from the major axis.

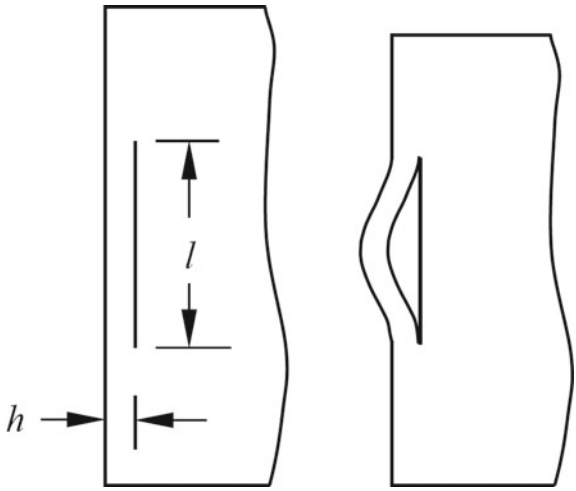

Fig. 11 Buckling driven delamination

Equation (37) indicates that, given a fixed fracture energy, Γ, the force required to tear decreases monotonically as the crack extends farther from the major axis. Other examples of such problems may be found in Roman (2013).

Example 6 Delamination of a layer from a substrate.

The delamination problem was considered by Chai et al. (1984). It is of importance in composite structures, thin film devices and other applications. Consider an elastic layer of thickness, h and modulus, E bonded to a thick substrate as illustrated in Fig. 11; the system is subjected to a compressive strain ε in the vertical direction. The length l of the layer is debonded from the substrate as illustrated in Fig. 11. At a critical strain level, the debonded layer reaches the Euler buckling load and is then able to take a buckled shape as indicated in Fig. 11. The interplay between the applied compressive loading, the post-buckled shape and the fracture energy at the tip of the delamination can be analyzed to determine the conditions for the growth of the delamination. We proceed as follows: first, we consider the Euler critical load; subsequently we assume a suitable buckled shape for the delaminated part and based on this, the energy release rate is calculated.

The onset of buckling of the delamination requires a critical strain level, ε_{cr}. The critical strain is obtained as follows, for a fixed-fixed Euler beam:

$$\varepsilon_{cr} = \frac{P_{cr}}{Eh} = \frac{\pi^2}{3}\left(\frac{h}{l}\right)^2 \tag{38}$$

where P_{cr} is the buckling load per unit thickness. For $\varepsilon < \varepsilon_{cr}$, the deformation is uniform compression. When $\varepsilon > \varepsilon_{cr}$, we need to estimate the post-buckled shape. Let the buckled shape be as follows:

$$y(x) = \frac{A}{2}\left(1 + \cos\frac{2\pi x}{l}\right) \tag{39}$$

This satisfies the conditions: $y\left(\pm\frac{1}{2}\right) = 0; y'\left(\pm\frac{1}{2}\right) = 0$. Also, $y(0) = A$. Next, we use the geometric compatibility condition to relate the peak deflection to the compressive strain; the shortening of the ends under a stain ε beyond the critical strain ε_{cr} is written as:

$$(\varepsilon - \varepsilon_{cr})l = \frac{1}{2}\int_{-l/2}^{l/2}(y')^2 dx = \frac{A^2\pi^2}{4l} \Rightarrow A = \sqrt{\varepsilon - \varepsilon_{cr}}\frac{2l}{\pi} \tag{40}$$

The strain energy is composed of two parts, one due to compression and the other due to bending. The strain energy of compression is

$$U_c = \frac{1}{2}E\varepsilon_{cr}^2 hl \Rightarrow \frac{U_c}{Eh} = \frac{l\varepsilon_{cr}^2}{2} \tag{41}$$

The bending energy is obtained as follows:

$$U_b = \frac{1}{2}EI\int_{-l/2}^{l/2}(y")^2 dx \Rightarrow \frac{U_b}{Eh} = (\varepsilon - \varepsilon_{cr})\frac{\pi^2}{3}\left(\frac{h^2}{l}\right) \Rightarrow \frac{U_b}{Eh} = l(\varepsilon\varepsilon_{cr} - \varepsilon_{cr}^2) \tag{42}$$

The energy release rate can be obtained as

$$G(l,\varepsilon) = -\lim_{\Delta t\to 0}\frac{l}{\Delta l}\left[\{U_b(l+\Delta l) - U_b(l)\} + \{U_c(l+\Delta l) - U_c(l)\} - \frac{1}{2}Eh\varepsilon^2\Delta l\right] \tag{43}$$

The last term inside the bracket is the compressive energy in the portion Δl that comes into the delaminated portion. Substituting and simplifying, we get the energy release rate as a function of the applied compressive strain ε and the length of the delamination, l:

$$\frac{G(l,\varepsilon)}{Eh} = \frac{1}{2}(\varepsilon - \varepsilon_{cr})(\varepsilon + 3\varepsilon_{cr}) = \frac{1}{2}\left[\varepsilon^2 + \frac{2}{3}\left(\frac{\pi h}{l}\right)^2\varepsilon - \frac{1}{3}\left(\frac{\pi h}{l}\right)^4\right] \tag{44}$$

Clearly, the energy release rate is positive only if $\varepsilon > \varepsilon_{cr}$; otherwise there is no buckling! However, even after onset of buckling, the delamination will not grow unless the fracture criterion is met. Figure 12a shows the variation of the normalized energy release rate as a function of normalized l for different fixed strain levels. In order to impose the fracture criterion Eq. (14), the fracture energy is indicated in the figure by the black dashed line. For a delamination with an initial length l_0

fracture criterion is met at the point labeled A corresponding to a strain level ε_0, and the crack may extend; however, the energy release rate will increase with the delamination length even at fixed strain level, and hence an unstable growth occurs until the point labeled B, where equilibrium is again established, but this time with a decrease in the energy release rate with increasing delamination length and hence a stable extension. Another way of indicating this is to apply the fracture criterion in Eq. (14) to the energy release rate in Eq. (44) and rearranging to yield the locus of equilibrium states in the delamination length versus applied strain plane:

$$\varepsilon^2 + \frac{2}{3}\left(\frac{\pi h}{l}\right)^2 \varepsilon - \frac{1}{3}\left(\frac{\pi h}{l}\right)^4 - \frac{4\Gamma}{Eh} = 0 \tag{45}$$

Rescaling the strain as $\varepsilon \left(\frac{Eh}{4\Gamma}\right)^{1/2}$ and crack length as $\frac{\sqrt{3}}{\pi}\frac{l}{h}\left(\frac{Eh}{4\Gamma}\right)^{1/4}$ the locus of critical states (ε_0, l_0) is plotted in Fig. 12b. As the strain increases, with a fixed delamination length, the fracture criterion is satisfied at the point labeled A but longer lengths of the delamination require smaller strain levels to be in equilibrium; clearly an unstable growth to the point labeled B must occur. More examples on delamination can be found in the article by Hutchinson and Suo (1992).

The examples above illustrate the power of the global point of view of fracture. Without paying attention to the details of the stress and strain fields in the vicinity of the crack tip, or to account for all inelastic and damage processes that occur with a small fracture process zone creating the new surface, the minimum potential energy criterion of Griffith (1921) has been applied to a number of problems of fracture. In the examples considered, we were able to calculate the energy release rate through application of mechanics solutions through various assumptions and approximations to determine the equilibrium crack length. Even in problems where this is not accomplished readily in closed-form, it is possible to determine the compliance of the component containing a crack, $C(a)$, either by performing repeated experiments

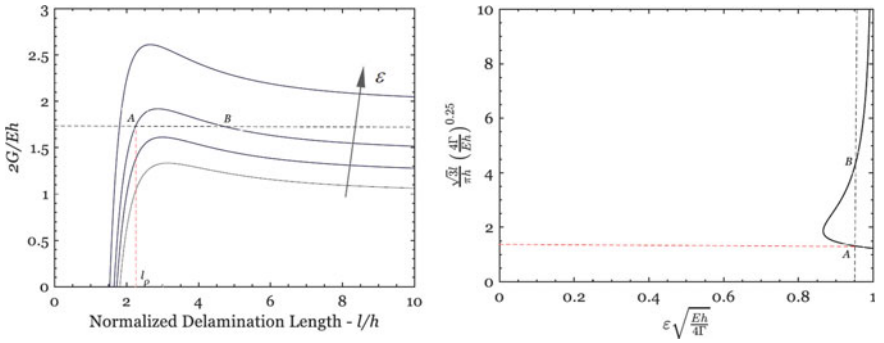

Fig. 12 **a** Variation of the energy release rate with delamination length for different applied strain levels. **b** Locus of critical strain level and delamination length

or numerical simulations of the geometry with different crack lengths and using Eq. (17) to estimate the energy release rate. However, for more complex structures this approach may be difficult. The practical use of fracture mechanics in promoting fail-safe, fracture-critical design was accomplished through the development of an engineering approach beginning with the works of Irwin (1957), Williams (1952, 1957), and others. This approach is called linear elastic fracture mechanics of LEFM and is discussed in the next section.

3 Linear Elastic Fracture Mechanics—The Local Approach to Fracture

The local approach to fracture relies on a linear elastic analysis of the stress, deformation and energy fields in the vicinity of the crack tip and postulating a fracture criterion in terms of these local quantities. We begin with a brief overview of the theory of linear elasticity. Complete treatments of the topic including solution techniques and details of the classical solutions can be found in the classical books by Love (1927), Timoshenko and Goodier (1951), Mushkhelishvili (1953) and others. Consider a body occupying the region Ω with boundaries $\partial\Omega$. Let the displacement vector be denoted by $u_i(\mathbf{x})$[2]; the strain tensor $\varepsilon_{ij}(\mathbf{x})$ is its symmetric gradient and hence its components are given by:

$$\varepsilon_{ij}(\mathbf{x}) = \frac{1}{2}\left(u_{i,j} + u_{j,i}\right) \tag{46}$$

Here we consider the infinitesimal strain tensor and therefore neglect higher order terms involving higher powers of the gradient of $\mathbf{u}(\mathbf{x})$. It is also assumed that $\mathbf{u}(\mathbf{x})$ is a continuous function of $\mathbf{x}$, with continuous derivatives as needed. The material of the body is assumed to be homogeneous, isotropic and linearly elastic. Therefore, the components of the stress tensor $\boldsymbol{\sigma}(\mathbf{x})$ are related to the components of the strain tensor by:

$$\varepsilon_{ij} = \frac{1}{E}\left[(1+\nu)\sigma_{ij} - \nu\sigma_{kk}\delta_{ij}\right] \tag{47}$$

where E is the modulus of elasticity, ν is the Poisson's ratio and δ_{ij} is the Kronecker delta. The balance of linear momentum results in the following equations of equilibrium

$$\sigma_{ij,j} + f_i = 0 \tag{48}$$

[2] Standard index notation will be used throughout this chapter. Latin subscripts take the range 1, 2, 3 while Greek subscripts take the range 1, 2. Repeated index implies summation over the range of the index and an index following a comma indicates partial differentiation with respect to the coordinate identified by that index.

where f_i are the body force components per unit volume. Balance of angular momentum dictates that the stress tensor must be symmetric. This is a system of three partial differential equations governing the displacements of points in the body. We shall assume that the body forces vanish and remove them from consideration in subsequent equations. To the set of equations in (48), we must add boundary conditions.

There are three fundamental problems that can be posed, depending on whether the displacements, tractions or some combination are prescribed on the boundaries. For the displacement boundary value problem

$$u_i(\mathbf{x}) = u_i^*(\mathbf{x}) \tag{49}$$

on $\partial\Omega$, where $u_i^*(\mathbf{x})$ is a prescribed function of position on the boundary. For the traction boundary value problem, the components of the traction vector, $t_i(\mathbf{x})$, are prescribed

$$t_i(\mathbf{x}) = \sigma_{ij}(\mathbf{x})n_j(\mathbf{x}) = t_i^*(\mathbf{x}) \tag{50}$$

on $\partial\Omega$, where $n_i(\mathbf{x})$ are the components of the unit outward normal and $t_i^*(\mathbf{x})$ are prescribed functions. The third problem is the mixed-boundary value problem for which the displacements are prescribed in a part of the boundary and tractions are prescribed over the remainder:

$$\begin{aligned} u_i(\mathbf{x}) &= u_i^*(\mathbf{x}) && \text{on } \partial\Omega_u \\ t_i(\mathbf{x}) &= \sigma_{ij}(\mathbf{x})n_j(\mathbf{x}) = t_i^*(\mathbf{x}) && \text{on } \partial\Omega_t \end{aligned} \tag{51}$$

with $\partial\Omega_u \cup \partial\Omega_t = \partial\Omega$ and $\partial\Omega_u \cap \partial\Omega_t = \phi$. In formulating boundary value problems involving cracks, it is convenient to separate the different loading symmetries to simplify the analysis and interpretation. Consider a crack as illustrated in Fig. 13a. Let **CP** indicate the crack plane (black shaded region), terminating at **CF**, the crack front. Let **t** denote the unit tangent to **CF** and **n** denote normal to **CP**; finally, let **b** denote a unit vector normal to both **n** and **t**. Locally to any point **s** on the **CF** we may consider a planar slice as illustrated in Fig. 13b and then consider three symmetries illustrated in Fig. 13c.

Mode I corresponds to opening of the crack with loads in the **n** direction, normal to the crack surface. Shearing of the crack with loads lying in the plane of the crack can be further decomposed into a shear perpendicular to the crack front (loading in the **b** direction), resulting in in-plane or longitudinal shear called ***Mode II***, and shear parallel to the crack front, (loading in the n direction) resulting in out-of-plane or anti-plane shear, called ***Mode III***. In the following sections, we will examine the Mode III problem first, and then follow with Modes I and II. Care should be exercised in identifying Mode III, since this is difficult to establish in bodies with finite thickness as we will highlight later.

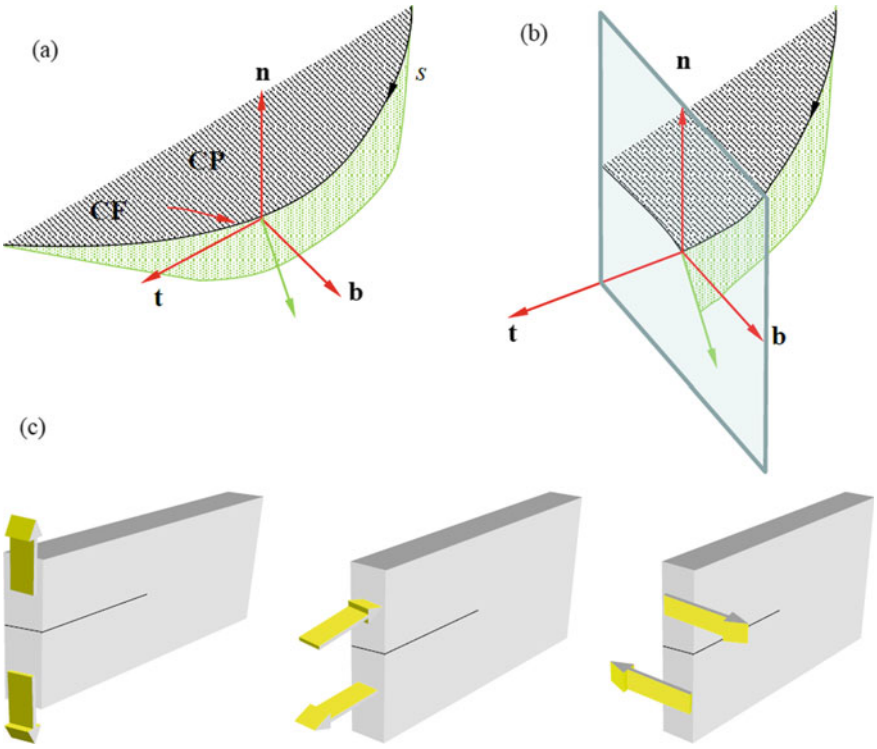

Fig. 13 Sketch illustrating the definitions of opening mode or Mode I, in-plane shear or Mode II and out-of-plane shear or Mode III loading of cracks

3.1 Anti-plane Shear—Mode III

The anti-plane shear deformation is based on the assumption that the only nonzero displacement component is in the x_3 direction and further that it is a function of x_1 and x_2:

$$u_\alpha = 0; u_3 = u_3(x_1, x_2) \tag{52}$$

As a consequence, the strain-displacement relations in Eq. (46) yield

$$\begin{aligned} &\varepsilon_{\alpha\beta} = 0; \quad \varepsilon_{33} = 0; \\ &2\varepsilon_{31} = u_{3,1}(x_1, x_2); \quad 2\varepsilon_{32} = u_{3,2}(x_1, x_2); \end{aligned} \tag{53}$$

Then substituting into the stress-strain relations in Eq. (47) results in the stresses:

$$\begin{aligned} &\sigma_{\alpha\beta} = 0; \quad \sigma_{33} = 0; \\ &\sigma_{31} = \mu u_{3,1}(x_1, x_2); \quad \sigma_{32} = \mu u_{3,2}(x_1, x_2); \end{aligned} \tag{54}$$

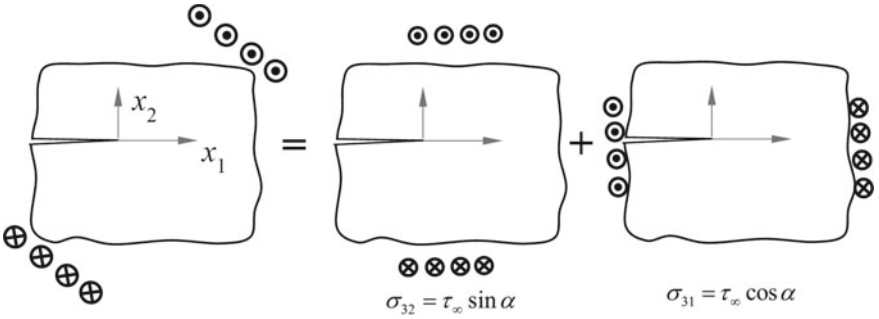

Fig. 14 Sketch illustrating Mode III loading of cracks

where $2\mu = E/(1+\nu)$. Substitution of the above into the equilibrium equations in Eq. (48) results in Laplace's equation for the out-of-plane displacement component u_3

$$\nabla^2 u_3 = u_{3,\alpha\alpha} = 0 \tag{55}$$

The u_3 displacement is prescribed on boundaries $\partial\Omega_u$,

$$u_3 = u_3^* \tag{56}$$

while on the traction boundaries $\partial\Omega_t$ we have $t_3 = (\sigma_{31}n_1 + \sigma_{32}n_2) = t_3^*$ yielding

$$\mu\frac{\partial u_3}{\partial n} = t_3^* \tag{57}$$

In general, we have a mixed Dirichlet-Neumann problem for the anti-plane shear problem. We will now look closely at what happens near a traction free crack tip as illustrated in Fig. 14. Specifically, for the crack surfaces on $x_2 = 0^{\pm}$, we must have

$$\sigma_{32} = \mu u_{3,2} = 0 \tag{58}$$

Let us consider a uniform shear stress τ^∞ applied in the far field at an angle α with respect to the x_1 direction as illustrated in the left of Fig. 14. This can be decomposed into the sum of two problems with components of shear $\sigma_{32} = \tau^\infty \sin\alpha$ and $\sigma_{31} = \tau^\infty \cos\alpha$ prescribed as shown in the middle and right of Fig. 14. For the case in the right, assuming that $\sigma_{31} = \tau^\infty \cos\alpha$ and $\sigma_{32} = 0$ everywhere satisfies the traction free conditions on the crack surface; hence the shear stress is parallel to the crack, bounded everywhere and crack plays no role in altering the stress field. Therefore, only the loading through the stress component $\sigma_{32} = \tau^\infty \sin\alpha$ is of importance in the fracture problem. We now consider the analysis of the structure of the solution near the crack tip, by enforcing the traction free boundary condition. It is convenient to use polar coordinates in developing the solution; Eq. (55) is then

rewritten in polar coordinates as

$$\frac{\partial^2 u_3}{\partial r^2} + \frac{1}{r}\frac{\partial u_3}{\partial r} + \frac{1}{r^2}\frac{\partial^2 u_3}{\partial \theta^2} = 0 \tag{59}$$

and the boundary condition is written as $u_{3,2}(r, \pm\pi) = 0$. We seek solutions by separation of variables, with $u_3(r, \theta) = r^\lambda f(\theta)$, anticipating a power-law form for the radial variation. Then Eq. (59) yields $f''(\theta) + \lambda^2 f(\theta) = 0$, with a general solution of the form

$$u_3(r, \theta) = r^\lambda [A \cos \lambda\theta + B \sin \lambda\theta] \tag{60}$$

Anti-plane symmetry requires $u_3(r, \theta) = -u_3(r, -\theta)$; hence we have $A = 0$, and

$$\begin{aligned} u_3(r, \theta) &= Br^\lambda sin\lambda\theta \\ \sigma_{32} &= \mu u_{3,2}(r, \theta) = \mu B r^{\lambda-1} \cos(\lambda - 1)\theta \end{aligned} \tag{61}$$

The boundary condition $u_{3,2}(r, \pm\pi) = 0$ implies that either $B = 0$ or $\cos(\lambda - 1)\pi = 0$. The non-trivial solution requires $\lambda = m/2$ with $m = \pm 1, \pm 3, \ldots$ and the general solution for the displacement as

$$u_3(r, \theta) = \sum_{m=\pm 1, \pm 3, \ldots} B_m r^{m/2} \sin\left(\frac{m\theta}{2}\right) \tag{62}$$

And the corresponding stress components can be calculated to be

$$\begin{aligned} \sigma_{31}(r, \theta) &= \sum_{m=\pm 1, \pm 3, \ldots} \frac{\mu m}{2} B_m r^{\frac{m}{2}-1} \sin\left(\frac{m}{2} - 1\right)\theta \\ \sigma_{32}(r, \theta) &= \sum_{m=\pm 1, \pm 3, \ldots} \frac{\mu m}{2} B_m r^{\frac{m}{2}-1} \cos\left(\frac{m}{2} - 1\right)\theta \end{aligned} \tag{63}$$

Equations (62)–(63) represent the structure of the solution in the vicinity of the crack tip compatible with traction free crack surfaces. The coefficients B_m are as yet undetermined, but should be related to the far-field boundary conditions. First, we examine the implications on the displacement and stress components as $r \to 0$. For all $m \leq -1$, $u_3(r, \theta) = B_m r^{-|m|/2} \sin\theta/2$, and hence $u_3(r, \theta) \to \infty$ as $r \to 0$; this singularity in displacements is physically unacceptable, and therefore all terms $m \leq -1$ must be eliminated from the solution. Next, if we examine terms with $m \geq 3$, $u_3(r, \theta) = B_m r^{m/2} \sin 3\theta/2$, $\sigma_{32} = B_m r^{(m-1)/2} \sin 3\theta/2$ and $\sigma_{31} = B_m r^{(m-1)/2} \sin 3\theta/2$; thus, these terms may be important at large distances from the crack tip, but since they tend to zero as $r \to 0$, they do not play a role in the vicinity of the crack tip. The term $m = 1$ results in

$$
\begin{aligned}
u_3(r,\theta) &= B_1 r^{1/2} \sin\frac{\theta}{2} \\
\sigma_{31}(r,\theta) &= -\frac{\mu B_1}{2} r^{-1/2} \sin\frac{\theta}{2} \\
\sigma_{32}(r,\theta) &= \frac{\mu B_1}{2} r^{-1/2} \cos\frac{\theta}{2}
\end{aligned}
\tag{64}
$$

Clearly, the stresses are singular, and one must reject this term just as we did with the $m \leq -1$ terms. However, in addition to the fact that this will eliminate all the terms near the crack tip, we retain the $m = 1$ term based on two simple arguments. First, if we neglect a small region $r < L_p$, where L_p is the small region in which failure processes occur, the variation in Eq. (64) might still be taken to represent the displacement and stress field in the vicinity of $r \to 0$. Second, if we calculate the strain energy density $W = \mu\left(u_{3,1}^2 + u_{3,2}^2\right)/2$ in this region, and integrate this over a circular region, we get

$$
U = \int W r dr d\theta \propto \int r^{m-1} dr d\theta \tag{65}
$$

Clearly, the strain energy is bounded for the $m = 1$ term. Thus, we can take Eq. (64) to characterize the crack tip stress field with a number of important attributes: the stress components are singular being proportional to $r^{-1/2}$; the displacement is proportional to $r^{1/2}$, and the strain energy is bounded. Furthermore, there is a coefficient, B_1, that governs the magnitude of the singular field that is undetermined from this local analysis, but can be determined by imposing the far field loading condition and solving the corresponding boundary value problem.

In the fracture mechanics literature, this amplitude term is redefined as the *Mode III stress intensity factor* through the following definition:

$$
K_{III} = \lim_{r\to 0} \sqrt{2\pi r}\,\sigma_{32}(r,0) \tag{66}
$$

essentially setting $\mu B_1 = \sqrt{2/\pi} K_{III}$. Using this redefinition, the crack tip displacement and stress field are written as

$$
\begin{aligned}
u_3(r,\theta) &= \frac{2K_{III}}{\mu}\sqrt{\frac{r}{2\pi}} \sin\frac{\theta}{2} \\
\sigma_{31}(r,\theta) &= -\frac{K_{III}}{\sqrt{2\pi r}} \sin\frac{\theta}{2} \\
\sigma_{32}(r,\theta) &= \frac{K_{III}}{\sqrt{2\pi r}} cos\frac{\theta}{2}
\end{aligned}
\tag{67}
$$

The field expressed above is expected to hold near the tip of any crack loaded with a Mode III loading symmetry, with the only difference being the magnitude of the Mode III stress intensity factor.

3.2 In-Plane Loading—Modes I and II

The problems of Modes I and II can be formulated either in the plane-strain or plane-stress condition. We consider plane-strain conditions first; for this condition, it is assumed that the u_3 displacement is either constant or linear in x_3, and further that the remaining components are independent of x_3:

$$u_{3,\alpha} = 0; \quad u_\alpha = u_\alpha(x_1, x_2) \tag{68}$$

As a consequence, the strain-displacement relations in Eq. (46) yield

$$2\varepsilon_{\alpha\beta} = u_{\alpha,\beta} + u_{\beta,\alpha}; \quad \varepsilon_{33} = 0 \quad \varepsilon_{3\alpha} = 0 \tag{69}$$

Then substituting into the stress-strain relations in Eq. (47) results in the stresses:

$$\varepsilon_{\alpha\beta} = \frac{1+\nu}{E}\left(\sigma_{\alpha\beta} - \nu\sigma_{\gamma\gamma}\delta_{\alpha\beta}\right); \quad \sigma_{33} = \nu\sigma_{\alpha\alpha}; \quad \sigma_{3\alpha} = 0 \tag{70}$$

Substitution of the above into the equilibrium equations in Eq. (48) results in a reduction of the dimension of the equation, but not any simplification:

$$\sigma_{\alpha\beta,\beta} + f_\alpha = 0 \tag{71}$$

The displacement boundary conditions on $\partial\Omega_u$ and the traction boundary conditions on $\partial\Omega_t$ are written as,

$$\begin{aligned} u_\alpha &= u_\alpha^* && \text{on } \partial\Omega_u \\ t_\alpha &= \sigma_{\alpha\beta} n_\beta = t_\alpha^* && \text{on } \partial\Omega_t \end{aligned} \tag{72}$$

Specifically, for the crack surfaces on $x_2 = 0^\pm$, we have traction free conditions, expressed in terms of the stress components as:

$$\sigma_{22}\left(x_1, 0^\pm\right) = 0; \qquad \sigma_{12}\left(x_1, 0^\pm\right) = 0 \tag{73}$$

The plane-strain problem is simplified by the introduction of the Airy stress function $\phi(x_1, x_2)$ from which the stress components are derived as follows:

$$\sigma_{11} = \phi_{,22} \qquad \sigma_{22} = \phi_{,11} \qquad \sigma_{12} = -\phi_{,12} \tag{74}$$

The equilibrium equations in Eq. (71) are automatically satisfied if the body forces are neglected. The strains calculated from this must then satisfy the compatibility equation $2\varepsilon_{12,12} = \varepsilon_{11,22} + \varepsilon_{11,22}$ which results in the biharmonic equation for the Airy stress function:

$$\nabla^2\nabla^2\phi = \nabla^4\phi = 0 \tag{75}$$

The boundary conditions in Eqs. (72) and (73) may be rewritten in terms of the derivatives of the Airy stress function.

The plane-stress formulation, applicable to thin sheets, begins with a simple assumption that the stress components in the x_3 direction can be set equal to zero and the other components to be independent of x_3.

$$\sigma_{3i} = 0; \qquad \sigma_{\alpha\beta,3} = 0 \tag{76}$$

As a consequence, the strain-displacement relations in Eq. (46) yield

$$2\varepsilon_{\alpha\beta} = u_{\alpha,\beta} + u_{\beta,\alpha}; \qquad \varepsilon_{3\alpha} = 0 \qquad \varepsilon_{33} = -\nu\sigma_{\alpha\alpha}/E \tag{77}$$

Then substituting into the stress-strain relations in Eq. (47) results in the stresses that appear similar to Eq. (70) when E is replaced by $E(1-\nu^2)$ and ν is replaced by $\nu(1-\nu)$. Using the Airy stress function in Eq. (74), the governing equation in (75) still holds for the plane stress problem. Hence, solutions to plane-strain problem and plane-stress problem are similar with the equivalent material properties as indicated above.

Following Williams (1957) we shall consider a wedge with an included angle 2α as illustrated in Fig. 15. With various values of α this can represent a wedge, a reentrant corner or notch as well as a crack as indicated in the figure. It is convenient to introduce polar coordinates (r, θ) to address this problem, with displacements denoted as (u_r, u_θ) in the radial and tangential directions. The strain-displacement relations are written as

$$\varepsilon_{rr} = \frac{\partial u_r}{\partial r}; \quad \varepsilon_{\theta\theta} = \frac{1}{r}\frac{\partial u_\theta}{\partial \theta} + \frac{u_r}{r}; \quad 2\varepsilon_{r\theta} = \frac{\partial u_\theta}{\partial r} - \frac{u_\theta}{r} + \frac{1}{r}\frac{\partial u_r}{\partial \theta} \tag{78}$$

The stress-strain relations become

$$\begin{aligned}
\varepsilon_{rr} &= \frac{k+1}{8\mu}\sigma_{rr} - \frac{3-k}{8\mu}\sigma_{\theta\theta} \\
\varepsilon_{\theta\theta} &= \frac{k+1}{8\mu}\sigma_{rr} - \frac{3-k}{8\mu}\sigma_{\theta\theta} \quad \text{with} \quad k = \begin{cases} 3-4\nu & \text{plane strain} \\ \dfrac{3-\nu}{1+\nu} & \text{plane stress} \end{cases} \\
\varepsilon_{r\theta} &= \frac{1}{2\mu}\sigma_{r\theta}
\end{aligned} \tag{79}$$

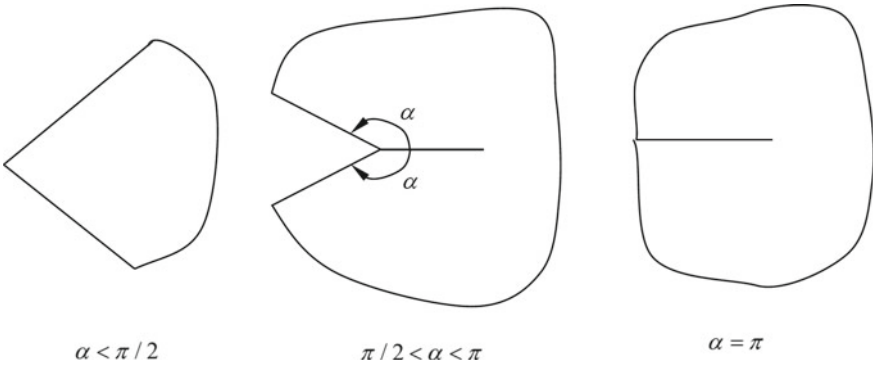

Fig. 15 Geometry of wedges and notches

The stress components in cylindrical polar coordinate in terms of the Airy stress function are expressed as:

$$\begin{aligned} \sigma_{rr} &= \frac{1}{r}\frac{\partial \phi}{\partial r} + \frac{1}{r^2}\frac{\partial^2 \phi}{\partial \theta^2}; \quad \sigma_{\theta\theta} = \frac{\partial^2 \phi}{\partial r^2}; \\ \sigma_{r\theta} &= -\frac{\partial}{\partial r}\left(\frac{1}{r}\frac{\partial \phi}{\partial \theta}\right) = \frac{1}{r^2}\frac{\partial \phi}{\partial \theta} - \frac{1}{r}\frac{\partial^2 \phi}{\partial r \partial \theta} \end{aligned} \tag{80}$$

The biharmonic equation is expressed as

$$\nabla^4 \phi = \left(\frac{\partial^2}{\partial r^2} + \frac{1}{r}\frac{\partial}{\partial r} + \frac{1}{r^2}\frac{\partial^2}{\partial \theta^2}\right)\left(\frac{\partial^2 \phi}{\partial r^2} + \frac{1}{r}\frac{\partial \phi}{dr} + \frac{1}{r^2}\frac{\partial^2 \phi}{\partial \theta^2}\right) = 0 \tag{81}$$

The traction free boundary conditions on the surfaces $\theta = \pm\alpha$ can be expressed as:

$$\sigma_{\theta\theta}(r, \pm\alpha) = 0; \quad \sigma_{r\theta}(r, \pm\alpha) = 0 \tag{82}$$

As in the case of the Mode III problem, we seek a solution to Eq. (81) subject to Eq. (82) through a separation of variables in the form $\phi(r, \theta) = r^{\lambda+1} f(\theta)$; substituting into Eq. (81) we get an ordinary differential equation for $f(\theta)$

$$f'''' + 2(\lambda^2 + 1) f'' + (\lambda^2 - 1) f = 0 \tag{83}$$

where the primes indicate differentiation with respect to the argument. The general solution to this is

$$f(\theta) = C_1 \cos(\lambda - 1)\theta + C_2 \sin(\lambda - 1)\theta + C_3 \cos(\lambda + 1)\theta + C_4 \sin(\lambda + 1)\theta \tag{84}$$

The traction free conditions in Eq. (82) imply that $f(\pm\alpha) = 0$, $f'(\pm\alpha) = 0$; substituting from the above results in four homogeneous equations for the four unknown

coefficients, C_i with $i = 1...4$. For nontrivial solutions, the determinant of the coefficients should be set equal to zero,

$$\begin{bmatrix} -(\lambda-1)\sin(\lambda-1)\alpha & (\lambda-1)\cos(\lambda-1)\alpha & -(\lambda+1)\sin(\lambda+1)\alpha & (\lambda+1)\cos(\lambda+1)\alpha \\ \cos(\lambda-1)\alpha & \sin(\lambda-1)\alpha & \cos(\lambda+1)\alpha & \sin(\lambda+1)\alpha \\ (\lambda-1)\sin(\lambda-1)\alpha & (\lambda-1)\cos(\lambda-1)\alpha & (\lambda+1)\sin(\lambda+1)\alpha & (\lambda+1)\cos(\lambda+1)\alpha \\ \cos(\lambda-1)\alpha & -\sin(\lambda-1)\alpha & \cos(\lambda+1)\alpha & -\sin(\lambda+1)\alpha \end{bmatrix} \begin{bmatrix} C_1 \\ C_2 \\ C_3 \\ C_4 \end{bmatrix} = 0$$

providing the characteristic equation for the determination of λ:

$$\lambda \sin(2\alpha) \pm \sin(2\alpha\lambda) = 0 \tag{85}$$

Clearly, the value of λ depends on the wedge/notch angle (see Williams 1952); it is found that $\lambda > 1$ for $\alpha < \pi/2$ indicating that the stresses will go to zero as $r \to 0$ for a wedge. For $\pi/2 < \alpha < \pi$, the minimum value of $Re\lambda < 1$, and therefore the stress components will be singular as $\sigma_{\alpha\beta} \sim r^{\lambda-1} \to \infty$ as $r \to 0$, indicating that reentrant corners or notches will generate a singular stress at the corner. For the particular case of a crack, $\alpha = \pi/2$ and the characteristic equation becomes $\sin(2\alpha\lambda) = 0$; the roots are

$$\lambda = \frac{n}{2} \quad \text{for} \quad n = 0, \pm 1, \pm 2, ... \tag{86}$$

with a set of coefficient in C_{in} with $i = 1...4$ for each n. Furthermore, the traction free boundary condition in Eq. (82) can be used to relate the coefficients of the different terms. Thus, we get

$$\text{for odd } n \begin{cases} C_{3n} = -\dfrac{n-2}{n+2} C_{1n} \\ C_{4n} = -C_{2n} \end{cases} \quad \text{for even } n \begin{cases} C_{3n} = -C_{1n} \\ C_{4n} = -\dfrac{n-2}{n+2} C_{2n} \end{cases} \tag{87}$$

The solution for the Airy stress function in the vicinity of the crack tip can then be written as:

$$\begin{aligned} \phi(r,\theta) = \sum_{n=1,3,...} r^{\frac{n}{2}+1} \begin{bmatrix} C_{1n}\{\cos\left(\frac{n}{2}-1\right)\theta - \frac{n-2}{n+2}\cos\left(\frac{n}{2}+1\right)\theta\} \\ +C_{2n}\{\sin\left(\frac{n}{2}-1\right)\theta - \sin\left(\frac{n}{2}+1\right)\theta\} \end{bmatrix} \\ + \sum_{n=0,2,4,...} r^{\frac{n}{2}+1} \begin{bmatrix} C_{1n}\{\cos\left(\frac{n}{2}-1\right)\theta - \cos\left(\frac{n}{2}+1\right)\theta\} \\ +C_{2n}\{\sin\left(\frac{n}{2}-1\right)\theta - \frac{n-2}{n+2}\sin\left(\frac{n}{2}+1\right)\theta\} \end{bmatrix} \end{aligned} \tag{88}$$

As we did for the Mode III problem, we will consider the different orders of terms to assess their behavior as $r \to 0$. Given that the Airy function goes as $\phi(r,\theta) \sim$

$r^{\frac{n}{2}+1}$, the stress and displacement components will behave as $\sigma_{\alpha\beta} \sim r^{\frac{n}{2}+1}$ and $u_\alpha \sim r^{\frac{n}{2}}$ for $n \neq 0$. The terms with $n < 0$ will cause displacement singularity and hence are not admissible. The term with $n = 0$ implies $\sigma_{\alpha\beta} \sim r^{-1}$ and $u_\alpha \sim \ln r$ is also not admissible because of the logarithmic singularity; note that this term is of importance in other problems such as dislocations. The terms corresponding to $n > 2$ lead to bounded stresses and are not of interest in the context of fracture. Finally, the term with $n = 1$ results in bounded displacements and square-root singular stress and strain fields, analogous to what was obtained for the anti-plane or Mode III problem; it can be shown to have bounded energy in the vicinity of the crack tip and hence becomes the most important term from a fracture mechanics point of view. For the term with $n = 1$, we have

$$\phi(r,\theta) = r^{\frac{3}{2}}\left[C_{11}\left(\cos\frac{\theta}{2} + \frac{1}{3}\cos\frac{3\theta}{2}\right) - C_{21}\left(\sin\frac{\theta}{2} + \sin\frac{3\theta}{2}\right)\right] \tag{89}$$

It should be noted that the terms with C_{11} indicate a symmetric field while the terms with C_{21} indicate an antisymmetric field; these correspond to the Mode I and Mode II loading conditions indicated in Fig. 13. The stress and displacement fields corresponding to Eq. (89) may be calculated; it is common practice to write the Cartesian components of the stress and displacement field in terms of polar coordinates as illustrated in the stress element in Fig. 16a. Also, the amplitudes C_{11} and C_{21} are replaced by defining the *Mode I and Mode II stress intensity factors* analogous to the definition in Eq. (66) for Mode III.

$$K_I = \lim_{r\to 0} \sqrt{2\pi r}\,\sigma_{22}(r, \theta = 0) \tag{90}$$

$$K_{II} = \lim_{r\to 0} \sqrt{2\pi r}\,\sigma_{12}(r, \theta = 0) \tag{91}$$

The nature of the crack tip displacement and stress fields given in Eqs. (92) and (93) are referred to as the $K - field$, and is assumed to be established near the vicinity of every crack under in-plane loading, with the only difference arising from the amplitudes of the singularities indicated by the Mode I and Mode II stress intensity factors, (K_I, K_{II}) .

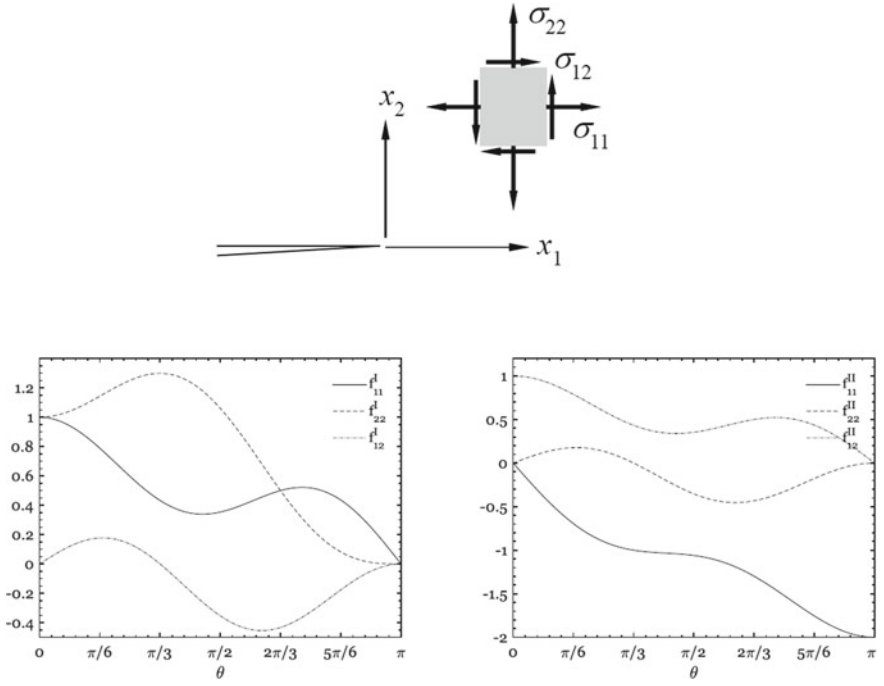

Fig. 16 **a** Stress element at (r, θ). **b** Angular variation of the stress components for modes I and II

$$\begin{Bmatrix} \sigma_{11} \\ \sigma_{22} \\ \sigma_{12} \end{Bmatrix} = \frac{K_I}{\sqrt{2\pi r}} \begin{Bmatrix} \cos\frac{\theta}{2}\left(1 - \sin\frac{\theta}{2}\sin\frac{3\theta}{2}\right) \\ \cos\frac{\theta}{2}\left(1 + \sin\frac{\theta}{2}\sin\frac{3\theta}{2}\right) \\ \sin\frac{\theta}{2}\cos\frac{\theta}{2}\cos\frac{3\theta}{2} \end{Bmatrix} + \frac{K_{II}}{\sqrt{2\pi r}} \begin{Bmatrix} -\sin\frac{\theta}{2}\left(2 + \cos\frac{\theta}{2}\cos\frac{3\theta}{2}\right) \\ \sin\frac{\theta}{2}\cos\frac{\theta}{2}\cos\frac{3\theta}{2} \\ \cos\frac{\theta}{2}\left(1 - \sin\frac{\theta}{2}\sin\frac{3\theta}{2}\right) \end{Bmatrix} \tag{92}$$

$$\begin{Bmatrix} u_1 \\ u_2 \end{Bmatrix} = \frac{K_I}{4\mu}\sqrt{\frac{r}{2\pi}} \begin{Bmatrix} (2k-1)\cos\frac{\theta}{2} - \cos\frac{3\theta}{2} \\ (2k+1)\sin\frac{\theta}{2} - \sin\frac{3\theta}{2} \end{Bmatrix} + \frac{K_{II}}{4\mu}\sqrt{\frac{r}{2\pi}} \begin{Bmatrix} (2k+3)\sin\frac{\theta}{2} + \sin\frac{3\theta}{2} \\ -(2k-3)\cos\frac{\theta}{2} - \cos\frac{3\theta}{2} \end{Bmatrix} \tag{93}$$

with k as defined in Eq. (79). The angular variation of the stress field for Mode I and Mode II conditions are displayed in Fig. 16b. It is important to note that the stress intensity factors are a function of the applied load, geometry of the specimen or structure and the length of the crack, and must be determined by solving the complete boundary value problem in linear elasticity that includes the full geometric description of the cracked structure and the applied load; the stress-intensity-factor has a dimension $\left[FL^{3/2}\right]$ and in SI units is indicated typically as $MPa\sqrt{m}$.

3.3 *Out-of-Plane Components of Displacement, Stress and Strain Fields*

When applying the fields determined in Sects. 3.1 and 3.2 to laboratory and field specimens, the three-dimensionality must be considered carefully. These restrictions in the applicability are discussed in this section with Fig. 17 indicating the limitations. First, for the anti-plane shear problem of Sect. 3.1, Eq. (54) requires that both the stress components $\sigma_{3\alpha}$ be nonzero; however, in contrast, the traction free surfaces at the $x_3 = \pm h/2$ of a finite thickness, h, plate demands that $\sigma_{32} = 0$. Hence, it is clear that anti-plane shear or mode III loading cannot be sustained in a plate of finite thickness in a layer near the free surfaces of the plate; by the same argument, it should be evident that the example of tearing of paper considered in Example 5 of Sect. 2 does not correspond to mode III loading.

For the plane strain problem, we have $\varepsilon_{33} = 0$, and hence,

$$\sigma_{33} = \nu\sigma_{\alpha\alpha} = \frac{2\nu K_I}{\sqrt{2\pi r}}\cos\frac{\theta}{2} \tag{94}$$

however, the traction free surfaces at $x_3 = \pm h/2$ of a finite thickness plate demands that $\sigma_{3i} = 0$. Hence, it is clear that a plane strain state cannot be sustained in a plate of finite thickness in a layer near the free surfaces of the plate.

Finally, let us consider plane stress: $\sigma_{33} = 0$, and hence,

$$\varepsilon_{33} = -\frac{\nu}{E}\sigma_{\alpha\alpha} = -\frac{2\nu K_I}{\sqrt{2\pi r}}\cos\frac{\theta}{2} \Rightarrow u_3 = \int_0^{x_3} \varepsilon_{33} dx_3 = -\frac{2\nu K_I x_3}{\sqrt{2\pi r}}\cos\frac{\theta}{2} \tag{95}$$

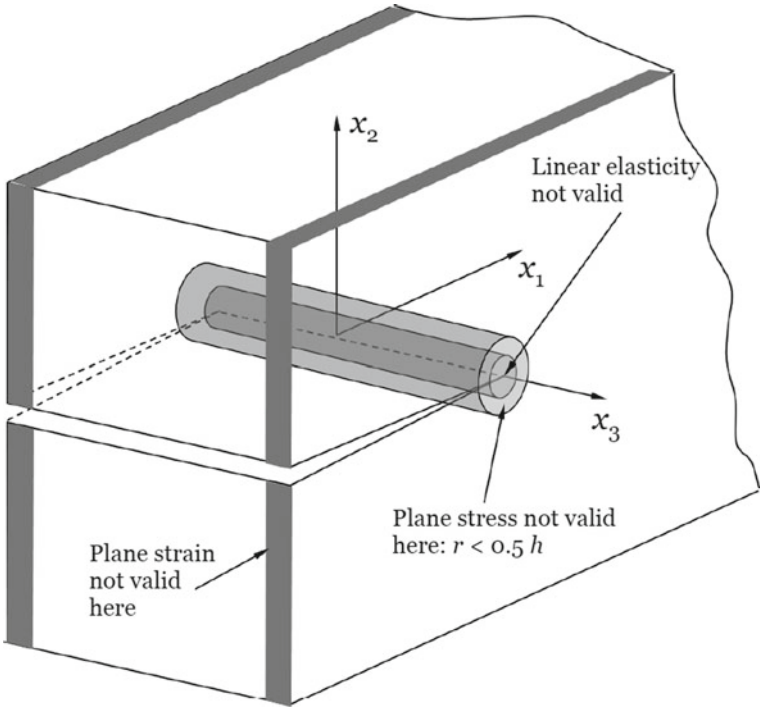

Fig. 17 Diagram indicating the zone of validity of two-dimensional fields

This implies a displacement singularity that is non-physical; hence this cannot be valid in a zone, estimated to be about $h/2$ (Rosakis and Ravi-Chandar 1985; Yang and Freund 1985). In the interior of the plate, in the vicinity of the crack tip $r \to 0$, we have a possible plane strain state.

3.4 The J-Integral

The local approach in terms of the stress intensity factor described in the previous sections, and the global approach of Sect. 2 can be connected through calculations of the energy release rate. This can be accomplished in a number of ways; here, we will use the idea of a path-independent conservation integral known as the J-integral (Eshelby 1970; Rice 1968a; Cherepanov 1967). There are three main results concerning the J-integral that are of importance. First, when the integral is taken over a closed contour that does not enclose any singularities or discontinuities, it is equal to zero. Second, when the contour begins at the bottom flank of a crack and goes counterclockwise around the crack to the top flank of the crack, the integral is independent of the details of the contour. Finally, when enclosing the crack, the

J-integral is equal to the negative of the potential energy change with crack extension and hence provides a useful method for determination of the fracture response.

We begin with Eshelby's energy momentum tensor, defined as $p_{ij} = W(\boldsymbol{\varepsilon})\delta_{ij} - \sigma_{kj}u_{k,i}$, where $W(\boldsymbol{\varepsilon})$ is the strain energy density. It can be shown that its divergence is zero:

$$p_{ij,j} = \frac{\partial W}{\partial \varepsilon_{mn}}\varepsilon_{mn,j}\delta_{ij} - \sigma_{kj,j}u_{k,i} - \sigma_{kj}u_{k,ij} = \sigma_{mn}u_{m,ni} - \sigma_{kj}u_{k,ij} = 0 \qquad (96)$$

Therefore, we can write an equivalent integral formulation or a conservation law by defining

$$J_i = \int_{\partial\Omega} p_{ij}n_j dA = \int_{\partial\Omega} (W(\boldsymbol{\varepsilon})\delta_{ij} - \sigma_{kj}u_{k,i})n_j dA \qquad (97)$$

where, as illustrated in Fig. 18a, $\partial\Omega$ is the boundary of the region Ω, n_i are the components of the unit outward normal and dA is the area element. If we consider a 2D problem, then we can write

$$J_i = \int_C (W(\boldsymbol{\varepsilon})\delta_{ij} - \sigma_{kj}u_{k,i})n_j dS \qquad (98)$$

where C is a closed contour and ds is line element. These integrals represent three quantities, and by the derivation above, $J_i = 0$ inside a closed area, whenever these derivatives exist (no singularities, discontinuities, etc.) and can be thought of as a conservation principle. Of the three components, we consider only J_1 for crack extension problems, and therefore, we will drop the subscript.

Next, we consider a contour that is wrapped around the crack tip as shown in Fig. 18b. Here, the boundaries of the contour are defined in four parts $C = \Gamma_1 \cap \Gamma^- \cap \Gamma_2 \cap \Gamma^+$. On the segments Γ^- and Γ^+, we have zero tractions and $n_1 = 0$;

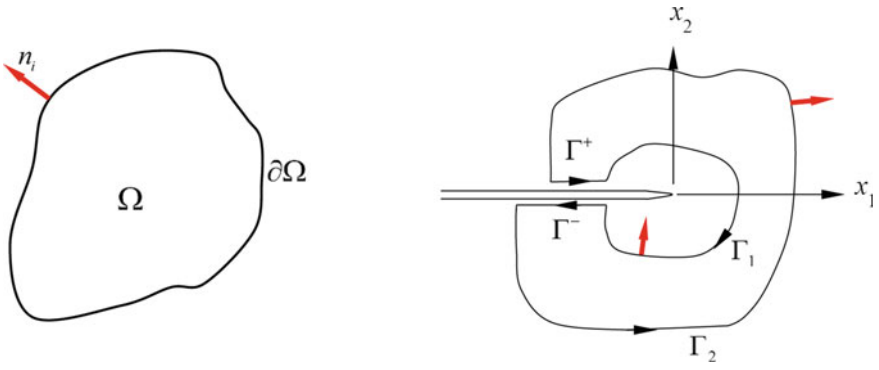

Fig. 18 **a** Closed contour not enclosing singularity or discontinuity. **b** Crack tip contours

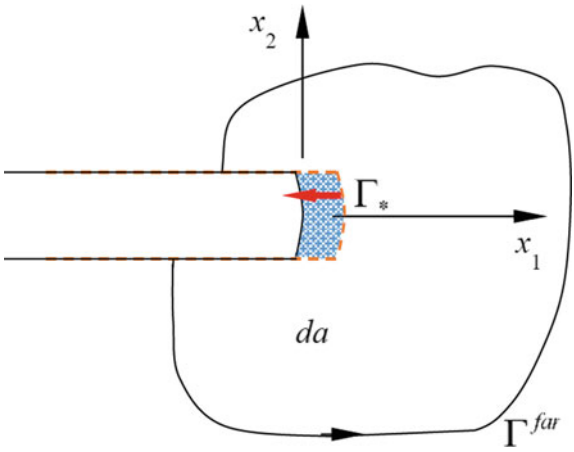

Fig. 19 **a** Closed contour not enclosing singularity or discontinuity. **b** Crack tip contours

hence the integral on these segments is zero. Noting that the direction of integration is reversed along Γ_1 and Γ_2, it is evident that the J-integral, defined as an integral from bottom flank of the crack, going counterclockwise around the crack tip to the top of the crack flank is then independent of the path.

Finally, we consider the connection of the J-integral to the potential energy change with crack extension. Here, we present a simple version of the proof; a more rigorous proof can be found in Jin and Sun (2004). Consider crack extension by an extent da as indicated Fig. 19. We can consider that the material in the shaded region has been removed or that the contour Γ_* has translated by an extent da in the $x_1$direction. The change in potential energy is the sum of the strain energy in the area removed and the change in the work of the external tractions:

$$d\Pi = da \int_{\Gamma_*} W(\varepsilon) n_1 ds - \int_{\Gamma_*} t_\alpha u_\alpha (x_1 + da) ds + \int_{\Gamma_*} t_\alpha u_\alpha (x_1) ds \tag{99}$$

Expanding $u_\alpha(x_1 + da) = u_\alpha(x_1) + u_{\alpha,1}(x_1)da$, the change in potential energy can be written as

$$d\Pi = da \int_{\Gamma_*} \left[W(\varepsilon) n_1 - t_\alpha u_{\alpha,1} \right] ds = -da \int_{\Gamma^{far}} \left[W(\varepsilon) n_1 - t_\alpha u_{\alpha,1} \right] \tag{100}$$

And hence, we have

$$-\frac{d\Pi}{da} = G = J \tag{101}$$

Thus, the J-integral defined in Eq. (98) represents the potential energy change with crack extension. We will use this result to motivate a local fracture criterion based on the stress intensity factor in the next section.

3.5 Linearly Elastic Fracture Mechanics (LEFM)

We now discuss the formulation of the fracture criterion in terms of the local stress field parameters in linear elasticity, restricting attention to mode I loading. There are two essential concepts involved in applying linear elastic stress and energy calculations to the fracture problem and these are discussed here.

3.5.1 K-Dominance

Let us examine the square-root singular stress field in Eq. (92) closely. First, this field implies unbounded stresses and strains as $r \to 0$; this is clearly inadmissible in the small deformation linear elastic model within which the field in Eq. (92) was determined. In practice, there must exist a zone near the crack of size r_p, within which finite deformation, nonlinearity, and processes of separation leading to failure will occur. This region is shown as a shaded region in Fig. 20; the K-field cannot hold in this region. Second, as we examine the stress-field at large distances from the crack tip, the $r^{-1/2}$ term will decay out at large distances and higher order terms in the crack tip solution will become larger, and so the K-field cannot describe the stress field in $r > \rho$ completely. So, the hope is that there exists an annular region outside the nonlinear zone, but still close enough to the crack tip where the K-field of Eq. (92) is adequate in describing the stress state. This concept is called *K-dominance*. If we now evaluate the J-integral, with the contour lying entirely within the K-dominant zone, the square-root singular K-field can be used to express the local stress, strain and displacement fields, to get

$$J = \frac{K_I^2}{\bar{E}} \tag{102}$$

where $\bar{E} = E/\left(1-\nu^2\right)$ for plane strain and $\bar{E} = E$ for plane stress conditions. Analogous expressions may be written for modes II and III, and these will be discussed in Sect. 4. Equation (102) provides an important result: it connects the local approach of the stress intensity factor to the potential energy change with crack extension, and connects to the energy based global approach of Sect. 2.

3.5.2 Small-Scale Yielding

In order to use this equivalence to develop a local fracture criterion, there must be a guarantee that all of the potential energy change can be attributed to the fracture process. This requires that the inelastic and fracture process zone near the crack be small in relation to some characteristic length, as yet undefined; this idea is called *small-scale yielding*. Irwin (1961) suggested that the effect of the plastic zone near the crack tip can be approximated by a very simple model; first, assume that the stress in the plastic zone near the crack tip must be limited to some multiple β of the yield stress, σ_y; from the square-root singular field, we can estimate that yielding initiates at

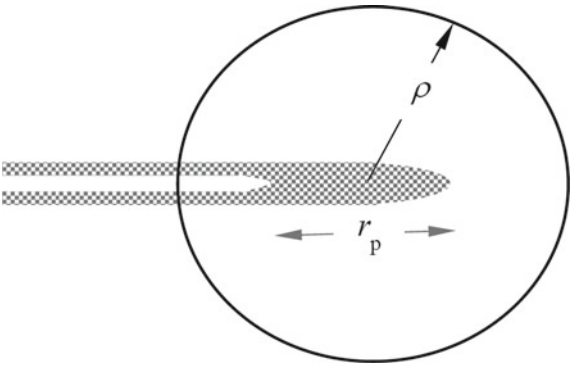

Fig. 20 **a** Closed contour not enclosing singularity or discontinuity. **b** Crack tip contours

a distance $r_y = \frac{1}{2\pi}\left(\frac{K_I}{\beta\sigma_Y}\right)^2$ from the crack tip. The perfectly plastic model requires $\sigma_{22}(r < r_y, 0) = \beta\sigma_Y$. This results in a redistribution of the elastic stress ahead of the yielded zone as indicated in Fig. 21; Irwin estimated this by considering that the elastic field is centered at an effective crack tip at the location α from the physical crack. Equilibrium then implies

$$\int_0^{r_y} \sigma_{22}(r, 0)dr = (\alpha + r_y)\beta\sigma_{\bar{Y}} \tag{103}$$

Evaluating the above yields $\alpha = r_y$ and hence the size of the plastic zone is $r_p = 2r_y$. If we assume a Tresca yield criterion, for thin plates with $\sigma_{33} = 0$, it is easy to show that $\beta = 1$. However, for conditions of plane strain expected to prevail near the crack tip, with $\sigma_3 = 2\nu\sigma_1$, the Tresca criterion yields $\beta = 1/(1 - 2\nu)$; using these, the plastic zone size can be shown to be

$$r_p = \begin{cases} \frac{1}{\pi}\left(\frac{K_I}{\sigma_Y}\right)^2 & \text{plane stress} \\ \frac{1}{3\pi}\left(\frac{K_I}{\sigma_Y}\right)^2 & \text{plane strain} \end{cases} \tag{104}$$

This simple estimate of the zone of yielding does remarkably well in capturing the extent of yielding near the crack tip. More importantly, this analysis indicates clearly that the *characteristic length scale in the fracture problem* is obtained as $(K_I/\sigma_Y)^2$. In applying the ideas of LEFM, it is now clear that one must ensure that $(K_I/\sigma_Y)^2$ is much smaller than other relevant lengths such as B, the specimen thickness, a, the crack length, and any other length defining the geometry of the specimen. This gives a qualitative meaning to the concept of small-scale yielding, and a more precise restriction must be obtained from experimental characterization of materials.

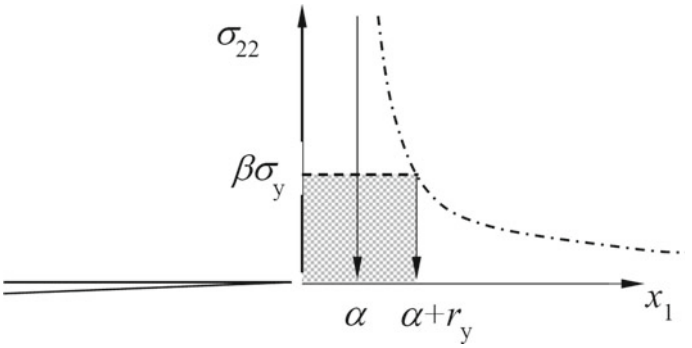

Fig. 21 Irwin's approximate redistribution of the stress arising from a perfectly plastic material model

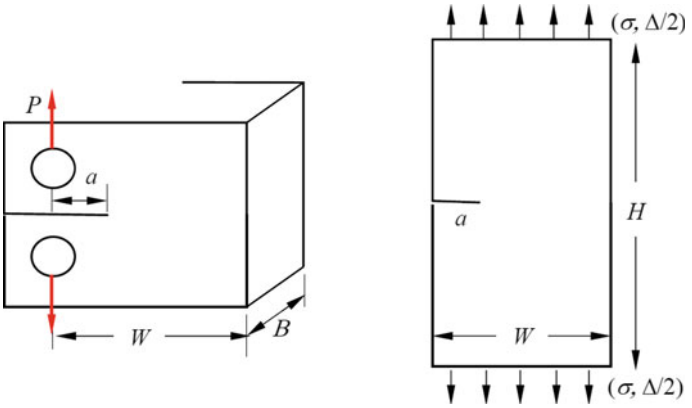

Fig. 22 **a** Compact tension specimen. **b** Single-edge-notched tension specimen

3.5.3 Fracture Criterion Under LEFM

Once the equivalence between the J-integral and the stress intensity factor is established, it is easy to formulate the fracture criterion in terms of a critical value of the stress intensity factor. Using the Griffith criterion in Eqs. (14), (102) can be rewritten as follows:

$$\frac{K_I^2}{\bar{E}} = 2\Gamma \quad \Leftrightarrow \quad K_I = K_c = \sqrt{2E\Gamma} \tag{105}$$

where K_c is the material property called the *fracture toughness*; note that it must be evaluated with special care to ensure that conditions of small scale yielding and K-dominance are assured since these are the restrictions under which Eq. (102) is valid. This equivalence forms the energetic basis on which Linearly Elastic Fracture Mechanics (LEFM) is applied in practical engineering applications to assess failure and structural integrity. This approach has been codified through the establishment of

a standard procedure for the calibration of the fracture energy. The American Society for Standards and Materials has developed a standard test ASTM E399-20 for the determination of the critical stress intensity factor at initiation of a crack in metallic materials under conditions of plane strain. The standard goes into lengthy details of the test procedure, the most important of which are on specimen preparation and generation of a natural crack through a fatigue process in which the conditions of small scale yielding and K-dominance can be established. One example specimen configuration called the compact tension specimen is shown in Fig. 22a. The stress intensity factor for this configuration is given as

$$K_I = \frac{P}{B\sqrt{W}} f\left(\frac{a}{W}\right) \tag{106}$$

where $f(x) = \dfrac{2+x}{(1-x)^{3/2}}\left[0.886 + 4.64x - 13.32x^2 + 14.72x^3 - 5.6x^4\right]$. Therefore, the critical stress intensity factor can be obtained from experiments in which the load at onset of crack growth is monitored. Experimental results revealed a typical variation of K_c with specimen thickness as shown in Fig. 23. The measured value of K_c is high for small specimen thicknesses and reaches a nearly constant lower plateau at large specimen thicknesses; it is this value of the critical stress intensity factor, labeled K_{IC}, that is taken to be a new material property called the *plane strain fracture toughness*. This dependence is governed primarily by the differences in how plastic deformation is constrained in the vicinity of the crack tip in thick specimens that permit a plane-strain state to develop near the crack tip. The main condition that arises here ensures that the radius r_p of the inelastic region near the crack tip is small enough; thus, in tests performed to evaluate the fracture toughness, one must have the crack length, a, and the specimen thickness, B, obey the following inequality:

$$a, (W-a), B \geq 2.5\left(\frac{K_{IC}}{\sigma_Y}\right)^2 \tag{107}$$

The characteristic length scale can be seen to arise from Irwin's scaling analysis in Sect. 3.5.2; the numerical factor was determined through numerous tests in different materials and loading geometries. Typical range of values of the fracture toughness for different materials is provided in Table 3.

As an illustration of the application of LEFM, consider a simple example: a large panel with a central crack of length 2a subjected to uniform stress σ; the stress intensity factor for this configuration is simply $K_I = \sigma\sqrt{\pi a}$. Applying the fracture criterion in Eq. (105) for plane strain results in the critical condition, expressed $\sigma\sqrt{\pi a} = K_{IC}$ This condition can be used in one of three ways in fracture-critical structures: first, at the design stage, one sets the crack length to be at the limit that is detectable by nondestructive inspection techniques. Then, for a desired design load, a material with the appropriate fracture toughness can be selected or alternatively for a given material, the maximum permissible stress can be determined. Second, for a given structural application (implying fixed fracture toughness and stress), the

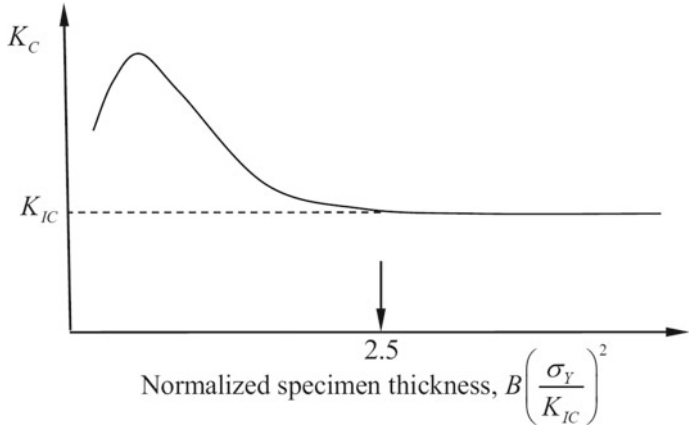

Fig. 23 Dependence of the fracture toughness on specimen thickness

Table 3 Typical values of fracture toughness for different materials

Material	$K_{IC} - MPa\sqrt{m}$
Ductile metals: Cu, Ni, Ag	100–350
A533 Steel	200
Mild steels	140
High strength steels	50–150
Al alloys	20–45
Ceramics: Al_2O_3, Si_3N_4	3–6
Polyethylene	2
Polycarbonate	1–2.5
Silica glass	0.7

critical crack length can be calculated and used in inspections to determine how close the structure is to fracture criticality. Considering that cracks grow during subcritical loading, for example, by fatigue, one may also determine how long the crack will grow in the time interval between inspections. Finally, for a given crack length and material, one can impose limits on loading such that critical conditions are not reached during operation. This approach permits a damage tolerant approach to design and operation of structures.

Stability of crack growth Consideration of stability of crack extension in the local approach follows along similar lines to the discussion in Sect. 2 concerning the global energetic approach. We will illustrate this with a simple example of a single-edge-notched tension (SENT) specimen; the specimen geometry is shown in Fig. 22b. The stress intensity factor and the load point displacement for this geometry are expressed as follows (Tada 1973):

$$K_I = \sigma\sqrt{\pi a}\, f\left(\frac{a}{W}\right);\ \Delta = \frac{4\sigma a}{E} V\left(\frac{a}{W}\right) + \frac{\sigma H}{E} \tag{108}$$

where

$$f(x) = \frac{\sqrt{\frac{2}{\pi x}\tan\frac{\pi x}{2}}}{\cos\left(\frac{\pi x}{2}\right)}\left[0.752 + 2.02x + 0.37\left(1 - \sin\frac{\pi x}{2}\right)^3\right]$$

$$V(x) = x\left[0.99 - x(1-x)(1.3 - 1.2x + 0.7x^2)\right](1-x)^{-2}$$

and the second term on the right side of Eq. (108) is the elongation of the uncracked specimen. Setting the stress intensity factor in Eq. (108) equal to the plane strain fracture toughness, K_{IC}, the critical stress, σ_c, is obtained as:

$$\frac{\sigma_c\sqrt{\pi W}}{K_{IC}} = \left[\sqrt{\frac{a}{W}} f\left(\frac{a}{W}\right)\right]^{-1} \tag{109}$$

The corresponding critical displacement can then be written by eliminating the critical stress:

$$\frac{E\sqrt{\pi}}{K_{IC}\sqrt{W}}\Delta_c = \left[\frac{4a}{W} V\left(\frac{a}{W}\right) + \frac{h}{W}\right]\left[\sqrt{\frac{a}{W}} f\left(\frac{a}{W}\right)\right]^{-1} \tag{110}$$

The critical values (Δ_c, σ_c) for different crack lengths a representing the locus of failure points is shown in Fig. 24 by the red dashed line, for the case $H = 3W$. For each marked point in the plot, a increases from 0.25 by 0.15. Both the critical stress and the critical load-point displacement decrease with increasing crack length, indicating that crack initiation will be unstable under both load and displacement controlled tests. This type of instability, called a *snap-back instability*, is encountered often in fracture problems. Continued crack growth under these conditions occurs at speeds comparable to the wave speed in the material and requires consideration of inertia effects.

4 Mixed-Mode Fracture

The discussion up to this point has focused on mode I loading. Under more general loading conditions, the problem of fracture is not only to identify the conditions for initiation and growth of the crack, but also to determine the path of the crack. In principle, the criterion for this is embedded in Griffith's postulate as we saw in Example 4 of Sect. 2: of all possible crack paths, the crack will choose the one along which the total energy E in Eq. (9) is an extremum, keeping in mind that the term $2\gamma a$ must be replaced by the fracture energy $U_s(a)$. However, this is quite difficult to estimate in general; the main hurdle is that the energy minimization

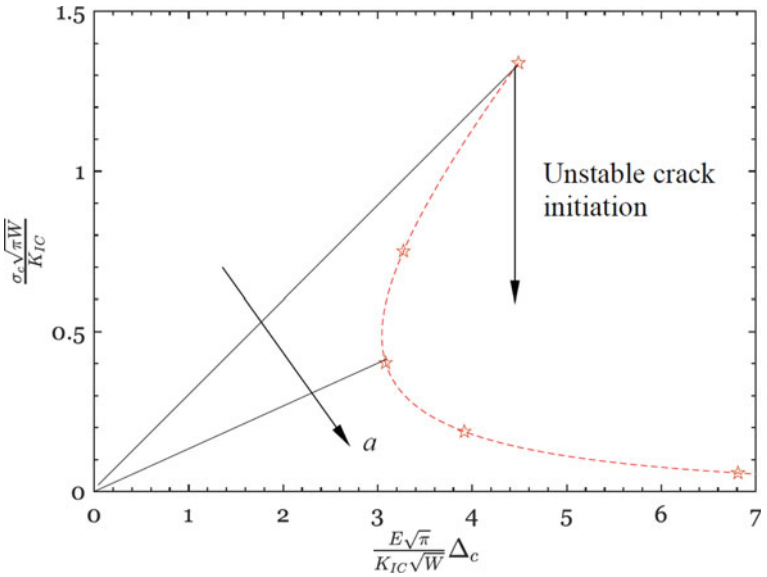

Fig. 24 Failure locus for a single-edge-notched tension specimen indicating snap-back instability

calculation must permit crack arbitrary surface evolution. Practical fracture *criteria* have been introduced since the time of Irwin (1957), that, while still based on the Griffith theory, are of restricted validity. Nevertheless, such criteria are of enormous practical significance since they permit the design of fracture critical structures, determination of residual strength of structural components in the presence of cracks, and assessment of structural integrity in a large number of applications. We will describe some of the more commonly used criteria, first under mixed-modes I + II and subsequently under mixed modes I + III.

4.1 In-Plane Mixed Mode Problem: Mixed-Modes I + II

The mixed-mode I + II problem is illustrated in Fig. 25; the initial crack, labeled parent crack is loaded with far field tractions so as to establish a K-dominant region near the crack tip with the loading defined by the mode I and mode II stress intensity factors, $(K_I^\infty, K_{II}^\infty)$. The two main questions that must be answered are the following: (i) What is the critical combination of stress intensity factors that trigger crack initiation? (ii) What initial path does the crack choose?

Maximum energy release rate criterion This is a direct extension of Griffith's criterion: the crack will extend in that direction along which the energy release rate equals the fracture energy of the material. Note that many textbooks use Eq. (101),

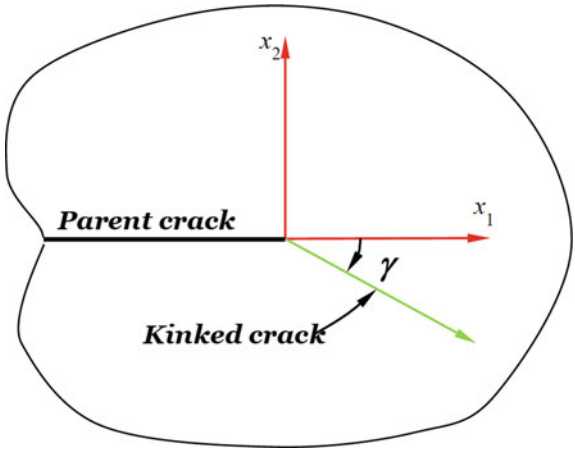

Fig. 25 Geometry of a mixed-mode crack and the kink crack that grows from the parent crack

apply the mixed mode singular stress field and write $G = \frac{1}{\bar{E}}\left[(K_I^\infty)^2 + (K_{II}^\infty)^2\right]$; however, this is incorrect since this calculation is based on the assumption that the kink angle is zero. Leblond (2020) showed that the energy release rate corresponding to a kinked crack at an angle γ may be calculated in terms of the stress intensity factors at the kinked cracks, (k_I, k_{II}). First, stress intensity factors (k_I, k_{II}) can be obtained from a perturbation analysis in terms of the kink angle, γ:

$$\begin{Bmatrix} k_I(\gamma) \\ k_{II}(\gamma) \end{Bmatrix} = \mathbf{F}(\gamma) \begin{Bmatrix} K_I^\infty \\ K_{II}^\infty \end{Bmatrix} \tag{111}$$

where expressions for $\mathbf{F}(\gamma)$ may be found in Amestoy and Leblond (1992). Second, the energy release rate can be calculated as

$$G = \frac{1}{\bar{E}}\left[k_I^2(\gamma) + k_{II}^2(\gamma)\right] \tag{112}$$

Hence, the fracture criterion may be written as

$$\max_\gamma G = \frac{1}{\bar{E}}\left[k_I^2(\gamma) + k_{II}^2(\gamma)\right] = 2\Gamma(\gamma) \tag{113}$$

where the possibility of orientation dependence of the fracture energy is taken into account by writing $\Gamma(\gamma)$.

Maximum tangential stress criterion Erdogan and Sih (1963) proposed a criterion for mixed mode fracture that is based on the idea that for a brittle material,hoop stress, $\sigma_{\theta\theta}$. Hence, the direction of crack initiation γ is found from

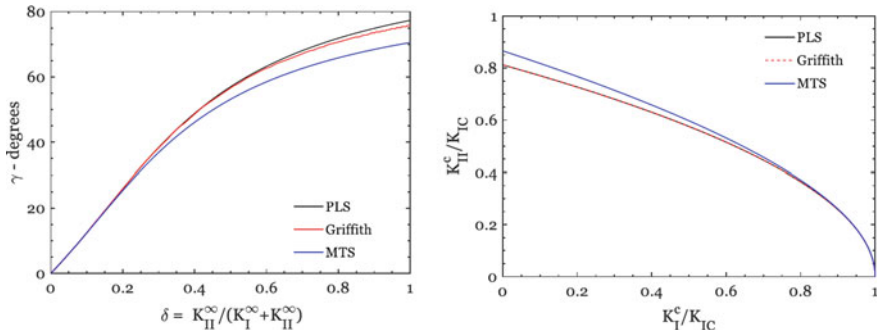

Fig. 26 Kink angle (**a**) and critical values (K_I^c, K_{II}^c) for initiation of mixed mode cracks

$$\frac{\partial \sigma_{\theta\theta}}{\partial \theta} = 0, \quad \frac{\partial^2 \sigma_{\theta\theta}}{\partial \theta^2} < 0 \tag{114}$$

This yields the kink angle γ in terms of the far field loading $(K_I^\infty, K_{II}^\infty)$

$$\gamma = 2 \tan^{-1} \left\{ \frac{K_1^\infty - \sqrt{(K_I^\infty)^2 + 8(K_{II}^\infty)^2}}{4 K^\infty K_{II}^\infty} \right\} \tag{115}$$

along which the crack initiates when

$$\sigma_{\theta\theta}(\gamma)\sqrt{2\pi r} = K_I^\infty \cos^3\left(\frac{\gamma}{2}\right) - 3K_{II}^\infty \sin\left(\frac{\gamma}{2}\right)\cos^2\left(\frac{\gamma}{2}\right) = K_{IC} \tag{116}$$

It turns out that $\sigma_{r\theta} = 0$ along this direction.

Principle of local symmetry The last of the criteria we consider was posed by Goldstein and Salganik (1974). This criterion is also motivated by physical considerations that cracks in brittle materials will be generated by normal stresses; hence cracks would turn to the direction that maximizes the normal stress or opening mode loading; thus, the principle of local symmetry (PLS) dictates that the crack will grow along the direction γ that satisfies

$$k_I(\gamma) = K_{IC}, \quad k_{II}(\gamma) = 0 \tag{117}$$

The values of (k_I, k_{II}) can be determined using the perturbation results of Amestoy and Leblond (1992) as indicated in Eq. (111).

Consequences of mixed-mode fracture criteria All three of the above fracture criteria for in-plane mixed-mode fracture provide critical values of (k_I, k_{II}) at which the crack will initiate and the angle γ at which crack growth will initiate. The predicted crack angle from all three criteria is plotted in Fig. 26a, as a function of the mode II stress intensity factor; the corresponding critical values of the far field stress

intensity factors is plotted in Fig. 26b. The predictions of all three criteria are quite close, with differences emerging only in the limit of approaching pure mode II loading. For pure mode II, all three criteria predict a kinked crack at an angle of about 70°. Experiments by numerous investigators exhibit a scatter that is quite large and could not discriminate between these criteria. In practice, the application of any of the criteria discussed above would provide acceptable predictions of crack growth under in-plane mixed-mode loading conditions. There are numerous examples of experiments in which the path of the crack dictated by mixed mode loading has been captured in numerical simulations through the application of one of these techniques.

4.2 Out-of-Plane Mixed Mode Problem: Mixed-Modes I + III

Considering the difficulty in establishing anti-plane shear conditions, the combination of mixed modes I + III occurs only under very special conditions. In contrast to the in-plane mixed-modes I + II, there are relatively few investigations of the mixed-mode I + III problem. The maximum energy release rate criterion, in its most general form, must still be valid, but it is difficult to implement in practice due to the complex geometry into which the crack surface may evolve. So, in practice fracture criterion is considered in the **n-b** plane indicated in Fig. 13, and identifying the direction of crack extension in this plane through different criteria. Then, determining the direction of crack extension as one moves along the **t**-direction creates the surface of crack extension. With reference to Fig. 25, the initial crack, labeled parent crack is loaded with far field tractions so as to establish a K-dominant region near the crack tip with the loading defined by the mode I and mode III stress intensity factors, $(K_I^\infty, 0, K_{III}^\infty)$. The two main questions that must be answered, as for the in-plane problem, are the following: (i) What is the critical combination of stress intensity factors that trigger crack initiation? (ii) What initial path path does the crack choose? The maximum energy release rate and the maximum principal stress criterion, with different extensions of principle of local symmetry have been applied to the mode I + III problem.

Maximum energy release rate criterion This criterion is similar to that used for the in-plane loading conditions, with the exception that the far field loading contains combination of modes I and III. As with the in-plane problem, the energy release rate corresponding to a kinked crack at an angle γ needs to be calculated; this is accomplished by first calculating the local stress intensity factors (k_I, k_{II}, k_{III}) at the kinked crack tip through a perturbation analysis in terms of the kink angle, γ:

$$\begin{Bmatrix} k_I(\gamma) \\ k_{II}(\gamma) \\ k_{III}(\gamma) \end{Bmatrix} = \mathbf{K}(\gamma) \begin{Bmatrix} K_I^\infty \\ 0 \\ K_{II}^\infty \end{Bmatrix} \tag{118}$$

where expressions for $\mathbf{K}(\gamma)$ have been obtained for different types of perturbations of the initial straight crack front (Gao and Rice 1986; Movchan et al. 1998; Lazarus and Leblond 2001; Leblond et al. 2011). Second, a combination of the PLS and the maximum energy release rate is applied as follows:

$$k_{II}(\gamma) = 0, \quad G = \frac{1-\nu}{2\mu}\left[k_I^2(\gamma) + \frac{1}{1-\nu}k_{III}^2(\gamma)\right] = 2\Gamma \tag{119}$$

where the first equation dictates the direction γ of crack extension and the second imposes the energy criterion for crack extension. This criterion is obtained by considering a smooth (continuous) evolution of the crack surface from the initial (parent) crack.

Maximum principal stress criterion This is an extension of the Erdogan and Sih maximum tangential stress criterion considered in Sect. 4.1, to the three-dimensional problem; once again, arguing that cracks in brittle materials will grow perpendicular to the maximum principal stress direction, this criterion poses that the kinked crack front will be under pure mode I (Sommer 1969; Knauss 1970; Pollard et al. 1982; Cooke and Pollard 1996; Hull 1993, 1995; Lin et al. 2010) and hence,

$$k_I(\gamma) = K_{IC}, \quad k_{II}(\gamma) = 0 \quad k_{III}(\gamma) = 0 \tag{120}$$

The angle can be determined by identification of the principal angle under combined mode I + III loading, and yields

$$\left(\frac{1}{2} - \nu\right)\tan(2\gamma) = \frac{K_{III}^{\infty}}{K_I^{\infty}} \tag{121}$$

However, this criterion cannot be applied uniformly along the crack front; from experiments, it is rather well-established that under combined modes I + III loading, an initially smooth crack front fragments into separate cracks, with each tilted by an angle γ given by Eq. (121).

Crack Growth Under Mixed-Mode I + III Early experimental results of Sommer (1969) and Knauss (1970) revealed unambiguously that a continuous crack front subjected to mixed mode I + III loading fragments or breaks up into multiple crack front segments with discontinuities. Through a detailed examination of the topography of the fracture surface Sommer showed that there was a critical combination of the global mode I and mode III loading at which the crack front segmented into facets. At the other extreme of pure mode III loading (Knauss 1970) showed that the crack front immediately fragments into multiple cracks, with each facet oriented at an angle of 45° with respect to the original fracture plane. Adams and Sines (1978), Cox and Scholz (1988), Pollard et al. (1982) and Younes and Engelder (1999) show spectacular mixed mode I + III cracking patterns. More recently, Lin et al. (2010), Pham and Ravi-Chandar (2014, 2017a) have shown that the fragmentation of the parent crack front occurs as soon as mode III loading is superposed on the parent

crack. This issue has been addressed by a number of authors (see for example, Xu et al. 1994; Pons and Karma 2010; and Leblond et al. 2011; Chen et al. 2015) through a linear stability analysis considering different pertubations of the crack front. The analysis provides a number of predictions, the most important of which is that sinusoidal and helicoidal perturbations of the crack front became unstable when the ratio of $\beta \equiv K_{III}^{\infty}/K_{I}^{\infty}$ exceeded a critical value $\beta_c(\nu)$ that is a function of the Poisson's ratio; hence the fragmentation. Experiments indicate that fragmentation occurs at ratios of $\beta \equiv K_{III}^{\infty}/K_{I}^{\infty}$ that are well below $\beta_c(\nu)$. Numerical simulations using the phase field method has been reported (see for example, Pons and Karma 2010, Pham and Ravi-Chandar 2017a), that indicate fragmentation of the crack front but this problem remains an active area of research.

5 Dynamic Fracture

We now turn to problems in which the crack grows with a speed comparable to the characteristic wave speeds in the material, necessitating consideration of the kinetic energy as well in the energy balance. We will consider this first through a global balance without the details of the crack tip stress analysis, and then examine the local approach.

5.1 Dynamic Lifting and Peeling of an Inextensible, Flexible Tape

Consider a thin, inextensible, flexible tape, of mass density ρ initially lying on a flat plane along $y = 0$ as illustrated in Fig. 27; it is subjected to a constant tension T, and adhesion is ignored at this point. Let $w(x, t)$ denote the transverse deflection of the tape. If the transverse deflections are assumed to be small, the equation of motion governing the transverse deflection can be shown to be the standard wave equation; we will derive this from consideration of the kinetic and potential energies so that the effect of adhesion can be considered subsequently in a similar manner. The kinetic and potential energies can be determined readily:

$$K = \frac{1}{2}\rho \dot{w}^2; \quad \Pi = \frac{1}{2} T w'^2 \tag{122}$$

where $\dot{w} = \dfrac{\partial w}{\partial t}$ is the particle velocity, and $w' = \dfrac{\partial w}{\partial x}$ is the slope of the tape. The potential energy can be obtained from Eq. (29), by noting that $\theta = w'$, and expanding the $\cos\theta$ term in that equation. The governing equation for the tape is obtained by the principle of least action:

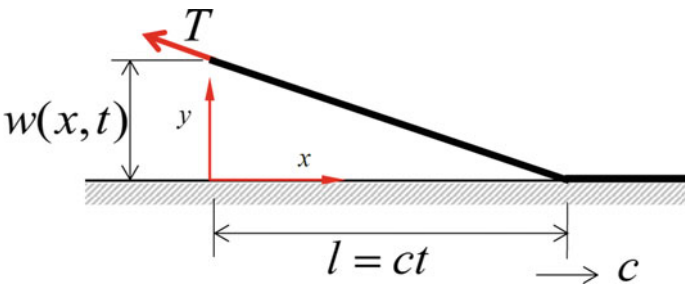

Fig. 27 Geometry of dynamic peeling of a tape

$$S = \int_0^t L(\dot{w}, w')dx \tag{123}$$

where

$$L(\dot{w}, w') = K - \Pi = \frac{1}{2}\int_x \left[\rho \dot{w}^2 - T w'^2\right] dx \tag{124}$$

is the Lagrangian of the system. The principle of least action results in the Euler-Lagrange equation, which is the standard wave equation:

$$\ddot{w} - c^2 w" = 0 \tag{125}$$

where, $c = \sqrt{T/\rho}$ is the characteristic speed of transverse waves in the tape. This wave equation can be recast in the standard quasilinear form by using the slope, w', and the particle velocity, $\dot{w}$, as the key variables; the equation of motion can now be written as:

$$\frac{\partial \dot{w}}{\partial x} - \frac{\partial w'}{\partial t} = 0 \quad c^2 \frac{\partial \dot{w}}{\partial t} - \frac{\partial w'}{\partial x} = 0 \tag{126}$$

where the first equation represents continuity or mass conservation and the second implies conservation of linear momentum. If we seek waves that propagate steadily at an arbitrary speed v, we can introduce a coordinate system moving with the wave as $\xi = x \pm vt$ and denote $w(x,t) = w(x \pm vt)$; the negative sign indicates a wave moving in the positive x-direction and the positive sign the wave moving in the negative x-direction. Simultaneous application of Eqs. (126) indicates that the wave can propagate only at the speed equal to the characteristic wave speed $v = c$; furthermore, both reduce to $(cw' \pm \dot{w})_{,\xi} = 0$, where the comma indicates differentiation with respect to the subscript, and the positive sign corresponds to the right going wave. In other words, if steady waves occur, we must have $cw' \pm \dot{w} =$ const. Now, if we consider two points x^+ and x^- to be two points ahead and behind a steadily propagating disturbance, then we must have

$$[\![\dot{w}]\!] \pm c\,[\![w']\!] = 0 \tag{127}$$

as the jump condition across the disturbance, where $[\![f]\!] = f(x^+) - f(x^-)$ represents the jump in the quantity f across the propagating disturbance.

Next, let us consider a specific initial-boundary value problem: the tape is initially flat on $x > 0$ and at rest: $w'(x,0) = 0$ and $\dot{w}(x,0) = 0$. For $t > 0$ the end $x = 0$ is lifted at a constant rate $\dot{w}_0$; this will propagate as a steady wave for $x > 0$ with the tape lifting from the floor. Hence in the absence of adhesion, the solution to the boundary initial value problem can be written as

$$\begin{array}{ll} \text{for} \quad x > ct & \begin{array}{l} \dot{w}(x,t) = 0 \\ w'(x,t) = 0 \end{array} \\ \text{for} \quad x < ct & \begin{array}{l} \dot{w}(x,t) = \dot{w}_0 \\ w'(x,t) = -\dot{w}_0/c \end{array} \end{array} \tag{128}$$

The result is quite simple: ahead of the wave moving at the speed c, the tape is at rest. Upon passage of the steady wave front, the tape acquires a speed in the y-direction, equal to the lifting speed, $\dot{w}_0$, imposed at $x = 0$, and the slope equal to $w' = -\dot{w}_0/c$ that satisfies the jump condition in Eq. (127). One can enrich this problem further by stopping the motion imposed at $x = 0$ and following the approach to equilibrium through wave reflections using the same jump conditions to calculate the changes in the slope and particle velocities across the reflections.

Next, we consider the same initial-boundary value problem as before, but now, we consider that the tape is adhered to the floor with an adhesive energy γ_A. The tape is initially flat on $x > 0$ and at rest: $w'(x,0) = 0$ and $\dot{w}(x,0)$. For $t > 0$ the end $x = 0$ is lifted at a constant rate $\dot{w}_0$; this will propagate as a steady wave for $x > 0$ with the tape peeling from the floor. However, it is no longer true that disturbances can propagate only at the speed c, and disturbances may do so at an arbitrary speed v. The continuity condition in Eq. (126) yields

$$[\![\dot{w}]\!] \pm v\,[\![w']\!] = 0 \tag{129}$$

where v is unknown; the full solution can be written as

$$\begin{array}{ll} \text{for} \quad x > vt & \begin{array}{l} \dot{w}(x,t) = 0 \\ w'(x,t) = 0 \end{array} \\ \text{for} \quad x < vt & \begin{array}{l} \dot{w}(x,t) = \dot{w}_0 \\ w'(x,t) = -\dot{w}_0/v \end{array} \end{array} \tag{130}$$

The additional condition for determination of the speed of the peel front must come from energy balance. The definition of the dynamic energy release rate and the complete procedure for calculating it will be described later in this section; for now, we provide a simple reasoning for its estimate: as described earlier, the energy release rate for the tape was calculated to be $G = T w'^2/2$ (assuming small slopes). While

this was equated in the quasistatic problem to the adhesive energy of the tape, here we must also attribute some of this energy to the kinetic energy acquired by the tape upon peeling. Hence, the dynamic energy release rate is

$$G = \frac{1}{2}\left(\left[\left[T w'^2\right]\right] - \rho\left[\left[\dot{w}^2\right]\right]\right) \tag{131}$$

Equating this to the adhesive energy, γ_A, yields the crack tip equation of motion:

$$G = \frac{T}{2}\frac{\dot{w}_0^2}{v^2}\left(1 - \frac{v^2}{c^2}\right) = \gamma_A \tag{132}$$

This indicates that as the peel speed v approaches the wave speed, c, the dynamic energy release rate approaches zero, indicating that this is the limiting speed for the peel front. One can also explore the dynamic effect physically by considering the critical slopes and particle velocities as a function of the peel speed. The critical slope of at steady peeling can be obtained from Eqs. (130) and (131) as

$$w'_{cr} = w'_{qs}\left(1 - \frac{v^2}{c^2}\right)^{-1/2} \tag{133}$$

where $w'_{qs} = -\sqrt{2\gamma_A/T}$ is the slope of the tape during steady quasi-static peeling; faster peeling indicates steeper peel angle. Finally, an explicit expression can be derived for the peel front speed:

$$\frac{v^2}{c^2} = \frac{\dot{w}_0^2/c^2}{\sqrt{2\gamma_A/T + \dot{w}_0^2/c^2}} \tag{134}$$

Clearly, as the imposed velocity $\dot{w}_0$ increases, the peel front speed and the magnitude of the slope of the tape increase. These indicate that more effort is needed to peel the tape, simply as a result of inertial effects. Although the setting discussed here is very simple, within the context of an inextensible, flexible tape, the influence of inertia is clearly demonstrated in this example. More details and variants of this problem can be found in the literature (Burridge and Keller 1978; Freund 1990; Dumouchel et al. 2008). Similar effects of inertia are encountered in two-dimensional elastodynamic crack growth problems.

5.2 Local Stress Analysis in Linear Elastodynamics

The approach to the calculation of the stress field near the vicinity of a dynamic crack follows quite along the lines of LEFM, with the addition of inertial effects. Consider a body occupying the region Ω with boundaries $\partial\Omega$. The balance of linear

momentum results in the following equation of motion

$$\sigma_{ij,j} + f_i = \rho \ddot{u} \tag{135}$$

where f_i are the body force components per unit volume and ρ is the mass density. Symmetry of the stress tensor ensures the balance of angular momentum. This is a system of three partial differential equations governing the displacements of points in the body.

$$(\lambda + \mu) u_{j,ji} + \mu u_{i,jj} + f_i = \rho \ddot{u}_i \tag{136}$$

where λ and μ are the Lame constants. We shall assume that the body forces vanish and remove them from consideration in subsequent equations. To the set of equations in (136), we must add initial and boundary conditions. There are three fundamental problems that were posed for the quasi-static problem could also be formulated here. In general there are two types of bulk waves—dilatational and distortional—that can propagate in elastic solids; an additional wave called the Rayleigh surface waves arises near free surfaces. There are numerous textbooks that deal with linear elastodynamics that contain the details of these and other guided waves in solids. We will discuss the important waves as they arise in the fracture problem of interest here.

Anti-plane shear As we did for the quasi-static case (Sect. 3.1), we will begin with the anti-plane shear problem due to its simplicity. Equations (52), (53), and (54) describe the kinematics and constitutive behavior; the equation of equilibrium (55) is replaced with the equation of motion which can be rewritten conveniently in the form of the standard wave equation for the nonzero displacement component u_3:

$$u_{3,\alpha\alpha} = \frac{1}{C_s^2} \ddot{u}_3 \tag{137}$$

where $C_s = \sqrt{\mu/\rho}$ is the shear wave speed in the material. The wave motion is in the $x_1 - x_2$ plane and the particle displacement is in the x_3 direction, indicating that this is a transverse wave.

Consider a traction free crack that is assumed to lie initially along $x_1 < 0,\ x_2 = 0$ to move along $x_2 = 0$ at a constant speed $v < C_s$. The traction free boundary condition on the crack can be written as:

$$\sigma_{32}(x_1 < vt, 0^{\pm}) = \mu u_{3,2}(x_1 < vt, 0^{\pm}) = 0 \tag{138}$$

where $x_2 = 0^{\pm}$ indicates approach to the crack surface from the positive or negative x_2 direction. In order to explore the asymptotic crack tip stress and deformation field, we use a Galilean transformation to a moving coordinate system (ξ_1, ξ_2), centered at the tip of the crack, such that $\xi_1 = x_1 - vt,\ \xi_2 = x_2$. Then, considering $u_3 = u_3(\xi_1, \xi_2)$ Eq. (137) can be written as

$$\left(1-\frac{v^2}{C_s^2}\right)\frac{\partial^2 u_3}{\partial \xi_1^2}+\frac{\partial^2 u_3}{\partial \xi_2^2}=0 \tag{139}$$

If $v < C_s$, as indicated above, this equation can be reduced to Laplace's equation with a rescaling; introducing $\xi_s = r_s e^{i\theta_s} = \xi_1 + i\alpha_s \xi_2$, Eq. (139) reduces to

$$\frac{\partial^2 u_3}{\partial \xi_1^2}+\frac{\partial^2 u_3}{\partial \xi_2^2}=0 \tag{140}$$

with

$$r_s=\sqrt{\xi_1^2+\alpha_s^2\xi_2^2},\ \theta_s=\arctan\left(\frac{\alpha_s\xi_2}{\xi_1}\right),\ \alpha_s=\sqrt{1-\frac{v^2}{C_s^2}} \tag{141}$$

As we did for the quasi-static problem, we seek a separable form of the solution to Eq. (140) subject to the traction free condition in Eq. (138):

$$u_3(r_s,\theta_s)=r_s^{\lambda} f(\theta_s;\lambda) \tag{142}$$

Substituting the above in Eq. (140) results in an ordinary differential equation for the unknown function f. The general solution corresponding to the antiplane symmetry is:

$$f(\theta_s;\lambda)=A\sin\lambda\theta_s \tag{143}$$

where A is a constant. Introducing this solution into the traction free boundary conditions in Eq. (138), as with the corresponding quasi-static problem, bounded displacement and energy are obtained only in the case $\lambda = 1/2$. Thus,

$$u_3(r_s,\theta_s)=2Ar_s^{1/2}\sin\frac{\theta_s}{2} \tag{144}$$

The amplitude can be redefined in terms of the mode III dynamic stress intensity factor:

$$K_{III}=\lim_{\xi_1\to 0}\sqrt{2\pi\xi_1}\sigma_{32}(r_s,0^{\pm}) \tag{145}$$

The stress components can then be written as

$$\begin{aligned}\sigma_{32}(r_s,\theta_s)&=\frac{K_{III}}{\sqrt{2\pi r}}\frac{1}{\sqrt{\gamma_s}}\cos\frac{\theta_s}{2}\\ \sigma_{31}(r_s,\theta_s)&=-\frac{K_{III}}{\sqrt{2\pi r}}\frac{1}{\alpha_s\sqrt{\gamma_s}}\sin\frac{\theta_s}{2}\end{aligned} \tag{146}$$

where

$$\gamma_s=\sqrt{1-(v\sin\theta/C_s)^2}\qquad \tan\theta_s=\alpha_s\tan\theta \tag{147}$$

The square-root singularity of the stress components is identical to that seen in the quasistatic problem; the only difference arises in the angular variation, which is distorted by the speed of the moving crack tip. In the limit as $v \to 0$, we recover the corresponding quasistatic stress and displacement fields. As in the quasi-static problem, the stress intensity factor must be determined from a solution of the appropriate initial-boundary value problem.

In-plane problem We will restrict attention to the plane-strain problem. Equations (68), (69), and (70) describe the kinematics and constitutive behavior. The equation of equilibrium (71) needs to be replaced with the equation of motion; towards this, the displacement is written in terms of the two scalar functions $\varphi(x_1, x_2, t)$ and $\psi(x_1, x_2, t)$ (this is the Helmholtz decomposition of a vector in two-dimensions) such that

$$u_1 = \varphi_{,1} + \psi_{,2};\ u_2 = \varphi_{,2} - \psi_{,1} \tag{148}$$

Then the components of stress can be written as

$$\begin{aligned} \sigma_{11} &= \lambda\left(\varphi_{,11} + \varphi_{,22}\right) + 2\mu\left[\varphi_{,11} + \psi_{,12}\right] \\ \sigma_{22} &= \lambda\left(\varphi_{,11} - \varphi_{,22}\right) + 2\mu\left[\varphi_{,22} - \psi_{,12}\right] \\ \sigma_{12} &= \mu\left[2\varphi_{,12} + 2\psi_{,22} - \psi_{,11}\right] \end{aligned} \tag{149}$$

The equations of motion, reduce to two scalar wave equations

$$\varphi_{,11} + \varphi_{,22} = \ddot{\varphi}/C_d^2;\ \psi_{,11} + \psi_{,22} = \ddot{\psi}/C_s^2 \tag{150}$$

where $C_d = \sqrt{(\lambda + 2\mu)/\rho}$ is the dilatational wave speed and $C_s = \sqrt{\mu/\rho}$ is the shear wave speed. The procedure for obtaining the asymptotic stress and displacement fields is identical to the mode III problem described in the previous section. Consider a traction free crack that is assumed to lie initially along $x_1 < 0,\ x_2 = 0$ and to move along $x_2 = 0$ at a constant speed $v < C_s$. The traction free boundary condition on the crack can be written as:

$$\sigma_{22}(x_1 < vt, 0^{\pm}) = 0;\ \sigma_{12}(x_1 < vt, 0^{\pm}) = 0 \tag{151}$$

Introducing a Galilean transformation $\xi_1 = x_1 - vt,\ \xi_2 = x_2$, and rescaling the coordinates $\zeta_d = r_d e^{i\theta_d} = \xi_1 + i\alpha_d\xi_2,\ \zeta_s = r_s e^{i\theta_s} = \xi_1 + i\alpha_s\xi_2$ with

$$r_d = \sqrt{\xi_1^2 + \alpha_d^2\xi_2^2},\ \theta_d = \arctan\left(\frac{\alpha_d\xi_2}{\xi_1}\right),\ \alpha_d = \sqrt{1 - \frac{v^2}{C_d^2}} \tag{152}$$

and $(\alpha_s, r_s, \theta_s)$ as defined in Eq. (143), the governing equations reduce to:

$$\nabla^2\varphi(r_d, \theta_d) = 0;\ \nabla^2\psi(r_s, \theta_s) = 0 \tag{153}$$

Now, we seek solutions to Eq. (153) of the form:

$$\varphi(r_d, \theta_d) = r_d^{\lambda} f(\theta_d; \lambda); \;\; \psi(r_s, \theta_s) = r_s^{\lambda} g(\theta_s; \lambda) \tag{154}$$

Substitution of Eq. (154) in to Eq. (153) results in two ordinary differential equations for f and g. The general solution contains symmetric (mode I) and antisymmetric (mode II) parts; we will consider only the symmetric part in the following;

$$\varphi(r_d, \theta_d) = A r_d^{\lambda} \cos(\lambda\theta_d); \;\; \psi(r_s, \theta_s) = B r_s^{\lambda} \sin(\lambda\theta_s) \tag{155}$$

Imposing the traction free boundary conditions using Eqs. (151) results in the following equations for A and B:

$$\begin{aligned} (1+\alpha_s^2) A \cos(\lambda-2)\pi + 2\alpha_s B \cos(\lambda-2)\pi = 0 \\ 2\alpha_d A \sin(\lambda-2)\pi + (1+\alpha_s^2) B \sin(\lambda-2)\pi = 0 \end{aligned} \tag{156}$$

For nontrivial solutions, the determinant of the above system of equations must be zero; this yields $\lambda = 1 + n/2$ for $n = 1, 2, 3...$ and $B = -2\alpha_d/(1+\alpha_s^2)A$ when n is odd and $B = -\left[(1+\alpha_s^2)/2\alpha_s\right] A$ when n is even. As in the quasi-static case, the term $n = 1$ results in square-root singular stress field, and bounded displacement field and energy. The term $n = 2$ results corresponds to the nonsingular $T - stress$ term. Defining the mode I dynamic stress intensity factor

$$K_I = \lim_{\xi_1 \to 0} \sqrt{2\pi\xi_1}\, \sigma_{22}(r, 0^{\pm}) \tag{157}$$

The dynamic crack tip stress and displacement fields may be written as

$$\begin{aligned} \sigma_{\alpha\beta}(r, \theta) &= \frac{K_I}{\sqrt{2\pi r}} \Sigma^I_{\alpha\beta}(\theta; v) + T(\alpha_d^2 - \alpha_s^2)\delta_{\alpha 1}\delta_{\beta 1} + ... \\ u_{\alpha}(r, \theta) &= \frac{K_I\sqrt{r}}{\sqrt{2\pi}} U^I_{\alpha}(\theta; v) + ... \end{aligned} \tag{158}$$

where we have included the terms corresponding to $n = 1$ and 2 for stresses and $n = 1$ for displacements; the term corresponding to $n = 2$ implies a stress component parallel to the crack and is typically denoted by σ_{0x} in the literature on experimental investigations (Kobayashi and Mall 1978) and is called the T-stress in the literature on quasi-static fracture (Cotterell and Rice 1980). The functions $\sum^I_{\alpha\beta}(\theta; v)$ and $U^I_{\alpha}(\theta; v)$ are given below

$$\Sigma_{11}^I(\theta; v) = \frac{1}{R(v)} \left\{ (1+\alpha_s^2)(1+2\alpha_d^2-\alpha_s^2) \frac{\cos\frac{\theta_d}{2}}{\sqrt{\gamma_d}} - 4\alpha_d\alpha_s \frac{\cos\frac{\theta_s}{2}}{\sqrt{\gamma_s}} \right\}$$
$$\Sigma_{22}^I(\theta; v) = \frac{1}{R(v)} \left\{ -(1+\alpha_s^2) \frac{\cos\frac{\theta_d}{2}}{\sqrt{\gamma_d}} + 4\alpha_d\alpha_s \frac{\cos\frac{\theta_s}{2}}{\sqrt{\gamma_s}} \right\} \tag{159}$$
$$\Sigma_{12}^I(\theta; v) = \frac{2\alpha_d(1+\alpha_s^2)}{R(v)} \left\{ \frac{\sin\frac{\theta_d}{2}}{\sqrt{\gamma_d}} - \frac{\sin\frac{\theta_s}{2}}{\sqrt{\gamma_s}} \right\}$$

and

$$U_1^I(\theta; v) = \frac{2}{\mu R(v)} \left\{ (1+\alpha_s^2)\sqrt{\gamma_d}\cos\frac{\theta_d}{2} - 2\alpha_d\alpha_s\sqrt{\gamma_s}\cos\frac{\theta_s}{2} \right\}$$
$$U_2^I(\theta; v) = \frac{2\alpha_d}{\mu R(v)} \left\{ (1+\alpha_s^2)\sqrt{\gamma_d}\sin\frac{\theta_d}{2} - 2\sqrt{\gamma_s}\sin\frac{\theta_s}{2} \right\} \tag{160}$$

where

$$\gamma_d = \sqrt{1-(v\sin\theta/C_d)^2} \qquad \tan\theta_d = \alpha_d\tan\theta \tag{161}$$

$$\gamma_s = \sqrt{1-(v\sin\theta/C_s)^2} \qquad \tan\theta_s = \alpha_s\tan\theta \tag{162}$$

$$R(v) = 4\alpha_d\alpha_s - \left(1+\alpha_s^2\right)^2 \tag{163}$$

Once again the correspondence to the quasi-static field is evident; we will elaborate on a number of aspects of the dynamic stress and displacement field in the following.

Remark 1 The dominant term exhibits a square-root singularity of stresses, with the amplitude dictated by the dynamic mode I stress intensity factor. The stress intensity factor itself must be determined from a full analysis of the appropriate initial-boundary value problem (see Remark 7).

Remark 2 The angular variations of the functions $\sum_{\alpha\beta}^I(\theta; v)$ are shown in Figs. 28, 29 and 30. The angular variation of the hoop component of the stress field $\sum_{\theta\theta}^I$ is given in Fig. 31; this component was examined by Yoffe (1951). The shift in the peak from $\theta = 0^\circ$ to $\theta = 60^\circ$ as the crack speed increased to about $v = 0.6C_R$ was suggested as the cause of crack branching. The angular variation of the principal stress is shown in Fig. 32. It should be noted that the maximum principal stress component does not act normal to the prospective crack line; Rice (1968b) observed that the $\sum_{11}^I(\theta; v) > \sum_{22}^I(\theta; v)$ and hence paradoxical that the crack continues to grow along the x_1 direction.

Remark 3 The denominator of the stress and displacement fields contain the function $R(v)$, called the Rayleigh function; it can be shown that $R(v) = 0$ at $v = 0$ and

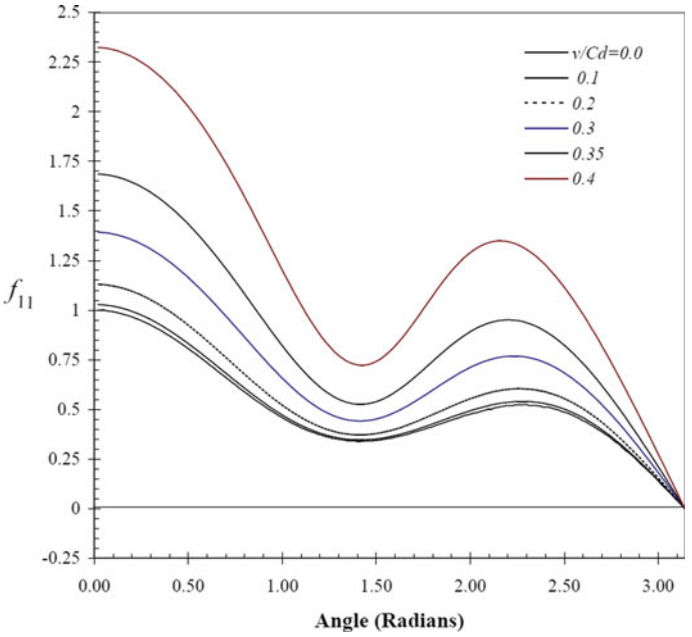

Fig. 28 Angular variation of $f_{11}(\theta)$ for a mode-I crack

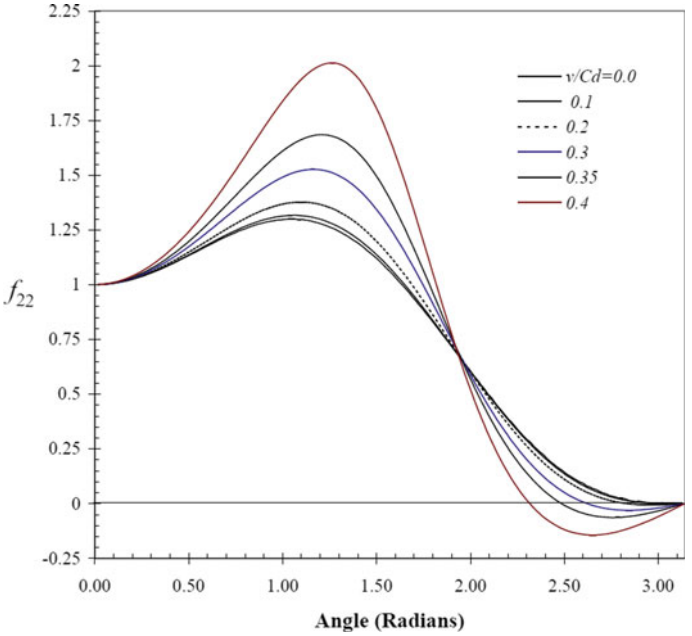

Fig. 29 Angular variation of $f_{22}(\theta)$ for a mode-I crack

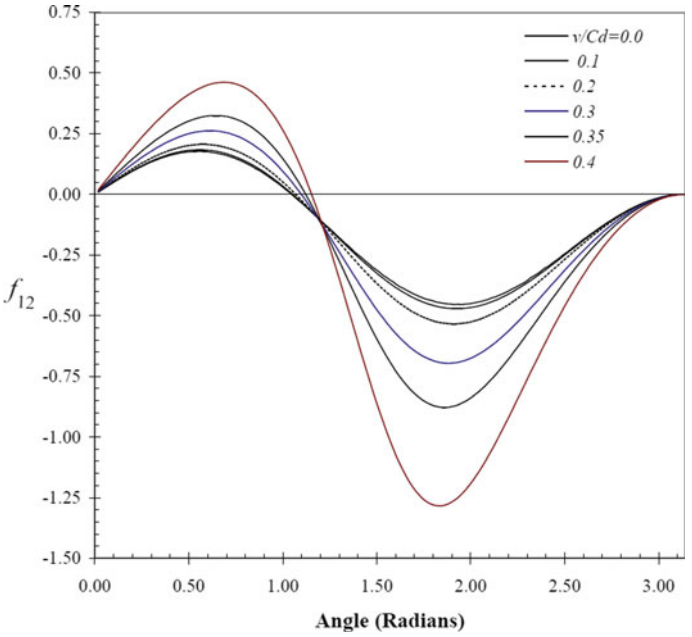

Fig. 30 Angular variation of $f_{12}(\theta)$ for a mode-I crack

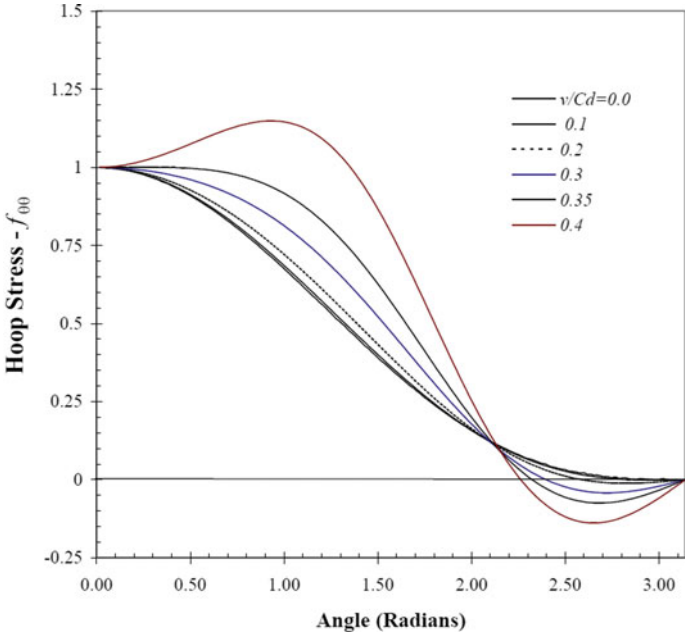

Fig. 31 Angular variation of $f_{\theta\theta}(\theta)$ for a mode-I crack

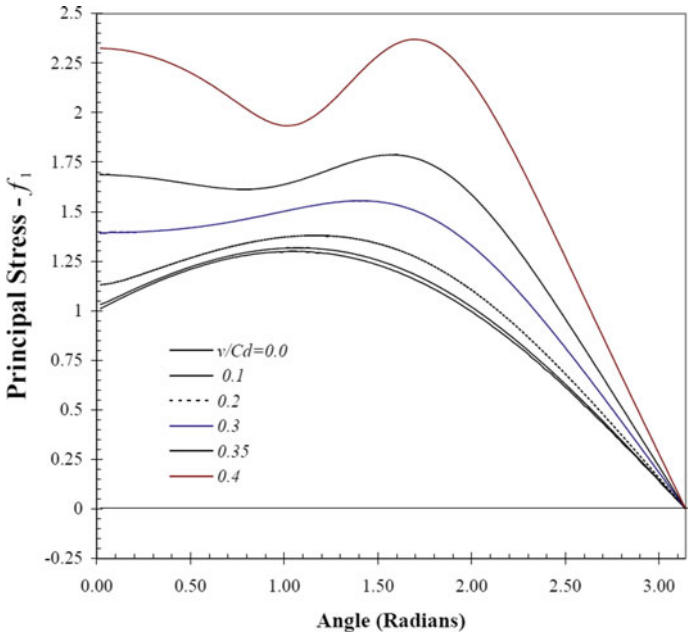

Fig. 32 Angular variation of $f_1(\theta)$ for a mode-I crack

$v = C_R$ where the speed C_R is called the Rayleigh surface wave speed. It represents a wave that travels along the surface $x_2 = 0$ in the x_1 direction, and shows an exponential decay along the x_2 direction. Viktorov (1967) developed an approximate representation for the Rayleigh wave speed:

$$C_R = \frac{0.862 + 1.14v}{1 + v} C_s, \tag{164}$$

Hence, the limit of the fields as $v \to 0$ must be taken with care to recover the quasi-static crack tip stress field. In the limit $v \to C_r$, the inertial effect is seen to lead to a singularity in the stress and displacement fields that can only be removed if the dynamic stress intensity factor tends to zero in this limit. From this, one can consider that the Rayleigh wave speed C_R would set the limit for crack speed; we will return to this after consideration of the energy balance.

Remark 4 Similar analysis of the anti-plane symmetric problem can be performed to determine the mode II dynamic stress field and displacement fields:

$$\sigma_{\alpha\beta}(r,\theta) = \frac{K_{II}}{\sqrt{2\pi r}}\Sigma^{II}_{\alpha\beta}(\theta;v) + \ldots$$
$$u_{\alpha}(r_s,\theta_s) = \frac{K_{II}\sqrt{r}}{\sqrt{2\pi}}U^{II}_{\alpha}(\theta;v) + \ldots \tag{165}$$

where the mode II dynamic stress intensity factor is defined as

$$K_{II} = \lim_{\xi_1\to 0}\sqrt{2\pi\xi_1}\sigma_{12}(r,0^{\pm}) \tag{166}$$

The corresponding angular distribution functions may be found in the literature (Freund 1990; Ravi-Chandar 2004).

Remark 5 The asymptotic fields determined here were obtained under the assumption of steady motion of the crack tip. Freund (1990) has shown that if the crack moves with a nonuniform speed, the result described above carries over completely, with the only change that the stress intensity factor can now be considered to be a function of time and the instantaneous crack speed, $K_I(t,v)$. The effects of the nonuniform motion of the crack do not become apparent in the singular term or the constant term, but only in terms of higher order. In some experimental methods crack tip field information is extracted from distances that are far from the crack tip; in these applications, the higher order transient expansion may be required to obtain an estimate of the stress intensity factor.

Remark 6 Consideration of the crack tip stress field for speeds $C_s < v < C_d$ indicates a square root singular field appears only in the case of mode II, and only at the speed $v = \sqrt{2}C_s$; this is important in frictional sliding and earthquakes. We do not consider these aspects here, but refer to the literature (Freund 1990; Broberg 1999).

Remark 7 Most of the analysis of dynamic fracture problems has focused on the determination of the dynamic stress intensity factor in a given initial-boundary value problem under the assumption of propagation of a straight crack at a constant speed; we remark on one very important result that makes such analysis simpler. Kostrov (1966, 1975), Freund (1972a, b, 1973, 1974), Slepyan (2002) and Willis (1992) have also addressed the issue of a crack growing at a nonuniform speed. Freund (1990) proved the following remarkable result: the stress intensity factor for mode I extension of a half-plane crack is given by the universal function $k(v)$ times the stress intensity factor appropriate for a crack of fixed length, equal to the instantaneous length, subjected to the given applied loading, whether this loading is time-independent or time dependent (Freund 1973); this is expressed as

$$K_I(t,a,v) = k(v)K^0_I(t,a,0);\ \ k(v) \approx \frac{1-v/C_R}{\sqrt{1-v/C_d}} \tag{167}$$

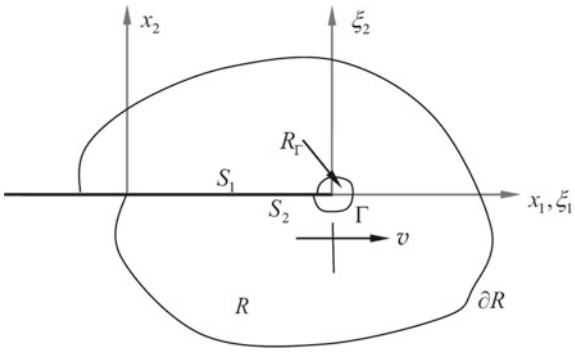

Fig. 33 Crack tip contour for evaluation of the energy flux integral

where $K_I^0(t, a, 0)$ is the dynamic stress intensity factor corresponding to a stationary crack of length a at time t. The function $k(v)$ decreases monotonically with $k(0) = 1$ and $k(C_R) = 0$. This is a powerful result because we can leverage of solutions to stationary crack problems.

In order to complete the formulation of the dynamic fracture problem, one must add the energy or power balance equation to the initial-boundary value problem and obtain the crack tip motion. This is considered in the next section.

Energy Failure criteria for dynamic fracture can be obtained by an extension of Griffith's ideas postulated for equilibrium cracks. Mott (1948) suggested that for rapidly growing cracks, kinetic energy must be incorporated in writing down the energy balance. However, the correct and complete formulation of the local energy rate balance equation was not provided until after the nature of the dynamic stress field had been determined completely (see the works of Broberg 1960; Atkinson and Eshelby 1968; Kostrov and Nikitin 1970; Freund 1972a; Willis 1975; and others). In order to determine the power balance, let us consider the situation illustrated in Fig. 33. Let us assume crack propagation in the x_1 direction at a constant speed v. R is any region near the crack tip bounded by the curve ∂R. R_Γ is a region near the crack tip bounded by the curve Γ that surrounds the crack tip fracture process zone and moves with the crack. The power balance may be written as

$$\frac{d}{dt}\int\limits_{R-R_\Gamma} \frac{1}{2}\left[\sigma_{\alpha\beta}\varepsilon_{\alpha\beta} + \rho\dot{u}_\alpha\dot{u}_\alpha\right] dA = \int\limits_{\partial R} \sigma_{\alpha\beta}n_\beta\dot{u}_\alpha ds + F \tag{168}$$

where the left hand side indicates the rate of change of strain energy and kinetic energy within the region $R - R_\Gamma$ and this is balanced by the power of the tractions on ∂R and the flux of energy out through Γ, into the fracture process zone. The traction free crack surfaces denoted as S_1, S_2 do not contribute to this balance. Taking the time derivative inside the integral, applying Reynold's transport theorem and divergence theorem, Eq. (168) can be evaluated to obtain the energy flux into the fracture process zone as

$$F = \lim_{\Gamma \to 0} \int_{\Gamma} \left[\sigma_{\alpha\beta} n_\beta \dot{u}_\alpha + \frac{1}{2} \left(\sigma_{\alpha\beta} \varepsilon_{\alpha\beta} + \rho \dot{u}_\alpha \dot{u}_\alpha \right) v n_1 \right] ds \tag{169}$$

For steady-state crack growth, the energy flux integral is independent of the path Γ; if this path is taken to be in the dynamic K-dominant zone, the energy flux to the fracture process zone can be calculated in terms of the dynamic stress intensity factor. If D is the total dissipation in the fracture process, $F = dD/dt = vdD/da = v\Gamma_D$, where Γ_D is the dissipation per unit crack extension and a is the crack length. Hence, we can define *the dynamic energy release rate* as $G = v^{-1}F$. Evaluating the energy flux in the K-dominant zone yields

$$\begin{aligned} G &= \frac{1-\nu^2}{E} \left[A_I(v) K_I^2 + A_{II}(v) K_{II}^2 \right] + \frac{1}{2\mu} A_{III}(v) K_{III}^2 \\ A_I(v) &= \frac{v^2 \alpha_d}{(1-\nu) C_s^2 R(v)}; \; A_{II}(v) = \frac{v^2 \alpha_s}{(1-\nu) C_s^2 R(v)}; \; A_{III}(v) = \frac{1}{\alpha_s} \end{aligned} \tag{170}$$

and the fracture criterion written as

$$G = \Gamma \tag{171}$$

Restricting attention to mode I loading, Eq. (171) can be written as the crack tip equation of motion:

$$\frac{(1+\nu)}{E} \frac{v^2 \alpha_d}{C_s^2 R(v)} \left[k(v) K_I^0(t, a, 0) \right]^2 = \Gamma \tag{172}$$

Given $K_I^0(t, a, 0)$, Eq. (172) can be solved to find the crack speed. We elaborate on the crack tip equation of motion in the following:

Remark 1 It is implied in Eq. (172) that the fracture energy is a material constant; however, it is likely to depend on the temperature, loading rate and other factors such as evolution of the fracture process zone, thus requiring $\Gamma_D = \Gamma_D \left(T, \dot{K}_I, v, ... \right)$, to be calibrated through experiments.

Remark 2 As with the quasi-static case, the additive expression for the dynamic energy release rate under mixed mode loading is applicable only as long as the crack follows a straight path; under mixed mode loading, the dynamic crack is expected to take a curved path following the criterion of local symmetry.

Remark 3 The functions $A_I(v)$ and $A_{II}(v)$ are singular as $v \to C_R$, while $A_{III}(v)$ the function is singular as $v \to C_s$; thus in-plane cracks have a limiting speed at the Rayleigh wave speed while the anti-plane shear cracks have a limiting speed at the shear wave speed.

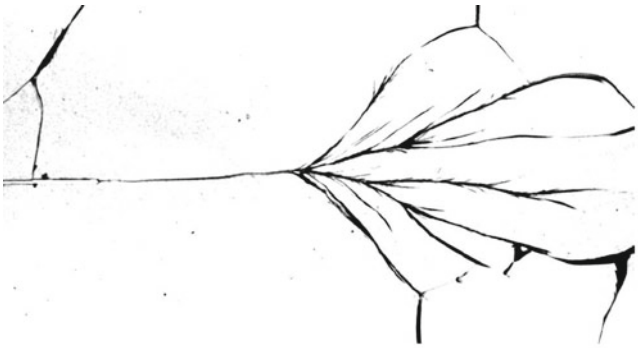

Fig. 34 Branching of cracks in a Homalite-100 specimen (from Ravi-Chandar and Knauss 1984c)

Remark 4 There have been a number of experimental investigations examining the applicability of the above equation of motion; experiments by Bergkvist (1974), Dally (1979), Ravi-Chandar and Knauss (1984a, b, c, d), Ramulu and Kobayashi (1985), Washabaugh and Knauss (1994), Sharon and Fineberg (1999), Sundaram and Tippur (2016), and others in a number of different brittle polymers showed that for cracks propagating at speeds $v < 0.4C_R$, the equation of motion represented the dynamic fracture problem accurately; some results indicated possible dependence of the fracture energy on the crack speed. Goldman et al. (2010) showed that by inhibiting three-dimensional effects in thin specimens of a brittle gel specimen, cracks could be made to grow at speeds close to the Rayleigh wave speed, and that the equation of crack tip motion in Eq. (172) was fully capable of capturing the crack tip behavior under such conditions.

Remark 5 *Limiting crack speed.* Experiments also showed consistently, and in different inorganic and organic glasses, that unless the crack path and the fracture process zone are somehow constrained, the speed of a growing crack seldom exceeded $0.6C_R$, and was typically in the range $0.4 - 0.65C_R$; this is in contrast to the energetic limit of C_R. In fact, Schardin (1959) measured the limiting crack speed in 29 different inorganic glasses, obtained by systematically varying the composition and found that the liming speed varied in the range from $0.347C_s$ to $0.614C_s$, indicating that the continuum formulation could not identify the origins of the lower observed limiting speed and that one must look towards models of the fracture process.

Remark 6 *Crack branching.* Upon reaching a crack speed of $\sim 0.4 - 0.6C_R$, the crack would branch into spectacular patterns as shown in Fig. 34. Branching of cracks in glass was recorded first by Schardin and Struth (1938) and Schardin (1959); other investigators have observed crack branching in crystalline as well as amorphous materials. Dally (1979) observed multiple branches emanating from a single crack in an explosively loaded crack in Homalite-100. Kobayashi et al. (1973) examined

branching in quasi-statically loaded specimens; cracks were driven into an increasing stress field and branching was promoted. Yoffe (1951) attempted to explain the branching of cracks from the crack tip asymptotic stress field. From the dynamic crack tip stress field shown in Eq. (158), she found that the maximum of the hoop stress acted normal to lines that make an angle of 60° with the direction of crack propagation when the crack speed exceeded $0.6C_R$; the angular variation of $\sigma_{\theta\theta}$ is shown in Fig. 31. Therefore, Yoffe suggested that this stress field rearrangement might lead to crack branching. Rice (1968a, b) suggested that since the direction of the major principal is parallel to the crack propagation direction there would be a tendency to deflect the crack away from its original path. Both these rearrangements of the stress field with crack speed should have an influence on how the damage mechanisms operate within the fracture process zone. High speed photographs of crack branching process shown in Ravi-Chandar and Knauss (1984b) indicate the complexity of the branching process through the interaction of multiple microbranches. Recent modeling efforts using the phase-field method (Borden et al. 2012a) and peridynamics (Bobaru and Zhang 2015) show some promise in being able to simulate crack branching.

Remark 7 *Crack surface roughening.* Even prior to crack branching, fracture surface roughness was observed to evolve with crack propagation, increasing the energy dissipated. Ravi-Chandar and Knauss (1984b) examined the crack structure in roughening dynamic cracks, and their corresponding fracture surface, and suggested that the propagation of the crack was not in the form of an ideal, single crack, but was due to the nucleation and growth of a cloud or ensemble of microcracks, with the dynamics of their interaction dictating in the fracture surface evolution and the branching instability. Fineberg et al. (1991) identified a critical crack speed at which a microbranching instability is triggered. Clear departure from the predictions of the crack tip equation of motion can be attributed to the emergence of these non-ideal fracture processes. There is also a large modeling effort aimed at replicating the observed branching based on damage mechanics, cohesive zone models, lattice models etc. But most of these models do not incorporate sufficient resolution of the fracture evolution to be able to capture the surface roughening triggered by processes that occur within the fracture process zone.

6 Phase-Field Model for Linearly Elastic Fracture Problems

The methods of analysis, both for quasi-static and dynamic fracture, are rather well-established. However, the tracking of growing cracks within this framework is quite a tedious task. Many numerical methods such as the cohesive zone model, extended finite element method etc. have been developed to make numerical calculations possible. Of all these methods the phase-field method appears to have developed into quite an efficient tool, firmly rooted in the energy minimization approach. We provide a very short introduction to this method.

The phase-field method is a versatile technique for solving problems of moving interfaces such as the formation of microstructures in solidification, multiphase flow, image segmentation, and other applications. In recent years, it has been applied to fracture mechanics in order to provide a remedy for the discontinuity of the displacement field along the crack surface which poses difficulty for many numerical solution techniques. There exist two kinds of phase-field formulations: the formulation based on Griffith's fracture theory (Bourdin et al. 2008) and the formulation based on Ginzburg-Landau theory (Karma et al. 2001). Ambati et al. (2015) provide a detailed comparative review of different formulations of phase-field models. Here, we summarize a quasi-static two-dimensional formulation based on the presentation of Borden et al. (2012a).

Consider a two dimensional solid enclosed in the domain Ω with the boundary $\partial\Omega$ and a crack S (shown in Fig. 4). The domain boundary $\partial\Omega$ is divided into non-overlapping subsets $\partial\Omega_t$ where the tractions are prescribed, and $\partial\Omega_u$ where the displacements are prescribed and the segment S that defines the crack. The total energy of the system can be written as:

$$E(\mathbf{u}, S) = \int_{\Omega} W_e(\boldsymbol{\varepsilon}) dA + \int_{S} \Gamma ds - \int_{\partial\Omega_t} t_i u_i ds \tag{173}$$

where $\mathbf{u}$ is the displacement vector, $W_e(\boldsymbol{\varepsilon})$ is the elastic strain energy density, $\boldsymbol{\varepsilon} = sym\nabla\mathbf{u}$ is the strain tensor, Γ is the fracture energy and $\mathbf{t}$ is the traction vector. The solution is to be obtained by minimization over the admissible displacement fields, and the unknown crack segment S. This problem is difficult to address in this generality because the crack (and its evolution) are part of the solution. The strategy for finding a solution is to use a scalar field to smear the line discontinuity corresponding to the crack over the spatial domain and reformulate the problem. This consists of essentially three steps: first, the integral over the segment S is smeared through the use of a scalar field $c(\mathbf{x})$, $c \in [0, 1]$, called the *phase-field* which represents the material state: $c = 0$ indicates that the material is fully damaged, while the material is intact for $c = 1$. With this definition, Bourdin et al. (2008) represented the second term in Eq. (173) with an integral over the domain Ω:

$$\int_{S} \Gamma ds \approx \int_{\Omega} \Gamma \left[\frac{(c-1)^2}{4l_0} + l_0 \frac{\partial c}{\partial x_i} \frac{\partial c}{\partial x_i} \right] dA \tag{174}$$

where l_0 is an intrinsic length scale that arises from representing the integral over the segment S by an integral over the domain Ω. Clearly wherever $c = 1$, the material is undamaged and the first term in Eq. (174) does not contribute to energy; wherever $c = 0$, the material is fully damaged and this term will account for the fracture energy Γ over this region. Second, gradients in the phase-field are penalized by adding a second term to the fracture energy representation; this enables appropriate modeling of the sharp discontinuity of the crack. The third, and last ingredient of the model is to

use the scalar phase-field parameter to degrade the elastic properties of the material. Thus, the elastic energy is written as

$$W(\boldsymbol{\varepsilon}, c) = g(c) W_e(\boldsymbol{\varepsilon}) \tag{175}$$

where $g(c)$ is called the *degradation function*. Thus, Eq. (173) is rewritten as

$$E(\mathbf{u}, c, \nabla c) \approx \int_{\Omega} \left[W(\boldsymbol{\varepsilon}, c) + \Gamma \left\{ \frac{(c-1)^2}{4 l_0} + l_0 \frac{\partial c}{\partial x_i} \frac{\partial c}{\partial x_i} \right\} \right] dA - \int_{\partial \Omega_t} t_i u_i ds \tag{176}$$

It has been shown (see for example, Chambolle 2004), following the ideas of Ambrosio and Tortorelli (1990) that the approximation in Eq. (176) approaches Eq. (173) as $l_0 \to 0$. The governing Euler-Lagrange equations are derived from Eq. (176) as:

$$\begin{cases} \dfrac{\partial \sigma_{ij}}{\partial x_j} = 0 \quad \text{in } \Omega \\ \dfrac{l_0}{2\Gamma} g'(c) W_e(\boldsymbol{\varepsilon}) + \dfrac{c-1}{4} - l_0^2 \dfrac{\partial^2 c}{\partial x_j \partial x_j} = 0 \quad \text{in } \Omega \end{cases} \tag{177}$$

where $\sigma_{ij} = \dfrac{\partial W}{\partial \varepsilon_{ij}}$ is the damaged stress. These equations are subjected to the boundary conditions:

$$\begin{cases} \mathbf{u} = \mathbf{g} \quad \text{on } \partial \Omega_u \\ \boldsymbol{\sigma}.\mathbf{n} = \mathbf{h} \quad \text{on } \partial \Omega_t \\ \nabla c.\mathbf{n} = 0 \quad \text{on } \partial \Omega \end{cases} \tag{178}$$

Many general types of degradation of elastic energy have been considered by Braides (1998), and studied in detail by Pham et al. (2011). Here, we follow Borden (2012b) and use a cubic degradation of the form:

$$g(c) = s\left(c^3 - c^2\right) + 3c^2 - 2c^3 \tag{179}$$

with $s > 0$. For the case when $s = 2$, we get $g(c) = c^2$, the degradation suggested by Bourdin et al. (2008) while a small value of s results a linear stress-strain response prior to the onset of damage; we will illustrate both in the following. This essentially completes the formulation of the phase-field model for fracture; the governing equations in Eq. (177) can now be solved using standard numerical methods such as the finite element method.

Note that the model is described by two elastic parameters (E, ν), the modulus of elasticity and Poisson's ratio, one fracture parameter, Γ, the fracture energy, and one discretization parameter, l_0. Bourdin et al. (2008) showed that the fracture energy is amplified in the phase-field simulation based on finite element discretization and

that this has to be taken into account in formulating the simulation. Therefore, the fracture energy must be scaled in simulations by the approximation proposed by Bourdin et al. (2008):

$$\Gamma_{sim} = \frac{\Gamma}{(1 + h/4l_0)} \tag{180}$$

where Γ is the actual material fracture energy, and h is the minimum size of the mesh; this leaves the intrinsic scale in the phase-field model l_0 yet to be chosen. One option is to let this be unspecified and all lengths are then scaled by the value of l_0. Another option is to obtain an estimate of l_0 by considering the response of the phase-field model to homogeneous uniaxial deformation (see Borden et al. 2012a); we will discuss this next.

Let us consider a one-dimensional example, in a linearly elastic material, with $W_e(\boldsymbol{\varepsilon}) = \frac{1}{2}E\varepsilon^2$, and the degradation function take to be $g(c) = c^2$; we impose a homogeneous deformation with a monotonically increasing applied strain ε. Considering that homogeneous deformation is imposed, we set $\nabla c = 0$ in Eq. $(177)_2$, and obtain

$$c = \left[\frac{4l_0}{\Gamma}W_e(\boldsymbol{\varepsilon}) + 1\right]^{-1} = \left[\frac{2l_0E}{\Gamma}\varepsilon^2 + 1\right]^{-1} \tag{181}$$

Equation $(177)_1$ implies that the stress σ is constant and can be determined to be

$$\sigma = c^2 E\varepsilon = \left[\frac{2l_0E}{\Gamma}\varepsilon^2 + 1\right]^{-2} E\varepsilon \tag{182}$$

Equations (181) and (182) together allow the determination of the phase-field and stress as a function of the uniaxial strain. A similar set of expressions can be found for the cubic degradation function (see Borden 2012b). The variation of the stress (normalized by the modulus of elasticity) and phase-field parameter with the applied strain is shown in Fig. 35, by the red lines. The corresponding results for the cubic degradation function with $s = 0.01$ is shown by the black lines. From these figures, it is clear that the stress increases with strain initially, becomes nonlinear, reaches a peak, and then begins to decrease as the material damages. Corresponding to this, the phase-field parameter decreases slowly from unity until the peak stress is reached, and then begins to decrease more rapidly with strain heading towards a fully damaged state. It is noted that the phase-field model yields a stress strain behavior that mimics a damage model. The quadratic degradation function generates damage from very early stages of straining, while in comparison, the cubic degradation function provides a linear response nearly up to the peak load point, and a much more rapid degradation beyond this point; the cubic degradation appears closer to representing truly brittle materials.

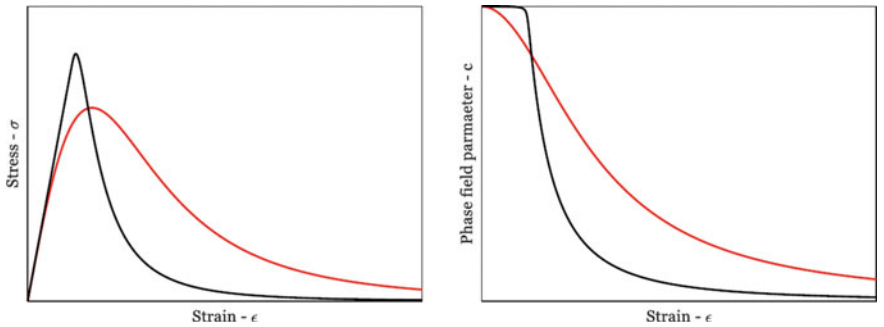

Fig. 35 Variation of the stress versus strain and the phase-field with strain. Both quadratic degradation function (black lines) and cubic degradation (red lines) are shown

From Eq. (182) it can be shown that the stress strain relation is non-monotonic and further that the stress attains a peak value of

$$\sigma_c = \frac{9}{16}\sqrt{\frac{\bar{E}\Gamma}{6l_0}} \tag{183}$$

when the strain level is $\varepsilon_c = \sqrt{\Gamma/(6l_0\bar{E})}$, where $\bar{E} = E/(1-\nu^2)$; at this strain level, the phase-field parameter reaches $c_c = 3/4$. Rearranging, Eq. (183), one can obtain the following estimate

$$\sigma_c^2 l_0 = \frac{27\bar{E}\Gamma}{512} \tag{184}$$

This implies that corresponding to any chosen value of l_0, there is an appropriate peak stress σ_c, that one might label the cohesive strength of the material. For any material with given elastic properties (E, υ), and fracture energy, Γ, the cohesive strength and the intrinsic length scale are to be chosen according to Eq. (184). In the limit of $l_0 \to 0$, we have $\sigma_c \to \infty$, recovering the elastic singularity. If we take a common thermoplastic polymer, polymethylmethacrylate (PMMA) as an example, we have: $E = 2.98$ GPa, $\nu = 0.35$, and $\Gamma = (1-\nu^2)K_{IC}^2/E = 0.285$ kJ/m^2, assuming that the peak stress is equivalent to the macroscopic tensile strength of the material ($\sigma_c \sim 50$MPa) yields $l_0 \sim 20 \times 10^{-6}$ m. This provides the scale at which numerical discretization must be accomplished.

Next, we turn to an example of non-homogeneous deformations, in a linearly elastic material, with $W_e(\boldsymbol{\varepsilon}) = \frac{1}{2}E\varepsilon^2$, and the degradation function taken to be $g(c) = c^2$. We set $W_e(\boldsymbol{\varepsilon}) = \frac{1}{2}E\varepsilon^2 = \frac{\sigma^2}{2Ec^4}$ in Eq. (177), and obtain

$$\left[\frac{2l_0}{E\Gamma c^4}\sigma^2 + 1\right]c - 4l_0^2\frac{d^2c}{d^2x} = 1 \tag{185}$$

Given a constant stress σ as $x \to \pm\infty$, Eq. (185) is a nonlinear ordinary differential equation for c. Details of the solution procedure can be found in Borden et al. (2012a); here we will only consider the case when the stress is zero everywhere uniformly, $c(0) = 0$ and $c(x \to \pm\infty) = 1$. The solution is obtained as

$$c(x) = 1 - \exp\left(-\frac{|x|}{2l_0}\right) \tag{186}$$

This is illustrated in Fig. 36. This result indicates that the zone of failure spreads exponentially, corresponding to the quadratic degradation function. Using the cubic degradation results in a significant decrease in the extent of the damaged region.

There are two significant limitations of the model represented in Eq. (177): first, it allows a crack to grow under compressive loading condition. Second, damage modeled in this manner is reversible. Both of these issues have been addressed extensively in the literature. In order to suppress the nonphysical behavior, Amor et al. (2011) presented a model in which material softening based on the decomposition of the strain energy density into "positive" W_e^+ and "negative" W_e^- parts was considered corresponding to the dilatational and deviatoric parts of the strain tensor; Miehe et al. (2010) used an alternative model where the strain tensor is decomposed into positive and negative parts based on the principal strains. The degradation function is then applied only to the "positive" part of the strain energy density to prohibit the crack to evolve under compressive loading:

$$W = g(c)W_e^+ + W_e^- \tag{187}$$

In order to prevent the crack from healing, additional equality (Bourdin 1999) or inequality (Giacomini 2005) constraints on the phase field evolution have been used. Miehe et al. (2010) enforced the irreversibility condition, through a strain-history field: $H_0 = H(x, t_0) = 0$ at the initial step $t = t_0$, $H = H(x, t_n)$ at the loading step $t = t_n$. The strain-history field for Bourdin's model can be written as:

$$H(x, t_n) = \begin{cases} W_e, \text{ for } W_e > H(x, t_{n-1}) \\ H(x, t_{n-1}), \text{ otherwise} \end{cases} \tag{188}$$

and for Miehe's model:

$$H(x, t_n) = \begin{cases} W_e^+, \text{ for } W_e^+ > H(x, t_{n-1}) \\ H(x, t_{n-1}), \text{ otherwise} \end{cases} \tag{189}$$

Substituting the strain-history field and material degradation model into the system of Eqs. (176), (177) yields:

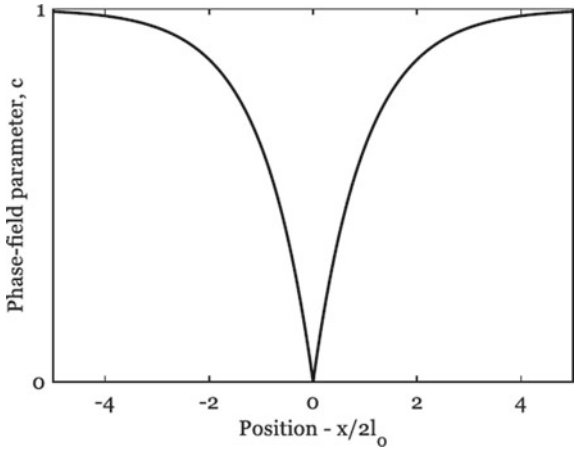

Fig. 36 Nonhomogeneous phase field solution corresponding to zero stress

$$\begin{cases} \dfrac{\partial \sigma_{ij}}{\partial x_j} = 0 \quad \text{in } \Omega \\ Q(c) - l_0^2 \dfrac{\partial^2 c}{\partial x_j \partial x_j} = 0 \quad \text{in } \Omega \end{cases} \tag{190}$$

$$\text{where} \quad Q(c) = \frac{l_0 H g'(c)}{2G_c} + \frac{c-1}{4},$$
$$\sigma_{ij} = \begin{cases} g(c)\dfrac{\partial W_e}{\partial \varepsilon_{ij}}, & \text{for Bourdin's model} \\ g(c)\dfrac{\partial W_e^+}{\partial \varepsilon_{ij}} + \dfrac{\partial W_e^-}{\partial \varepsilon_{ij}}, & \text{for Miehe's model} \end{cases} \tag{191}$$

The governing equations Eqs. (190) are coupled between the displacement field and phasefield and can be solved with a coupled formulation or operator splitting schemes. The literature on the use of phase-field models to simulate fracture problems is already vast and growing rapidly. A number of investigators have considered quantitative validation of simulations and experimental measurements (see for example, Mesgarnejad et al. 2015; Nguyen et al. 2016; Pham et al. 2017b).

7 Summary

The methods of linear elastic fracture mechanics summarized in this article have provided the foundations for design and operation of fracture critical structures and a fundamental paradigm shift in safety and reliability assessment as illustrated in the flow-chart in Fig. 37. Prior to the establishment of these methods, the philosophy behind design and safety assessment relied on material strength based criterion,

assuming that the structure contained no defects and that during its entire life, the structure was not expected to exceed the limits established based on material strength. However, in practice, catastrophic and sudden failures always resulted from flaws inherent in the materials/structures. Based on the ideas of fracture mechanics, a new design and safety assessment procedure has been well established, in which it is assumed that flaws/defects/cracks exist in the material/structure and are taken into account by ensuring that the structure is safe in spite of the flaws/defects. If the structure is designed to undergo stable crack growth, progression of flaw growth may be monitored and the structure removed from service or repaired prior to reaching fracture critical conditions. This approach to design and operation is known as fracture critical design, flaw-tolerant design or fail-safe design and eliminates catastrophic failure. The key idea is that as long as the flaws are subcritical within the framework of LEFM, the structure could be used—the failure is considered to be 'graceful' rather than catastrophic. This shift from strength-based to fracture-critical design and operation relies on Fracture Mechanics as the central framework as illustrated in Fig. 37. It is supported by three pillars: *non-destructive characterization methods* (NDE) that provide a quantitative characterization of the flaw geometry; *material characterization methods* that provide determination of the material properties, including fracture toughness; and *stress analysis methods* such as the finite element method that provide estimates of the stress intensity factors or energy release rates under different loading conditions on the flaw that was characterized through NDE. Modern structures, especially aircraft structures have benefited enormously from this approach to fracture-critical design, safety and reliability assessment.

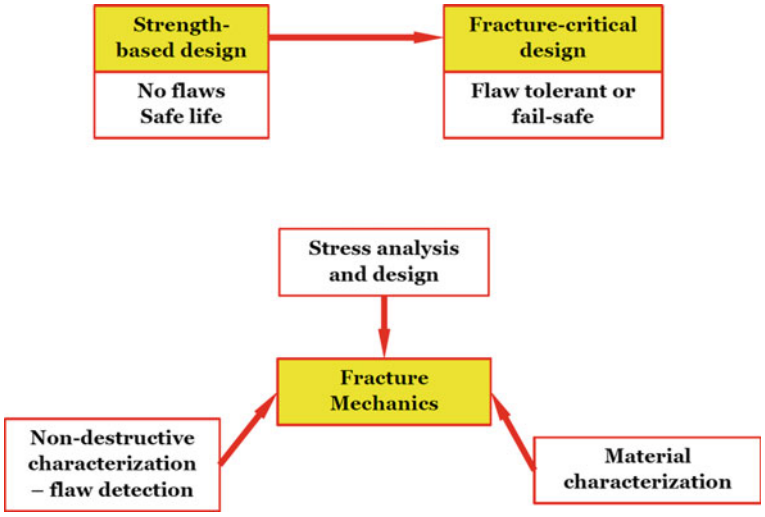

Fig. 37 Flow chart illustrating the flaw tolerant approach to design and operation of fracture critical structures

References

Adams M, Sines G (1978) Crack extension from flaws in a brittle material subjected to compression. Tectonophysics 49:97–118

Ambati M, Gerasimov T, De Lorenzis L (2015) A review on phase-field models of brittle fracture and a new fast hybrid formulation. Comput Mech 55:383–405

Ambrosio L, Tortorelli VM (1990) Approximation of functionals depending on jumps by elliptic functionals via -convergence. Commun Pure Appl Math 43:999–1036

Amestoy M, Leblond JB (1992) Crack paths in plane situations - II: detailed form of the expansion of the stress intensity factors. Int J Solids Struct 29:465–501

Amor H, Marigo JJ, Maurini C (2009) Regularized formulation of the variational brittle fracture with unilateral contact: numerical experiments. J Mech Phys Solids 57:1209–1229

Atkinson C, Eshelby JD (1968) The flow of energy into the tip of a moving crack. Int J Fract 4(1968):3–8

Bergkvist H (1974) Some experiments on crack motion and arrest in polymethylmethacry-late. Eng Fract Mech 6:621–626

Bobaru F, Zhang G (2015) Why do cracks branch? A peridynamic investigation of dy-namic fracture. Int J Fract 196:59–98

Borden MJ, Verhoosel CV, Scott MA, Hughes TJR, Landis CM (2012) A phase-field de-scription of dynamic brittle fracture. Comput Methods Appl Mech Eng 217–220:77–95

Borden MJ (2012) Isogeometric analysis of phase-field models for dynamic brittle and ductile failure. Ph.D Dissertation, The University of Texas at Austin

Bourdin B (1999) Image segmentation with a finite element method. M2AN Math Model Numer Anal 33:229–244

Bourdin B, Francfort GA, Marigo JJ (2001) Numerical experiments in revisited brittle fracture. J Mech Phys Solids 48:797–826

Bourdin B, Francfort GA, Marigo J (2008) The variational approach to fracture. J Elast 91:5–148

Braides A (1998) Approximation of free-discontinuity problems. Number 1694 in Lecture notes in mathematics. Springer

Broberg KB (1960) The propagation of a brittle crack. Arkiv fur Fysik 18:159–192

Broberg KB (1999) Cracks and fracture. Academic Press

Burridge R, Keller JB (1978) Slipping and cracking - Some one-dimensional free-boundary prob-lems in mechanics. SIAM Rev 20:31–61

Chai H, Babcock CD, Knauss WG (1984) One dimensional modeling of failure in laminated plates by delamination buckling. Int J Solids Struct 17:1069–1083

Chambolle A (2004) An approximation result for special functions with bounded variations. J Math Pure Appl 83:929–954

Chen CH, Cambonie T, Lazarus V, Nicoli M, Pons A, Karma A (2015) Crack front seg-mentation and facet coarsening in mixed mode fracture. Phys Rev Lett 115:265503

Cherepanov GP (1967) The propagation of cracks in a continuous medium. J Appl Math Mech 31:503–512

Cooke ML, Pollard DD (1996) Fracture propagation paths under mixed mode loading within rect-angular blocks of polymethylmethacrylate. J Geophys Res 101:3387–3400

Cotterell B, Rice JR (1980) Slightly curved or kinked cracks. Int J Fract 16:155–169

Cox SJD, Scholz CH (1988) On the formation and growth of faults: an experimental study. J Struct Geol 10:413–430

Dally JW (1979) Dynamic photoelastic studies of fracture. Exp Mech 19:349–361

Dumouchel PE, Marigo JJ, Charlotte M, (2008) Dynamic fracture: an example of convergence towards a discontinuous quasistatic solution. Contin Mech Thermodyn 20:1–19

Erdogan F, Sih GC (1963) On the crack extension in plates under plane loading and transverse shear. J Basic Eng 85:519–525

Eshelby JD (1970) Energy relations and the energy-momentum tensor in continuum mechanics. In: Kanninen MF et al (eds) Inelastic behavior of solids. McGraw-Hill, New York, pp 77–115

Fineberg J, Bouchbinder E (2015) Recent developments in dynamic fracture: some perspectives. Int J Fract 196:33–57
Fineberg J, Gross SP, Marder M, Swinney HL (1991) Instability in the propagation of fast cracks. Phys Rev B 45:5146–5154
Freund LB (1972) Energy flux into the tip of an extending crack in an elastic solid. J Elast 2:341–349
Freund LB (1972) Crack propagation in an elastic solid subjected to general loading. I. Constant rate of extension. J Mech Phys Solids 20:129–140
Freund LB (1972) Crack propagation in an elastic solid subjected to general loading. II. Nonuniform rate of extension. J Mech Phys Solids 20:141–150
Freund LB (1973) Crack propagation in an elastic solid subjected to general loading. III. Stress wave loading. J Mech Phys Solids 21:47–61
Freund LB (1974) Crack propagation in an elastic solid subjected to general loading. IV. Obliquely incident stress pulse. J Mech Phys Solids 22:137–146
Freund LB (1990) Dynamic fracture mechanics. Cambridge University Press
Gao H, Rice JR (1986) Shear stress intensity factors for a planar crack with slightly curved front. J Appl Mech 53:774
Giacomini A (2005) Ambrosio-Tortorelli approximation of quasi-static evolution of brittle fractures. Calc Var Partial Differ Eqs 22:129–172
Goldstein RV, Salganik RL (1974) Brittle fracture of solids with arbitrary cracks. Int J Fract 10:507–523
Goldman T, Levine A, Fineberg J (2010) Acquisition of inertia by a moving crack. Phys Rev Lett 114:114301
Griffith AA (1921) On the theory of rupture. Philos Trans Roy Soc A Math Phys Eng Sci 221:582–593
Hull D (1993) Tilting cracks: the evolution of fracture surface topology in brittle solids. Int J Fract 62:119–138
Hull D (1995) The effect of mixed mode I/III on crack evolution in brittle solids. Int J Fract 70:59–79
Hutchinson JW, Suo Z (1992) Mixed-mode cracking in layered materials. Adv Appl Mech 29:63–191
Irwin GR (1957) Analysis of stresses and strains near the end of a crack traversing a plate. J Appl Mech 24:361–364
Irwin GR (1961) Plastic zone near a crack and fracture toughness. In: Sagamore research conference proceedings, p 4
Inglis CE (1913) Stresses in plates due to the presence of cracks and sharp corners. Trans Inst Nav Arch 55:219–241
Jin ZH, Sun CT (2004) On J-integral and potential energy variation. Int J Fract 126:L19–L24
Karma A, Kessler DA, Levine H (2001) Phase-field model of mode III dynamic fracture. Phys Rev Lett 87:045501
Kendall K (1971) The adhesion and surface energy of elastic solids. J Phys D Appl Phys 4:1186–1195
Kendall K (1975) Thin-film peeling - the elastic term. J Phys D Appl Phys 8:1449–1452
Kim KS, Aravas N (1988) Elastoplastic analysis of the peel test. Int J Solids Struct 24:417–435
Kinloch AJ, Lau CC, Williams JG, The peeling of flexible laminates. Int J Fract 66:45–70
Knauss WG (1970) An observation of crack propagation in anti-plane shear. Int J Fract 6:183–187
Kobayashi AS, Wade BG, Bradley WB (1973) Fracture dynamics of Homalite-100. In: Hausch HH et al (eds) De-formation and fracture of high polymers. Plenum Press, New, York, pp 487–500
Kobayashi AS, Mall S (1978) Dynamic fracture toughness of Homalite-100. Exp Mech 18:11–18
Kostrov BV (1966) Unsteady crack propagation of longitudinal shear cracks. Appl Math Mech 30:1241–1248. English translation from PMM 30:1042–1049
Kostrov BV (1975) On the crack propagation with variable velocity. Int J Fract 11:47–56
Kostrov BV, Nikitin LV (1970) Some general problems of mechanics of brittle fracture. Arch Mech Stosow 22:749–775

Lazarus V, Leblond JP (2001) Crack front rotation and segmentation in mixed mode I + III or I + II + III. Part I: calculation of stress intensity factors. J Mech Phys Solids 49:1399–1420
Leblond JB (2020) CISM Volume
Leblond JB, Karma A, Lazarus V (2011) Theoretical analysis of crack front instability in mode I+III. J Mech Phys Solids 59:1872–1887
Lin B, Mear ME, Ravi-Chandar K (2010) Criterion for initiation of cracks under mixed-mode I+III loading. Int J Fract 165:175–188
Love AEH (1927) A treatise on the mathematical theory of elasticity, 4th edn. Cambridge University Press
Mesgarnejad A, Bourdin B, Khonsari MM (2015) Validation simulations for the variational approach to fracture. Comput Methods Appl Mech Eng 290:420–437
Miehe C, Hofacker M, Welschinger F (2010) A phase field model for rate-independent crack propagation: Robust algorithmic implementation based on operator splits. Comput Methods Appl Mech Eng 199:2765–2778
Mott NF (1948) Brittle fracture in mild steel plates. Engineering 165:16–18
Movchan AB, Gao H, Willis JR (1998) On perturbations of plane cracks. Int J Solids Struct 35:3419–3453
Mushkhelishvili NI (1953) Some basic problems in the theory of elasticity. Noordhoff Ltd
Nguyen TT, Yvonnet J, Bornert M, Chateau C, Sab K, Romani R, Le Roy R (2016) On the choice of parameters in the phase field method for simulating crack initiation with experimental validation. Int J Fract 197:213–226
O'Keefe R (1994) Modeling the tearing of paper. Am J Phys 62:299–305
Obreimoff JW (1930) The splitting strength of mica. Proc R Soc Lond Ser A 127:290–297
Orowan E (1948) Fracture and strength of solids. Rep Prog Phys 185
Ortiz M (1985) A constitutive theory for the inelastic behavior of concrete. Mech Mater 4:67–93
Pham K, Amor H, Marigo JJ, Maurini C (2011) Gradient damage models and their use to approximate brittle fracture. Int J Damage Mech 20:618–652
Pham KH, Ravi-Chandar K (2014) Further examination of the criterion for crack initiation under mixed-mode I+III loading. Int J Fract 189:121–138
Pham KH, Ravi-Chandar K (2017) The formation and growth of echelon cracks in brittle materials. Int J Fract 206:229–244
Pham KH, Ravi-Chandar K, Landis CM (2017) Experimental validation of a phase-field model for fracture. Int J Fract 205:83–101
Pollard DD, Segall P, Delaney PT (1982) Formation and interpretation of dilatant echelon cracks. GSA Bull 93:1291–1303
Pons AJ, Karma A (2010) Helical crack-front instability in mixed-mode fracture. Nat Lett 464:85–89
Ramulu M, Kobayashi AS (1985) Mechanics of crack curving and branching - a dynamic fracture analysis. Int J Fract 27:177–201
Ravi-Chandar K (2004) Dynamic fracture. Elsevier
Ravi-Chandar K, Knauss WG (1984) An experimental investigation into dynamic fracture - I. Crack initiation and crack arrest. Int J Fract 25:247–262
Ravi-Chandar K, Knauss WG (1984) An experimental investigation into dynamic fracture - II. Microstructural aspects. Int J Fract 26:65–80
Ravi-Chandar K, Knauss WG (1984) An experimental investigation into dynamic fracture - III. On steady state crack propagation and branching. Int J Fract 26:141–154
Ravi-Chandar K, Knauss WG (1984) An experimental investigation into dynamic fracture -IV. On the interaction of stress waves with propagating cracks. Int J Fract 26:189–200
Rice JR (1968a) A path independent integral and the approximate analysis of strain con-centration by notches and cracks. J Appl Mech 35:379–386
Rice JR (1968b) Mathematical analysis in the mechanics of fracture. In: Liebowitz H (ed) Fracture: an advanced treatise, vol 2. Mathematical fundamentals. Academic Press

Roman B (2013) Fracture path in brittle thin sheets: a unifying review on tearing. Int J Fract 182:209–237
Rosakis AJ, Ravi-Chandar K (1986) On crack tip stress state: an experimental evaluation of three-dimensional effects. Int J Solids Struct 22:121–134
Schardin H, Struth W, 1938, Hochfrequenzkinematographische untersuchung der bruchvorgänge in glas. Glastechnische Berichte 219
Schardin H (1959) Velocity effects in fracture. In: Averbach et al. (eds) Fracture. Wiley, New York, pp 297–330
Sharon E, Fineberg J (1996) Microbranching instability and the dynamic fracture of brittle materials. Phys Rev B 54:7128–7139
Slepyan LI (2002) Models and phenomena in fracture mechanics. Springer, Berlin
Sommer E (1969) Formation of fracture 'lances' in glass. Eng Fract Mech 1:539–546
Sundaram B, Tippur HV (2016) Dynamics of crack penetration vs branching at a weak interface: an experimental study. J Mech Phys Solids 96:312–332
Tada H (1973) The stress analysis of cracks handbook. Del Research Corporation
Tetelman AS, McEvily AJ (1967) Fracture of structural materials. Wiley, New York
Timoshenko SP, Goodier JN (1951) Theory of elasticity. McGraw Hill
Viktorov IA (1967) Rayleigh and Lamb waves: physical theory and applications. Plenum Press, New York
Washabaugh P, Knauss WG (1993) Nonsteady periodic behavior in the dynamic fracture of PMMA. Int J Fract 59:189
Wei Y, Hutchinson JW (1998) Interface strength, work of adhesion and plasticity in the peel test. Int J Fract 93:315–333
Williams ML (1952) Stress singularities resulting from various boundary conditions in angular corners of plates in extension. J Appl Mech 19:526–528
Williams ML (1957) On the tress distribution at the base of a stationary crack. J Appl Mech 24:109–114
Willis JR (1975) Equations of motion for propagating cracks. In: The mechanics and physics of fracture. The Metals Society, pp 57–67
Willis JR (1992) The stress field near the tip of an accelerating crack. J Mech Phys Solids 40:1671–1681
Xu G, Bower AF, Ortiz M (1994) An analysis of non-planar crack growth under mixed mode loading. Int J Solids Struct 31:2167–2193
Yang W, Freund LB (1985) Transverse shear effects for through-cracks In an elastic plate. Int J Solids Struct 21:977–994
Yoffe E (1951) The moving Griffith crack. Philosophical Magazine 42:739–750
Younes AI, Engelder T (1999) Fringe cracks: key structures for the interpretation of the progressive Alleghanian deformation of the Appalachian plateau. GSA Bull 111:219–239

Perturbations of Cracks

Jean-Baptiste Leblond

Abstract This chapter, of theoretical character, is devoted to the description of various methods of analysis of geometric perturbations of cracks in linear elastic media, in both 2D and 3D. Important applications to the prediction of crack paths are presented.

1 General Introduction

At the time when Linear Elastic Fracture Mechanics (LEFM) gradually emerged as a new branch of solid mechanics, cracks were viewed as structural defects to be avoided at all costs. For this reason the theory initially focussed essentially on conditions on the magnitude of the loading warranting non-propagation of cracks.

However the multiplication of accidents, and the development of experimental methods of crack detection, soon led to the realization that cracks were unavoidable, and that one ought to learn to live with them, rather than vainly try to eradicate them. Since it was clear that the detrimental effect of cracks highly depends on where they decide to go, prediction of crack paths soon became a theme of major importance in LEFM.

The need for predictions of this kind in turn motivated the development of methods of analysis of geometrical perturbations of cracks. Indeed studies of crack paths are inextricably entangled with perturbation analyses: to predict the geometric development of a crack, it is necessary to envisage all its possible geometric configurations, before applying some physical criterion that will decide which one, among all of them, is the "most favourable" that will be selected.

For these reasons perturbations of cracks should not be viewed as an amusing but basically futile mathematical distraction, but as a theme of central importance in LEFM, from both the theoretical and practical points of view.

J.-B. Leblond (✉)
Sorbonne Université, Institut Jean Le Rond d'Alembert, Paris, France
e-mail: jbl@lmm.jussieu.fr

L. Ponson (ed.), *Mechanics and Physics of Fracture*, CISM International Centre for Mechanical Sciences 608,
https://doi.org/10.1007/978-3-031-18340-9_2

There are several ways to establish categories among perturbations of cracks. One of them consists of distinguishing between perturbations of *Type I*, wherein the sole vicinity of the crack tip (in 2D) or front (in 3D) is perturbed through addition of an extension of small length, and perturbations of *Type II*, wherein the entire lips (in 2D) or faces (in 3D) of the crack are perturbed.

- Perturbations of Type I are essentially relevant to the definition and study of physical criteria of prediction of the geometrical features of the future crack path, to be followed from a given "initial" configuration of the crack. Indeed most of the time such criteria, be they relevant to mode I+II, mode I+III or completely general mixed-mode situations, do not simply refer to the mechanical fields in this initial configuration; they require consideration of these fields in virtual, slightly extended configurations.
- Perturbations of Type II are more pertinent for the study of such "global" questions as the *configurational stability or instability* of the propagation path: will a mode I crack, envisaged in a 2D (plane strain) situation, grow along a straight line or tend to depart more and more from its initial direction? Similarly, will a mode I+III crack, envisaged in a fully 3D situation, grow in a coplanar way or tend to gradually deviate from its initial plane? In order to address such questions, it is necessary to envisage perturbations of the whole crack lips (in 2D) or surfaces (in 3D).

Perturbations of cracks may also be categorized according to their degree of geometric complexity:

- The simplest ones, envisaged from the 70s, are crack perturbations in 2D (plane strain) situations. They permit to address the basic problem of defining a suitable criterion for propagation of cracks loaded in mode I+II, thus paving the way to numerical predictions of crack paths in 2D bodies, covering many situations of practical interest.
- A group of intermediary complexity, considered from the mid-80s, consists of *coplanar* perturbations of cracks in 3D situations. Such perturbations are not relevant only to problems of propagation of mode I cracks in 3D bodies having homogeneous or heterogeneous fracture properties, but also to some mixed-mode situations involving crack propagation channelled along a weak interface.
- Finally the most complex group consists of *out-of-plane* perturbations of cracks loaded arbitrarily in 3D situations. Such perturbations were not convincingly addressed before the late 90s. They permit to consider some still unresolved, topical issues of modern LEFM, like the explanation of the well-documented tendency of cracks loaded in mode I+III to propagate in the form of small facets tilted around the direction of propagation.

For the sake of clarity, the order of presentation of topics adopted here will be based on the second classification rather than the first.

Section 2 will first be devoted to 2D crack perturbations. The perturbations considered will essentially be of Type I; this will lead to a detailed discussion of the

choice of the "optimal" criterion for prediction of the future crack path in mixed-mode I+II conditions. Perturbations of Type II will also be envisaged secondarily, thus permitting to examine the issue of directional stability or instability of cracks propagating in 2D bodies under mode I conditions.

Section 3 will then envisage coplanar perturbations of cracks in 3D situations. By definition, such perturbations are exclusively of Type I. We shall first discuss methods of derivation of the variations of the stress intensity factors (SIFs) resulting from some small but otherwise arbitrary in-plane perturbation of the crack front. Various special crack configurations will then be envisaged, with applications to some interesting problems of crack propagation in mode I in homogeneous and heterogeneous bodies.

Section 4 will finally consider out-of-plane perturbations of cracks in 3D situations. Such perturbations may be of Type I or II. Type I ones, considered first, will quickly appear to fail short of permitting to address the basic issue of instability of coplanar propagation of cracks loaded in mixed mode I+III. Type II perturbations will then be envisaged, and this will permit to discuss various modern, tentative explanations of this well-known, but still fairly mysterious instability.

A last remark concerning literature citations is in order. In spite of its length, this review makes no claim to completeness, which would require even (many) more pages. The selection made in the large body of literature available today is in a large part arbitrary, and based on such subjective motivations as familiarity with the works and personal taste. In advance, the author offers his sincere apologies to colleagues who may feel that the review does not properly acknowledge the importance of their contribution.

2 2D Crack Perturbations in Mixed Mode I+II

2.1 Introduction

In this section we shall consider perturbations of cracks subjected to mode I+II loadings in 2D, plane strain situations. Special emphasis will be placed on use of the solutions of these perturbation problems to formulate a physical criterion providing the direction of future crack growth in such situations.

The bulk of the papers summarized and discussed here was published between the early 70s and the early 90s. (The focus of papers on crack perturbations and crack paths has shifted since toward consideration of more complex, 3D situations).

Following the terminology defined in the General Introduction, one may distinguish between perturbations of *Type I* involving geometry changes confined to the immediate vicinity of the crack tip, and perturbations of *Type II* implying modifications of the entire crack geometry. In perturbations of Type I, the initial crack is endowed with a short, arbitrarily kinked and curved extension, whose length is used as a "small parameter" in the perturbation procedure. Consideration of such perturbations is useful—not to say indispensable—to formulate a criterion providing the

kink angle of the future crack extension as a function of the local stress field. In perturbations of Type II, the crack lips are displaced perpendicularly to themselves by a distance depending on position, proportional to some small quantity used as the "small parameter" of the perturbation procedure. The tangents to the initial and perturbed crack lips are then necessarily almost parallel, so that situations involving important mode II loading components, inducing large kink angles, are out of the scope of such perturbation analyses; but they are well fit to the study of problems of configurational stability of the crack path under predominantly mode I conditions.

A connection between the two types of perturbations may be established in the case of cracks endowed with a short, *slightly* kinked and curved extension, since both perturbative procedures are relevant to such cracked geometries. Comparison of the results obtained is useful to assess the soundness of the two approaches.

The *study of perturbations of Type I* started with consideration of the important special case of an infinite body containing a crack composed of two straight branches, and loaded in some arbitrary combination of modes I and II through some uniform remote stresses. To be more exact, the problem was not treated at first through some perturbation approach but exactly, without any hypothesis on the respective lengths of the two branches (Dudukalenko and Romalis 1973; Hussain et al. 1974; Chatterjee 1975). Only in a second step was it treated by a perturbative procedure, assuming one of the two branches to be much shorter than the other one (Bilby and Cardew 1975; Wu 1978); in these last works this assumption was introduced from the start, and no attempt was made to establish a link between the treatments pertaining to the two geometrical situations. This link was however evidenced in the later works of Amestoy (1987) and Amestoy and Leblond (1992), who showed how to derive the solution for an infinitesimal extension from that for an extension of finite length. These two works provided the final, most complete treatment of the problem, including in particular formulae as explicit as possible for the functions of the kink angle connecting the SIFs just before and just after a change of direction of the crack.

In another paper, Leblond (1989) showed that some—*not* all!—of the results obtained previously, in the specific case of a two-branch crack located in an infinite body and loaded through uniform stresses at infinity, in fact applied to much more general situations. His approach consisted in establishing general formulae for the successive terms of the expansion of the SIFs at the extended crack tip in powers of the crack extension length; the arguments used were based on scale changes on the one hand, and Rice (1989)s re-formulation of Bueckner (1987)s weight function theory on the other hand. In these general formulae appeared a number of "universal" functions of the kink angle, which could be identified in full generality—precisely thanks to their universality—through consideration of the special case referred to above.

Mention must also be made here of several papers which, though not primarily devoted to perturbation analyses of Type I, used the results of such analyses to investigate such basic questions as the expression of the energy-release-rate in the presence of a kink, and the prediction of the direction of future crack growth. The first question, after having raised numerous controversies, was solved in a definitive manner by Ichikawa and Tanaka (1982). The second was also the topic of many

contributions, the most important of which—in the author's view—were those of Erdogan and Sih (1963) and Goldstein and Salganik (1974). All these papers will be commented in detail below.

The prototype of *studies of perturbations of Type II* is the celebrated work of Cotterell and Rice (1980), who derived general formulae for the variations of the SIFs resulting from an arbitrary perturbation of the entire crack lips, and applied them to the study of configurational stability of a mode I crack. Their treatment and conclusions were confirmed and completed much more recently by Movchan et al. (1998) and Ponson et al. (2020).

A similar technique was used by Karihaloo et al. (1981), Sumi et al. (1983), Sumi (1986, 1992), to study the problem of cracks endowed with a *slightly* kinked and curved extension. Of special interest were the works of Sumi et al. (1983) and Sumi (1992). Sumi et al. (1983) dealt, for the first time, with a body of finite dimensions instead of an infinite one; they evidenced an impact of the location and shape of the external boundary upon some terms of the expression of the SIFs at the extended crack tip, implying the loss of the universality property in these terms—a result later confirmed by Leblond (1989) and Leguillon (1993). Sumi (1992) pursued the expansion of the SIFs at the extended crack tip up to second order in the distance between the original and perturbed crack lips; he found some discrepancies between his expressions of the SIFs just after the kink, supposedly accurate to second order in the kink angle, and the exact ones found by Amestoy (1987) and Amestoy and Leblond (1992) using a perturbation approach of Type I. He ascribed these discrepancies to limitations of perturbation approaches of Type II when pursued to second order, due to some incorrect treatment of the weak singularities of the mechanical fields near the angular points of the crack lips at the kink.

We shall review perturbations of both types in this Section, but emphasis will be placed on perturbations of Type I, more relevant to our major concern of formulation of a physical criterion for prediction of the direction of future crack growth. The Section is organized as follows:

- Section 2.2 expounds general hypotheses and notations used in the entire Section.
- As a prerequisite, Sect. 2.3, based on the work of Leblond (1989), establishes a basic property of continuity of the mechanical fields, considered as functions of the crack extension length, when a kink occurs.
- Sections 2.4 and 2.5, essentially based on the works of Amestoy (1987), Leblond (1989) and Amestoy and Leblond (1992), use this basic property combined with various other arguments involving notably a perturbation of Type I, to establish the expressions of the SIFs just after a kink, as functions of the SIFs just before the kink and the kink angle.
- Section 2.6, based on the same works, presents as a complement—again within the context of a perturbation of Type I—the expressions of the next two terms of the expansion of the SIFs at the extended crack tip, in powers of the crack extension length.
- Section 2.7 extends Irwin (1958)s expression of the energy-release-rate for a crack extending along its original direction, to a crack extending in some completely

arbitrary direction. The proof, which combines the property established in Sect. 2.3 with a basic mathematical theorem, is an improved version of an argument of Ichikawa and Tanaka (1982).

- After a presentation, in Sect. 2.8, of some classical criteria of prediction of the kink angle, Sect. 2.9 combines the results of the preceding sections with some purely logical considerations, to conclude on the relative superiority of Goldstein and Salganik (1974)s *principle of local symmetry*. Although the arguments presented here have already been debated to some extent in various other papers, their logical combination leading to such a conclusion seems to be new.
- Section 2.10 expounds Cotterell and Rice (1980)s classical perturbation analysis of Type II of a straight crack, as completed by Movchan et al. (1998), and its application to the study of configurational stability of a mode I crack, as completed by Ponson et al. (2020).
- Finally Sect. 2.11, based on the works of Autesserre (1995) and Feulvarch et al. (2013), presents an application of the preceding results to the numerical prediction of the path followed by a crack, in a practical situation of industrial interest.

2.2 Hypotheses and Notations

We consider (Fig. 1), within a linearized geometrical framework, a 2D, isotropic, linearly elastic body Ω loaded in plane strain conditions; the complementary portions $\partial\Omega_T$ and $\partial\Omega_u$ of its boundary $\partial\Omega$ are subjected respectively to prescribed line tractions $\mathbf{T}^p$ and displacements $\mathbf{u}^p$, which may vary in time. This body contains a crack of arbitrary shape, the initial tip of which is denoted O. Since the geometry

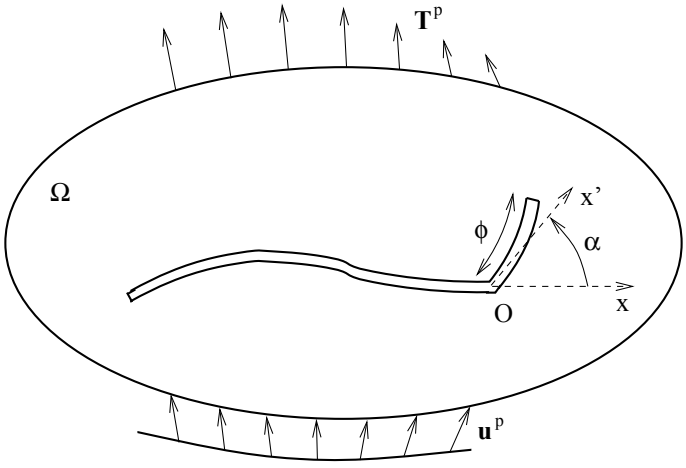

Fig. 1 Kinking of a 2D crack loaded in mode I+II

and the loading are arbitrary, the crack is loaded in mixed-mode I+II. Thus it does not extend in its original direction Ox but in a new one Ox', at an angle α (the *kink angle*) with the former. The instantaneous curvilinear length of the kinked and curved crack extension is denoted ϕ. Note that addition of such an extension to the original crack constitutes a perturbation of Type I, in the terminology defined in the General Introduction.

2.3 Continuity of Mechanical Fields with Respect to the Crack Extension Length

As a necessary prerequisite, we shall establish the following result:

At any given, fixed point M of the body Ω, the displacement vector $\mathbf{u}(M;\phi)$ and the stress tensor $\boldsymbol{\sigma}(M;\phi)$, considered as functions of the observation point M and the length $\phi > 0$ of the crack extension, are both continuous with respect to ϕ at $\phi = 0^+$.

(In intuitive terms, the displacement and stresses at a given point do not suddenly "jump" from one value to another when crack kinking occurs).

We follow here the treatment of Leblond (1989). The first step consists in separating, in the variations of $\mathbf{u}(M;\phi)$ and $\boldsymbol{\sigma}(M;\phi)$, the effects of variations of the loading $(\{\mathbf{T}^p\}, \{\mathbf{u}^p\})$, and those of variations of the crack extension length ϕ. The loading is naturally assumed to vary regularly in time and generate continuous variations of $\mathbf{u}(M;\phi)$ and $\boldsymbol{\sigma}(M;\phi)$; hence it is sufficient to study the variations of these quantities arising from the sole variations of ϕ, the loading $(\{\mathbf{T}^p\}, \{\mathbf{u}^p\})$ being considered as fixed.

This being said, we consider the crack in two situations:

1. The crack extends only up to the point O. Following a classical LEFM trick, one may consider it as endowed with an extension of length ϕ, provided this extension is closed by line tractions $\mathbf{T}(s^{\pm}) \equiv \boldsymbol{\sigma}(s).\mathbf{n}(s^{\pm})$. In this expression s $(< \phi)$ denotes the curvilinear distance from the original tip O to the observation point $s^{\pm}$ located on the upper $(+)$ or lower $(-)$ lip of the crack extension, $\boldsymbol{\sigma}$ the stress tensor prior to crack kinking (continuous across the crack extension), and $\mathbf{n}$ the local unit normal vector to the $+$ or $-$ lip, oriented toward the other lip. The displacement at M in this situation is denoted $\mathbf{u}(M)$.
2. The crack extends up to its final tip, located at the endpoint of the extension of length ϕ; in other words the preceding line tractions are released. The displacement at M in that situation is denoted $\mathbf{u}(M;\phi)$.

Taking the difference between situations (2) and (1), we obtain a *Problem A* where zero line tractions are prescribed on $\partial\Omega_T$ and zero displacements on $\partial\Omega_u$; the original crack lips are also free of tractions, but tractions $-\mathbf{T}(s^{\pm})$ are prescribed on the lips of its extension; the displacement at M is $\mathbf{u}(M;\phi) - \mathbf{u}(M)$.

We now define a *Problem B* in the following way: zero tractions are prescribed on $\partial\Omega_T$ and zero displacements on $\partial\Omega_u$; both the original crack and its extension are

free of tractions; but a unit point force in the direction of the basis vector $\mathbf{e}_i$ ($i = x, y$) is applied on the point M. (This point force is equilibrated by reactions on $\partial\Omega_u$). The resulting displacement at the point $s^{\pm}$ of the $+$ or $-$ lip of the crack extension is denoted $\mathbf{v}^{(i)}(M, \phi; s^{\pm})$. (Note that the symbols (i) and M here do not refer to the component and point of observation of the displacement, but to the direction and point of application of the force; the observation point being $s^{\pm}$).

Applying Betti's reciprocity theorem to Problems A and B, one gets

$$u_i(M; \phi) - u_i(M) = -\int_0^{\phi} \left[\mathbf{T}(s^+).\mathbf{v}^{(i)}(M, \phi; s^+) + \mathbf{T}(s^-).\mathbf{v}^{(i)}(M, \phi; s^-)\right] ds. \tag{1}$$

But $\mathbf{v}^{(i)}(M, \phi; s^+)$ and $\mathbf{v}^{(i)}(M, \phi; s^-)$, being displacements, are bounded, and $\mathbf{T}(s^+)$ and $\mathbf{T}(s^-)$, being connected to the original stress tensor $\boldsymbol{\sigma}$, are $O(s^{-1/2})$; it follows that

$$|u_i(M; \phi) - u_i(M)| \leq A \int_0^{\phi} \frac{ds}{\sqrt{s}} = O(\sqrt{\phi}) \tag{2}$$

where A is a positive constant. Equation (2) implies that $|u_i(M; \phi) - u_i(M)|$ goes to zero with ϕ, which shows that $u_i(M; \phi)$ is a continuous function of ϕ at $\phi = 0^+$, as announced.

To establish the analogous property for the stresses, differentiate equation (1) with respect to the coordinates x_j of the point M and get:

$$\begin{aligned} \frac{\partial u_i}{\partial x_j}(M; \phi) - \frac{\partial u_i}{\partial x_j}(M) = -\int_0^{\phi} \Bigg[& \mathbf{T}(s^+).\frac{\partial \mathbf{v}^{(i)}}{\partial x_j}(M, \phi; s^+) \\ & + \mathbf{T}(s^-).\frac{\partial \mathbf{v}^{(i)}}{\partial x_j}(M, \phi; s^-)\Bigg] ds. \end{aligned} \tag{3}$$

In this equation the quantities $\frac{\partial \mathbf{v}^{(i)}}{\partial x_j}(M, \phi; s^{\pm})$ may be interpreted as the displacements, at the points $s^{\pm}$ of the $+$ and $-$ lips of the crack extension, resulting from application of a "unit dipole" at the point M; this dipole consisting of two opposite forces of infinite intensity parallel to the basis vector $\mathbf{e}_i$, exerted on two points separated by an infinitesimal vector parallel to the vector $\mathbf{e}_j$, the product of the intensity of the forces and the distance between the points being unity.[1] Thus $\frac{\partial \mathbf{v}^{(i)}}{\partial x_j}(M, \phi; s^+)$ and $\frac{\partial \mathbf{v}^{(i)}}{\partial x_j}(M, \phi; s^-)$, being displacements, are bounded like $\mathbf{v}^{(i)}(M, \phi; s^+)$ and $\mathbf{v}^{(i)}(M, \phi; s^-)$, so that the reasoning made above for the displacement component $u_i(M; \phi)$ equally applies to its derivative $\frac{\partial u_i}{\partial x_j}(M; \phi)$; with the similar conclusion that the gradient of the displacement, and therefore by linearity the stress tensor $\boldsymbol{\sigma}(M; \phi)$, are continuous functions of ϕ at $\phi = 0^+$.

[1] When the vectors $\mathbf{e}_i$ and $\mathbf{e}_j$ are distinct, such a unit dipole is just a unit point torque.

2.4 The Stress Intensity Factors Just After the Kink

When crack kinking occurs, in contrast to the displacement and stresses at a given point which evolve continuously, the SIFs evolve in a discontinuous manner. Thus one must distinguish between the original SIFs just before the kink, K_I^0 and K_{II}^0, and those just after the kink, K_I^* and K_{II}^*. The object of this subsection is to study the connection between the two pairs of SIFs. We shall make use for compactness of vectorial notations, defining "SIF-vectors" made from the mode I and mode II SIFs and noted with bold letters; this means associating the vector

$$\mathbf{K}^0 \equiv \begin{pmatrix} K_I^0 \\ K_{II}^0 \end{pmatrix} \tag{4}$$

to the initial SIFs, and similar vectors to the various other pairs of SIFs.

We again follow the treatment of Leblond (1989). In a first step, we consider (Figs. 2 and 3) the special case where the body is a circular disk of centre O (the initial crack tip) and radius R, containing an *edge* crack, and subjected to prescribed *line tractions* $\mathbf{T}$ (no prescribed displacements). Just like before, the kink angle is denoted α and the length of the crack extension ϕ (see Fig. 2). In addition, the crack is assumed to have a finite curvature c just before the kink, so that the equation of its initial branch (left of the point O) reads

$$y = \frac{c}{2} x^2 + O\left(x^3\right) \tag{5}$$

in the frame Oxy "adapted" to this branch (see Fig. 3). In contrast the crack extension is assumed to have an *infinite curvature* just after the kink, its equation being of the type

$$y' = a^* x'^{3/2} + O\left(x'^2\right) \tag{6}$$

where a^* is a "pseudo-curvature" parameter, in the frame $Ox'y'$ "adapted" to this extension (see Fig. 3).[2] The necessity of assuming such an a priori strange shape for the crack extension, in order to continuously satisfy the propagation criterion, will be apparent in subsubsection **Application to the problem of directional stability** below.

The SIFs at the tip of the crack extension of length ϕ are denoted $K_I(\phi)$, $K_{II}(\phi)$, and the SIF-vector they define $\mathbf{K}(\phi)$. These SIFs depend on the geometry and, linearly, on the loading; this will be written symbolically

$$\mathbf{K}(\phi) \equiv \mathbf{L}\left[\alpha, R, c, a^*, \phi; \{\mathbf{T}\}\right] \tag{7}$$

[2] The symbol * in the parameter a^* is intended to underline its relevance to the geometry *after* the kink.

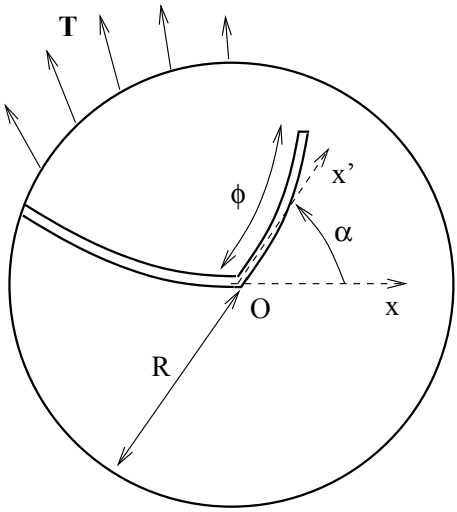

Fig. 2 A kinked and curved crack in a 2D circular body: general view

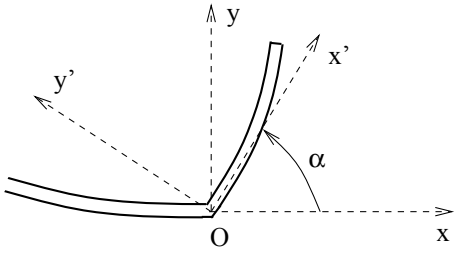

Fig. 3 A kinked and curved crack in a 2D circular body: magnified view near the kink

where $\mathbf{L}\,[\alpha, R, c, a^*, \phi; .]$ is a linear functional of the traction field $\{\mathbf{T}\}$ exerted on the boundary of the disk, depending on all geometric parameters α, R, c, a^*, ϕ. (Note that the length of the main branch of the crack is not an argument of $\mathbf{L}$, since this branch is supposed to extend up to the external boundary of the disk).

Starting from the solution of some problem of linear elasticity, one gets a new solution by multiplying all distances and displacements by a common arbitrary positive factor ρ; in the new solution the strains, and therefore the stresses and boundary tractions, are unchanged. When such a homothetical transformation is applied to the problem depicted in Figs. 2 and 3, the geometric parameters α, R, c, a^*, ϕ become α, ρR, c/ρ, $a^*/\sqrt{\rho}$, $\rho\phi$ respectively, the line tractions $\mathbf{T}$ are left unchanged, and the SIFs, being limits of certain stress components times the square root of the distance to the crack tip, are multiplied by $\sqrt{\rho}$. It follows that the functional $\mathbf{L}\,[\alpha, R, c, a^*, \phi; .]$ obeys the following "positive homogeneity" property:

$$\mathbf{L}\left[\alpha, \rho R, c/\rho, a^*/\sqrt{\rho}, \rho\phi; \{\mathbf{T}\}\right] = \sqrt{\rho}\,\mathbf{L}\left[\alpha, R, c, a^*, \phi; \{\mathbf{T}\}\right] \quad (\forall \rho > 0). \tag{8}$$

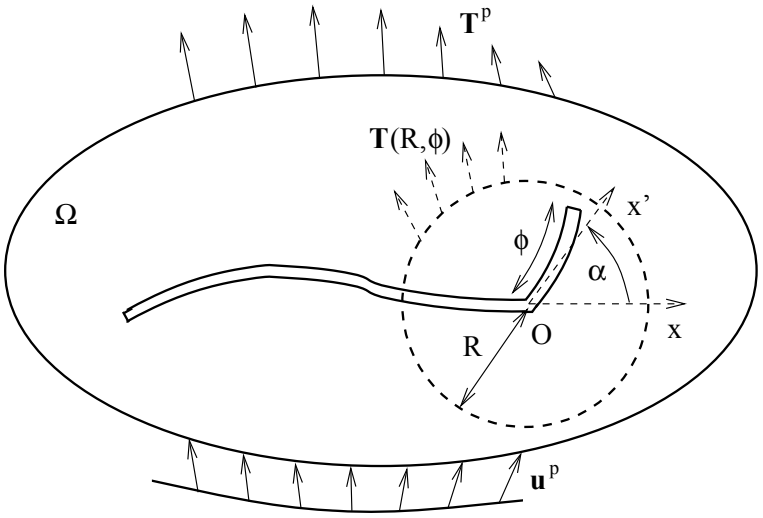

Fig. 4 A circular disk centered at the initial tip of a 2D crack loaded in mode I+II

We now introduce the assumption that the functional $\mathbf{L}[\alpha, R, c, a^*, \phi; .]$ goes to a certain limit $\mathbf{L}^*[\alpha, R, c, a^*; .]$ when the crack extension length ϕ goes to 0^+. (This formalizes the intuitive idea that the SIFs at the tip of the extended crack admit finite limits for a vanishingly small extension). Taking the limit $\phi \to 0^+$ in Eq. (8), we then get another positive homogeneity property, now for the functional $\mathbf{L}^*[\alpha, R, c, a^*; .]$:

$$\mathbf{L}^*\left[\alpha, \rho R, c/\rho, a^*/\sqrt{\rho}; \{\mathbf{T}\}\right] = \sqrt{\rho}\,\mathbf{L}\left[\alpha, R, c, a^*; \{\mathbf{T}\}\right] \quad (\forall \rho > 0), \tag{9}$$

which is analogous to Eq. (8) except that the argument ϕ no longer appears.

We now come back to the general case, considering a circular disk within the body Ω, with centre at the initial crack tip O and sufficiently small radius R for the crack to reach its boundary, so as to ensure applicability of formula (7) (Fig. 4). Let $\{\mathbf{T}(R, \phi)\}$ denote the traction field exerted on the boundary of this disk, as a result of the application of the loading $(\{\mathbf{T}^p\}, \{\mathbf{u}^p\})$ on the boundary of Ω, when the length of the crack extension is ϕ. (Of course this traction field depends on both R and ϕ, whence the notation). Assume that the crack extension length ϕ is small enough for the extension to be entirely contained within the disk. The SIFs $K_I(\phi)$, $K_{II}(\phi)$ at the tip of the extended crack are obviously unchanged if one eliminates the exterior of the disk while preserving the tractions exerted on its boundary; hence the vector they define may be expressed, using Eq. (7), as

$$\mathbf{K}(\phi) = \mathbf{L}\left[\alpha, R, c, a^*, \phi; \{\mathbf{T}(R, \phi)\}\right]. \tag{10}$$

Now take the limit $\phi \to 0^+$ in Eq. (10), R being momentarily fixed. By definition, the vector $\mathbf{K}(\phi)$ goes to the vector $\mathbf{K}^*$ of SIFs just after the kink; the functional

$\mathbf{L}[\alpha, R, c, a^*, \phi; .]$ goes to the functional $\mathbf{L}^*[\alpha, R, c, a^*; .]$; and *the traction field* $\{\mathbf{T}(R, \phi)\}$ *goes to the traction field* $\{\mathbf{T}(R)\}$ *exerted on the boundary of the disk prior to kinking*, by the property of continuity established in Sect. 2.3 above. One thus gets

$$\mathbf{K}^* = \mathbf{L}^*\left[\alpha, R, c, a^*; \{\mathbf{T}(R)\}\right]. \tag{11}$$

Note the remarkable property that in this formula providing the SIFs just *after the kink*, the mechanical fields appear only through the field $\{\mathbf{T}(R)\}$ pertaining to the situation *prior to kinking*.[3]

Equation (11) applies for all sufficiently small values of R, so one may take the limit $R \to 0^+$ in it. Prior to doing this, however, we shall transform this equation so as to deal with a disk of fixed radius, instead of one of ever decreasing radius; such a transformation may be achieved by using equation (9) with $\rho = 1/R$, leading to a radius of unity:

$$\mathbf{K}^* = \sqrt{R}\,\mathbf{L}^*\left[\alpha, 1, Rc, \sqrt{R}\,a^*; \{\mathbf{T}(R)\}\right] = \mathbf{L}^*\left[\alpha, 1, Rc, \sqrt{R}\,a^*; \sqrt{R}\,\{\mathbf{T}(R)\}\right] \tag{12}$$

where the linearity of the functional $\mathbf{L}^*[\alpha, R, c, a^*; .]$ with respect to the loading has been used.

We may now take the limit $R \to 0^+$ in the expression (12) of $\mathbf{K}^*$. In this limit the functional $\mathbf{L}^*\left[\alpha, 1, Rc, \sqrt{R}\,a^*; .\right]$ goes to $\mathbf{L}^*[\alpha, 1, 0, 0; .]$. (In intuitive terms, the curvature parameters c and a^* disappear because we are looking at a disk of ever decreasing radius R, through some magnifying glass of ever increasing magnification $\rho = 1/R$). Also, the asymptotic expression of the stress tensor $\boldsymbol{\sigma}$ near the initial crack tip O is of the form, in polar coordinates (r, θ) of origin O:

$$\boldsymbol{\sigma}(r, \theta) = K_I^0 \frac{\mathbf{f}_I(\theta)}{\sqrt{r}} + K_{II}^0 \frac{\mathbf{f}_{II}(\theta)}{\sqrt{r}} + O(r^0) \tag{13}$$

where $\mathbf{f}_I(\theta)$ and $\mathbf{f}_{II}(\theta)$ are universal trigonometric functions. It follows that the asymptotic expression, for $R \to 0^+$, of the traction field $\{\mathbf{T}(R)\}$ exerted on the boundary of the disk of radius R reads

$$\{\mathbf{T}(R)\} = \{\boldsymbol{\sigma}(R, \theta).\mathbf{e}_r(\theta)\} = \frac{K_p^0}{\sqrt{R}}\left\{\mathbf{f}_p(\theta).\mathbf{e}_r(\theta)\right\} + O(R^0) \tag{14}$$

where $\mathbf{e}_r(\theta)$ denotes the local unit radial vector associated to the polar coordinates, and Einstein's implicit summation convention is used for the index $p = I, II$. Thus in the limit $R \to 0^+$ the field $\sqrt{R}\,\{\mathbf{T}(R)\}$ goes to the limit $K_p^0\left\{\mathbf{f}_p(\theta).\mathbf{e}_r(\theta)\right\}$, and the expression (12) of $\mathbf{K}^*$ becomes

[3] This does not mean that the kink has no effect; the geometric parameters α and a^* of the crack extension indeed appear in the arguments of the functional $\mathbf{L}^*\left[\alpha, R, c, a^*; .\right]$.

$$\mathbf{K}^* = \mathbf{L}^*\left[\alpha, 1, 0, 0; K_p^0\left\{\mathbf{f}_p(\theta).\mathbf{e}_r(\theta)\right\}\right] = K_p^0\,\mathbf{L}^*\left[\alpha, 1, 0, 0; \left\{\mathbf{f}_p(\theta).\mathbf{e}_r(\theta)\right\}\right]$$

where the linearity of $\mathbf{L}^*[\alpha, 1, 0, 0; .]$ with respect to the loading has been used. This expression is of the form

$$\mathbf{K}^* = \mathbf{F}(\alpha).\mathbf{K}^0 \quad \Leftrightarrow \quad K_p^* = F_{pq}(\alpha)K_q^0 \tag{15}$$

where $\mathbf{F}(\alpha) \equiv [F_{pq}(\alpha)]_{p,q=I,II}$ is a linear operator depending only on the kink angle α.

Equation (15) concludes this subsection. It shows that *whatever the (2D) geometry and the loading, the SIFs just after the kink depend only on those before the kink (in a linear way) and the kink angle*, through some universal operator $\mathbf{F}(\alpha)$.

2.5 Practical Calculation of the Functions $F_{pq}(\alpha)$

The universality property of the operator $\mathbf{F}(\alpha)$ makes it possible to evaluate its components by considering special cases. The simplest of these (Fig. 5) consists of a crack composed of two straight branches—one of infinitesimal length ϕ—located in an infinite 2D body loaded through uniform remote stresses σ_{xx}^{∞}, σ_{yy}^{∞}, σ_{xy}^{∞}.

This problem was considered in several papers even before 1980, at a time when the universality of the operator $\mathbf{F}(\alpha)$ was not yet established, so that it was not clear whether the results obtained could be applied to more general situations. The papers of Bilby and Cardew (1975) and Wu (1978), among others, represent important

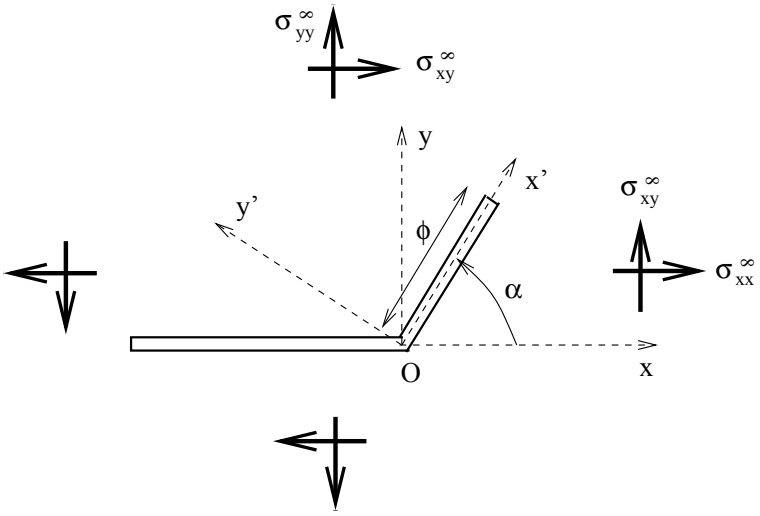

Fig. 5 A two-branch crack in an infinite 2D body

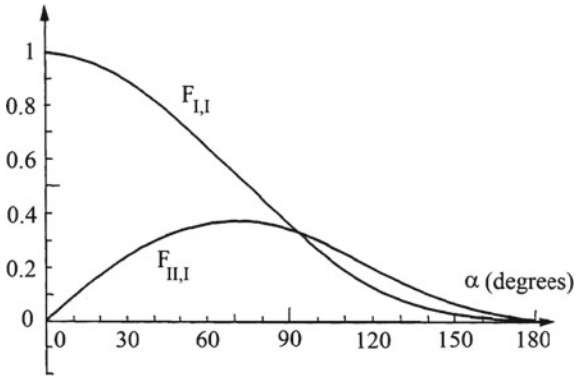

Fig. 6 The functions $F_{I,I}$ and $F_{II,I}$ (after Amestoy (1987), with permission)

contributions to the topic. However the most complete treatment of the problem was provided some 10 years later by Amestoy (1987) and Amestoy and Leblond (1992). Combining the formalism of Muskhelishvili (1953) for problems of planar elasticity with a conformal mapping technique—using the explicit expression of the conformal mapping of the exterior of the two-branch crack of Fig. 5 onto the exterior of a circle, provided by Dudukalenko and Romalis (1973)—they reduced the problem to solving an integral equation in the complex plane. Considering first the case of a finite value of the crack extension length ϕ, they obtained the same integral equation as in the previous works of Dudukalenko and Romalis (1973), Hussain et al. (1974) and Chatterjee (1975).[4] Then they showed how to let ϕ go to zero in this equation, thus obtaining another, simpler integral equation; again, this equation was identical to that obtained earlier by another author—this time (Wu 1978); but with the difference that in Wu (1978)s work based from the start on direct consideration of the limit $\phi \to 0^+$, the connection between the cases of a finite and an infinitesimal ϕ had not been established.

Amestoy (1987) and Amestoy and Leblond (1992) showed that the solution of the integral equation could be found formally in the form of an infinite series of integrals. This did not, unfortunately, lead to analytical, explicit expressions of the functions $F_{pq}(\alpha)$. But it led to two distinct ways of expressing these functions:

- In the form of numerical values, upon numerical calculation of the series of integrals. Figures 6 and 7, adapted from Amestoy (1987)s thesis, illustrate the results obtained.
- In the form of expansions in powers of the "normalized kink angle"

$$m \equiv \alpha/\pi\,. \tag{16}$$

[4] This equation was solved incorrectly, analytically, in the first two works, but correctly, numerically, in the third one.

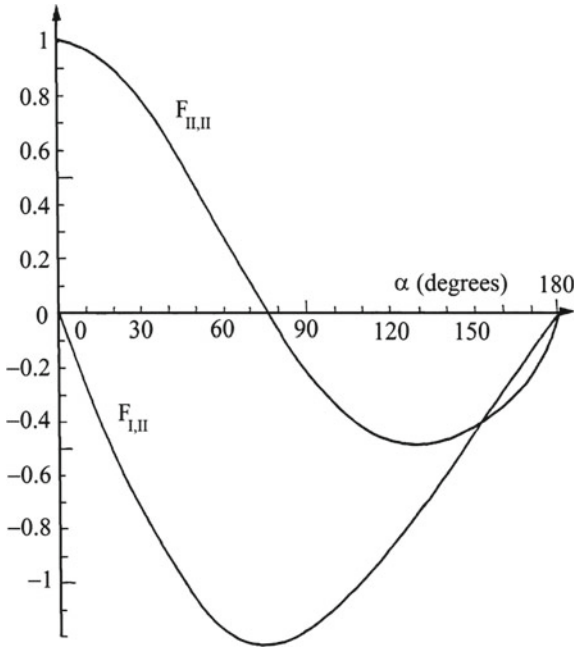

Fig. 7 The functions $F_{I,II}$ and $F_{II,II}$ (after Amestoy (1987), with permission)

Indeed Amestoy and Leblond (1992)s solution can be used to generate induction formulae permitting to calculate the *exact expressions of the coefficients* in these expansions, up to any pre-specified order. The formulae obtained in this way read at order 20:

$$\begin{aligned} F_{I,I}(\alpha) = 1 &- \frac{3\pi^2}{8}\, m^2 + \left(\pi^2 - \frac{5\pi^4}{128}\right) m^4 \\ &+ \left(\frac{\pi^2}{9} - \frac{11\pi^4}{72} + \frac{119\pi^6}{15360}\right) m^6 + 5.07790\, m^8 \\ &-2.88312\, m^{10} - 0.0925\, m^{12} + 2.996\, m^{14} - 4.059\, m^{16} \\ &+1.63\, m^{18} - 4.1\, m^{20} + O\left(m^{22}\right); \end{aligned} \tag{17}$$

$$\begin{aligned} F_{II,I}(\alpha) = \frac{\pi}{2}\, m &- \left(\frac{4\pi}{3} + \frac{\pi^3}{48}\right) m^3 + \left(-\frac{2\pi}{3} + \frac{13\pi^3}{30} - \frac{59\pi^5}{3840}\right) m^5 \\ &-6.176023 m^7 + 4.44112 m^9 - 1.5340 m^{11} - 2.0700 m^{13} \\ &+4.684\, m^{15} - 3.95\, m^{17} - 1.32\, m^{19} + O\left(m^{21}\right); \end{aligned} \tag{18}$$

$$\begin{aligned} F_{I,II}(\alpha) = &-\frac{3\pi}{2}\,m + \left(\frac{10\pi}{3} + \frac{\pi^3}{16}\right) m^3 \\ &+ \left(-2\pi - \frac{133\pi^3}{180} + \frac{59\pi^5}{1280}\right) m^5 + 12.313906\, m^7 \\ &-7.32433\, m^9 + 1.5793\, m^{11} + 4.0216\, m^{13} - 6.915\, m^{15} \\ &+4.21\, m^{17} + 4.56\, m^{19} + O\left(m^{21}\right); \end{aligned} \tag{19}$$

$$\begin{aligned} F_{II,II}(\alpha) = 1 &- \left(4 + \frac{3\pi^2}{8}\right) m^2 + \left(\frac{8}{3} + \frac{29\pi^2}{18} - \frac{5\pi^4}{128}\right) m^4 \\ &+ \left(-\frac{32}{15} - \frac{4\pi^2}{9} - \frac{1159\pi^4}{7200} + \frac{119\pi^6}{15360}\right) m^6 \\ &+10.58254 m^8 - 4.78511 m^{10} - 1.8804 m^{12} + 7.280 m^{14} \\ &-7.591\, m^{16} + 0.25\, m^{18} + 12.5\, m^{20} + O\left(m^{22}\right). \end{aligned} \tag{20}$$

The coefficients in these formulae are polynomials in π with rational coefficients; they were calculated in this form up to order 6 but purely numerically at higher orders.[5] The formulae provide values of the functions $F_{pq}(\alpha)$ with an accuracy of the order of 10^{-6} for kink angles α smaller than 90°, which is largely sufficient for practical purposes.

2.6 *Higher-Order Terms of the Expansion of the Stress Intensity Factors*

In this subsection we exceptionally assume that the loading $(\{\mathbf{T}^p\}, \{\mathbf{u}^p\})$ *does not vary* as the crack propagates.

It may be shown, following Leblond (1989), that when the crack extends under such conditions, the SIF-vector $\mathbf{K}(\phi)$ at its tip admits an expansion in semi-integral powers of the crack extension length ϕ:

$$\mathbf{K}(\phi) = \mathbf{K}^* + \mathbf{K}^{(1/2)}\sqrt{\phi} + \mathbf{K}^{(1)}\phi + \ldots \tag{21}$$

Amestoy (1987), Leblond (1989) and Amestoy and Leblond (1992) studied the quantities $\mathbf{K}^{(1/2)}$ and $\mathbf{K}^{(1)}$ appearing in the second and third terms of the expansion (21), by combining methods extending those expounded in Sects. 2.4 and 2.5 for the study of $\mathbf{K}^*$, and results derived from Rice (1989)s re-formulation of Bueckner (1987)s weight function theory—summarized in its fully 3D format in Sect. 3.2 below. The results are summarized hereafter.

[5] The numerical evaluation of the coefficients was still based on the induction formulae, *not* on numerical calculation of integrals. Thus the errors made (minimized by performing the calculations in quadruple precision) arose *only* from the replacement of polynomials in π by numbers with a limited number of digits.

Second term of the expansion of the stress intensity factors. The quantity $\mathbf{K}^{(1/2)}$ appearing in the second term of the expansion (21) admits the following expression:

$$\mathbf{K}^{(1/2)} = \mathbf{G}(\alpha)\, T_{xx}^0 + a^* \mathbf{H}(\alpha).\mathbf{K}^0 \tag{22}$$

where T_{xx}^0 is the non-singular stress appearing in the second term of the stress expansion before the kink near the initial crack tip O, representing a uniform stress σ_{xx} parallel to the initial crack direction; a^* is the pseudo-curvature parameter appearing in the equation (6) of the crack extension; and $\mathbf{G}(\alpha) \equiv [G_p(\alpha)]_{p=I,II}$ and $\mathbf{H}(\alpha) \equiv [H_{pq}(\alpha)]_{p,q=I,II}$ are a universal vectorial function and operator, depending both only on the kink angle α. Thus $\mathbf{K}^{(1/2)}$ admits a universal expression applicable to all geometries and loadings just like $\mathbf{K}^*$, albeit with a more complex expression.

Prior to the work of Leblond (1989), that which had gone farthest in the study of the quantity $\mathbf{K}^{(1/2)}$ was the work of Sumi et al. (1983). These authors were the first to consider a body of arbitrary shape instead of an infinite one, although they still made some restrictive hypotheses (straight initial crack, small parameters α and a^*). The expression they found for $\mathbf{K}^{(1/2)}$ with these hypotheses was fully consistent with the completely general expression (22).

The vectorial function $\mathbf{G}(\alpha)$ pertains to the expansion of $\mathbf{K}(\phi)$ for a kinked but *straight* extension ($a^* = 0$). Hence it may be calculated by considering the same special case as for the calculation of the operator $\mathbf{F}(\alpha)$, see Sect. 2.5. This was done by Amestoy (1987) and Amestoy and Leblond (1992), again considering first the case of a finite crack extension length ϕ, and then pursuing the expansion in powers of ϕ one step further than for the operator $\mathbf{F}(\alpha)$. Again, the method generated both numerical values of the functions $G_p(\alpha)$ and exact expansions of these functions up to any pre-specified order. The results obtained at order 3 were as follows:

$$G_I(\alpha) = (2\pi)^{3/2} m^2 + O\left(m^4\right) \quad ; \quad G_{II}(\alpha) = -2\sqrt{2\pi}\, m + 12\sqrt{2\pi}\, m^3 + O\left(m^5\right) \tag{23}$$

where the normalized kink angle m is defined by Eq. (16).

The calculation of the operator $\mathbf{H}(\alpha)$ is more difficult since it pertains to the expansion of $\mathbf{K}(\phi)$ for a *curved* crack extension, as is obvious from the fact that it appears multiplied by a^* in Eq. (22). However, one fundamental remark is that this parameter enters the formula only through its *first power*. This means that we may consider it as a small parameter in a first-order perturbative procedure; the results obtained in this way for the operator $\mathbf{H}(\alpha)$, valid in appearance only for small values of a^*, must in fact be applicable to arbitrary values, thanks to the generality of equation (22). Such an approach was carried out by Amestoy and Leblond (1992), combining their treatment of the problem of the crack with two straight branches in an infinite body with Sumi et al. (1983)s first-order perturbative procedure for a slightly curved crack—the difference being the use, in Amestoy and Leblond (1992)s work, of a "reference" crack with two straight branches instead of just one, so as to allow for arbitrary values of the kink angle instead of just small ones. (This of course made the problem and its treatment considerably more complex). This led to the following expansions of the functions $H_{pq}(\alpha)$ at order 1:

$$H_{I,I}(\alpha) = -\frac{9\pi}{8}\, m + O\left(m^3\right) \quad ; \quad H_{II,I}(\alpha) = \frac{3}{4} + O\left(m^2\right) \quad ;$$
$$H_{I,II}(\alpha) = -\frac{9}{4} + O\left(m^2\right) \quad ; \quad H_{II,II}(\alpha) = \left(-8 + \frac{3\pi}{8}\right) m + O\left(m^3\right). \tag{24}$$

Third term of the expansion of the stress intensity factors. Both the treatment necessary to get the next term $\mathbf{K}^{(1)}$ of the expansion (21) of the SIF-vector $\mathbf{K}(\phi)$, and the final result obtained for it, are considerably more involved and will not be detailed. It will suffice to say that the main novelty in this term is the *disappearance of the universality property*. More precisely, both quantities $\mathbf{K}^*$ and $\mathbf{K}^{(1/2)}$ possess the remarkable property of being expressible, in a fully general way, in terms of (i) the coefficients of the stress expansion near the *initial* crack tip O, prior to kinking; and (ii) the parameters characterizing the *local* geometry of the crack and its extension near this point. *The term* $\mathbf{K}^{(1)}$ *no longer satisfies this property*.

The loss of the universality property in the term $\mathbf{K}^{(1)}$ was established in full generality in the work of Leblond (1989), and confirmed by Leguillon (1993) using a completely different technique. It had however been noted earlier by Sumi et al. (1983), in the special case of a straight initial crack and small parameters α and a^*—but of course consideration of such a counterexample is sufficient to establish the *loss* of the universality property. Sumi et al. (1983)s work also made it clear that this loss arose from an influence of the position and shape of the external boundary of the body upon the evolution of the SIFs as the crack propagates, incompatible with the kind of universal expressions that provide $\mathbf{K}^*$ and $\mathbf{K}^{(1/2)}$.

It is difficult to explain in simple qualitative terms why the universality property must be lost precisely in the *third* term in the expansion (21) of $\mathbf{K}(\phi)$ (and of course beyond). It is not difficult, however, to explain why this property must be lost at *some* stage in this expansion. The reasoning, expounded below, perfectly illustrates Sumi et al. (1983)s point that this arises from the impact of the position and shape of the external boundary.

Indeed let us come back to Fig. 4 and the problem it depicts of propagation of a kinked and curved crack in an arbitrary body Ω, the boundary of which is subjected to some loading $(\{\mathbf{T}^p\}, \{\mathbf{u}^p\})$ (assumed invariable in time in this subsection). Again, consider a circular disk of centre O, the initial crack tip, and radius R, contained within Ω; and denote the traction field exerted on the boundary of this disk, as a result of the application of the external loading, by the symbols $\{\mathbf{T}(R)\}$ prior to kinking, and $\{\mathbf{T}(R, \phi)\}$ when the length of the crack extension is $\phi > 0$. For any position of the extended crack tip, that is any value of ϕ, eliminate the exterior of the disk, considering two options for the value of the traction field exerted on its boundary:

1. the field $\{\mathbf{T}(R)\}$, taken invariable in time;
2. the field $\{\mathbf{T}(R, \phi)\}$, continuously adjusted in time according to the value of ϕ.

In Option 1, when the extended crack tip gets close to the boundary of the disk, the SIFs $K_I(\phi)$, $K_{II}(\phi)$ diverge to infinity, as shown for instance by Leguillon (1990) in his study of cracks approaching free boundaries. (The presence of a loading invariable in time on the boundary of the disk does not change the conclusion). In Option 2,

however, nothing special occurs when the extended crack tip reaches the boundary of the disk, because the loading on this boundary is continuously adjusted in such a way that the mechanical fields within the disk are exactly the same, at every instant, as if the crack propagated in the original body Ω subjected to the loading $(\{\mathbf{T}^p\}, \{\mathbf{u}^p\})$. Hence it is clear that the SIFs $K_I(\phi)$, $K_{II}(\phi)$ must be different in the two options, at least when the extended crack tip approaches the boundary of the disk.

Now the coefficients of the stress expansion prior to kinking near the initial crack tip O, and the geometrical parameters of the crack and its extension near the point O, are the same in the two options. Therefore, *if* all successive terms of the expansion of $\mathbf{K}(\phi)$ admitted universal expressions in terms of these sole quantities, they would all be identical in the two options, and it would follow that the SIF-vectors $\mathbf{K}(\phi)$ themselves would be identical, in contradiction with what has just been said. The inescapable conclusion is that there must exist *some* term of the expansion of $\mathbf{K}(\phi)$ which does not admit such a universal expression. (And Sumi et al. (1983)s and Leblond (1989)s analyses have shown that this occurs for the first time in the *third* term).

2.7 Extended Irwin Formula in the Presence of a Kink

Irwin (1958)s celebrated formula

$$G^0 = \frac{1-\nu^2}{E}\left[(K_I^0)^2 + (K_{II}^0)^2\right] \tag{25}$$

(where E and ν denote Young's modulus and Poisson's ratio) relates the energy-release-rate G^0 to the SIFs K_I^0, K_{II}^0, in the case where the crack extends along its original direction, without any kink. (See for instance Bui (1978) for a clear and general proof). Extending it to the case where the crack suddenly kinks is more difficult than it seems at first sight; extensions of classical reasonings based on Bui (1978)s approach or Rice (1968)s integral fail for various technical reasons, the details of which are uninteresting here.

The only reasoning leading to the correct conclusion, due to Ichikawa and Tanaka (1982), is indirect and relies on study of the energy-release-rate *after* the kink. Unfortunately Ichikawa and Tanaka (1982)s presentation of this reasoning was somewhat vague, and its lack of mathematical rigour was the cause for a number of fruitless subsequent controversies. It is the intention of the presentation given here to remove all possible doubts by precisely stating the (elementary and easily proved) mathematical result it relies on:

Let $f(x)$ denote a real function of a real variable x, defined for $x \geq 0$, continuous at $x = 0^+$, differentiable for $x > 0$, and such that $f'(x)$ goes to some finite limit ℓ when x goes to 0^+. Then $f(x)$ is differentiable at $x = 0^+$ and $f'(0^+) = \ell$.

We shall apply this simple theorem to the total potential energy $\mathcal{P}$ of the body, considered as a function of the crack extension length ϕ. This energy, being the sum of the elastic potential energy and the potential energy of the line tractions prescribed on $\partial\Omega_T$, may be expressed as ($\boldsymbol{\epsilon}$ denoting the linearized strain tensor):

$$\mathcal{P} = \int_{\Omega} \frac{1}{2}\,\boldsymbol{\sigma} : \boldsymbol{\epsilon}\, d\Omega - \int_{\partial\Omega_T} \mathbf{T}^p.\mathbf{u}\, dS = \frac{1}{2}\int_{\partial\Omega_u} \mathbf{T}.\mathbf{u}^p\, dS - \frac{1}{2}\int_{\partial\Omega_T} \mathbf{T}^p.\mathbf{u}\, dS \qquad (26)$$

where the principle of virtual work has been used; the fields $\{\mathbf{T}\}$ on $\partial\Omega_u$ and $\{\mathbf{u}\}$ on $\partial\Omega_T$ here obviously depend upon the crack extension length ϕ.

Now consider the following elements:

- As shown in Sect. 2.3, at a fixed point of the body, both $\mathbf{u}$ and $\boldsymbol{\sigma}$ (and consequently $\mathbf{T} = \boldsymbol{\sigma}.\mathbf{n}$ on the boundary of Ω) are continuous functions of ϕ at $\phi = 0^+$; hence the second expression of $\mathcal{P}$ in formula (26) (where the integration domains $\partial\Omega_u$ and $\partial\Omega_T$ do not meet the crack tip) implies that it is also a continuous function of ϕ at $\phi = 0^+$.
- After the initial kink, there is no further kink (the crack propagates regularly beyond the point O); therefore $\mathcal{P}$ is differentiable for $\phi > 0$ and its derivative is given by Irwin's classical formula (25), in terms of the present energy-release-rate $G(\phi)$ and SIFs $K_I(\phi)$, $K_{II}(\phi)$:

$$\mathcal{P}'(\phi) \equiv -G(\phi) = -\frac{1-\nu^2}{E}\left[(K_I(\phi))^2 + (K_{II}(\phi))^2\right] \quad (\forall \phi > 0).$$

- In the limit $\phi \to 0^+$, $K_I(\phi)$ and $K_{II}(\phi)$ go to K_I^* and K_{II}^* so that $\mathcal{P}'(\phi)$ goes to the limit

$$-\frac{1-\nu^2}{E}\left[\left(K_I^*\right)^2 + \left(K_{II}^*\right)^2\right].$$

It then follows from the above theorem that $\mathcal{P}$ is a differentiable function of ϕ at $\phi = 0^+$, the value of $\mathcal{P}'(\phi = 0^+)$ being given by the above limit; in other words the value of the energy-release-rate at the kink is

$$G^* \equiv -\mathcal{P}'(\phi = 0^+) = \frac{1-\nu^2}{E}\left[(K_I^*)^2 + (K_{II}^*)^2\right]. \qquad (27)$$

Note that this formula reduces to the classical one (25) in the absence of a kink—as it should—since the operator $\mathbf{F}(\alpha)$ is identical to the unit tensor for $\alpha = 0$ (see Eqs. (17)–(20)).

2.8 *Presentation of Classical Criteria of Prediction of the Kink Angle*

In all reasonings presented up to now, the initial SIFs K_I^0, K_{II}^0 and the kink angle α were implicitly considered as independent quantities; there was no reference to any physical propagation criterion connecting the kink angle to the SIFs, and use was made only of the equations and theorems of elasticity. The technical results obtained so far permit us to now discuss the very important question of such a criterion. We shall begin by a short presentation of some of the most important criteria which have been proposed.

The maximum hoop stress criterion. This criterion—historically the first—was proposed by Erdogan and Sih (1963) at a time when no technical elements on the SIFs or the energy-release-rate just after a kink were available; for this reason it was based on consideration of the sole asymptotic stress field near the *initial* crack tip, prior to kinking. Using polar coordinates (r, θ) with origin at this tip, Erdogan and Sih (1963) introduced the reasonable assumption that the critical quantity governing the appearance of a *putative* future kinked crack extension in the direction θ was the "opening stress" $\sigma_{\theta\theta}(r, \theta)$ acting on the lips of this extension. This led to the idea of postulating that the *actual* kink angle α coincides with the value of θ maximizing this opening stress. (Of course, $\sigma_{\theta\theta}(r, \theta)$ depends upon the radial coordinate r, but Erdogan and Sih (1963) proposed to heuristically fix this coordinate in the maximization process). With this hypothesis, α is determined by the condition $\frac{\partial \sigma_{\theta\theta}}{\partial \theta}(r, \theta = \alpha) = 0$, or equivalently, owing to the asymptotic expression of $\sigma_{\theta\theta}(r, \theta)$ for $r \to 0^+$, by:

$$K_I^0 \sin\alpha + K_{II}^0 (3\cos\alpha - 1) = 0. \tag{28}$$

This equation is transcendental in appearance only, being reducible to a polynomial equation of the second degree on the variable $t \equiv \tan\frac{\alpha}{2}$, the solution of which is elementary.

Equation (28) determines the kink angle α as a function of the "mixity ratio" K_{II}^0/K_I^0. The values predicted evolve from $0°$ for $K_{II}^0/K_I^0 = 0$ (pure mode I) to $\mp \arccos\frac{1}{3} \simeq \mp 70.5°$ for $K_{II}^0/K_I^0 = \pm\infty$ (pure mode II). They are in acceptable agreement with those observed in actual experiments—which, as a rule, always involve a significant margin of error.[6]

The maximum energy-release-rate criterion. The "inventors" of this second criterion were again Erdogan and Sih (1963), who mentioned it as a more satisfactory proposal, which unfortunately had to be postponed until technical elements on the SIFs and the energy-release-rate just after a kink became available. It is in line with Griffith (1920)s theory of fracture which stipulates that crack propagation occurs when the energy-release-rate reaches some material-dependent critical value G_c. With such a postulate, it is logical to assume that the crack extends in the *first*

[6] For through-the thickness cracks propagating in thin plates for instance, the kink angles observed on the two surfaces of the plate are often notably different, for no apparent reason.

direction where G^* reaches G_c, that is where G^* is maximum. The expression of G^* as a function of α being given by Eqs. (15) and (27), such a condition leads to the following equation defining the value of the angle α:

$$K_p^*(\alpha)\,\frac{\partial K_p^*}{\partial \alpha}(\alpha) = 0 \quad \Leftrightarrow \quad F_{pq}(\alpha)F'_{pr}(\alpha)K_q^0 K_r^0 = 0 \tag{29}$$

where Einstein's implicit summation convention is again used for the indices $p, q, r = I, II$.

The approximate expressions (17)–(20) of the functions $F_{pq}(\alpha)$ permit to solve this equation in α with sufficient accuracy for any value of the mixity ratio K_{II}^0/K_I^0. The values predicted vary from $0°$ for $K_{II}^0/K_I^0 = 0$ to about $\mp 75.8°$ for $K_{II}^0/K_I^0 = \pm\infty$. They are thus just a bit different from those predicted by the maximum hoop stress criterion.

The principle of local symmetry (PLS). This third criterion was proposed much later by Goldstein and Salganik (1974), with a rather opaque physical justification which will not be reproduced here. These authors proposed to postulate that the crack extends in pure mode I, that is in the direction where the SIF K_{II}^* of mode II just after the kink vanishes. By Eq. (15) this condition reads

$$K_{II}^* = F_{II,I}(\alpha)K_I^0 + F_{II,II}(\alpha)K_{II}^0 = 0. \tag{30}$$

Again, the approximate expressions (18) and (20) of the functions $F_{II,I}(\alpha)$ and $F_{II,II}(\alpha)$ permit to solve this equation in α with sufficient accuracy. The values predicted range from $0°$ for $K_{II}^0/K_I^0 = 0$ to about $\mp 77.3°$ for $K_{II}^0/K_I^0 = \pm\infty$, and are thus *very close* to those predicted by the maximum energy-release-rate criterion.

2.9 Discussion of Criteria

The margins of error encountered in experimental measurements of kink angles of crack subjected to various combinations of mode I and mode II have already been evoked. These margins are too important for a discrimination of criteria based on experiments to be possible. But this does not mean that nothing can be said in favour of one criterion or another. We shall now see that strong theoretical arguments favour the PLS (in the case of isotropic materials, as considered here).

Property ($\mathcal{P}$) and Its Logical Implications. We begin by introducing the following definition:

A given criterion satisfies property ($\mathcal{P}$) if it predicts the following implication:

$$\left[\, K_{II}^* \neq 0 \;\Rightarrow\; \alpha \neq 0 \,\right] \quad \text{or equivalently} \quad \left[\, \alpha = 0 \;\Rightarrow\; K_{II}^* = 0 \,\right]. \tag{31}$$

(Presence of some mode II necessarily implies crack kinking).

Property $(\mathcal{P})$ is physically reasonable, except in some special cases like crack propagation channelled along a weak interface; it could be considered as a necessary condition to be required from *any* envisageable criterion. But independently of such a consideration, it is satisfied anyway by all three criteria presented in Sect. 2.8; this is easily proved using the second, more convenient form of the implication (31), combined with equations (28) for the maximum hoop stress criterion, Eqs. (17)–(20) and (29) for the maximum energy-release-rate criterion, and Eqs. (18), (20) and (30) for the PLS.

The importance of property $(\mathcal{P})$ stems from the following proposition:

The PLS is the only criterion which satisfies property $(\mathcal{P})$ *while predicting a geometrically regular crack path (no kinks) after the initial kink.*

To establish this proposition, consider a crack initially loaded in mode I+II, and propagating according to some criterion (i) satisfying property $(\mathcal{P})$, and (ii) predicting a regular crack path after the initial kink. Application of the criterion *after* the kink reveals that $K_{II}(\phi) = 0$ then; otherwise, since the criterion verifies property $(\mathcal{P})$, there would be a second kink, implying a non-regular crack path after the first one. But the property $K_{II}(\phi) = 0$ is true for all positive values of the crack extension length ϕ. Hence, taking the limit $\phi \to 0^+$, we get the conclusion that application of the criterion *after* the kink implies that necessarily $K_{II}^* = 0$ *at* the kink. In other words, *the predictions of the criterion* (applied after the kink) *are identical to those of the PLS.*

The reasoning may also be presented in an equivalent, but maybe more intuitive format. Consider a crack initially loaded in mode I+II, and propagating according to some criterion (i) satisfying property $(\mathcal{P})$, *but* (ii) making predictions different from those of the PLS. Since $K_{II}^0 \neq 0$ initially, the crack kinks. But just after the kink, $K_{II}^* \neq 0$ also, since the kink angle resulting from the criterion differs from that satisfying the condition $K_{II}^* = 0$. Hence, since the criterion satisfies property $(\mathcal{P})$, the crack must kink again, and this must not occur after some finite distance of propagation (whatever small it may be), but instantaneously. It is difficult to figure out what the crack path will be under such conditions, but it certainly *cannot be geometrically regular*.

This proposition clearly favours the PLS among all "reasonable" criteria satisfying property $(\mathcal{P})$.[7] However, before concluding on the prediction of crack paths in mixed mode I+II conditions, it is necessary to examine its impact upon the other two criteria presented in Sect. 2.8, that is Erdogan and Sih (1963)s maximum hoop stress and maximum energy-release-rate criteria.

Consequences for the Various Criteria. A basic remark is in order here. All three criteria presented in Sect. 2.8 have been seen to yield close predictions for the kink angle, whatever the combination of modes I and II envisaged. Hence the shortcomings of the maximum hoop stress and maximum energy-release-rate criteria to be discussed below are of little consequence upon their *practical* usefulness; the values

[7] Note that this justification of the PLS, based on essentially logical arguments, has nothing to do whatsoever with Goldstein and Salganik (1974)s obscure physical justification.

of the kink angle they predict both stand as acceptable, though imperfect, approximations of that resulting from the PLS, and these criteria may be used without any great harm to predict crack paths in situations of practical interest, for instance by step-by-step methods. Their flaws are of a more *theoretical* nature.

Consider the maximum hoop stress criterion first. Its lack of coincidence with the PLS (see Sect. 2.8), combined with its fulfilment of property ($\mathcal{P}$) (see subsection **Property** ($\mathcal{P}$) **and its logical implications**), implies that it is incoherent in the sense that it fails to predict a geometrically regular crack path after the initial kink. But this is not a very disturbing conclusion: Erdogan and Sih (1963) proposed this criterion on purely phenomenological grounds; it is independent of, and exterior to, Griffith (1920)s fundamental theory of fracture, and its inconsistency is of no consequence upon this theory.

For the maximum energy-release-rate criterion, the situation is both more critical and less clear. It is *more critical* because of the evident link of this criterion with Griffith (1920)s theory: if crack propagation occurs when the energy-release-rate reaches some critical value G_c, it is hard to imagine that it does so in a direction where G^* is not maximum; indeed this would imply that G^* has already reached G_c in some other (nearby) direction without triggering crack propagation! The consequences of a possible inconsistency of the criterion upon Griffith (1920)s theory are thus potentially far-reaching and disturbing.

The situation is also *less clear* because—as underlined in Sect. 2.8—the predictions of the maximum energy-release-rate criterion and the PLS are *so very close*, and furthermore obtained by solving equations (29) or (30) which involve the functions $F_{pq}(\alpha)$ for which no exact, analytical formulae are available. Therefore, before drawing any disturbing conclusions from the lack of coincidence of the two criteria, one must first decide in a definitive way whether this lack of coincidence is real or simply arises from inaccuracies in the evaluation of the predicted kink angles.

Numerical calculations of the functions $F_{pq}(\alpha)$, such as those performed by Amestoy (1987) and illustrated in Figs. 6 and 7, are not accurate enough to permit to settle this question. But we shall now see, following again Amestoy and Leblond (1992), that a clear conclusion may be reached thanks to the analytical high-order expansions (17)–(20) of the functions.

In a first step, we shall transform the question of the possible coincidence of the two criteria into a mathematical conjecture on the functions $F_{pq}(\alpha)$. Coincidence of the two criteria would mean that—adding an interrogation mark to all uncertain implications and equalities, to avoid any possible ambiguity:

$$\left[\, K_{II}^* = 0 \quad \Rightarrow ? \quad G^* \text{ is maximum with respect to } \alpha \,\right],$$

that is

$$\left[K_{II}^* = 0 \quad \Rightarrow ? \quad K_I^*(\alpha) \frac{\partial K_I^*}{\partial \alpha}(\alpha) + K_{II}^*(\alpha) \frac{\partial K_{II}^*}{\partial \alpha}(\alpha) = 0 \right]$$

or equivalently

$$\left[K_{II}^* = 0 \quad \Rightarrow ? \quad K_I^*(\alpha) \frac{\partial K_I^*}{\partial \alpha}(\alpha) = 0 \right].$$

But the accuracy on the numerical values of the functions $F_{pq}(\alpha)$ is largely sufficient to ascertain that K_I^* and K_{II}^* do not vanish simultaneously. Hence the preceding implication would entail that

$$\left[K_{II}^* = 0 \quad \Rightarrow ? \quad \frac{\partial K_I^*}{\partial \alpha}(\alpha) = 0 \right],$$

that is in terms of the functions $F_{pq}(\alpha)$:

$$\left[F_{II,I}(\alpha) K_I^0 + F_{II,II}(\alpha) K_{II}^0 = 0 \quad \Rightarrow ? \quad F'_{I,I}(\alpha) K_I^0 + F'_{I,II}(\alpha) K_{II}^0 = 0 \right].$$

For this implication to be true for all possible values of the kink angle α, the two linear forms (of $\mathbf{K}^0$) $F_{II,I}(\alpha) K_I^0 + F_{II,II}(\alpha) K_{II}^0$ and $F'_{I,I}(\alpha) K_I^0 + F'_{I,II}(\alpha) K_{II}^0$ should be proportional for all α; that is, the equality

$$\frac{F'_{I,I}}{F_{II,I}}(\alpha) = ? \frac{F'_{I,II}}{F_{II,II}}(\alpha) \quad (\forall \alpha) \tag{32}$$

should hold.

In a second step, the conjectural identity (32) may be put to test by using formulae (17)–(20) for the functions $F_{pq}(\alpha)$. Using the expressions at order 6, one gets after a very lengthy but elementary calculation:

$$\begin{cases} \dfrac{F'_{I,I}}{F_{II,I}}(\alpha) = -\dfrac{3}{2} + \left(4 - \dfrac{3\pi^2}{8}\right) m^2 + \left(10 - \dfrac{41\pi^2}{30} + \dfrac{\pi^4}{32}\right) m^4 + O\left(m^6\right) \\ \dfrac{F'_{I,II}}{F_{II,II}}(\alpha) = -\dfrac{3}{2} + \left(4 - \dfrac{3\pi^2}{8}\right) m^2 + \left(10 - \dfrac{23\pi^2}{18} + \dfrac{\pi^4}{32}\right) m^4 + O\left(m^6\right) \end{cases} \tag{33}$$

where again the normalized kink angle m is defined by Eq. (16). Equations (33) show that the conjectural identity (32) is wrong, which implies in a definitive way that *the values of the kink angle predicted by the maximum energy-release-rate criterion and the PLS are different*, although very close. (The fact that the left- and right-hand sides of the erroneous equality (32) are identical up to order 2, and differ only *slightly* at order 4, as can easily be checked, should be no surprise in view of the *almost perfect* coincidence of the criteria).

It is impossible to deny that this disturbing conclusion raises serious problems within the theoretical framework proposed by Griffith (1920). These problems should however be balanced against other, probably even more important difficulties: after all, Griffith (1920)s ideas are commonly used within the context of the theory of LEFM, the very foundations of which are shaky (since the hypothesis of infinitesimal strains and stresses it is based upon leads to the conclusion that the stress components diverge at a crack tip, which is both logically incoherent and physically impossible).

To resolve the issue, one may be tempted to postulate a dependence of the critical energy-release-rate G_c upon the mixity ratio K_{II}^0/K_I^0; the maximum-energy-release-rate criterion would then become [$(G^* - G_c)$ max vs. α] instead of just [G^* max vs. α], and the dependence of G_c upon K_{II}^0/K_I^0 could be adjusted in such a way as to ensure coincidence of the new criterion with the PLS, thereby solving all difficulties. But such a "solution" would be artificial. Indeed a dependence of G_c upon K_{II}^0/K_I^0 is perfectly conceivable (perhaps even probable) from a physical perspective, but it should be determined by a dependence, to be specified, of the *physical mechanisms of fracture* upon the mixity ratio. In contrast, enforcing identity of the values of α determined by the conditions [$(G^* - G_c)$ max vs. α] and $K_{II}^* = 0$ means tying the dependence of G_c upon K_{II}^0/K_I^0 to the values of the functions $F_{pq}(\alpha)$, which are entirely determined by the *equations of elasticity*, without any reference to fracture processes.

Conclusion on the prediction of crack paths in mixed mode I+II. It follows from what precedes that the most reasonable prediction of the kink angle α, as a function of the mixity ratio K_{II}^0/K_I^0 just before the kink, is that made by the PLS, expressed by condition (30). Note that this condition reduces to $K_{II}(\phi) = 0$ after the initial kink, since there is no difference between the SIFs "before and after the kink" in the regular part of the crack path, in the absence of a new kink.

It remains to prescribe the intensity of the loading promoting propagation. The most natural way of doing so is to assume that Griffith (1920)s standard criterion $G^* = G_c$ applies as usual, the energy-release-rate G^* being of course evaluated in the new direction of the crack. Since K_{II}^* is assumed to be zero in this direction, the criterion may be written in the equivalent forms

$$G^*(\alpha) = G_c \quad \Leftrightarrow \quad K_I^*(\alpha) = K_{Ic} \tag{34}$$

where $G^*(\alpha)$ and $K_I^*(\alpha)$ denote the energy-release-rate and SIF of mode I in the direction defined by the kink angle α, and K_{Ic} the fracture toughness.

It is important to note that for Griffith's criterion (34) to be continuously satisfied as the crack propagates, the loading must be allowed to vary in time. Indeed if it is kept constant, the energy-release-rate necessarily varies as the crack propagates—as a consequence of its dependence upon the geometry of the cracked body—and thus cannot remain equal to its critical value which is a constant.

In general, the variation of the loading in time must be accounted for when writing condition (30) expressing the PLS. However, in the important special case where the loading varies *proportionally*, that is through mere multiplication by a time-dependent scalar $\rho(t)$, one may disregard its variation when writing the PLS. This stems from the fact that the kink angle α determined from condition (30) does not depend upon the individual values of the SIFs K_I^0, K_{II}^0, but only upon their ratio which remains unchanged when they are both multiplied by $\rho(t)$. This means for instance that one may safely combine the PLS with the expansion (21) of the SIF-vector $\mathbf{K}(\phi)$, with $\mathbf{K}^*$ and $\mathbf{K}^{1/2}$ given by Eqs. (15) and (22), although Eq. (22) was obtained by Amestoy (1987), Leblond (1989) and Amestoy and Leblond (1992)

under the restrictive hypothesis of constant loading. This remark will play a role in Sect. 2.10 below.

The"double" criterion consisting of the PLS and Griffith's condition, Eqs. (30) and (34), seems to rest on very firm ground, since the arguments expounded above in its favour are of essentially logical, apparently indisputable nature. This should *not*, however, conceal its weaknesses:

- The two parts of the double criterion result from independent, disconnected arguments, instead of being deduced and expressed within a single theoretical framework.
- More importantly, the PLS, and the property ($\mathcal{P}$) it rests upon, are essentially tied to the hypothesis of material *isotropy* (from both points of view of elasticity and fracture properties). In the presence of privileged directions of fracture (if the crack meets a weak interface for instance), there is no reason to believe that the crack must necessarily extend in the direction of vanishing mode II. In such cases the PLS is inapplicable, and there is at present no better solution than to adopt the [$(G^* - G_c)$ max] criterion, in spite of its deficiencies.

2.10 Analysis of Directional Stability of a Mode I Crack

The aim of this Subsection is to summarize the complementary perturbation analyses of Cotterell and Rice (1980) and Movchan et al. (1998), and some applications of these works. They are interesting in two respects. First, they provide simple and elegant examples of perturbation analyses of Type II, as defined in the General Introduction: in these analyses the *whole crack* is perturbed, unlike in those of Type I expounded in Sect. 2.2 to 2.6 where the sole vicinity of the crack tip was. Second, they permit to draw interesting conclusions about the *directional stability* of a mode I crack.

Cotterell and Rice (1980)s and Movchan et al. (1998)s analyses of perturbation of a straight crack. The problem considered by Cotterell and Rice (1980) and Movchan et al. (1998) is illustrated in Fig. 8. An infinite 2D body contains a semi-infinite crack extending from $x = -\infty$ to $x = \ell$. This crack is considered in two configurations, the "unperturbed" one where it is straight and extends along the Ox axis, and a "perturbed" one where it is slightly displaced perpendicularly to itself. The small orthogonal distance from the unperturbed crack to the perturbed one is denoted $\psi(x)$. The SIFs are denoted $K_I^0(\ell)$ and $K_{II}^0(\ell)$ in the unperturbed configuration, and $K_I(\ell)$ and $K_{II}(\ell)$ in the perturbed one.

The approaches of Cotterell and Rice (1980) and Movchan et al. (1998) differed in detail, since the former used Muskhelishvili (1953)s formalism and the latter Bueckner (1987)s weight function theory. However their principle was basically the same. It consisted of first writing the boundary conditions of zero tractions on the actual, perturbed configuration of the crack, and second expanding the equations in powers of the perturbation ψ. At the first order, the output was a problem posed on

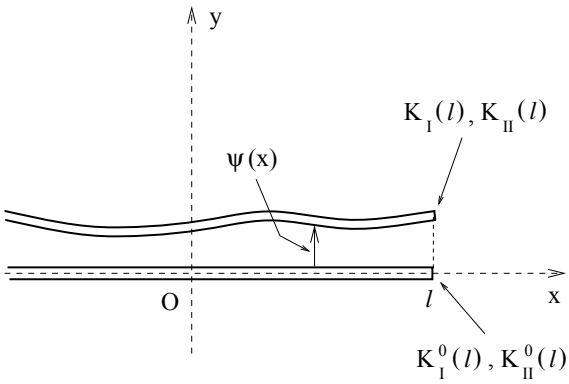

Fig. 8 Perturbation of a 2D semi-infinite straight crack

the unperturbed crack, but with nonzero tractions on its lips, arising from the gap between this fictitious crack and the true one having traction-free lips. These tractions depended linearly on both the unperturbed stress field in the vicinity of the straight crack, and the perturbation $\psi(x)$. Once the problem was solved at the first order, the perturbations of the SIFs could be obtained by examining the asymptotic behaviour of the mechanical fields near the crack tip. The expressions of the perturbed SIFs included integrals over the unperturbed crack, involving the unperturbed stress field plus the perturbation $\psi(x)$.

These integrals also involved a weight function proportional to the inverse square root of the distance to the crack tip. This implied a gradual decrease of the influence of the unperturbed stress field and the perturbation with this distance, which in turn suggested a reasonable approximation, consisting in considering only the first terms of the expansion of the unperturbed stress field in powers of the distance to the crack tip. Consideration of the first three terms led to the following first-order expressions of the perturbed SIFs $K_I(\ell)$, $K_{II}(\ell)$:

$$\left\{\begin{array}{l} K_I(\ell) \;\; = K_I^0(\ell) + \dfrac{\partial K_I^0}{\partial y}(\ell)\,\psi(\ell) - \dfrac{3\psi'(\ell)}{2}\,K_{II}^0(\ell) \\ K_{II}(\ell) = K_{II}^0(\ell) + \dfrac{\partial K_{II}^0}{\partial y}(\ell)\,\psi(\ell) + \dfrac{\psi'(\ell)}{2}\,K_I^0(\ell) \\ \qquad\qquad -\sqrt{\dfrac{2}{\pi}}\,T_{xx}^0(\ell)\displaystyle\int_{-\infty}^{\ell}\frac{\psi'(x)}{\sqrt{\ell-x}}\,dx \end{array}\right. \tag{35}$$

where $(\partial K_I^0/\partial y)(\ell)$ and $(\partial K_{II}^0/\partial y)(\ell)$ denote the derivatives of the unperturbed SIFs with respect to the vertical position of the crack, and $T_{xx}^0(\ell)$ the unperturbed non-singular stress.

An interesting connection may be established with the expansion of the SIFs in powers of the length of a kinked and curved extension, studied in Sect. 2.4 to 2.6. Consider the special case where the crack is unperturbed up to the point O, but

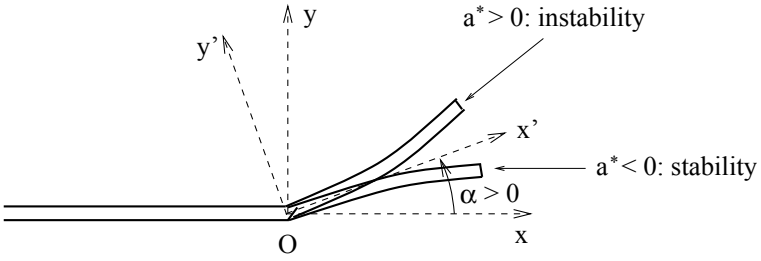

Fig. 9 A straight crack with a slightly kinked and curved extension

endowed with a short kinked and curved extension of the type described by equation (6), with small parameters α and a^* (Fig. 9).

Then the position ℓ of the crack tip along the Ox axis must be identified to the short length ϕ of the crack extension, and the perturbation $\psi(x)$ is of the form, in the axes Ox, Oy "adapted" to the unperturbed configuration of the crack (in line with the convention adopted by Cotterell and Rice (1980) and Movchan et al. (1998)):

$$\psi(x) = \begin{cases} 0 & \text{if } x \leq 0 \\ \alpha x + a^* x^{3/2} + O(x^2) & \text{if } 0 < x < \phi. \end{cases}$$

Equations (35) are then easily checked to reduce to

$$\begin{cases} K_I(\phi) &= K_I^0(\phi) - \dfrac{3}{2}\,\alpha K_{II}^0(\phi) - \dfrac{9}{4}\,a^* K_{II}^0(\phi)\sqrt{\phi} + O(\phi) \\ K_{II}(\phi) &= K_{II}^0(\phi) + \dfrac{\alpha}{2}\,K_I^0(\phi) + \left(\dfrac{3}{4}\,a^* K_I^0(\phi) - 2\sqrt{\dfrac{2}{\pi}}\,\alpha T_{xx}^0(\phi)\right)\sqrt{\phi} \\ & \quad + O(\phi)\,. \end{cases} \tag{36}$$

(The terms proportional to $(\partial K_I^0/\partial y)(\phi)$ and $(\partial K_{II}^0/\partial y)(\phi)$ in Eqs. (35) are embedded in the remainder $O(\phi)$ terms here).

To perform a comparison between the expressions provided by Eqs. (36) and those deduced from the expansion (21) of the SIF-vector $\mathbf{K}(\phi)$, with the expressions (15) and (22) of $\mathbf{K}^*$ and $\mathbf{K}^{(1/2)}$, one must beware that K_I^0 and K_{II}^0 in equations (15) and (22) represent the SIFs for an unperturbed crack with tip at $x = 0$, whereas $K_I^0(\phi)$ and $K_{II}^0(\phi)$ in equations (36) represent those for an unperturbed crack with tip at $x = \phi$. However the difference between these pairs of SIFs is $O(\phi)$, and therefore negligible here since terms of this order are disregarded. Hence the SIFs $K_I^0(\phi)$, $K_{II}^0(\phi)$ may be confounded with K_I^0, K_{II}^0 and renoted in that way, without generating any ambiguity. The non-singular stress $T_{xx}^0(\phi)$ will similarly be renoted T_{xx}^0 for simplicity.

It then easy to check that expressions (36) do coincide with those deduced from equations (21), (15) and (22) with the expressions (17)–(20), (23) and (24) of the components of the operator $\mathbf{F}(\alpha)$, vectorial function $\mathbf{G}(\alpha)$ and operator $\mathbf{H}(\alpha)$, pro-

vided one retains only terms of order 0 and 1 in the pair (α, a^*), in line with Cotterell and Rice (1980)s and Movchan et al. (1998)s first-order perturbation analyses.

Application to the problem of directional stability. Consider a mode I crack propagating in an infinite 2D body. This crack may be termed *directionally stable* if, in qualitative terms, it "does not tend to deviate from a straight line as it propagates". The inaccuracy of such a statement leaves room for several interpretations and treatments of the problem. Two versions, leading to fully compatible conclusions, will be proposed.

Version 1. This was the version proposed by Cotterell and Rice (1980) themselves. A small imperfection of the geometry and/or the loading is assumed to generate a bit of mode II, $0 < |K_{II}^0| \ll K_I^0$. The crack then kinks by a small angle α. The analysis focusses on propagation *just after* the kink point. Configurational stability/instability is considered to prevail if the curvature of the crack extension after this point tends to reduce/enhance the effect of the kink angle, that is if the kink angle α and the pseudo-curvature parameter a^* are of opposite/identical signs; see Fig. 9 where α is assumed to be positive.

Now the PLS implies that $K_{II}(\phi) = 0$ all along the crack path, where $K_{II}(\phi)$ is given by the second of equations (36). At order $\phi^0 = 1$, this condition yields the following classical expression of the kink angle under conditions of dominant mode I loading:

$$\alpha = -2\,\frac{K_{II}^0}{K_I^0}\,. \tag{37}$$

At order $\phi^{1/2} = \sqrt{\phi}$, it yields

$$a^* = \frac{8}{3}\sqrt{\frac{2}{\pi}}\,\frac{T_{xx}^0}{K_I^0}\,\alpha. \tag{38}$$

Since K_I^0 is necessarily positive, one sees that α and a^* are of opposite/identical signs if T_{xx}^0 is negative/positive. The conclusion is that in this version of the problem, *directional stability of crack propagation prevails if, and only if, the non-singular stress T_{xx}^0 is negative*.

Version 2. This more recent, probably more satisfying version was proposed by Ponson et al. (2020). No initial imperfection (in the form of a small K_{II}^0) is postulated, and the analysis considers the entire propagation instead of focussing on a small portion only. Of course, in the absence of mode II the straight configuration of the crack continuously satisfies the PLS during propagation. The question investigated is whether another configuration gradually departing from a straight line, while still continuously satisfying the PLS, can be found; this configuration is looked for, more specifically, in the following standard form for stability analyses:

$$\psi(x) = A\,e^{\lambda x} \tag{39}$$

where A and λ are parameters homogeneous to a length and the inverse of a length respectively, λ being positive.

Use must be made of the second of equations (35) providing the expression of $K_{II}(\ell)$ during propagation, ℓ being now identified to x, the current position of the crack tip. Let us disregard in this expression, in a first approximation, the term $\frac{\partial K_{II}^0}{\partial y}\,\psi(x)$ connected to the dependence of the unperturbed SIF K_{II}^0 upon the vertical position of the crack. With $K_{II}^0 = 0$, this expression becomes

$$K_{II}(x) = \frac{\psi'(x)}{2}\,K_I^0 - \sqrt{\frac{2}{\pi}}\,T_{xx}^0 \int_{-\infty}^{x} \frac{\psi'(x')}{\sqrt{x-x'}}\,dx' = A\lambda e^{\lambda x}\left(\frac{K_I^0}{2} - \sqrt{\frac{2}{\lambda}}\,T_{xx}^0\right)$$

where we have used the property $\int_0^{+\infty} \frac{e^{-u}}{\sqrt{u}}\,du = \sqrt{\pi}$. Satisfaction of the PLS during the entire propagation then requires that

$$A\lambda e^{\lambda x}\left(\frac{K_I^0}{2} - \sqrt{\frac{2}{\lambda}}\,T_{xx}^0\right) = 0.$$

- If $T_{xx}^0 < 0$, the term (...) is necessarily positive, so A must be zero: there is no solution other than the trivial one, corresponding to a straight crack.
- If $T_{xx}^0 > 0$, there is a non-trivial solution having $A \neq 0$, with λ given by

$$\lambda = 8\left(\frac{T_{xx}^0}{K_I^0}\right)^2. \tag{40}$$

The conclusion is that *there exists a non-trivial configuration of the crack departing more and more in time from a straight line if, and only, if, the non-singular stress T_{xx}^0 is positive*. It is completely in line with that obtained in Version 1 of the problem.

One should note, however, that this conclusion is dependent on the neglect of the term $\frac{\partial K_{II}^0}{\partial y}\,\psi(x)$ in the second of equations (35) providing $K_{II}(x)$. The picture becomes much more complex if this term is included; this topic was discussed in depth in the work of Ponson et al. (2020).

2.11 Application: Deviation of a Crack Propagating in a Quenched Plate

Formulae (21), (15) and (22) providing the expansion of the SIF-vector $\mathbf{K}(\phi)$ in powers of the crack extension length ϕ, combined with some propagation criterion, may be used to predict crack paths by step-by-step methods. In such predictions each step involves three operations: calculating the SIFs numerically for the present configuration of the crack; applying the criterion to these SIFs so as to predict the

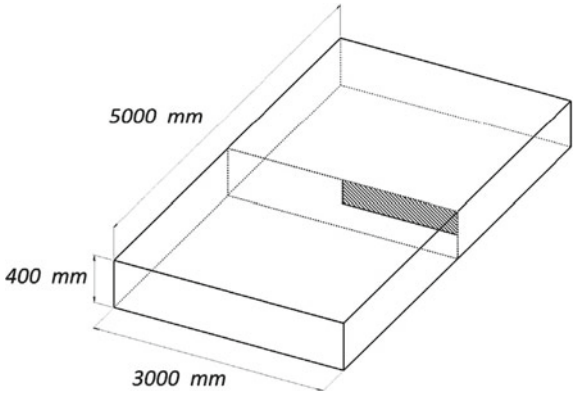

Fig. 10 Geometry of the quenched plate and the modelled zone (after Feulvarch et al. (2013), with permission)

geometric parameter(s) of the future crack path; and finally updating the cracked geometry by adding an extension endowed with this (these) parameter(s), of small prescribed length. Several options are possible for: (i) the numerical method of calculation of the SIFs; (ii) the choice of the propagation criterion—although the PLS is preferable for the reasons explained in Sect. 2.9; and (iii) the number of geometric parameters of the crack extension predicted at each step. In this subsection, we shall present two numerical studies due to Autesserre (1995) and Feulvarch et al. (2013) of the same problem of crack propagation in a situation of practical interest, differing in all three respects. Emphasis will be placed mainly on the second, more recent and complete work.

Presentation of the problem. In the industrial process considered in the works of Autesserre (1995) and Feulvarch et al. (2013), large steel plates were quenched and subsequently sawed into smaller pieces. Two alternative quenching treatments were used, a "normal" water quench, and an innovative "interrupted" quench wherein the plate was extracted from the water bath after 3000 s, and subsequently cooled much more slowly in air. No special problem was encountered during sawing after a normal quench. On the other hand, in the case of the interrupted quench, sawing was observed to induce undesired quick unstable propagation, followed by deviation at 90°, of a crack ahead of the saw blade. The aim of the simulations discussed below was to explain this phenomenon, so as to foresee and avoid similar difficulties in the future.

Figure 10 shows the geometry of the plate, of dimensions 5000 mm × 3000 mm × 400 mm. It was sawed downwards, along a section lying halfway along its intermediary dimension of 3000 mm, perpendicularly to the direction of this dimension. Because of its large horizontal dimensions, 2D plane strain simulations could be performed in a section lying halfway along the largest dimension of 5000 mm, perpendicularly to the direction of this dimension; in fact presence of symmetries permitted to mesh only one fourth of this section, represented in grey in Fig. 10.

Simulation of the quenching process. The first task was to simulate the quenching process, in order to determine the resulting residual stresses. In processes of this kind,

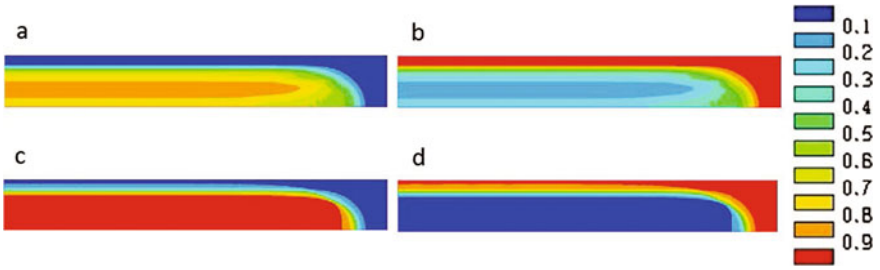

Fig. 11 Final volume fractions of metallurgical phases resulting from quenching (after Feulvarch et al. (2013), with permission). **a** Normal quenching, bainite—**b** Normal quenching, martensite—**c** Interrupted quenching, bainite—**d** Interrupted quenching, martensite

residual stresses depend in a crucial manner upon the metallurgical transformations occurring during cooling (from austenite to ferrite, bainite and martensite for low, intermediate and high cooling rates, respectively), making it necessary to simulate them. The object of the present paper is not to discuss such simulations in detail, and we shall be content with merely expounding the results obtained by Feulvarch et al. (2013).

Figure 11 shows the final distributions of the volume fractions of bainite and martensite resulting from the two quenching processes. In both cases the structure is essentially bainitic at the core and martensitic near the surface. But for the interrupted quenching the outer martensitic zone is thinner, and the predominance of bainite at the core is more marked. This is an obvious consequence of the slow cooling rates resulting from interruption of the quench, which favour formation of bainite rather than martensite.

Figure 12 shows the final distributions of the horizontal residual stress σ_{xx}, perpendicular to the plane of the vertical saw blade moving downwards and the future crack. There are some common features in the distributions resulting from the two processes: a very thin compression zone near the surface, and a tension zone deeper in the plate. But the different metallurgical structures entail significant differences: for the normal quench the stress distribution is quite homogeneous and the stress remains moderate; but for the interrupted quench the upper half of the modelled zone is subject to high tensile stresses, whereas the lower half undergoes compressive ones.

These results are appealing in that in the case of the interrupted quench, the presence of the positively stressed zone just below the surface explains the experimental observation of initiation and quick propagation of a crack ahead of the saw blade. But they also raise the following issue: since the crack encounters *compressive* residual stresses in the lower half of the modelled zone, why does it choose to deviate at 90° instead of just stopping halfway down this zone?

Simulation of crack propagation. Clearly, the only way to answer such a question is to simulate crack propagation. Such simulations have been performed by Feulvarch et al. (2013) with the following options:

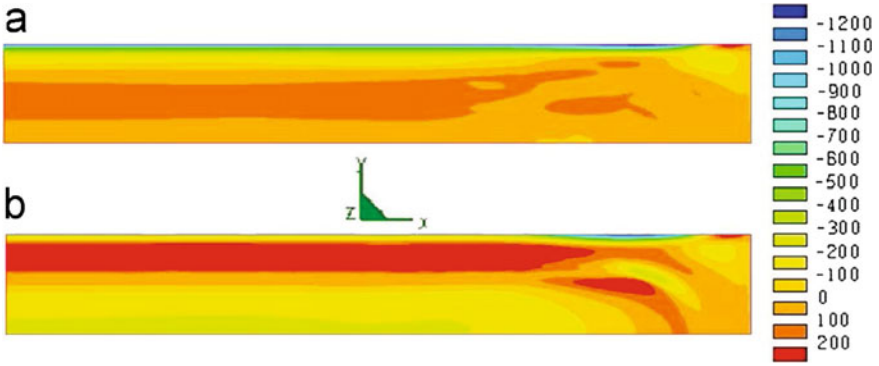

Fig. 12 Final distributions of the horizontal residual stress σ_{xx} resulting from the quenching process (after Feulvarch et al. (2013), with permission). **a** Normal quenching—**b** Interrupted quenching

- Use of Moës et al. (1999)s XFEM method to compute the SIFs for a given cracked geometry. In this method the crack is not accounted for explicitly in the mesh as a free surface, but rather through addition of new trial displacement fields allowing for discontinuities and singularities, "adapted" to the position of the lips and tip of the crack. The major advantage is to avoid cumbersome remeshing operations at all steps of the simulation.
- Use of the maximum hoop stress criterion to predict the future crack path. (The choice of the PLS would have been preferable for the reasons expounded in Sect. 2.9, but in practice it would not have changed the results in any significant way, considering the small kink angles encountered in the problem).
- Prediction of the sole kink angle of the future crack extension (no prediction of curvature).

Two additional remarks are in order:

- The presence of residual stresses, arising from some inelastic (plastic) strains, implies that the problem does not rigorously fit into the theoretical framework developed in the preceding sections, based on the hypothesis of pure elasticity. This issue was considered in depth by Autesserre (1995), with the conclusion that provided that the inelastic strains are smooth in space and invariable in time—that is, unaffected by the crack advance—all results expounded above still apply; thus presence of such strains only requires that they be accounted for in the calculation of the SIFs, without modifying the way in which the crack path is deduced from these SIFs.
- The mode I SIF K_I is only required to remain positive, the crack being considered to stop if it does not. It is *not* required to equal the fracture toughness K_{Ic}—the aim being to permit unstable propagation of the crack.

Figure 13 shows the crack path resulting from sawing of the plate after an interrupted quench, superimposed upon the *instantaneous* distribution of the residual

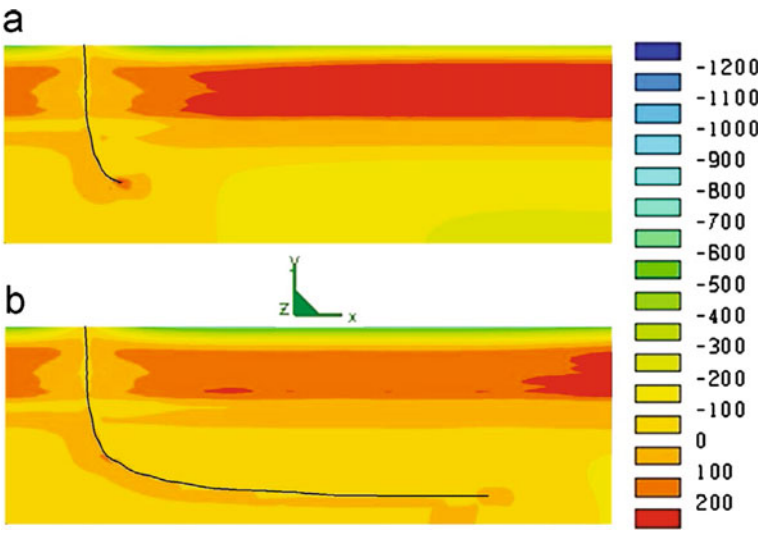

Fig. 13 Crack path at different steps, resulting from sawing after an interrupted quench (after Feulvarch et al. 2013, with permission)

stress σ_{xx}, at two different steps of the calculation.[8] The deviation at 90° following the crack's entry into the zone of negative *initial* residual stresses (apparent in Fig. 12b) is spectacular.

The distributions of residual stresses shown with the crack path shed some light on this phenomenon. Comparing Figs. 12 and 13, one sees that in the upper half of the modelled zone, propagation of the crack erases strongly positive stresses in its wake; in the lower half strongly negative stresses give way to mildly negative or positive ones. Crack propagation therefore induces a major *redistribution* of residual stresses, which explains why simple reasonings based on consideration of the sole *initial* residual stress field fail short of predicting the behaviour of the crack. Unfortunately it is very difficult to a priori predict what this redistribution will be, so that resorting to complex numerical simulations seems the only way to predict the crack path.

Autesserre (1995)s earlier simulations were based on different options:

- Use of the standard finite element method to compute the SIFs for a given cracked geometry; this approach required a remeshing operation at each step of the propagation.
- Use of the PLS to predict the future crack path.
- Prediction of the kink angle *and* the curvature of the future crack extension.

Figure 14 compares the crack paths predicted by Autesserre (1995) and Feulvarch et al. (2013). (There are in fact two almost coincident paths for Feulvarch et al. (2013)s

[8] Note that the crack is initiated numerically close to, but not exactly on, the symmetry plane of the plate coinciding with the left boundary of the region modelled—the aim being to avoid simulating a crack forking into two symmetric branches.

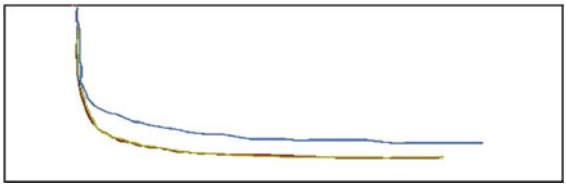

Fig. 14 Comparison of crack paths predicted by Autesserre (1995) (in blue) and Feulvarch et al. (2013) (in red and green) (with permission of the authors)

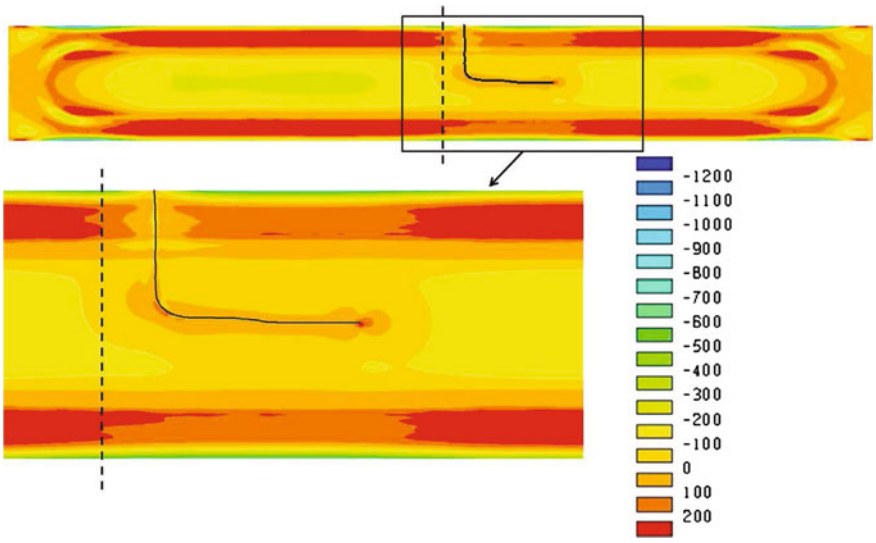

Fig. 15 Crack path in a mesh of the full plate (after Feulvarch et al. (2013), with permission)

simulations, obtained for crack advances between successive steps of 8 mm and 12 mm). Autesserre (1995)s calculation predicts a somewhat more abrupt deviation of the crack. The reason may reside in his more accurate geometric description of the crack path including curvature, but this is uncertain since there are other differences between the simulations.

A final remark is in order. Although consideration of only one quarter of the section of the plate shown in Fig. 10, with symmetry conditions, is perfectly reasonable for the computation of the volume fractions of the phases and the residual stresses, it is more debatable for the simulation of crack propagation, since the deviation of the crack at 90° breaks the geometrical symmetries. Simulations of crack propagation in a quarter of a section with symmetry conditions, as presented above, in fact imply presence of *four symmetrical cracks*—three of which are non-existent in reality. For this reason Feulvarch et al. (2013) performed complementary simulations on a complete mesh of the full plate. Figure 15 show the crack path obtained; one sees that the crack still deviates at 90°—in fact, even more sharply—which confirms the findings of the simpler simulations.

2.12 Concluding Summary

In this Section we considered perturbations of cracks in 2D plane strain situations, in mixed-mode I+II loading conditions. Emphasis was placed on application of such perturbations to the formulation of a criterion providing the direction of future crack growth.

Having expounded general hypotheses and notations in Sect. 2.2, and established an important preliminary result in Sect. 2.3, we studied in Sect. 2.4—following the work of Leblond (1989)—the general expression of the SIFs just after a kink, using this result combined with arguments of scale changes. It was shown that the SIFs just after the kink depend only on those just before the kink plus the kink angle α, irrespectively of the (2D) geometry of the body and the loading imposed on it (universality property). The formula connecting the two sets of SIFs involves an operator (2×2 matrix) $\mathbf{F}(\alpha)$ depending only on α, which may be determined once and for all by considering some relevant special case.

This was done in Sect. 2.5 by referring to the works of Amestoy (1987) and Amestoy and Leblond (1992), devoted to the special case of a crack composed of two straight branches—one of them of infinitesimal length—in an infinite body subjected to uniform remote stresses. These two works—the most comprehensive on the topic—provide, in addition to numerical values of the components $F_{pq}(\alpha)$ $(p, q = I, II)$ of the operator $\mathbf{F}(\alpha)$, exact expressions of the coefficients appearing in the expansions of these components in powers of α, up to any pre-specified order. In practice, the expansions at order 20 provide values of the functions $F_{pq}(\alpha)$ with sufficient accuracy for all practical purposes.

As a complement, Sect. 2.6 provided (without any detailed proof) the expressions of the second and third terms of the expansion of the SIFs in powers of the crack extension length ϕ, proportional to $\sqrt{\phi}$ and ϕ respectively. Reference was made there to the works of Amestoy (1987) and Leblond (1989) who obtained these expressions in full generality. The loss of the universality property was observed in the third term proportional to ϕ, following Leblond (1989)s remarks—noting however that this loss had already been remarked in a special case in the earlier work of Sumi et al. (1983).

Section 2.7, based on a reasoning of Ichikawa and Tanaka (1982) (presented in a more rigorous setting), showed how Irwin (1958)s standard expression of the energy-release-rate of a crack, in the absence of a kink, may be extended to a fully general situation involving an arbitrary kink. The appealing conclusion was that Irwin (1958)s formula still applies in the presence of an arbitrary kink angle, provided that the usual SIFs *before* the kink appearing in this formula are replaced by those just *after* the kink.

A presentation was then made in Sect. 2.8 of three classical criteria for prediction of the future direction of crack growth: (i) Erdogan and Sih (1963)s maximum hoop stress criterion, of purely heuristic nature; (ii) Erdogan and Sih (1963)s maximum energy-release-rate criterion, intimately tied to Griffith (1920)s theory of brittle fracture; and (iii) Goldstein and Salganik (1974)s principle of local symmetry (PLS), initially deduced from some rather obscure "physical reasoning".

It was next shown in Sect. 2.9 that among these three criteria, the PLS is the only one that predicts, after the initial abrupt change of direction, a geometrically regular crack path (no further kink). It was concluded from there that the PLS is the "best" criterion for reasons of sheer logic (having nothing to do with Goldstein and Salganik (1974)s "physical reasoning"); and difficulties arising in the context of other criteria were analyzed in detail.

Section 2.10, based on the works of Cotterell and Rice (1980), Movchan et al. (1998) and Ponson et al. (2020), was devoted to the application of these results to the issue of configurational stablity of the propagation path of a mode I crack, and especially to the influence of the non-singular stress upon this stability.

Finally Sect. 2.11 presented some numerical predictions, based on the preceding results, of the path followed by a crack induced by sawing of a quenched plate. The simulations reproduced and explained some puzzling experimental observations of deviation at 90° of the crack, in the case of an "interrupted" quench.

3 3D Coplanar Crack Perturbations

3.1 Introduction

In this section we shall consider *coplanar* perturbations of cracks loaded in mode I or mixed mode I+II+III in 3D situations. Applications pertain to cracks propagating along a planar surface, either because of symmetry reasons (case of a tensile crack in an elastically homogeneous material for instance), or because of "channeling" of the crack along a thin weaker layer (case of an interface crack propagating along the junction between distinct elastic materials bonded onto one another).

The papers reviewed here were published in a period extending between 1985 and the present day. The field is still quite active, with in particular a number of recent papers devoted to the interpretation—generally assisted by numerical simulations—of experiments of fracture of materials having heterogeneous fracture properties.

By definition, coplanar perturbations of cracks involve an in-plane perturbation of the crack *front*, but no perturbation of the crack *surface*. This means that the perturbations considered in this section will be exclusively of Type I, in the terminology defined in the General Introduction.

Methods available at present for the treatment of such crack perturbations are of two types. *Special methods* aim at sparing the analyst the effort of completely solving the elasticity problem implied on the perturbed cracked geometry, by concentrating instead on the sole quantities of interest—generally the distributions of SIFs along the perturbed crack front. Only one such method, based on Rice (1985, 1989)s reformulation of Bueckner (1987)s weight function theory—summarized below—is available at present. The aim of *general methods*, in contrast, is not to attempt such a "reduction" of the problem but to fully solve it on the perturbed geometry, using general methods of solution of 3D elasticity problems.

The first, seminal paper in the field was published by Rice (1985). In this work, devoted to the case of a semi-infinite tensile crack in some infinite medium, the author used both types of methods, to derive a formula for the variation of the mode I SIF resulting from some small but otherwise arbitrary in-plane perturbation of the crack front, exact to first-order in this perturbation. His special method of solution involved, as a prerequisite, a new point of view on the theory of Bueckner (1987)s weight functions, which led to a convenient expression of the first-order variation of the local displacement discontinuity across the crack surface caused by the perturbation of the front. On the other hand his general method of solution was based on a special choice of Papkovich (1932)—Neuber (1934) potentials.

Rice (1985)s very efficient and economical special method of solution was extended in subsequent papers of his and coworkers to various cases, always pertaining to infinite bodies: a semi-infinite crack loaded arbitrarily (Gao and Rice 1986), a penny-shaped crack loaded in mode I (Gao and Rice 1987a), then arbitrarily (Gao 1988), and finally an exterior circular crack loaded in mode I (Gao and Rice 1987b). In all these specific cases, the 3D weight functions were known explicitly from some previous works. In a further paper, however, Rice (1989) extended the perturbation solution to arbitrary tensile cracks in arbitrary bodies, for which the relevant mode I weight function is not known in explicit form. He showed how to express—under certain conditions[9]—the first-order variation of the mode I SIF along the crack front, in the form of some integral over this front involving the unperturbed SIF, the perturbation of the front, and some function related to the mode I weight function, referred to as the mode I *fundamental kernel* (FK) in the work of Leblond et al. (1996) and subsequent ones. In addition, as a consequence of the fact that this FK was itself related to the distribution of the mode I SIF generated on the crack front by some special loading, he could also derive—again under certain conditions—the first-order variation of the mode I FK itself, resulting from the same perturbation. These results, extended to arbitrary combinations of modes by Favier et al. (2006), paved the way to numerical calculations, under mildly restrictive conditions, of the SIFs and FKs for planar cracks of arbitrary contour, through gradual deformation of this contour from some initial "reference" shape involving known expressions of these SIFs and FKs.

Many papers were devoted to the numerical application of these works. In most of these, the SIF(s) was (were) updated for successions of crack front shapes, but the FK(s) was (were) not, thus restricting the approach to nearly straight crack fronts; this was done in papers, generally originating from the physics community and too numerous to be cited here, devoted to the propagation of tensile cracks in materials having heterogeneous fracture properties—generally with the aim of studying the overall, "apparent" fracture toughness resulting from heterogeneities. In some rarer papers, however, the FK(s) itself (themselves) was (were) continuously updated, thus permitting to consider arbitrary deformations of the crack front (Bower and Ortiz 1990; Lazarus 2003; Favier et al. 2006; Vasoya et al. 2016a).

[9] Specified in Sect. 3.3 below.

Following a different line of thought, Leblond and coworkers pursued the search for analytical solutions of coplanar crack perturbation problems for new crack geometries, generally (though not always) using Rice (1985, 1989)s special method of solution, based on Bueckner (1987)s weight functions. Rice (1989)s first-order formula for the variation of the mode I SIF, and its extension by Favier et al. (2006) to arbitrary combination of modes, permitted to reduce the problem to finding the FK(s) for these geometries. In a first step, Leblond et al. (1996) considered the case of a tensile slit- (or tunnel-) crack in some infinite body; they showed how to derive the mode I FK from Rice (1989)s first-order expression of its variation, using special perturbations of the crack front preserving its shape and thus leading to some "self-consistent" conditions on this FK. The work was extended to a slit-crack under arbitrary loading, using Favier et al. (2006)s extension of Rice (1989)s work, by Lazarus and Leblond (2002a, b). The same method was employed by Lazarus and Leblond (1998a, b) for a 3D semi-infinite interface crack (between different elastic materials) under general loading, and Pindra et al. (2010) and Legrand et al. (2010) for a system of two collinear tensile slit-cracks. Finally Legrand et al. (2011) derived the mode I FK for a crack lying on the mid-plane of a plate of arbitrary thickness. Exceptionally, they did not use for this purpose Rice (1985, 1989)s special method of solution but a general method, based on combination of an analytical solution for thin plates derived from Kirchhoff-Love's theory, and numerical, finite element solutions for thick plates.

In addition, Rice (1985)s expression of the first-order variation of the mode I SIF resulting from some arbitrary crack front perturbation was extended to the second order by Leblond et al. (2012) and Vasoya et al. (2013). This was done by (i) considering a primary perturbation of the front of small but finite amplitude; (ii) using Rice (1989)s formula for the variation of the FK to evaluate it at first order on the perturbed configuration thus defined; (iii) considering an additional, secondary perturbation of the front proportional to the primary one, of *infinitesimal* amplitude; (iv) using Rice (1989)s formula for the resulting infinitesimal variation of the SIF, with the first-order expression of the FK, to get the first-order expression of the derivative of the SIF with respect to the amplitude of the perturbation; (v) integrating with respect to this amplitude to get the second-order expression of the SIF. Vasoya et al. (2016b) employed the same method to extend Legrand et al. (2011)s perturbation solution for a crack lying on the mid-plane of a plate to the second order. The final formula obtained by Vasoya et al. (2016b) for the SIF along the perturbed front, including the effects of both the finite thickness of the plate and geometrical nonlinearities, was applied to the prediction of the deformation of a crack front encountering a harder obstacle; a remarkable agreement was found between theoretical predictions and crack front shapes actually observed in dedicated experiments.

In this section we shall review a selection of the theoretical papers quoted above, concentrating mainly—though not exclusively—on Rice (1985, 1989)s special method of solution, based on Bueckner (1987)s weight functions; some applications, pertaining especially to the deformation of a crack front encountering a harder obstacle, will also be considered. The section is organized as follows:

- Section 3.2 first expounds Rice (1985, 1989)s re-formulation of the theory of Bueckner (1987)s weight functions, leading to a first-order formula for the variation of the displacement discontinuity across the crack surface resulting from some small, but otherwise arbitrary coplanar perturbation of the front.
- Following again the work of Rice (1989), Sect. 3.3 deduces from there general first-order formulae for the variations of the mode I SIF and FK resulting from such a perturbation, for an arbitrary tensile crack in an arbitrary body.
- Section 3.4 then specializes to the case of a semi-infinite mode I crack in an infinite body, providing fully explicit formulae for this case. The formulae obtained for the first- and second-order variations of the SIF are those of Rice (1985) and Leblond et al. (2012); Vasoya et al. (2013).
- As a first illustration of the effect of the finite crack dimensions, Sect. 3.5 considers the case of a tensile slit-crack in an infinite body. We follow the work of Leblond et al. (1996) to show how the mode I FK for this case may be deduced from Rice (1989)s formula for the variation of the FK, using suitably chosen perturbations of the two parts of the front. The results obtained are applied in Sect. 3.6 to the study of the configurational stability of the propagating front.
- In Sect. 3.7, we follow the works of Legrand et al. (2011) and Vasoya et al. (2016b), to derive the first- and second-order expressions of the mode I SIF along the perturbed front of a crack lying on the mid-plane of a plate of arbitrary thickness. In Sect. 3.8 an accurate formula is deduced from there, following the work of Vasoya et al. (2016b), for the deformation of the front resulting from encounter of a harder obstacle; and the predictions of this formula are compared to experimental observations.
- Finally, following the work of Lazarus and Leblond (1998a, b), Sect. 3.9 considers the problem of coplanar perturbation of the front of a 3D semi-infinite interface crack between different elastic materials, under arbitrary loading. Using the results of this subsection together with those of Sects. 3.7, 3.10 draws some interesting conclusions about the interpretation of some experiments of debonding of plates bonded onto rigid substrates.

3.2 *Rice (1985, 1989)s Re-formulation of Bueckner (1987)s Theory of Weight Functions*

We consider (Fig. 16), within a linearized geometrical framework, an arbitrary 3D body Ω made of some isotropic, linearly elastic material, subjected to some loading consisting of prescribed surface tractions $\mathbf{T}^p$ and displacements $\mathbf{u}^p$ imposed on the complementary portions $\partial\Omega_T$ and $\partial\Omega_u$ of its boundary $\partial\Omega$, respectively. This body contains a planar crack of arbitrary contour—the crack front $\mathcal{F}$—slightly perturbed within its plane; the orthogonal distance from the original front to the perturbed one is denoted $\phi(s)$ where s denotes some curvilinear distance along the contour, and is considered to be of the form

$$\phi(s) \equiv \eta\bar{\phi}(s) \tag{41}$$

where η is a small parameter and $\bar{\phi}(s)$ a given, fixed function.

The aim of this section is to derive an expression, accurate to first order in η, of the variation $\delta\mathbf{u}(M)$ of the displacement $\mathbf{u}(M)$ at any point M of the body resulting from the perturbation of the crack front, the loading $(\{\mathbf{T}^p\}, \{\mathbf{u}^p\})$ remaining fixed. An arbitrary Cartesian basis $(\mathbf{e}_x, \mathbf{e}_y, \mathbf{e}_z)$ being introduced, we shall do so, following Rice (1985, 1989), by (i) adding to the main loading $(\{\mathbf{T}^p\}, \{\mathbf{u}^p\})$, a secondary one consisting of a point force $P\mathbf{e}_i$ $(i = x, y, z)$ exerted on the arbitrary point M (equilibrated by reaction forces on $\partial\Omega_u$), and (ii) considering small, independent variations of the parameters η and P, the primary loading $(\{\mathbf{T}^p\}, \{\mathbf{u}^p\})$ remaining fixed.

Let $W \equiv \int_\Omega \frac{1}{2}\boldsymbol{\sigma} : \boldsymbol{\epsilon}\, d\Omega$ denote the elastic potential energy for the resultant loading, and $\Phi \equiv \int_{\partial\Omega_T} \mathbf{T}^p.\mathbf{u}\, dS$ the opposite of the potential energy of the surface tractions $\mathbf{T}^p$—so that the opposite of the potential energy of the ensemble of prescribed forces is $\Phi + P\mathbf{e}_i \,.\, \mathbf{u}(M) = \Phi + Pu_i(M)$. The following relation then holds for arbitrary independent infinitesimal variations of η and P:

$$dW = d\Phi + Pdu_i(M) - \int_{\mathcal{F}} G(s)\, d\phi(s)\, ds = d\Phi + Pdu_i(M) - d\eta \int_{\mathcal{F}} G(s)\bar{\phi}(s)\, ds \tag{42}$$

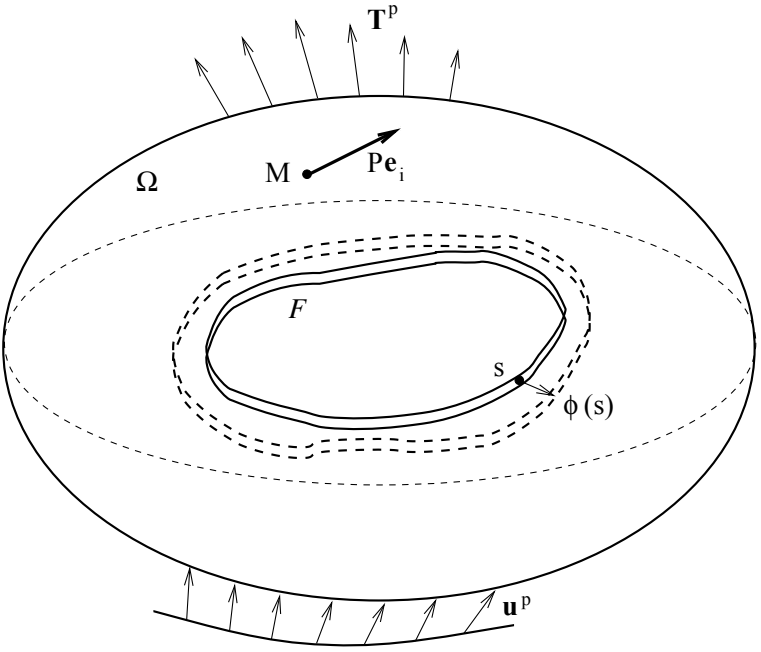

Fig. 16 Coplanar perturbation of a crack in an arbitrary 3D body

where $G(s)$ denotes the local energy-release-rate. Indeed for fixed P and variable η, it is a consequence of the relation defining the local energy-release-rate, and for fixed η and variable P, it is a consequence of the principle of virtual work.

Now define the quantity

$$\Psi \equiv \Phi + P u_i(M) - W. \tag{43}$$

(This is the opposite of the total potential energy, noted $\mathcal{P}$ in Sect. 2.7). By Eq. (42),

$$d\Psi = d\Phi + u_i(M)\, dP + P du_i(M) - dW = u_i(M)\, dP + d\eta \int_{\mathcal{F}} G(s)\bar{\phi}(s)\, ds.$$

It follows from there, considering Ψ as a function of the variables P and η, that

$$\frac{\partial \Psi}{\partial P} = u_i(M) \quad ; \quad \frac{\partial \Psi}{\partial \eta} = \int_{\mathcal{F}} G(s)\bar{\phi}(s)\, ds \tag{44}$$

and therefore, by the identity of cross-derivatives, that

$$\frac{\partial u_i(M)}{\partial \eta} = \frac{\partial}{\partial P}\left(\int_{\mathcal{F}} G(s)\bar{\phi}(s)\, ds \right) = \int_{\mathcal{F}} \frac{\partial G(s)}{\partial P}\, \bar{\phi}(s)\, ds \quad \left(= \frac{\partial^2 \Psi}{\partial P \partial \eta} \right). \tag{45}$$

We shall make use of this identity at the point $(\eta, P) = (0, 0)$.

Define $k_{pi}(M; s)$—one of Bueckner (1987)s 3D weight functions—as the pth SIF generated at the point s of the unperturbed crack front ($\eta = 0$) by a point force of *unit* intensity parallel to the basis vector $\mathbf{e}_i$, applied on the point M, zero surface tractions and displacements being simultaneously imposed on $\partial\Omega_T$ and $\partial\Omega_u$, respectively. For the resultant loading defined above, the SIFs at the point s of the unperturbed crack front are given by

$$K_p(s) = K_p^0(s) + P k_{pi}(M; s) \quad (p = I, II, III) \tag{46}$$

where $K_p^0(s)$ denotes the p-th unperturbed SIF due to the primary loading ($\{\mathbf{T}^p\}$, $\{\mathbf{u}^p\}$) alone. It then follows from Irwin's formula that the derivative of the energy-release-rate at the point $(\eta, P) = (0, 0)$ is given by

$$\begin{aligned} \frac{\partial G(s)}{\partial P}|_{(\eta,P)=(0,0)} = 2 \Bigg\{ & \frac{1-\nu^2}{E} \left[K_I^0(s) k_{Ii}(M; s) + K_{II}^0(s) k_{IIi}(M; s) \right] \\ & + \frac{1+\nu}{E} K_{III}^0(s) k_{IIIi}(M; s) \Bigg\} \end{aligned} \tag{47}$$

where E and ν denote Young's modulus and Poisson's ratio. Identity (45) then yields at the same point:

$$\frac{\partial u_i(M)}{\partial \eta}|_{(\eta,P)=(0,0)} = \int_{\mathcal{F}} 2\left\{\frac{1-\nu^2}{E}\left[K_I^0(s)k_{Ii}(M;s) + K_{II}^0(s)k_{IIi}(M;s)\right] + \frac{1+\nu}{E}K_{III}^0(s)k_{IIIi}(M;s)\right\}\bar{\phi}(s)\,ds. \tag{48}$$

It then follows from multiplication of this equation by η, that the variation $\delta u_i(M)$ of the i-th component of the displacement at M resulting from the perturbation $\phi(s) = \eta\bar{\phi}(s)$ of the crack front, the body being subjected to the *sole original loading* ($\{\mathbf{T}^p\}$, $\{\mathbf{u}^p\}$), is given to first order in η by the following formula (Rice 1985, 1989):

$$\delta u_i(M) = \int_{\mathcal{F}} 2\left\{\frac{1-\nu^2}{E}\left[K_I^0(s)k_{Ii}(M;s) + K_{II}^0(s)k_{IIi}(M;s)\right] + \frac{1+\nu}{E}K_{III}^0(s)k_{IIIi}(M;s)\right\}\phi(s)\,ds. \tag{49}$$

Of special interest is the variation $\delta[\![\mathbf{u}]\!](M)$ of the displacement discontinuity $[\![\mathbf{u}]\!](M)$ at an arbitrary point M of the crack surface. The i-th component of this variation may be obtained from equation (49) by taking the difference of the variations $\delta u_i(M^+)$, $\delta u_i(M^-)$ at the points M^+, M^- of the upper (+) and lower (−) faces of the crack. The result reads

$$\delta[\![u_i]\!](M) = \int_{\mathcal{F}} 2\left\{\frac{1-\nu^2}{E}\left[K_I^0(s)h_{Ii}(M;s) + K_{II}^0(s)h_{IIi}(M;s)\right] + \frac{1+\nu}{E}K_{III}^0(s)h_{IIIi}(M;s)\right\}\phi(s)\,ds \tag{50}$$

where

$$h_{pi}(M;s) \equiv k_{pi}(M^+;s) - k_{pi}(M^-;s) \quad (p = I, II, III), \tag{51}$$

a *crack face weight function* (CFWF), denotes the p-th SIF generated at the point s of the unperturbed crack front by a *pair* of point forces of unit intensity parallel to the vectors $\pm\mathbf{e}_i$, applied on the points $M^{\pm}$ of the upper and lower faces of the crack, zero surface tractions and displacements being simultaneously imposed on $\partial\Omega_T$ and $\partial\Omega_u$.

3.3 Variations of the Mode I Stress Intensity Factor and the Fundamental Kernel: General Formulae

We specialize from now on to the case where both the body and the loading are symmetric with respect to the crack plane; as a consequence, the crack is loaded in pure mode I at every point of its front, in both its original and perturbed configurations. We shall therefore adopt lighter notations wherein $\delta[\![u_y]\!](M)$ (y denoting the direction orthogonal to the crack plane), $K_I^0(s)$, $\delta K_I(s)$ and $h_{Iy}(M;s)$ will simply be denoted $\delta[\![u]\!](M)$, $K^0(s)$, $\delta K(s)$ and $h(M;s)$.

Also, the reasonings below will be based on inspection of the variation of the displacement discontinuity *near the crack front*. We shall therefore assume the point M of observation of this discontinuity to be located behind the point s_1 of the front, at a small orthogonal distance r_1 from this point. For more clarity the quantities $\delta[\![u]\!](M)$ and $h(M;s)$ will then be renoted $\delta[\![u]\!](s_1,r_1)$ and $h(s_1,r_1;s)$.

Representation and properties of the crack face weight function and the fundamental kernel. It is known, for instance from the works of Rice (1989) and Leblond et al. (1999), that when the point M of the crack surface goes to the point s_1 of the crack front ($r_1 \to 0^+$), the CFWF $h(s_1,r_1;s)$ goes to zero proportionally to $\sqrt{r_1}$. This justifies the introduction of a function $Z(s_1,s)$ defined by

$$Z(s_1,s) \equiv \frac{1}{4} \lim_{r_1 \to 0^+} \sqrt{\frac{2\pi}{r_1}}\, h(s_1,r_1;s). \tag{52}$$

It is also known from the same work of Rice that when s_1 goes to s, the function $Z(s_1,s)$ diverges to infinity like $\frac{1}{2\pi D^2(s_1,s)}$ where $D(s_1,s)$ denotes the Cartesian distance between the points s_1 and s. This justifies the representation of this function in the form

$$Z(s_1,s) \equiv \frac{W(s_1,s)}{2\pi D^2(s_1,s)} \tag{53}$$

where $W(s_1,s)$ is a regular (finite and continuous) function of the pair (s_1,s), obeying the property $W(s,s)=1$. In the sequel the expression *fundamental kernel* (FK) will refer, with a slight lack of rigour, either to the function $Z(s_1,s)$ or to the function $W(s_1,s)$, depending on the context.

To establish a symmetry property of the functions $Z(s_1,s)$ and $W(s_1,s)$, assume that point forces of unit intensity parallel to $\pm\mathbf{e}_y$ (orthogonal to the crack surface) are applied at the points $M^\pm \equiv (s_1,r_1)^\pm$ of the crack faces, zero surface tractions and displacements being simultaneously imposed on $\partial\Omega_T$ and $\partial\Omega_u$. The value of the displacement discontinuity in the direction y at the point of the crack surface located behind the point s of the front, at a small orthogonal distance r from this point, is then at the lowest significant order in r,

$$8\,\frac{1-\nu^2}{E}\sqrt{\frac{r}{2\pi}}\,h(s_1,r_1;s) \sim 32\,\frac{1-\nu^2}{E}\sqrt{\frac{r}{2\pi}}\sqrt{\frac{r_1}{2\pi}}\,Z(s_1,s).$$

Consider now the case where the forces are applied at the points $(s,r)^{\pm}$ instead of $(s_1,r_1)^{\pm}$, and the displacement discontinuity observed at the point (s_1,r_1) instead of (s,r): applying Betti's reciprocity theorem, one concludes that $\sqrt{r/(2\pi)}\,\sqrt{r_1/(2\pi)}\,Z(s_1,s) = \sqrt{r_1/(2\pi)}\,\sqrt{r/(2\pi)}\,Z(s,s_1)$ so that

$$Z(s_1,s) = Z(s,s_1) \quad \text{or equivalently} \quad W(s_1,s) = W(s,s_1) \quad (\forall s_1, s). \tag{54}$$

Variation of the Stress Intensity Factor. Following Rice (1985, 1989), we assume in a first step that *the point s_1 of the crack front remains fixed in the perturbation*: $\phi(s_1) = 0$. In this case the displacement discontinuity $[\![u]\!](s_1,r_1)$ at a distance r_1 behind the point s_1 of the crack front is given, whatever the (small) "amplitude" η of the perturbation, by the classical formula

$$[\![u]\!](s_1,r_1) \sim 8\,\frac{1-\nu^2}{E}\,K(s_1)\sqrt{\frac{r_1}{2\pi}} \tag{55}$$

where $K(s_1)$ denotes the local perturbed SIF. It follows that the first-order variation of the displacement discontinuity resulting from the perturbation of the front is related to the first-order variation of the local SIF through the relation

$$\delta[\![u]\!](s_1,r_1) \sim 8\,\frac{1-\nu^2}{E}\,\delta K(s_1)\sqrt{\frac{r_1}{2\pi}}\,. \tag{56}$$

Therefore the first-order variation of the local SIF is given by the formula

$$\begin{aligned}\delta K(s_1) &= \frac{E}{8(1-\nu^2)}\lim_{r_1\to 0^+}\sqrt{\frac{2\pi}{r_1}}\,\delta[\![u]\!](s_1,r_1)\\ &= \frac{1}{4}\lim_{r_1\to 0^+}\sqrt{\frac{2\pi}{r_1}}\int_{\mathcal{F}} K^0(s)h(s_1,r_1;s)\phi(s)\,ds\end{aligned} \tag{57}$$

where equation (50) has been used.

The calculation of the limit in equation (57) is less simple than it may seem at first sight, because the limit of the expression $\sqrt{2\pi/r_1}\;h(s_1,r_1;s)$ for $r_1\to 0^+$ is $4Z(s_1,s)$, which diverges likes $D^{-2}(s_1,s)$ when the points s_1 and s become close to each other. The solution to this problem, provided by Rice (1989) and completed by Favier et al. (2006), consists in splitting the crack front $\mathcal{F}$ into a small interval $[s_1-\rho, s_1+\rho]$ centered at the point s, plus the remaining part $\mathcal{F}-[s_1-\rho,s_1+\rho]$. The small distance ρ being fixed, in the integral over $\mathcal{F}-[s_1-\rho,s_1+\rho]$, uniform convergence of $\sqrt{2\pi/r_1}\;h(s_1,r_1;s)$ toward $4Z(s_1,s)$ for $r_1\to 0^+$ ensures that in this limit, the former quantity may safely be replaced by the latter. Furthermore for small ρ, the limit of the remaining integral over $[s_1-\rho,s_1+\rho]$ may be evaluated by replacing the CFWF $h(s_1,r_1;s)$ by its value for a semi-infinite crack in an infinite body. The reader is referred to Favier et al. (2006) for details. The result reads in the

limit $\rho \to 0^+$:

$$\delta K(s_1) = PV \int_{\mathcal{F}} Z(s_1, s) K^0(s) \phi(s)\, ds = \frac{1}{2\pi} PV \int_{\mathcal{F}} \frac{W(s_1, s)}{D^2(s_1, s)} K^0(s) \phi(s)\, ds \tag{58}$$

where the symbol PV denotes a Cauchy principal value.

We now consider *the general case where* $\phi(s_1) \neq 0$. One difficulty is that equation (56) may no longer be deduced in this simple form from equation (55), because the distance r_1 from the perturbed front to the point of observation of $[\![u]\!]$ varies with the perturbation, and its differentiation introduces an extra (singular) term in the expression of $\delta[\![u]\!]$, which is not easily dealt with. An astute remedy to this problem was proposed by Rice (1985, 1989). It consists in assuming the existence of a special perturbation $\phi_*(s)$ of the front taking the same value as $\phi(s)$ at the point s_1, and for which the value $\delta_* K(s_1)$ of the variation of the local SIF is known from some independent argument. The original perturbation $\phi(s)$ is then considered as the sum of this special perturbation and the perturbation $\phi(s) - \phi_*(s)$, which vanishes at the point s_1. Application of formula (58) to the last perturbation then yields

$$\begin{aligned} \delta K(s_1) &= \delta_* K(s_1) + PV \int_{\mathcal{F}} Z(s_1, s) K^0(s) [\phi(s) - \phi_*(s)]\, ds \\ &= \delta_* K(s_1) + \frac{1}{2\pi} PV \int_{\mathcal{F}} W(s_1, s) K^0(s) \frac{\phi(s) - \phi_*(s)}{D^2(s_1, s)}\, ds. \end{aligned} \tag{59}$$

Equation (59) will be referred to as *Rice's first formula* (for the variation of the SIF) in the sequel.

Variation of the fundamental kernel. We again follow here the work of Rice (1989), completed by Favier et al. (2006). The FK $Z(s_1, s)$ being itself related to the SIF generated on the crack front by a special loading, the expression of its variation may be derived similarly to that of the variation of the SIF.

Assume in a first step that *the points* s_1 *and* s_2 *of the crack front remain immobile in the perturbation*: $\phi(s_1) = \phi(s_2) = 0$. Consider the loading consisting of a pair of point forces of unit intensity parallel to $\pm \mathbf{e}_y$ (orthogonal to the crack surface), applied at the points $(s_1, r_1)^{\pm}$ of the crack faces, zero surface tractions and displacements being simultaneously imposed on $\partial\Omega_T$ and $\partial\Omega_u$. The SIF at an arbitrary point s of the crack front is then by definition $h(s_1, r_1; s)$, so that its first-order variation at the point s_2 generated by the perturbation is, by equation (58) (which is applicable since $\phi(s_2) = 0$):

$$\delta h(s_1, r_1; s_2) = PV \int_{\mathcal{F}} Z(s_2, s) h(s_1, r_1; s) \phi(s)\, ds. \tag{60}$$

Now by Eq. (52), the relation

$$h(s_1, r_1; s_2) \sim 4Z(s_1, s_2)\sqrt{\frac{r_1}{2\pi}},$$

valid for small r_1, holds for all (small) values of the amplitude of the perturbation. Since the point s_1 of the front remains fixed in the perturbation, the distance r_1 from this point to those where the forces are applied remains constant; hence it follows from the preceding equation that

$$\delta h(s_1, r_1; s_2) \sim 4\,\delta Z(s_1, s_2)\sqrt{\frac{r_1}{2\pi}}$$

which implies that

$$\begin{aligned}\delta Z(s_1, s_2) &= \frac{1}{4}\lim_{r_1\to 0^+}\sqrt{\frac{2\pi}{r_1}}\,\delta h(s_1, r_1; s_2)\\ &= \frac{1}{4}\lim_{r_1\to 0^+}\sqrt{\frac{2\pi}{r_1}}\,PV\int_{\mathcal{F}} Z(s_2, s)h(s_1, r_1; s)\phi(s)\,ds\end{aligned} \tag{61}$$

where equation (60) has been used. The calculation of the limit here follows the same lines as that of the limit in equation (57), and the result reads

$$\delta Z(s_1, s_2) = PV\int_{\mathcal{F}} Z(s_1, s)Z(s, s_2)\phi(s)\,ds \tag{62}$$

where the symmetry relation (54) has been used; equivalently in terms of the function $W(s_1, s_2)$,

$$\delta W(s_1, s_2) = \frac{D^2(s_1, s_2)}{2\pi}\,PV\int_{\mathcal{F}} \frac{W(s_1, s)}{D^2(s_1, s)}\,\frac{W(s, s_2)}{D^2(s, s_2)}\,\phi(s)\,ds. \tag{63}$$

Note that there are in fact *two* principal values in the integrals of equations (62) and (63), at the points $s = s_1$ and $s = s_2$ respectively.

We now consider *the general case where* $\phi(s_1) \neq 0$, $\phi(s_2) \neq 0$. Following again Rice (1989), we assume that there exists a special perturbation $\phi_{**}(s)$ of the front taking the same value as $\phi(s)$ at the points s_1 and s_2, and for which the variation $\delta_{**}Z(s_1, s_2)$ of $Z(s_1, s_2)$, or the variation $\delta_{**}W(s_1, s_2)$ of $W(s_1, s_2)$, is known from some independent argument. Decomposing $\phi(s)$ as $\phi_{**}(s) + [\phi(s) - \phi_{**}(s)]$ and applying equation (62) to the perturbation $\phi(s) - \phi_{**}(s)$ which vanishes at s_1 and s_2, we get

$$\delta Z(s_1, s_2) = \delta_{**}Z(s_1, s_2) + PV\int_{\mathcal{F}} Z(s_1, s)Z(s, s_2)[\phi(s) - \phi_{**}(s)]\,ds \tag{64}$$

or equivalently

$$\delta W(s_1, s_2) = \delta_{**} W(s_1, s_2) + \frac{D^2(s_1, s_2)}{2\pi} PV \int_{\mathcal{F}} \frac{W(s_1, s)}{D^2(s_1, s)} \frac{W(s, s_2)}{D^2(s, s_2)} [\phi(s) - \phi_{**}(s)] \, ds. \quad (65)$$

Equation (64) or its equivalent form (65) will be referred to as *Rice's second formula* (for the variation of the FK) in the sequel.

3.4 First- and Second-Order Perturbation of a Semi-infinite Mode I Crack in an Infinite Body

In this subsection we consider the simplest example of a semi-infinite tensile crack embedded in some infinite body, in which case the geometry does not involve any characteristic lengthscale.

Preliminaries. The cracked geometry is schematized in Fig. 17. The loading, which is symmetric with respect to the crack plane and thus generates a state of pure mode I at every point of the crack front, consists only of forces imposed at various locations in the body and/or on the crack faces (no prescribed displacements). Following the usual convention, the origin O of the Cartesian system of coordinates is chosen arbitrarily somewhere on the crack plane, the direction x is taken parallel to the direction of propagation, the direction y orthogonal to the crack plane, and the direction z parallel to the crack front. This front is slightly perturbed within the crack plane, its equation in this plane being of the form

$$x(z) = \ell + \phi(z) = \ell + \eta \bar{\phi}(z) \quad (66)$$

where ℓ denotes the distance from the Oz axis to some "reference straight front", and the meaning of the symbols η, $\phi(z)$ and $\bar{\phi}(z)$ is the same as above. The position of the crack front within the crack plane is thus characterized by the parameters ℓ and η, and the position of a current point on this front by the parameter z.

We are interested in the second-order expansion of the perturbed mode I SIF, $K(\ell, \eta; z)$, and the first-order expansion of the perturbed mode I FK, $Z(\eta; z_1, z_2)$, in powers of η:

$$\begin{cases} K(\ell, \eta; z) & \equiv K^0(\ell) + K^1(\ell; z)\, \eta + K^2(\ell; z)\, \eta^2 + O(\eta^3) \\ Z(\eta; z_1, z_2) & \equiv Z^0(z_1, z_2) + Z^1(z_1, z_2)\, \eta + O(\eta^2). \end{cases} \quad (67)$$

It is assumed here for simplicity that the loading has a translatory invariance in the direction z of the crack front, so that the unperturbed SIF $K^0(\ell)$ is independent of the position z of its point of observation on this front. Also, the value of the unperturbed

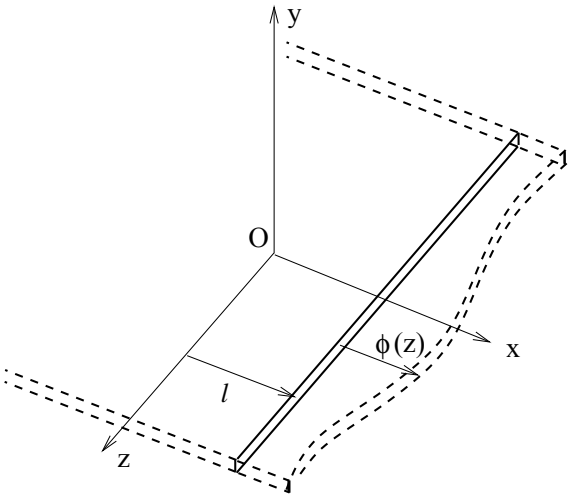

Fig. 17 Coplanar perturbation of a semi-infinite crack in an infinite 3D body

FK for a semi-infinite crack in an infinite body is Rice (1985, 1989)

$$W^0(z_1, z_2) = 1 \quad \Leftrightarrow \quad Z^0(z_1, z_2) = \frac{1}{2\pi(z_1 - z_2)^2}\,. \tag{68}$$

The invariance of the problem in translatory motions along the direction z of the crack front will make it convenient to use Fourier transforms of functions in this direction. The definition adopted here for the transform $\widehat{\chi}(k)$ of an arbitrary function $\chi(z)$ will be

$$\chi(z) \equiv \int_{-\infty}^{+\infty} \widehat{\chi}(k) e^{ikz} dk \quad \Leftrightarrow \quad \widehat{\chi}(k) \equiv \frac{1}{2\pi} \int_{-\infty}^{+\infty} \chi(z) e^{-ikz} dz. \tag{69}$$

First-order variation of the stress intensity factor. The first-order variation of the SIF, $K^1(\ell; z)\,\eta$, may directly be obtained from Rice's first formula (59) by choosing, for the auxiliary perturbation $\phi_*(s) \equiv \phi_*(z)$, a translatory motion of the front in the direction x bringing the point $s_1 \equiv z_1$ to its correct position in the perturbation $\phi(z)$: $\phi_*(z) \equiv \phi(z_1)$, $\forall z$. For such a perturbation the first-order variation of the SIF is $\delta_* K(\ell; z_1) \equiv \frac{dK^0}{d\ell}(\ell)\,\phi(z_1)$ where $\frac{dK^0}{d\ell}(\ell)$ denotes the—supposedly known—derivative of the unperturbed SIF $K^0(\ell)$ with respect to the crack advance. Thus, by Eqs. (68), (59) becomes:

$$K^1(\ell; z_1)\,\eta = \frac{dK^0}{d\ell}(\ell)\,\phi(z_1) + \frac{1}{2\pi}\,PV\int_{-\infty}^{+\infty} K^0(\ell)\,\frac{\phi(z)-\phi(z_1)}{(z-z_1)^2}\,dz$$
$$= \frac{dK^0}{d\ell}(\ell)\,\phi(z_1) + \frac{1}{2\pi}\,PV\int_{-\infty}^{+\infty} K^0(\ell)\,\frac{\phi'(z)}{z-z_1}\,dz \tag{70}$$

where an integration by parts has been used to obtain the second expression.

With the definition (69), one easily gets the following classical expression of the Fourier transform $\widehat{K^1}(\ell; k)\,\eta$ of the first-order variation $K^1(\ell; z_1)\,\eta$, see e.g. Chopin et al. (2011):

$$\widehat{K^1}(\ell; k)\,\eta = \left[\frac{dK^0}{d\ell}(\ell) - K^0(\ell)\frac{|k|}{2}\right]\widehat{\phi}(k). \tag{71}$$

First-order variation of the fundamental kernel. To obtain the first-order variation $Z^1(z_1, z_2)\,\eta$ of the FK from Rice's second formula (64), we may choose, for the auxiliary perturbation $\phi_{**}(s) \equiv \phi_{**}(z)$, a suitable combination of a translatory motion and a rotation of the front bringing points z_1 and z_2 to their correct positions in the perturbation $\phi(z)$; this auxiliary perturbation is given by the equivalent formulae

$$\phi_{**}(z) \equiv \phi(z_1) + \frac{\phi(z_2)-\phi(z_1)}{z_2-z_1}\,(z-z_1) \equiv \phi(z_2) + \frac{\phi(z_1)-\phi(z_2)}{z_1-z_2}\,(z-z_2)\,. \tag{72}$$

Such a motion of the crack front preserves its straight shape and the distances along it (to first order in η), so that it leaves the FK unchanged, $\delta_{**}Z(s_1, s_2) = 0$. Rice's second formula (64) then takes—after some transformations—the following form Leblond et al. (2012):

$$Z^1(z_1, z_2)\,\eta = \frac{1}{4\pi^2(z_1-z_2)^2}\,PV\int_{-\infty}^{+\infty}\left[\left(\frac{1}{z-z_1}+\frac{1}{z-z_2}\right)\phi'(z)\right.$$
$$\left.+\frac{2}{z_1-z_2}\left(\frac{1}{z-z_2}-\frac{1}{z-z_1}\right)\phi(z)\right]dz. \tag{73}$$

Second-order variation of the stress intensity factor. To determine the second-order variation $K^2(\ell; z)\,\eta^2$, we follow the approach of Leblond et al. (2012) and Vasoya et al. (2013). The principle consists in considering a primary perturbation of the front of the form $\phi(z) = \eta\bar{\phi}(z)$, upon which is added a secondary perturbation

$$d\phi(z) \equiv \bar{\phi}(z)d\eta \tag{74}$$

having the *same* function $\bar{\phi}(z)$ as the primary one, but some *infinitesimal* amplitude $d\eta$. Then Rice's first formula (59), applied to the variation of the SIF resulting from the *additional* perturbation, provides upon division by $d\eta$ the value of the derivative $(\partial K/\partial\eta)(\ell, \eta; z_1)$. The formula involves the values of the SIF and FK on the primar-

ily perturbed configuration of the front. If expressions of these quantities accurate to first order in η are used, the result is the first-order expression of $(\partial K/\partial\eta)(\ell,\eta;z_1)$. The second-order expression of $K(\ell,\eta;z_1)$ then follows through integration on η.

More precisely, the expression of $(\partial K/\partial\eta)(\ell,\eta;z_1)$ obtained in this way is easily seen to be

$$\begin{aligned}
&\frac{\partial K}{\partial\eta}(\ell,\eta;z_1)=\frac{\partial}{\partial\ell}\left[K^0(\ell)+K^1(\ell;z_1)\,\eta\right]\bar\phi(z_1)+\\
&PV\int_{-\infty}^{+\infty}\left[Z^0(z_1,z)+Z^1(z_1,z)\eta\right]\left[K^0(\ell)+K^1(\ell;z_1)\eta\right]\left[\bar\phi(z)-\bar\phi(z_1)\right]dz\\
&=\frac{dK^0}{d\ell}(\ell)\,\bar\phi(z_1)+PV\int_{-\infty}^{+\infty}Z^0(z_1,z)K^0(\ell)\left[\bar\phi(z)-\bar\phi(z_1)\right]dz+\\
&\left\{\frac{\partial K^1}{\partial\ell}(\ell;z_1)\,\bar\phi(z_1)\right.\\
&\left.+PV\int_{-\infty}^{+\infty}\left[Z^0(z_1,z)K^1(\ell;z)+Z^1(z_1,z)K^0(\ell)\right]\left[\bar\phi(z)-\bar\phi(z_1)\right]dz\right\}\eta
\end{aligned}$$

at the first order in η. Integrating with respect to η and identifying the term proportional to η^2, one gets the second-order variation of the SIF:

$$\begin{aligned}
&K^2(\ell;z_1)\,\eta^2=\left\{\frac{\partial K^1}{\partial\ell}(\ell;z_1)\,\bar\phi(z_1)\right.\\
&\left.+PV\int_{-\infty}^{+\infty}\left[Z^0(z_1,z)K^1(\ell;z)+Z^1(z_1,z)K^0(\ell)\right]\left[\bar\phi(z)-\bar\phi(z_1)\right]dz\right\}\frac{\eta^2}{2}\\
&=\frac{1}{2}\,\frac{\partial K^1}{\partial\ell}(\ell;z_1)\eta\,\phi(z_1)\\
&+\frac{1}{2}\,PV\int_{-\infty}^{+\infty}\left[Z^0(z_1,z)\,K^1(\ell;z)\eta+Z^1(z_1,z)\eta\,K^0(\ell)\right]\left[\phi(z)-\phi(z_1)\right]dz.
\end{aligned}$$

Accounting for the expressions (70) of $K^1(\ell;z_1)\,\eta$ and (73) of $Z^1(z_1,z_2)\,\eta$, one gets from there the final expression of $K^2(\ell;z_1)\,\eta^2$ (Vasoya et al. 2013):

$$K^2(\ell;z_1)\,\eta^2 = \frac{1}{2}\frac{d^2K^0}{d\ell^2}(\ell)\,[\phi(z_1)]^2 + \frac{1}{2\pi}\frac{dK^0}{d\ell}(\ell)\,PV\int_{\mathcal{F}}\frac{\phi(z)\phi'(z)}{z-z_1}\,dz$$
$$+\frac{K^0(\ell)}{8\pi^2}\,PV\int_{-\infty}^{+\infty}\int_{-\infty}^{+\infty}\left[\left(\frac{1}{z'-z_1}+\frac{2}{z'-z}\right)\phi'(z')\right. \tag{75}$$
$$\left.+\frac{2}{z-z_1}\left(\frac{1}{z'-z_1}-\frac{1}{z'-z}\right)\phi(z')\right]\frac{\phi(z)-\phi(z_1)}{(z-z_1)^2}\,dz\,dz'.$$

Again, the expression of this variation will be needed in Fourier's space. This expression was derived by Vasoya et al. (2016b) and reads

$$\widehat{K^2}(\ell;k_1)\,\eta^2 = \int_{-\infty}^{+\infty} R(\ell;k,k_1-k)\widehat{\phi}(k)\widehat{\phi}(k_1-k)\,dk \tag{76}$$

where

$$R(\ell;k,k') \equiv \frac{1}{2}\frac{d^2K^0}{d\ell^2}(\ell) - \frac{1}{4}\frac{dK^0}{d\ell}(\ell)|k+k'|$$
$$+\frac{K^0(\ell)}{16}\left[2|k+k'|\left(|k|+|k'|\right)-(k+k')^2-k^2-k'^2\right]. \tag{77}$$

In Sect. 3.7 below, it will be shown how to extend formulae (71) and (76) for the first- and second-order variations of the SIF for a perturbed semi-infinite crack in an infinite body, to a crack lying on the mid-plane of a plate of arbitrary thickness. In Sect. 3.8, the extended formulae will be applied to the predition of the deformation of a crack front encountering a harder obstacle, with some comparisons with experimental observations.

3.5 *Perturbation of a Mode I Slit-Crack in an Infinite Body*

To initiate the study of the influence of the finite dimensions of the body and/or the crack, we now consider the simplest possible cracked geometry introducing a characteristic lengthscale, namely a tensile slit- (or tunnel-) crack of finite width $2a$ in an infinite body. The case of a semi-infinite crack envisaged in the previous subsection will be recovered in the limit $a \to +\infty$.

Preliminaries. The situation considered is depicted in Fig. 18. The crack lies on the plane $y = 0$, and the fore and rear parts of the front are parallel straight lines of equation $x = a$ and $x = -a$ respectively. The position of a point on the front is specified through the Cartesian coordinate $z^{\pm}$, equipped with an upper index indicating whether it belongs to the fore $(+)$ or rear $(-)$ part of this front. The crack is loaded in pure mode I at every point of its front through some uniform stress σ^{∞}_{yy} (orthogonal to

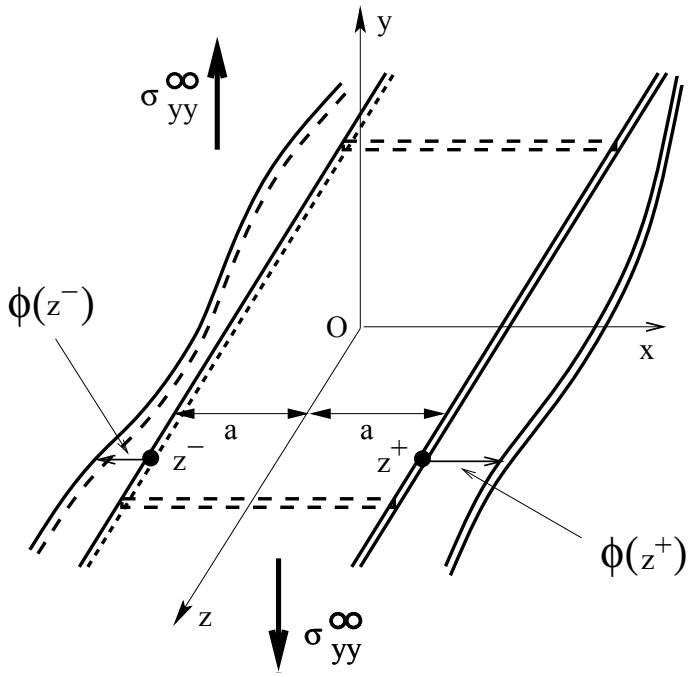

Fig. 18 A tensile slit-crack in an infinite 3D body

the crack plane) applied remotely. The fore and rear parts of the front are perturbed within the plane $y = 0$. The small crack advance is denoted $\phi(z^+)$ on the fore part of the front and $\phi(z^-)$ on its rear part. (Note that $\phi(z^+)$ is counted positively toward the right, whereas $\phi(z^-)$ is counted positively toward the left).

The only geometric parameter in the problem is the half-width a of the crack; the influence of the geometry upon the FK thus reduces to a dependence of this kernel upon this half-width. Also, simple dimensional considerations show that the functions $Z(s_1, s) \equiv Z(a; z_1^{\pm}, z^{\pm})$ and $W(s_1, s) \equiv W(a; z_1^{\pm}, z^{\pm})$ are positively homogeneous of degree -2 and 0, respectively, with respect to the arguments a, z_1, z. Finally, the problem is invariant in translatory motions in the direction z of the crack front, and symmetries about the two coordinate planes Oxy and Oyz. One concludes from these elements that the FK may be written in the form

$$\left\{\begin{array}{l} Z(a; z_1^+, z^+) \equiv Z(a; z_1^-, z^-) \equiv \dfrac{f\,[(z_1 - z)/a]}{(z_1 - z)^2} \quad \text{or equivalently} \\ W(a; z_1^+, z^+) \equiv W(a; z_1^-, z^-) \equiv 2\pi f\,[(z_1 - z)/a]\ ; \\ \\ Z(a; z_1^+, z^-) \equiv Z(a; z_1^-, z^+) \equiv \dfrac{g\,[(z_1 - z)/a]}{a^2} \end{array}\right. \tag{78}$$

where f and g are *even* functions called the *components of the FK* in the sequel. (Note that the evenness of these functions, a consequence of the symmetry about the plane Oxy, also results from the general symmetry relations (54)). The function f satisfies the property

$$f(0) = \frac{1}{2\pi} \tag{79}$$

resulting from the fact that in the limit $a \to +\infty$, the FK $Z(a; z_1^+, z^+)$ must reduce to that for a semi-infinite crack, that is $\frac{1}{2\pi(z_1-z)^2}$ (Eq. (68)).

To apply Rice's first formula (59) for the variation of the SIF at the point z_1^+ of the fore part of the crack front, we may choose, for the auxiliary perturbation $\phi_*(s) \equiv \phi_*(z)$, a translatory motion of this fore part bringing the point z_1^+ to its correct position in the perturbation $\phi(z)$, while leaving the rear part unaffected: $\phi_*(z^+) \equiv \phi(z_1^+)$, $\phi_*(z^-) \equiv 0$, $\forall z$. In this auxiliary perturbation, the half-width a of the crack increases by $\phi(z_1^+)/2$ so that the initial SIF $K^0(a) \equiv \sigma_{yy}^\infty \sqrt{\pi a}$ becomes $\sigma_{yy}^\infty \sqrt{\pi[a + \phi(z_1^+)/2]} = \sigma_{yy}^\infty \sqrt{\pi a}\,[1 + \phi(z_1^+)/(4a)]$ to first order in $\phi(z_1^+)$; from which follows that $\delta_* K(z_1^+) = K^0(a)\,\phi(z_1^+)/(4a)$. Rice's first formula (59) then takes the form, upon division by $K^0(a)$:

$$\begin{aligned} \frac{\delta K(a; z_1^+)}{K^0(a)} = \frac{\phi(z_1^+)}{4a} + PV \int_{-\infty}^{+\infty} f\left(\frac{z_1 - z}{a}\right) \frac{\phi(z^+) - \phi(z_1^+)}{(z - z_1)^2}\, dz \\ + \int_{-\infty}^{+\infty} g\left(\frac{z_1 - z}{a}\right) \frac{\phi(z^-)}{a^2}\, dz\,. \end{aligned} \tag{80}$$

A property of the function g may be derived by considering a special motion of the front, in which the fore part remains immobile while the rear part recedes by some small, constant distance: $\phi(z^+) \equiv 0$, $\phi(z^-) \equiv Cst. \equiv \eta$, $\forall z$. By the same reasoning as before, $\delta K(a; z_1^+)/K^0(a) = \eta/(4a)$; on the other hand the expression (80) of $\delta K(a; z_1^+)/K^0(a)$ reduces to the last term involving g. Comparison of these two expressions yields

$$\int_{-\infty}^{+\infty} g(u)\, du = \frac{1}{4} \tag{81}$$

where the change of variable $u \equiv (z_1 - z)/a$ has been used.

Again, we shall make use of Fourier transforms $\widehat{\chi}(k)$ of functions $\chi(z)$ in the direction z of the crack front, as defined by equation (69). Also, we shall use "reduced", dimensionless distances u and wavenumbers p along this direction, obtained from real distances and wavenumbers through division and multiplication by a, respectively; the Fourier transform $\widehat{\chi}(p)$ of a function $\chi(u)$ will again be defined by formula (69), with the substitutions $z \to u$, $k \to p$.

Integrodifferential equations on the components of the fundamental kernel. We now proceed to the calculation of the components, f and g, of the FK. A general method of calculation, based on an integral equation of Bui (1978), was proposed in Mouchrif (1994)s thesis. Leblond et al. (1996)s special method, presented here, is more economical and yield identical results.

Leblond et al. (1996)s special method is based on Rice's second formula (64) for the variation of the FK. Rice (1989)s own view was that this formula could be employed to determine the FK for new crack shapes through numerical integration, starting from some reference shape for which it would be known. We use it here in a different way: instead of generating new crack shapes, we consider only motions preserving the original shape of the crack, though possibly modifying its size and orientation. This procedure yields integro-differential equations on the components of the FK, the solution of which provides these components.

Consider first, like above, a translatory motion of the sole rear part of the crack front, defined by $\phi(z^+) \equiv 0$, $\phi(z^-) \equiv \eta$, $\forall z$, where η is a small parameter (Fig. 19). To apply Rice's second formula (64) at two points z_1^+, z_2^+ of the fore part of the front, where ϕ is zero, one may take a zero auxiliary perturbation $\phi_{**}(z)$. One gets, accounting for equations (78):

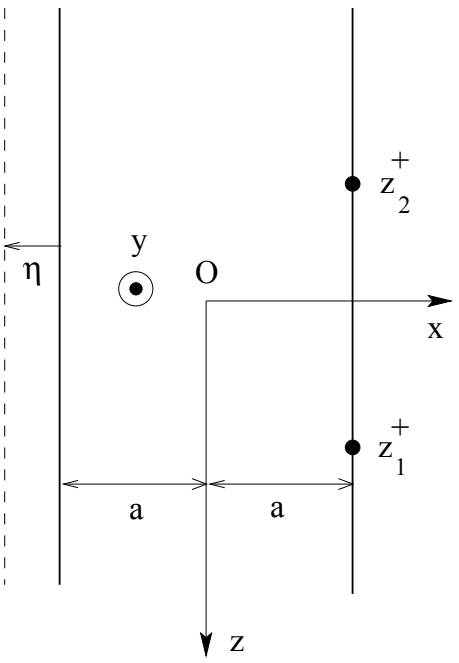

Fig. 19 Translatory motion of the rear part of the crack front

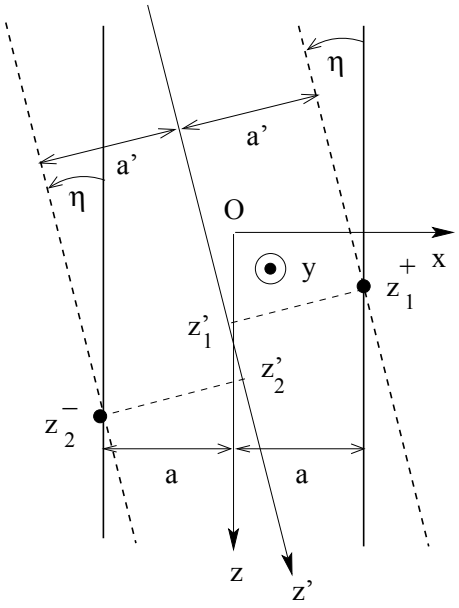

Fig. 20 Rotation of both parts of the crack front by the same angle

$$\frac{\partial}{\partial\eta}\left\{\frac{f[(z_1-z_2)/(a+\eta/2)]}{(z_1-z_2)^2}\right\}_{|_{\eta=0}}\eta=\int_{-\infty}^{+\infty}\frac{g[(z_1-z)/a]}{a^2}\,\frac{g[(z-z_2)/a]}{a^2}\,\eta\,dz$$

or equivalently using the changes of variable $u_1\equiv(z_1-z_2)/a$, $u\equiv(z_1-z)/a$:

$$f'(u_1)=-2u_1\int_{-\infty}^{+\infty}g(u_1-u)g(u)\,du. \tag{82}$$

Now consider a perturbation of the crack front defined by a rotation of its fore and rear parts by the same small angle η about the points z_1^+ and z_2^- (Fig. 20). To apply Rice's second formula (64) at the points z_1^+, z_2^-, where again ϕ is zero, we may again take a zero auxiliary perturbation $\phi_{**}(z)$, getting thus

$$\begin{aligned}\frac{\partial}{\partial\eta}\left\{\frac{g[(z_1'-z_2')/a']}{a'^2}\right\}_{|_{\eta=0}}\eta&\\ =PV\int_{-\infty}^{+\infty}\frac{f[(z_1-z)/a]}{(z_1-z)^2}\,\frac{g[(z-z_2)/a]}{a^2}\,\eta(z-z_1)\,dz&\\ +PV\int_{-\infty}^{+\infty}\frac{g[(z_1-z)/a]}{a^2}\,\frac{f[(z-z_2)/a]}{(z-z_2)^2}\,\eta(z_2-z)\,dz&\end{aligned}$$

where z_1' and z_2' denote the abscissae of the projections of the points z_1^+, z_2^- onto an axis parallel to the new crack front, and a' the new half-width of the crack (Fig. 20). Now it is easy to see that to first order in η,

$$a' = a - \frac{z_1 - z_2}{2}\,\eta \quad ; \quad z_1' - z_2' = z_1 - z_2 + 2a\eta,$$

and it then follows, upon use of the same changes of variables as above, that the preceding equation reads

$$\left[\left(1 + \frac{u_1^2}{4}\right) g(u_1)\right]' = -PV \int_{-\infty}^{+\infty} g(u_1 - u)\,\frac{f(u)}{u}\,du. \tag{83}$$

Solution of integrodifferential equations in Fourier's space. In this subsubsection and the next we shall exceptionally use, in addition to the Fourier transform defined by equation (69), a variant defined, for any function $\chi(u)$, by the formula[10]

$$\overline{\chi}(p) \equiv 2\pi\widehat{\chi}(-p) = \int_{-\infty}^{+\infty} \chi(u) e^{ipu} du. \tag{84}$$

Taking the Fourier transform of equations (82) and (83) is easy for the former, a bit more difficult for the latter, see details in Leblond et al. (1996). The resulting equations read

$$\begin{cases} p\overline{f}(p) & = -4\overline{g}(p)\overline{g}'(p) \\ p\left[\overline{g}(p) - \dfrac{\overline{g}''(p)}{4}\right] & = \overline{F}(p)\overline{g}(p) \end{cases} \tag{85}$$

where

$$\overline{F}(p) \equiv \int_0^p \overline{f}(p')\,dp'. \tag{86}$$

One remarkable feature of the system (85) of ordinary differential equations is that it may be explicitly integrated once with respect to p. Indeed multiplying equation $(85)_2$ by $\overline{g}'(p)/p$, and replacing $\overline{g}(p)\overline{g}'(p)/p$ by $-\overline{f}(p)/4 = -\overline{F}'(p)/4$ in the right-hand side, thanks to equation $(85)_1$, we get

$$\overline{g}(p)\overline{g}'(p) - \frac{\overline{g}'(p)\overline{g}''(p)}{4} = -\frac{\overline{F}(p)\overline{F}'(p)}{4} \quad \Rightarrow \quad \frac{\overline{g}^2(p)}{2} - \frac{\overline{g}'^2(p)}{8} + \frac{\overline{F}^2(p)}{8} = Cst.$$

[10] In other subsubsections the definition (69) leads to the simplest possible expression of the second-order variation of the SIF, devoid of cumbersome factors of 2π; but conversely in this subsubsection use of this definition would generate such factors in nearly all equations.

Now at the point $p = 0$, $\overline{g}(0) = 1/4$ by equation (81), $\overline{g}'(0) = 0$ since $\overline{g}$ is an even function like g, and $\overline{F}(0) = 0$; hence the value of the constant is $1/32$ so that

$$4\overline{g}^2(p) - \overline{g}'^2(p) + \overline{F}^2(p) = \frac{1}{4} \quad \Rightarrow \quad \overline{F}(p) = \mathrm{sgn}(p)\left[\frac{1}{4} - 4\overline{g}^2(p) + \overline{g}'^2(p)\right]^{1/2} \tag{87}$$

where $\mathrm{sgn}(p)$ denotes the sign of p. The choice of the sign here results from the fact that for obvious physical reasons, f and $\overline{f}$ must be positive, "bell-shaped" functions, so that the sign of $\overline{F}$ must be the same as that of p.

Eliminating then $\overline{F}$ in Eq. $(85)_2$ thanks to equation (87), one gets the remarkable equation

$$\overline{g}''(p) = 4\overline{g}(p)\left\{1 - \frac{1}{|p|}\left[\frac{1}{4} - 4\overline{g}^2(p) + \overline{g}'^2(p)\right]^{1/2}\right\}. \tag{88}$$

Equation (88) is a second-order, nonlinear ordinary differential equation on the sole function $\overline{g}$, which may be solved numerically for positive values of p using the initial conditions $\overline{g}(0) = 1/4, \overline{g}'(0) = 0$; values of this function over the entire real line then follow from its evenness. The values of $\overline{f}$ then follow from equation $(85)_1$, and those of the functions f and g through inverse Fourier transform. All this may be done once and for all, since the functions do not depend on any parameter other than their argument u or p.

Figure 21 shows the functions $f(u)$ and $g(u)$ obtained finally (for positive values of their argument only, since they are even). The numerical values may be completed

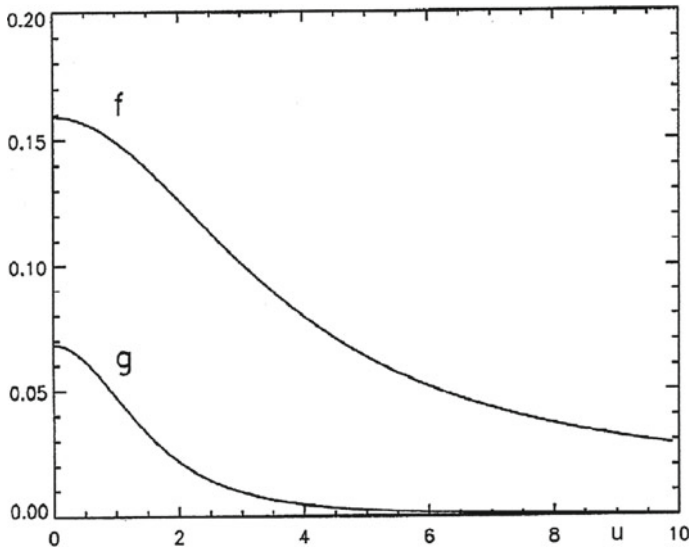

Fig. 21 The functions $f(u)$ and $g(u)$

by asymptotic expressions of the functions near zero and infinity, see Leblond et al. (1996).

3.6 Application 1: Configurational Stability of the Front of an Expanding Mode I Slit-Crack

As an interesting application of the preceding results, we shall now—following again Leblond et al. (1996)—investigate the following problem of bifurcation and configurational stability of the crack front. The fracture toughness of the material being assumed to be homogeneous, do the two parts of the front of the slit-crack necessarily remain straight as it expands, or can they become curved—in other words, can one find configurations of the two parts of the crack fronts, other than the trivial straight ones, warranting satisfaction of Griffith (1920)s criterion everywhere on these two parts (bifurcation problem)? And if the answer is yes, does a given perturbation of the front increase or decay as the crack expands (configurational stability problem)?

The bifurcation problem is equivalent to looking for perturbations $\phi(z^+)$, $\phi(z^-)$ of the fore and rear parts of the fronts generating zero perturbations $\delta K(a; z_1^+)$, $\delta K(a; z_1^-)$ of the SIF on them. It will be solved with the aid of the Fourier transform, denoting $\widehat{\delta K}^+(a;k)$, $\widehat{\delta K}^-(a;k)$, $\widehat{\phi}^+(k)$, $\widehat{\phi}^-(k)$ the Fourier transforms of the functions $\delta K(a; z_1^+)$, $\delta K(a; z_1^-)$, $\phi(z^+)$, $\phi(z^-)$. The Fourier transform of the expression (80) of the variation of the SIF on the fore part of the front, duly completed by an analogous expression on its rear part, reads (Leblond et al. 1996):[11]

$$\begin{cases} \dfrac{\widehat{\delta K}^+(a;k)}{K^0(a)} = \dfrac{1}{a}\left[\overline{\mathcal{F}}(ka)\widehat{\phi}^+(k) + \overline{g}(ka)\widehat{\phi}^-(k)\right] \\ \dfrac{\widehat{\delta K}^-(a;k)}{K^0(a)} = \dfrac{1}{a}\left[\overline{g}(ka)\widehat{\phi}^+(k) + \overline{\mathcal{F}}(ka)\widehat{\phi}^-(k)\right] \\ \overline{\mathcal{F}}(p) \equiv \dfrac{1}{4} - \displaystyle\int_0^p \overline{F}(p')\,dp'. \end{cases} \tag{89}$$

Now we are looking for a perturbation for which $\widehat{\delta K}^+(a;k)$ and $\widehat{\delta K}^-(a;k)$ are both zero for all values of k. For fixed k, equations (89) then provide a linear, homogeneous system in $\widehat{\phi}^+(k)$ and $\widehat{\phi}^-(k)$, the solution of which is non-trivial if and only if

$$\overline{\mathcal{F}}^2(ka) - \overline{g}^2(ka) = 0$$

or equivalently

[11] In Leblond et al. (1996) our function $\overline{\mathcal{F}}$ is denoted $\overline{f}$, and our function $\overline{f}$ is denoted $\widehat{f}$.

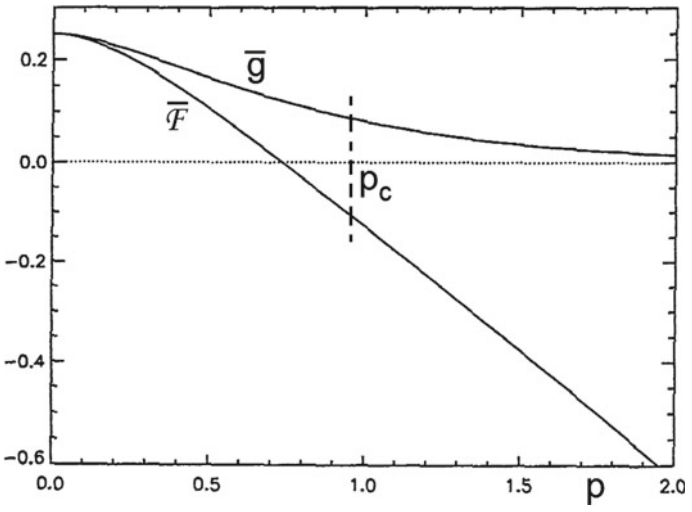

Fig. 22 The functions $\overline{\mathcal{F}}(p)$ and $\overline{g}(p)$

$$\begin{cases} \overline{\mathcal{F}}(ka) + \overline{g}(ka) = 0 \\ \text{or} \\ \overline{\mathcal{F}}(ka) - \overline{g}(ka) = 0. \end{cases} \tag{90}$$

Figure 22 shows the functions $\overline{\mathcal{F}}(p)$ and $\overline{g}(p)$ (again for positive values of their argument only since they are even), as determined numerically from the functions $f(u)$ and $g(u)$ shown in Fig. 21. It follows from the graphs that the solutions of equations $(90)_1$ and $(90)_2$ are

$$\begin{cases} ka = \pm p_c, \ p_c \simeq 0.925 \\ \text{and} \\ ka = 0 \end{cases} \tag{91}$$

respectively.

For the first solution, for which $\overline{\mathcal{F}}(ka) + \overline{g}(ka) = 0$, the system of equations on $\widehat{\phi}^+(k)$ and $\widehat{\phi}^-(k)$ reduces to $\widehat{\phi}^+(k) - \widehat{\phi}^-(k) = 0$, that is $\widehat{\phi}^+(k) = \widehat{\phi}^-(k)$: the bifurcation mode is *symmetric* with respect to the central axis Oz of the crack. For the second solution, for which $\overline{\mathcal{F}}(ka) - \overline{g}(ka) = 0$, the system reduces to $\widehat{\phi}^+(k) + \widehat{\phi}^-(k) = 0$, that is $\widehat{\phi}^+(k) = -\widehat{\phi}^-(k)$: the bifurcation mode is *antisymmetric* with respect to the axis Oz. However since the wavenumber k for this mode is zero, it represents a mere common translatory motion of the two parts of the front in the same direction x; the existence of such a trivial bifurcation mode was obvious from the start, since the position of the crack within its plane has no influence on the SIFs.

The conclusion is that *there exists a non-trivial bifurcation mode, which is symmetric about the central axis Oz of the crack, and sinusoidal of characteristic wavelength*

$$\lambda \equiv \frac{2\pi}{|k|} = \lambda_c \equiv \frac{2\pi a}{p_c} \simeq 6.79\, a. \tag{92}$$

To now solve the associated configurational stability problem, consider an arbitrary symmetric sinusoidal perturbation of the two parts of the crack front, of the form

$$\phi(z^+) = \phi(z^-) = \eta \cos(kz + \theta)$$

where η, k and θ are parameters, the first being small and the second positive. Then by Eqs. (89),

$$\frac{\delta K(a; z^+)}{K^0(a)} = \frac{\delta K(a; z^-)}{K^0(a)} = \left[\overline{\mathcal{F}}(ka) + \overline{g}(ka)\right] \frac{\eta}{a} \cos(kz + \theta).$$

Now it is clear from Fig. 22 that $\overline{\mathcal{F}}(ka) + \overline{g}(ka)$ is positive or negative according to whether ka is smaller or larger than p_c; that is, whether the wavelength $\lambda = 2\pi/k$ of the perturbation is larger or smaller than the critical value λ_c. Thus if λ is larger than λ_c, the maxima of $\delta K(a; z^+) = \delta K(a; z^-)$ coincide with those of $\phi(z^+) = \phi(z^-)$, so that the perturbation of the front must increase; whereas if λ is smaller than λ_c, the maxima of $\delta K(a; z^+) = \delta K(a; z^-)$ coincide with the minima of $\phi(z^+) = \phi(z^-)$, and the perturbation of the front must decay: that is, *instability prevails for wavelengths λ larger than the "threshold" λ_c*.

These various conclusions may be rationalized as follows:

- Consider first a symmetric perturbation of the two parts of the crack front of small wavelength, $\lambda \ll a$ (Fig. 23). The crack advance is maximum at point A and minimum at point B. Draw small circles centered at these points. Because of the local curvature of the crack front, that part of the interior of the circle occupied by the intact material ahead of the crack (hatched in Fig. 23) is larger at point A than at point B; therefore the opening of the crack is hindered more near the first point than near the second. Thus the stress intensity factors $K(A)$, $K(B)$ at points A and B must satisfy the inequality $K(A) < K(B)$.
- Consider now a symmetric perturbation of large wavelength, $\lambda \gg a$, and again points A and B where the crack advance is respectively maximum and minimum (Fig. 24). The stress intensity factors at points A and B are almost the same as for two slit-cracks of uniform width, equal to the local width at these points (indicated by dashed arrows in Fig. 24). It follows that necessarily $K(A) > K(B)$.
- The difference $K(A) - K(B)$ being thus negative for small λ and positive for large λ, some special value λ_c for which $K(A) - K(B)$ vanishes must necessarily exist.

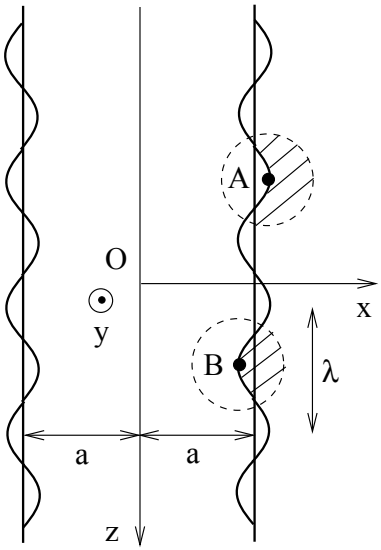

Fig. 23 Crack front perturbation of small wavelength

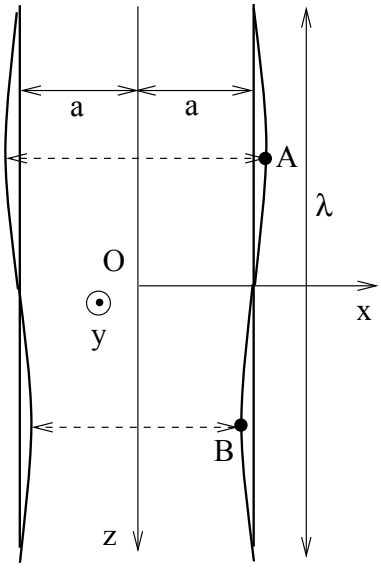

Fig. 24 Crack front perturbation of large wavelength

- These elements explain why the SIF is uniform along the crack front if $\lambda = \lambda_c$, varies in phase with the crack front perturbation if $\lambda > \lambda_c$, and with a 180° phase difference with the perturbation if $\lambda < \lambda_c$. The conclusions on configurational stability of the crack follow from there.

3.7 First- and Second-Order Perturbation of a Semi-infinite Mode I Crack Lying on the Mid-Plane of a Plate

Preliminaries. In this subsection, following Legrand et al. (2011), we shall consider a 3D cracked geometry much closer to some of those used in actual experiments than the highly idealized ones studied previously. Figures 25 and 26 provide two complementary 2D views of this geometry. A semi-infinite plate, made of some isotropic elastic material with Young's modulus E and Poisson's ratio ν, occupies the domain $0 \leq x < +\infty, -h \leq y \leq h, -\infty < z < +\infty$ in the 3D space. This plate contains a plane crack occupying the region $0 \leq x \leq a(z), -\infty < z < +\infty$ in the plane $y = 0$, where

$$a(z) \equiv a + \phi(z) \equiv a + \eta\bar{\phi}(z); \tag{93}$$

in these expressions a denotes the orthogonal distance from the Oz axis to some "reference" straight crack front, and the meaning of the symbols η, $\phi(z)$ and $\bar{\phi}(z)$ is the same as above. At each point M of the actual, perturbed crack front, we define some local axes Mx_1, Mx_2, Mx_3 with Mx_1 perpendicular to the front within the Oxz plane, Mx_2 parallel to the Oy axis and Mx_3 tangent to the front (Fig. 26). The loading consists of uniform, opposite displacements v_0, $-v_0$ in the y direction imposed on the upper and lower halves of the left boundary of the plate (Fig. 25). The crack is thus loaded in a state of pure mode I at all points of its front, and when this front is straight, the mode I SIF $K^0(a)$ is uniform along it.

For plates of arbitrary thickness $2h$, the problem is not amenable to some analytic solution.

It can be solved analytically, however, in the limit of plates of infinitesimal thickness ($h \to 0^+$), using Love-Kirchhoff's plate theory, which is known to be asymptot-

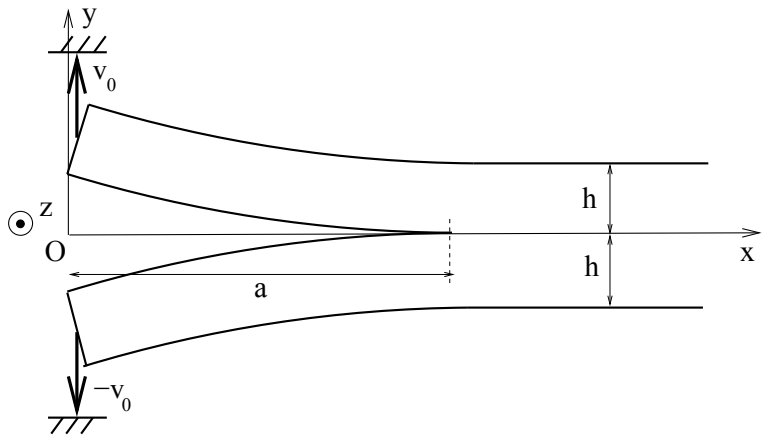

Fig. 25 In-plane perturbation of a crack lying on the mid-plane of a plate with prescribed opening displacement: view in the Oxy plane

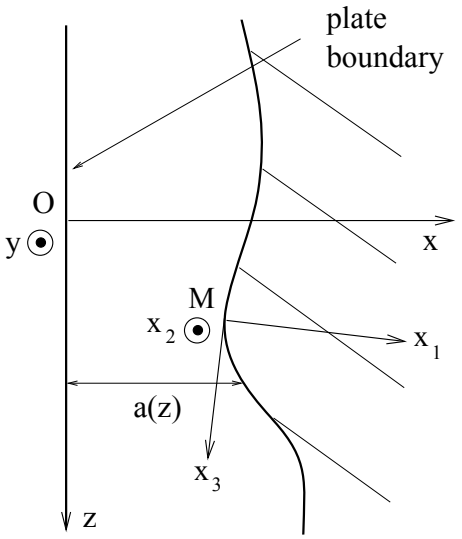

Fig. 26 In-plane perturbation of a crack lying on the mid-plane of a plate with prescribed opening displacement: view in the Oxz plane

ically exact in this limit. This means, exceptionally, using a *general method* providing the full solution rather than a *special method* concentrating on the sole distribution of the SIF along the perturbed crack front.

At the heart of the solution is a relation connecting the out-of-plane displacement $u_2(x_1, x_3) \equiv v(x_1, x_3)$ of the upper half of the plate, behind and near the point M, to the local SIF $K(M) \equiv K(z)$. To derive it, note first that the bonding of the two halves of the plate ahead of the crack front implies that behind and near the point M,

$$v(x_1, x_3 = 0) = \frac{1}{2}\, c_{11}(M) x_1^2 + O(x_1^3) \qquad (x_1 \to 0^-) \tag{94}$$

where $c_{11}(M)$ denotes the "11" component of the curvature tensor $\mathbf{c} \equiv \mathbf{grad}(\mathbf{grad}\, v)$ of the plate at M. The asymptotic behaviour of the out-of-plane displacement v near the crack front thus differs from the usual one characterized by the $\sqrt{-x_1}$ singularity; this is because the Love-Kirchhoff plate theory only provides an "outer" view of the problem disregarding its fully 3D nature near the crack front. This outer view must be completed by an "inner" one wherein distances are magnified in the x_1 and x_2 directions, so as to deal with a plate of *unit* (not infinitesimal) thickness. In such a view the curvature component $c_{11}(M)$ acts as a remote boundary condition, so that owing to linearity, there exists a constant γ such that

$$K(M) = \frac{1}{2\gamma}\, c_{11}(M). \tag{95}$$

Combination of equations (94) and (95) yields the asymptotic expression of $v(x_1, x_3 = 0)$ looked for:

$$v(x_1, x_3 = 0) = \gamma K(M) x_1^2 + O(x_1^3) \qquad (x_1 \to 0^-). \tag{96}$$

Although the precise value of the constant γ will not matter in the sequel, it may be useful in other contexts, so we shall provide it for completeness. The natural way to calculate it would to use formal matched asymptotic expansions to fully solve the inner 3D elasticity problem. A more expedient way of doing so, however, consists in: (i) considering a small advance of the crack front, and evaluating the resulting variation of energy of a small parallelepiped surrounding the point M, using Love-Kirchhoff's plate theory (since it is energetically exact in the limit $h \to 0^+$); (ii) using Irwin (1958)s formula to relate this variation of energy to the local SIF $K(M)$—see details in Legrand et al. (2011). The final result reads:

$$\gamma = \sqrt{3}\,\frac{1-\nu^2}{Eh^{3/2}}. \tag{97}$$

First-order solution for a plate of infinitesimal thickness. To get the full analytical solution for a plate of infinitesimal thickness, we first use Love-Kirchhoff's plate theory to write the equations of the outer problem, for a crack front perturbation of arbitrary amplitude. These equations (vertical equilibrium equation, boundary conditions on the left side of the plate, clamping conditions on the crack front) read

$$\begin{cases} \left(\dfrac{\partial^2}{\partial x^2} + \dfrac{\partial^2}{\partial z^2}\right)^2 v(x,z) = 0 & \text{for } 0 \le x \le a(z),\ -\infty < z < +\infty \\ v(x=0,z) = v_0 \\ \dfrac{\partial^2 v}{\partial x^2}(x=0,z) = 0 & \Big\} \text{ for } -\infty < z < +\infty \\ v[x = a(z), z] = 0 \\ \dfrac{\partial v}{\partial n}[x = a(z), z] = 0 & \Big\} \text{ for } -\infty < z < +\infty \end{cases} \tag{98}$$

where the symbol $\partial/\partial n$ denotes the in-plane normal derivative to the front.

Consider now a crack front perturbation of small amplitude $\phi(z) = \eta\bar{\phi}(z)$, $\eta \to 0^+$, and denote δv the resulting variation, under constant loading $\pm v_0$, of the normal displacement v of the upper half of the plate. Differentiation of equations $(98)_{1,2,3}$ at constant v_0 yields the equilibrium equation and boundary conditions satisfied by δv:

$$\begin{cases} \left(\dfrac{\partial^2}{\partial x^2} + \dfrac{\partial^2}{\partial z^2}\right)^2 \delta v(x,z) = 0 & \text{for } 0 \le x \le a,\ -\infty < z < +\infty \\ \delta v(x=0,z) = 0 \\ \dfrac{\partial^2 \delta v}{\partial x^2}(x=0,z) = 0 & \Big\} \text{ for } -\infty < z < +\infty. \end{cases} \tag{99}$$

The conditions verified by δv on the unperturbed crack front cannot however be obtained in such a simple way. To derive them, it is necessary to write equation (96) for a perturbed crack front in the general frame $Oxyz$, and expand it in powers of the perturbation amplitude η and the distance $a - x$ from the point of observation of v to the point M of the crack front; see details in Legrand et al. (2011). One thus gets the two following conditions:

$$\begin{cases} \delta v(x = a, z) & = 0 \\ \dfrac{\partial \delta v}{\partial x}(x = a, z) & = -2\gamma K^0(a)\phi(z) \end{cases} \quad \text{for } -\infty < z < +\infty. \tag{100}$$

To solve equations (99) and (100), it is natural to use a Fourier transform—defined by the equivalent equations (69)—in the direction z of the crack front. The general solution in $\widehat{\delta v}(x, k)$ of equation $(99)_1$ is a sum of terms proportional to $\cosh(kx)$, $x\cosh(kx)$, $\sinh(kx)$ and $x\sinh(kx)$, and the four multiplicative constants appearing in these terms may be identified using equations $(99)_{2,3}$ and (100); see details in Legrand et al. (2011). One thus gets

$$\widehat{\delta v}(x, k) = 2\gamma K^0(a)\, \frac{a\cosh(ka)\sinh(kx) - x\sinh(ka)\cosh(kx)}{\cosh(ka)\sinh(ka) - ka}\, \widehat{\phi}(k)\,. \tag{101}$$

The local variation of the SIF may be obtained from there using again a double expansion of equation (96), and the final result reads in Fourier's space (Legrand et al. 2011):

$$\frac{\widehat{\delta K}(a; k)}{K^0(a)} = \frac{2ka\cosh(2ka) - \sinh(2ka)}{2ka - \sinh(2ka)}\, \frac{\widehat{\phi}(k)}{a}\,. \tag{102}$$

We shall essentially be interested in the sequel in a special case, wherein the typical distance of variation of the crack front perturbation $\phi(z)$ is much smaller than the distance a from the left side of the plate, where the displacement is prescribed, to the unperturbed crack front. This case corresponds to the limit $ka \to \pm\infty$ in Eq. (102), which becomes

$$\frac{\widehat{\delta K}(k)}{K^0} = -2|k|\widehat{\phi}(k) \quad (|ka| \gg 1)\,. \tag{103}$$

Numerical solution for plates of arbitrary thickness. For plates of arbitrary thickness h, the solution may be obtained numerically, by the finite element method; considering a sinusoidal perturbation of the crack front of wavelength $\lambda \equiv 2\pi/|k|$ permits to directly obtain results in Fourier's space. This has been done by Legrand et al. (2011), considering various values of the dimensionless number $q \equiv |k|h = 2\pi h/\lambda$. The results obtained led them to propose the approximate but accurate following formula (in the limit $ka \to \pm\infty$):

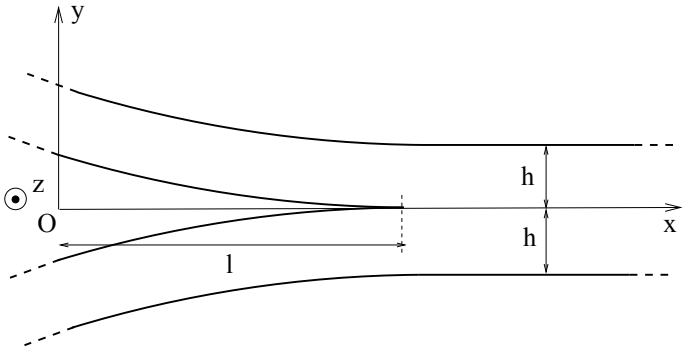

Fig. 27 In-plane perturbation of a semi-infinite crack lying on the mid-plane of an infinite plate: view in the plane Oxy

$$\frac{\widehat{\delta K}(k)}{K^0} \simeq -X(kh)\,|k|\widehat{\phi}(k) \quad \text{where} \quad X(q) = \frac{1}{2}\left[1 + \frac{3}{1+\frac{1}{3}\,|q|^{4/3}}\right] \quad (q \equiv kh). \tag{104}$$

Note that:

- In the limit $h \to 0^+$ (plate of infinitesimal thickness), $X(kh) \to 2$ so that equation (104) yields $\frac{\widehat{\delta K}(k)}{K^0} \simeq -2|k|\widehat{\phi}(k)$, in agreement with the result (103).
- In the limit $h \to +\infty$ (infinitely thick plate, equivalent to an infinite body), $X(kh) \to \frac{1}{2}$ so that equation (104) yields $\frac{\widehat{\delta K}(k)}{K^0} \simeq -\frac{|k|}{2}\widehat{\phi}(k)$, in agreement with the result (71) without the term $\frac{dK^0}{d\ell}(\ell)\widehat{\phi}(k)$. This term, which is connected to the variation of the unperturbed SIF K^0 with the distance of propagation, is absent here because in the limit $a \to +\infty$ considered, the loading, consisting of two opposite vertical displacements imposed on the far left sides of the two halves of the plate, becomes equivalent to opposite remote bending moments prescribed on these two halves: the unperturbed SIF then becomes a function of these opposite moments, independent of the length $\ell \equiv a$ of the crack.

Complete first- and second-order solution for plates of arbitrary thickness. We now wish, following Vasoya et al. (2016b), to provide the complete, first- and second-order solution, for the in-plane perturbation of a semi-infinite crack lying on the mid-plane of an infinite plate of arbitrary thickness h, loaded in pure mode I through some system of prescribed forces only (no prescribed displacements). Figures 27 and 28 provide 2D views of the cracked geometry; they are identical to Figs. 25 and 26, *except* that the plate now has no left boundary, and ℓ, which has been substituted for the distance a from the unperturbed crack front to the left boundary, now merely represents the distance from this front to some arbitrary axis Oz, parallel to it within the crack plane.

The solution considered above in Eqs. (103) and (104), obtained in the limit $ka \to \pm\infty$, corresponded to a loading equivalent to opposite remote bending moments prescribed on the two halves of the plate; the unperturbed SIF K^0 was

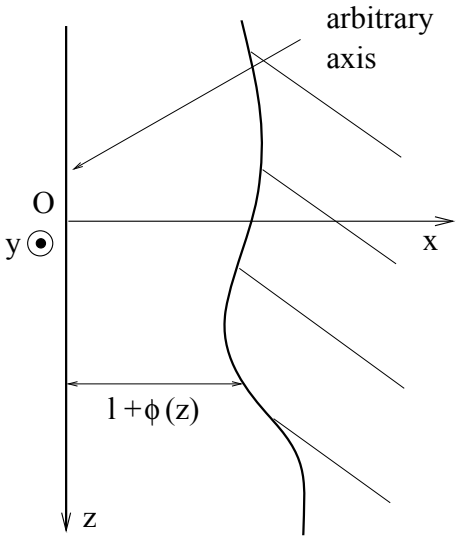

Fig. 28 In-plane perturbation of a semi-infinite crack lying on the mid-plane of an infinite plate: view in the plane Oxz

then (i) independent of the position of the crack front within the crack plane, and (ii) independent of its point of observation along the front. Here we wish to retain feature (ii) but not feature (i); that is, to consider K^0 as a function of ℓ but not of z. The dependence of K^0 upon ℓ will reveal indispensable in Sect. 3.8 for a rigorous, unambiguous calculation of the deformation of a crack front deformed by a hard obstacle.

The first-order variation of the SIF, for a small but otherwise arbitrary perturbation $\phi(z) \equiv \eta\bar{\phi}(z)$ of the crack front, is given in Fourier's space by

$$\widehat{K^1}(\ell; k)\,\eta = \left[\frac{dK^0}{d\ell}(\ell) - K^0(\ell)X(kh)\,|k|\right]\widehat{\phi}(k). \tag{105}$$

Equation (105) is obtained (through Fourier's transform) from Rice's first formula (59) by: (i) choosing, for the auxiliary perturbation $\phi_*(s) \equiv \phi_*(z)$, a translatory motion of the crack front by the small distance $\phi(z_1)$, and identifying the resulting variation $\delta_* K(s_1) \equiv \delta_* K(z_1)$ to $\frac{dK^0}{d\ell}(\ell)\phi(z_1)$; (ii) noting that the FK, for the general loading considered here, is the same as for the special loading considered in equations (103) and (104) above (neither of these loadings involves prescribed displacements); so that it suffices to add $\frac{dK^0}{d\ell}(\ell)\widehat{\phi}(k)$ to the expression of $\widehat{\delta K}(k)$ provided by Eq. (104).

The derivation of the second variation of the SIF is more elaborate, but basically similar to that presented in subsubsections **First-order variation of the fundamental kernel** and **Second-order variation of the stress intensity factor** for a semi-infinite crack in an infinite body. A key point of this derivation is that the auxiliary perturbation ϕ_{**}, in Rice's second formula (64) or (65), may again be taken as a combination of a translatory motion and a rotation *without any modification of distances*, thus preserving the thickness h of the plate, and therefore also the FK ($\delta_{**}Z = 0$ or equivalently $\delta_{**}W = 0$). The result reads (Vasoya et al. 2016b):

$$\widehat{K^2}(\ell; k_1)\,\eta^2 = \int_{-\infty}^{+\infty} R(h; \ell; k, k_1 - k)\widehat{\phi}(k)\widehat{\phi}(k_1 - k)dk \tag{106}$$

where

$$\begin{aligned} R(h; \ell; k, k') \equiv{}& \frac{1}{2}\frac{d^2K^0}{d\ell^2}(\ell) - \frac{1}{2}\frac{dK^0}{d\ell}(\ell)X((k+k')h)\,|k+k'| \\ &+K^0(\ell)\left\{\frac{1}{2}X((k+k')h)\,|k+k'|\left[X(kh)\,|k| + X(k'h)\,|k'|\right]\right. \\ &\left.-\frac{1}{4}\left[X^2((k+k')h)(k+k')^2 + X^2(kh)k^2 + X^2(k'h)k'^2\right]\right\}. \end{aligned} \tag{107}$$

Note that for a plate of infinite thickness h (all $X()$s $\to \frac{1}{2}$), equivalent to an infinite body, Eqs. (105), (106) and (107) reduce to (71), (76) and (77), as expected. On the other hand reducing the thickness to zero (all $X()$s $\to 2$) modifies the expressions of the first and second variations of the SIF in the following way:

- in the expression of $\widehat{K^1}(\ell; k)\,\eta$, the term proportional to $(dK^0/d\ell)(\ell)$ is unchanged, but that proportional to $K^0(\ell)$ is multiplied by a factor of 4;
- in the expression of $\widehat{K^2}(\ell; k)\,\eta^2$, the term proportional to $(d^2K^0/d\ell^2)(\ell)$ is unchanged, but that proportional to $(dK^0/d\ell)(\ell)$ is multiplied by a factor of 4, and that proportional to $K^0(\ell)$ by a factor of 16.

In Sect. 3.8 below, the expansion of the Fourier transform $\widehat{G}(\ell, \eta; k)$ of the elastic energy-release-rate $G(\ell, \eta; z)$ will be more useful than that of the SIF. This expansion is readily deduced from Irwin (1958)s formula, using the expressions (105) and (106) of $\widehat{K^1}(\ell; k)\,\eta$ and $\widehat{K^2}(\ell; k)\,\eta^2$:

$$\widehat{G}(\ell, \eta; k) \equiv G^0(\ell)\,\delta(k) + \widehat{G^1}(\ell; k)\,\eta + \widehat{G^2}(\ell; k)\,\eta^2 + O(\eta^3) \tag{108}$$

where δ denotes Dirac's function, $G^0(\ell)$ the unperturbed elastic energy-release-rate, and

$$\left\{\begin{array}{l}\widehat{G^1}(\ell;k)\,\eta \;\;=\left[\dfrac{dG^0}{d\ell}(\ell)-2G^0(\ell)X(kh)|k|\right]\widehat{\phi}(k)\\ \widehat{G^2}(\ell;k_1)\,\eta^2 \;=\displaystyle\int_{-\infty}^{+\infty} S(\ell;h;k,k_1-k)\,\widehat{\phi}(k)\,\widehat{\phi}(k_1-k)\,dk\\ S(\ell;h;k,k') \;\equiv\\ \quad\dfrac{1}{2}\dfrac{d^2G^0}{d\ell^2}(\ell)-\dfrac{1}{2}\dfrac{dG^0}{d\ell}(\ell)\left[X((k+k')h)|k+k'|+X(kh)|k|+X(k'h)|k'|\right]\\ \quad+G^0(\ell)\left\{-\dfrac{1}{2}\left[X((k+k')h)|k+k'|-X(kh)|k|-X(k'h)|k'|\right]^2\right.\\ \quad\left.+2X(kh)X(k'h)|kk'|\right\}.\end{array}\right. \tag{109}$$

3.8 *Application 2: Deformation of a Crack Front by a Hard Obstacle in a Plate*

The equilibrium shape of the front of a crack propagating in a heterogeneous plate. The preceding results will now be applied, following Vasoya et al. (2016b), to coplanar propagation of a crack along the mid-plane of a plate; propagation will be assumed to be governed by Griffith (1920)s criterion, with a spatial distribution of fracture energy $G_c(x,z)$ given by

$$G_c(x,z)\equiv\overline{G_c}\,[1+\eta g_c(x,z)]\,, \tag{110}$$

where $\overline{G_c}$ denotes some "mean" fracture energy, η a small parameter, and $g_c(x,z)$ a given dimensionless function describing fracture energy fluctuations. Propagation of the unperturbed crack in a homogeneous material ($g_c(x,z)\equiv 0$) will be assumed to be *stable*, that is, the derivative $dG^0/d\ell$ to be *negative*.

For a given loading, and with the assumption that G is identical to G_c all along the crack front, the fluctuations of G_c specify the shape of this front in the form

$$x\equiv\ell+\phi^1(\ell;z)\,\eta+\phi^2(\ell;z)\,\eta^2+O(\eta^3) \tag{111}$$

where the parameter ℓ and the functions $\phi^1(\ell;z)$ and $\phi^2(\ell;z)$, all homogenenous to a length, are to be determined. In the sequel the quantities $\phi^1(\ell;z)\,\eta$ and $\phi^2(\ell;z)\,\eta^2$ will be called the *first- and second-order deformations of the crack front*, respectively.

Let $\widehat{\mathcal{G}^1}\left[\ell;\{\widehat{\phi}\}\right](k)$ and $\widehat{\mathcal{G}^2}\left[\ell;\{\widehat{\phi}\}\right](k_1)$ denote the linear and quadratic functionals of the function $\widehat{\phi}$ defined by the right-hand sides of equations $(109)_{1,2}$. For the crack front shape given by Eq. (111), corresponding to the perturbation function $\phi\equiv\phi^1\,\eta+\phi^2\,\eta^2$, the expression (108) of $\widehat{G}$ becomes

$$\begin{aligned}\widehat{G}(\ell,\eta;k) = G^0(\ell)\,\delta(k) + \widehat{\mathcal{G}}^1\left[\ell;\{\widehat{\phi}^1\}\right](k)\,\eta \\ + \left\{\widehat{\mathcal{G}}^1\left[\ell;\{\widehat{\phi}^2\}\right](k) + \widehat{\mathcal{G}}^2\left[\ell;\{\widehat{\phi}^1\}\right](k)\right\}\eta^2 + O(\eta^3).\end{aligned} \tag{112}$$

Expanding now the local fracture energy

$$\overline{G_c}\left\{1 + \eta g_c\left[\ell + \phi^1(\ell;z)\,\eta + \phi^2(\ell;z)\,\eta^2 + O(\eta^3), z\right]\right\}$$

in powers of η, taking the Fourier transform of the result, and identifying the various terms to those of the expansion (112) of $\widehat{G}$, one finds at the various orders in η:

- At order 0:
$$G^0(\ell) = \overline{G_c}\,, \tag{113}$$
which determines the mean location ℓ of the crack front (as a function of the loading applied).
- At order 1:
$$\begin{aligned}\widehat{\mathcal{G}}^1\left[\ell;\{\widehat{\phi}^1\}\right](k) = \overline{G_c}\,\widehat{g}_c(\ell,k) \quad \Rightarrow \\ \widehat{\phi}^1(\ell;k)\,\eta = -\frac{\eta\widehat{g_c}(\ell,k)}{2X(kh)|k| - \frac{1}{G^0(\ell)}\frac{dG^0}{d\ell}(\ell)}\end{aligned} \tag{114}$$
where Eqs. $(109)_1$ and (113) have been used.
- At order 2:
$$\begin{aligned}\widehat{\mathcal{G}}^1\left[\ell;\{\widehat{\phi}^2\}\right](k_1) = -\widehat{\mathcal{G}}^2\left[\ell;\{\widehat{\phi}^1\}\right](k_1) \\ + \overline{G_c}\int_{-\infty}^{+\infty}\frac{\partial\widehat{g_c}}{\partial x}(\ell,k)\,\widehat{\phi}^1(\ell;k_1-k)dk \quad \Rightarrow\end{aligned}$$

$$\begin{aligned}\widehat{\phi}^2(\ell;k_1)\,\eta^2 = \frac{1}{2X(k_1h)|k_1| - \frac{1}{G^0(\ell)}\frac{dG^0}{d\ell}(\ell)}\left\{\int_{-\infty}^{+\infty} S(\ell;h;k,k_1-k)\right. \\ \times\frac{\eta\widehat{g_c}(\ell,k)}{2X(kh)|k| - \frac{1}{G^0(\ell)}\frac{dG^0}{d\ell}(\ell)}\,\frac{\eta\widehat{g_c}(\ell,k_1-k)}{2X((k_1-k)h)|k_1-k| - \frac{1}{G^0(\ell)}\frac{dG^0}{d\ell}(\ell)}\,dk \\ \left. + \int_{-\infty}^{+\infty}\eta\frac{\partial\widehat{g_c}}{\partial x}(\ell,k)\frac{\eta\widehat{g_c}(\ell,k_1-k)}{2X((k_1-k)h)|k_1-k| - \frac{1}{G^0(\ell)}\frac{dG^0}{d\ell}(\ell)}\,dk\right\}\end{aligned} \tag{115}$$

where equations $(109)_{1,2}$, (113) and (114) have been used.

Note that the assumed negativeness of $dG^0/d\ell$ implies that the denominators in equations (114) and (115) never vanish, which warrants convergence of the integrals when one Fourier-inverts the expressions $\widehat{\phi}^1$ and $\widehat{\phi}^2$ to get those of ϕ^1 and ϕ^2.

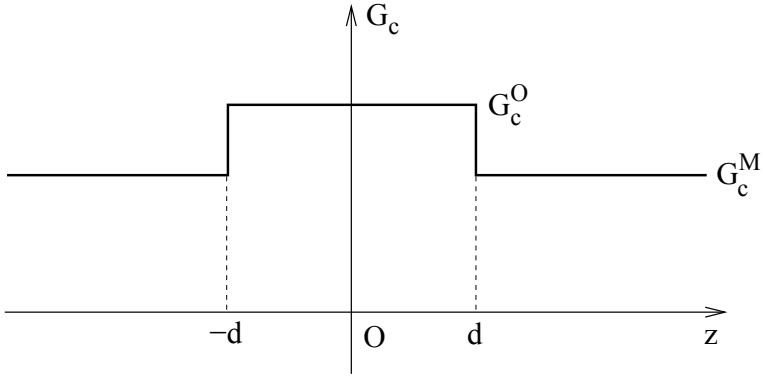

Fig. 29 Distribution of fracture energy on a plane containing a single obstacle infinitely elongated in the direction of crack propagation

Deformation of a crack front by a single obstacle. We now consider the simplest special case of a single harder obstacle, of infinite length in the direction x of propagation, and width $2d$ in the direction z of the crack front (Fig. 29). The fracture energy of the matrix will be denoted G_c^{M} and that of the obstacle G_c^{O}. We shall be particularly interested in the limit-case where $\frac{dG^0}{d\ell}(\ell) \to 0^-$, corresponding to the situation where the typical distance of variation of the unperturbed energy-release-rate is much larger than d.

The distribution of fracture energy may be represented by formula (110) with

$$\overline{G_c} \equiv G_c^{\mathrm{M}} \quad ; \quad \eta \equiv \frac{G_c^{\mathrm{O}} - G_c^{\mathrm{M}}}{G_c^{\mathrm{M}}} \quad ; \quad g_c(x,z) \equiv g_c(z) \equiv \begin{cases} 1 & \text{if } |z| < d \\ 0 & \text{if } |z| > d. \end{cases} \tag{116}$$

At order 1, one gets from equations (114) and (116):

$$\widehat{\phi^1}(\ell;k)\,\eta = -\frac{\eta\,\sin(kd)}{\pi k\left[2|k|X(kh) - \frac{1}{G^0(\ell)}\frac{dG^0}{d\ell}(\ell)\right]} \quad \Rightarrow$$

$$\phi^1(\ell;z)\,\eta = -\frac{2\eta}{\pi}\int_0^{+\infty} \frac{\sin(kd)}{k\left[2kX(kh) - \frac{1}{G^0(\ell)}\frac{dG^0}{d\ell}(\ell)\right]}\cos(kz)\,dk. \tag{117}$$

One cannot directly take the limit $\frac{dG^0}{d\ell}(\ell) \to 0^-$ in the last expression, since the resulting integral would be divergent at the lower bound of integration. However we are not really interested in the absolute position of the crack front, but only in its deviation from straightness, characterized by the quantity $\phi^1(\ell;z)\,\eta - \phi^1(\ell;0)\,\eta$. When considering this quantity in the limit $\frac{dG^0}{d\ell}(\ell) \to 0^-$, one may simply discard the

term $-\frac{1}{G^0(\ell)}\frac{dG^0}{d\ell}(\ell)$ in the denominator in equation (117) without getting a divergent integral, and obtain

$$\phi^1(z)\,\eta - \phi^1(0)\,\eta = \frac{\eta}{\pi}\int_0^{+\infty} \frac{\sin(kd)}{k^2 X(kh)}\,[1-\cos(kz)]\,dk\,. \tag{118}$$

Here and in the sequel superfluous indications of dependence upon ℓ have been discarded. In the two limiting cases $h \to 0^+$ (infinitely thin plate) and $h \to +\infty$ (infinite 3D body), the integral may be calculated explicitly, and the result is (Vasoya et al. 2016b):

$$\phi^1(z)\,\eta - \phi^1(0)\,\eta = \frac{\eta d}{2\kappa\pi}\big[\,(1+u)\ln(|1+u|) + (1-u)\ln(|1-u|)\,\big]\,,\ u \equiv \frac{z}{d} \tag{119}$$

where

$$\kappa = \begin{cases} 2 \text{ for } h \to 0^+ \\ \frac{1}{2} \text{ for } h \to +\infty. \end{cases} \tag{120}$$

At order 2, the calculations are much more elaborate, but still lead to completely explicit results in the two limits $h \to 0^+$ and $h \to +\infty$ (Vasoya et al. 2016b):

$$\phi^2(z)\,\eta^2 - \phi^2(0)\,\eta^2 = \begin{cases} -\dfrac{\eta^2 d}{4\kappa\pi}\big[(1+u)\ln(1+u) + (1-u)\ln(1-u)\big] \\ \qquad \text{if } |u| \le 1 \\ -\dfrac{\eta^2 d}{4\kappa\pi}\left[(|u|-1)\ln\left(\dfrac{|u|+1}{|u|-1}\right) + 2\ln 2\right] \\ \qquad \text{if } |u| \ge 1. \end{cases} \tag{121}$$

Comparison with experiments. Vasoya et al. (2016b) performed peeling tests of thin films bonded onto some rigid block, depicted schematically in Fig. 30. Details about the experimental apparatus and procedure are given in their paper, so a few indications will suffice here. The free end of the film was peeled off at a constant vertical velocity v_y, whereas the rigid block was moved with a constant horizontal velocity v_x, so as to maintain a constant "peeling angle" θ_p; the line marking the separation between the film and the block was interpreted as a "crack front". The block consisted of a transparency glued irreversibly onto a glass substrate. An obstacle of controlled geometry and fracture energy was introduced between the film and the transparency, by simply printing it onto the transparency. The contrast of fracture energy η defined by equation (116) could be varied, by varying the level of grey of the printed obstacle; this contrast was measured independently and controlled, so it was a perfectly defined, non-adjustable parameter of the experiments. The crack front deformation $\delta x(z)$ defined by

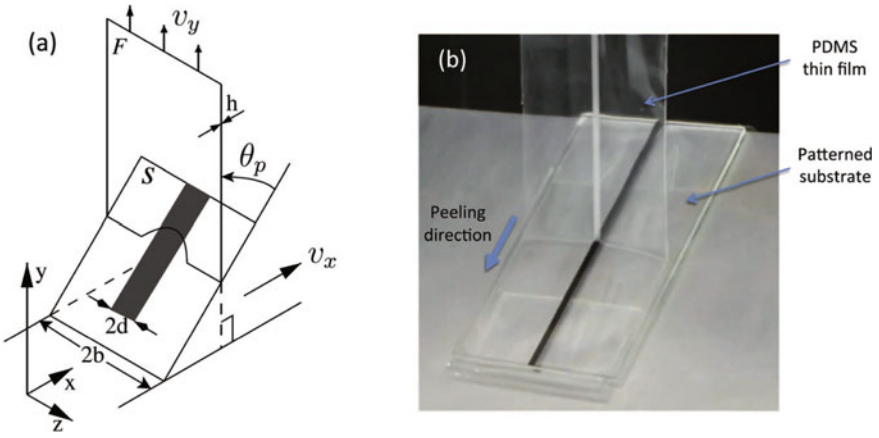

Fig. 30 Experimental setup. **a** Schematic representation of the peeling test—the substrate is moved horizontally at the velocity v_x in order to maintain a constant peeling angle θ_p. **b** Photograph of the experiment

$$\delta x(z) \equiv x(z) - x(0) \equiv \phi^1(z)\,\eta - \phi^1(0)\,\eta + \phi^2(z)\,\eta^2 - \phi^2(0)\,\eta^2 \qquad (122)$$

was recorded, in order to be compared to theoretical predictions. In the comparison, use was made of the theoretical formulae (119) and (121), with the value $\kappa = 2$ corresponding to the case of an infinitely thin plate (see equation (120)).

Figure 31 shows the comparison. In Fig. 31a the "first-order predictions" correspond to defining the theoretical value of $\delta x(z)$ by Eq. (122) but with the terms in η only, whereas the "second order predictions" correspond to the full definition including the terms in η^2. Note also that the quantity $\delta x(d)/d$ in Fig. 31b is a normalized measure of the "amplitude" of the crack front deformation.

Several points are noteworthy here:

- The agreement between the experiments and the second-order theory is excellent (Fig. 31a), despite the absence of any adjustable parameter.
- The agreement would obviously be very bad for the value $\kappa = 1/2$ corresponding to an infinitely thick plate, since the theoretical value of $\delta x(z)$ would be 4 times larger; this clearly illustrates the inadequacy of equation (70), valid for a semi-infinite crack in some infinite body, to interpret thin film experiments.
- The agreement is less good for the first-order theory than for the second-order one (Fig. 31a), which evidences the importance of non-linear geometric effects in the experiments considered.
- The second-order theory correctly predicts the "saturation" of the amplitude of the crack front deformation $\delta x(d)$ when the contrast of fracture energy η is increased (Fig. 31b).

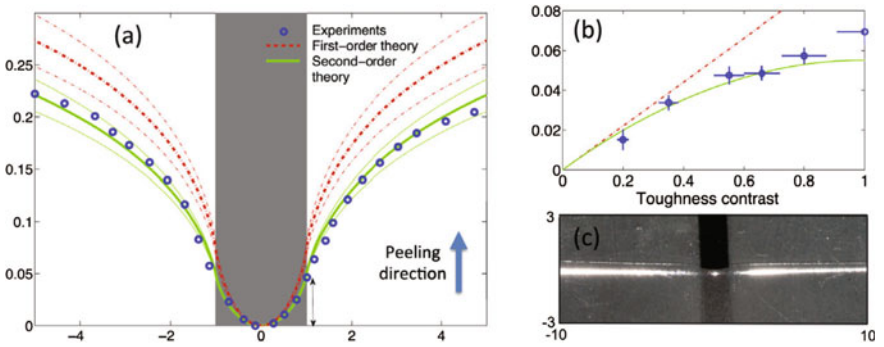

Fig. 31 **a** Equilibrium shape of a crack front pinned by a single obstacle of contrast $\eta = 0.66 \pm 0.06$, and comparison with the first- and second-order theoretical predictions. **b** Variations of the amplitude $\delta x(d)/d$ of the crack front deformation as a function of contrast, and comparison with the predictions of the first- and second-order theories. **c** Typical photograph of the peeling front as it crosses the obstacle

3.9 Perturbation of a Semi-infinite Interface Crack in an Infinite Body

In this subsection, following the works of Lazarus and Leblond (1998a, b) and Pindra et al. (2008), we extend the results of Sect. 3.4 on the first-order perturbation of a semi-infinite mode I crack in an infinite body, to an *interface* crack (lying between two elastic bodies with different elastic moduli) loaded arbitrarily.

Preliminaries and notations. The notations adopted are similar to those in the classical work of Hutchinson et al. (1987). We consider an infinite heterogeneous body made of two isotropic elastic materials, perfectly bonded together on their planar interface occupying the plane $y = 0$. Materials "+" and "−", with shear moduli μ_+ and μ_- and Poisson ratios ν_+ and ν_-, occupy the half-spaces $y > 0$ and $y < 0$ respectively. The "bielastic constant" ϵ and the "equivalent Poisson ratio" ν are defined by the following formulae:

$$\epsilon \equiv \frac{1}{2\pi} \ln \frac{(3-4\nu_+)/\mu_+ + 1/\mu_-}{(3-4\nu_-)/\mu_- + 1/\mu_+} \quad ; \quad 1-\nu \equiv \frac{(1-\nu_+)/\mu_+ + (1-\nu_-)/\mu_-}{(1/\mu_+ + 1/\mu_-)\cosh^2(\pi\epsilon)} \,. \tag{123}$$

The definition of the bielastic constant here is classical; that of the equivalent Poisson ratio is less standard but will reveal useful.

Now consider (Fig. 32): (i) a crack with arbitrary smooth contour lying on the interface; (ii) some arbitrary point M on this contour; and (iii) a frame $Mx_1x_2x_3$ with axes Mx_1, $Mx_2 \equiv My$, Mx_3 defined as usual, as parallel to the local direction of crack propagation, perpendicular to the crack plane, and coincident with the local tangent to the crack front, respectively.

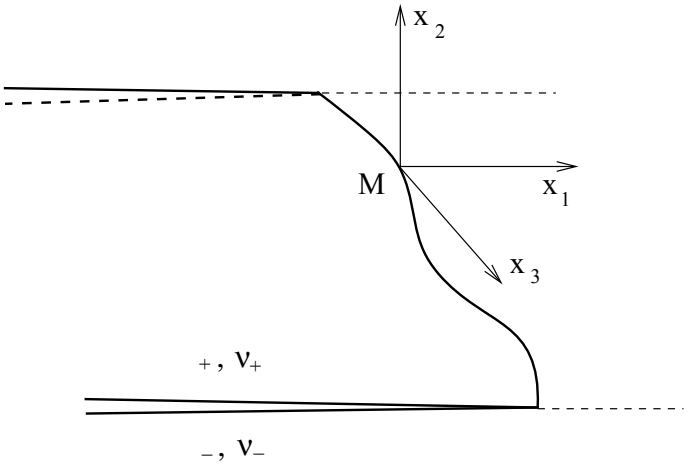

Fig. 32 Planar interface crack with arbitrary contour in an infinite body

The SIFs at the point M are related to the asymptotic expressions of the displacement discontinuity across the crack surface, and the stresses on the interface ahead of the crack front. The displacement discontinuity $[[\mathbf{u}]] \equiv \mathbf{u}_+ - \mathbf{u}_-$ across the crack surface is given, near the point M, by

$$\begin{cases} [[u_2 + iu_1]]\,(x_1 < 0, x_3 = 0) \\ \qquad\qquad \sim 2(1-\nu)\dfrac{\cosh(\pi\epsilon)}{1+2i\epsilon}\left(\dfrac{1}{\mu_+}+\dfrac{1}{\mu_-}\right)K(M)\sqrt{\dfrac{|x_1|}{2\pi}}\;|x_1|^{i\epsilon} \\ [[u_3]]\,(x_1 < 0, x_3 = 0) \sim 2\left(\dfrac{1}{\mu_+}+\dfrac{1}{\mu_-}\right)K_{III}(M)\sqrt{\dfrac{|x_1|}{2\pi}} \end{cases} \tag{124}$$

where $K(M) \equiv K_I(M) + iK_{II}(M)$ is the local complex (plane) SIF and $K_{III}(M)$ the local mode III (antiplane) SIF. The stress components σ_{21}, σ_{22} and σ_{23} on the interface are given, near the point M, by

$$\begin{cases} (\sigma_{22} + i\sigma_{21})(x_1 > 0, x_2 = 0, x_3 = 0) \sim \dfrac{K(M)\,x_1^{i\epsilon}}{\sqrt{2\pi x_1}} \\ \sigma_{23}(x_1 > 0, x_2 = 0, x_3 = 0) \qquad\quad \sim \dfrac{K_{III}(M)}{\sqrt{2\pi x_1}}\,. \end{cases} \tag{125}$$

Finally the energy release rate $G(M)$ at the point M is given by Irwin's formula:

$$G(M) = \frac{1}{4}\left(\frac{1}{\mu_+}+\frac{1}{\mu_-}\right)\left\{(1-\nu)\,|K(M)|^2 + [K_{III}(M)]^2\right\}. \tag{126}$$

First-order variations of the stress intensity factors and the energy-release-rate. We now consider the same problem of in-plane perturbation of the crack as in Sect. 3.4—see Fig. 17—with the same notations: in particular a general frame $Oxyz$ "adapted" to the unperturbed semi-infinite crack is used, the position of the unperturbed crack front in the direction x is denoted ℓ, and the perturbation of the crack front $\phi(z)$. The only differences are that now the crack lies on the interface between two different materials, and the loading is arbitrary and so generates all three modes.

To get the first-order variations $\delta K(z)$, $\delta K_{III}(z)$ of the SIFs by a special method (in the terminology of Sect. 3.1), the first task is to extend Rice (1985, 1989)s reformulation of Bueckner (1987)s weight function theory, expounded in Sect. 3.2, to the case of an interface crack. The task is easy and has been fulfilled by Lazarus and Leblond (1998a), the only novelty being the more complex expression (126) of the energy-release-rate. The output consists of the expressions of the components of the variation $\delta[\![\mathbf{u}]\!](M)$ of the displacement discontinuity $[\![\mathbf{u}]\!](M)$ arising from the perturbation $\phi(z)$ of the crack front. The second task then consists of extending the reasoning of subsubsection **Variation of the stress intensity factor** of Sect. 3.3, leading to Rice's first formula (59) for the variation of the mode I SIF, to the case of an interface crack. The task, which again was fulfilled by Lazarus and Leblond (1998a), makes a fundamental use of the special homogeneity properties, involving the bielastic constant ϵ, of the 3D weight functions for a semi-infinite interface crack. The final results read:

$$\left\{\begin{array}{l}
\delta K(z) = \dfrac{dK}{d\ell}(z)\,\phi(z) \\
\quad + \dfrac{1+2i\epsilon}{8\cosh(\pi\epsilon)} \left\{ PV \displaystyle\int_{-\infty}^{+\infty} \left[\frac{\gamma_+}{|z'-z|^{2i\epsilon}} \overline{K(z')} + \gamma_- K(z') \right] \frac{\phi(z')-\phi(z)}{(z'-z)^2} dz' \right. \\
\quad \left. + \dfrac{2\gamma_{III}}{1-\nu}\, FP \displaystyle\int_{-\infty}^{+\infty} \mathrm{sgn}(z'-z)\, K_{III}(z')\, \frac{\phi(z')-\phi(z)}{|z'-z|^{2+i\epsilon}}\, dz' \right\} \\
\delta K_{III}(z) = \dfrac{dK_{III}}{d\ell}(z)\,\phi(z) + \dfrac{\gamma}{4}\, PV \displaystyle\int_{-\infty}^{+\infty} K_{III}(z')\, \frac{\phi(z')-\phi(z)}{(z'-z)^2}\, dz' \\
\quad + \dfrac{1-\nu}{4}\, \mathrm{Re} \left[\gamma_z\, FP \displaystyle\int_{-\infty}^{+\infty} \mathrm{sgn}(z'-z)\, \overline{K(z')}\, \frac{\phi(z')-\phi(z)}{|z'-z|^{2+i\epsilon}}\, dz' \right].
\end{array}\right. \tag{127}$$

In these expressions the symbols $PV\int$ and $FP\int$ denote the Cauchy principal value and Hadamard finite part (see Lazarus and Leblond 1998a) of the integral considered, respectively. Also, γ_+, γ_-, γ_{III}, γ_z and γ are unknown quantities at this stage.

Unfortunately the values of the constants γ_+, γ_-, γ_{III}, γ_z, γ cannot be derived by a special method, although first-order expressions of these values were derived by Lazarus and Leblond (1998b) for small values of the bielastic constant ϵ. But the

exact values (for an arbitrary ϵ) of these constants were derived by Piccolroaz et al. (2007), employing a general method of solution, in the terminology of Sect. 3.1, making use of the homogeneity properties of the weight functions. These values are as follows:

$$\begin{cases} \gamma_+ &= -\dfrac{4}{\sqrt{\pi}}\,\dfrac{\Gamma(1+i\epsilon)}{\Gamma(1/2\ +i\epsilon)}\,\cosh(\pi\epsilon)\,\dfrac{\cosh(\pi\epsilon)-1/(1-\nu)}{\cosh(\pi\epsilon)+1/(1-\nu)} \\ \gamma_- &= \dfrac{8}{\pi(1+2i\epsilon)}\,\dfrac{\cosh^2(\pi\epsilon)}{\cosh(\pi\epsilon)+1/(1-\nu)} \\ \gamma_{III} &= -\dfrac{2^{2-i\epsilon}}{\sqrt{\pi}}\,\dfrac{\epsilon(1+i\epsilon)}{1+2i\epsilon}\,\dfrac{\Gamma(1/2\ -i\epsilon)}{\Gamma(1-i\epsilon)}\,\dfrac{\cosh^2(\pi\epsilon)}{\cosh(\pi\epsilon/2)\,[\cosh(\pi\epsilon)+1/(1-\nu)]} \\ \gamma_z &= -\dfrac{1+2i\epsilon}{(1-\nu)\cosh(\pi\epsilon)}\,\gamma_{III} \\ \gamma &= -\dfrac{2}{\pi}\,\dfrac{\cosh(\pi\epsilon)-3/(1-\nu)}{\cosh(\pi\epsilon)+1/(1-\nu)} \end{cases} \tag{128}$$

where Γ denotes the classical Gamma function, see Gradshteyn and Ryzhik (1980).

The expression of the variation of the energy-release-rate $\delta G(z)$ may be derived from those of the variations of the SIFs, using Irwin's formula (126). Assuming a dependence of the unperturbed SIFs $K^0(\ell)$, $K^0_{III}(\ell)$ upon the position ℓ of the unperturbed front of the type

$$\begin{cases} K^0(\ell) &\equiv k\,\ell^{\beta-i\epsilon} \\ K^0_{III}(\ell) &\equiv k_{III}\,\ell^{\beta} \end{cases} \tag{129}$$

where k and k_{III} are constants independent of ℓ, and β some real exponent, the result reads in Fourier's space (Pindra et al. 2008)[12]:

$$\frac{\widehat{\delta G}(k)}{G^0(\ell)} = \frac{2}{\ell}\,[\beta - f(k\ell)]\,\widehat{\phi}(k) \quad , \quad f(p) \equiv A|p| + \mathrm{Re}\left(B|p|^{1+2i\epsilon}\right) \tag{130}$$

where

$$\begin{cases} A &\equiv H^{-1}\left\{(1-\nu)\cosh(\pi\epsilon)|k|^2 + \dfrac{1}{2}\left[\dfrac{3}{1-\nu} - \cosh(\pi\epsilon)\right]k_{III}^2\right\} \\ B &\equiv H^{-1}\,[1-(1-\nu)\cosh(\pi\epsilon)]\,\dfrac{\Gamma(1/2-i\epsilon)}{\Gamma(1/2+i\epsilon)}\,\dfrac{\bar{k}^2}{2^{1+2i\epsilon}} \\ H &\equiv [1+(1-\nu)\cosh(\pi\epsilon)]\left(|k|^2 + \dfrac{k_{III}^2}{1-\nu}\right). \end{cases} \tag{131}$$

[12] The function f here has of course nothing to do with that in Sect. 3.5.

3.10 Application 3: On the Interpretation of Some Experiments of Debonding of Plates Bonded onto Rigid Substrates

Many observations have been made of coplanar propagation of a slightly wavy crack front lying on the interface between some *elastic medium* and some *rigid substrate*. The experiments analyzed in subsubsection **Comparison with experiments** are a typical example. But most of the time, the interpretation of these experiments were based on use of first-order expressions of the perturbed SIFs applicable to a *homogenous body*—generally, in the case of pure mode I, formula (70) for a semi-infinite crack in an infinite medium. There is no a priori reason why such extrapolations of formulae out of their domain of validity should be permissible; and this sheds some doubts on the interpretation of the experiments. The object of this subsection is to clarify the situation by showing, using the results of Sects. 3.7 and 3.9, that use of formulae for homogeneous bodies is admissible even for interface cracks, in *some special but important cases*.

Crack propagation along the interface between a thin film and a rigid substrate. The first case (that of the experiments discussed in subsubsection **Comparison with experiments**) is that of a *thin film* ($h \to 0^+$ with the notations of Sect. 3.7) stuck onto some rigid substrate. This film is debonded from the substrate through application of some load perpendicular to the interface; thus, following the method sketched in Sect. 3.7, calculation of the energy-release-rate may be based on use of Love-Kirchhoff's theory of thin plates subjected to normal loads, involving a single out-of-plane displacement component v, the in-plane components being zero.

Consider first, like in Sect. 3.7, the symmetric situation where *two identical films* are separated from each other. Within the framework of Love-Kirchhoff's theory, and with the notations of Sect. 3.7, the equilibrium equation and clamping conditions on the crack front read, on the upper $(+)$ and lower $(-)$ halves of the plate:

$$\left\{\begin{array}{l} \left(\dfrac{\partial^2}{\partial x^2}+\dfrac{\partial^2}{\partial z^2}\right)^2 v(x,0^+,z)=0 \quad \text{for } 0\le x\le a(z),\ -\infty<z<+\infty \\ \left.\begin{array}{l} v[x=a(z),0^+,z]=0 \\ \dfrac{\partial v}{\partial n}[x=a(z),0^+,z]=0 \end{array}\right\} \text{for } -\infty<z<+\infty \\ + \text{ boundary conditions} \end{array}\right. \tag{132}$$

$$\left\{\begin{array}{l} \left(\dfrac{\partial^2}{\partial x^2}+\dfrac{\partial^2}{\partial z^2}\right)^2 v(x,0^-,z)=0 \quad \text{for } 0\le x\le a(z),\ -\infty<z<+\infty \\ \left.\begin{array}{l} v[x=a(z),0^-,z]=0 \\ \dfrac{\partial v}{\partial n}[x=a(z),0^-,z]=0 \end{array}\right\} \text{for } -\infty<z<+\infty \\ + \text{ symmetric boundary conditions} \end{array}\right. \tag{133}$$

Now come back to the original non-symmetric problem of *debonding of a film from a rigid substrate*. Equations (132) on the upper half of the plate remain unchanged, whereas equations (133) on the lower half merely disappear, being replaced by the simple condition $v(x, 0^-, z) = 0$ for all x and z. Thus on the upper half of the plate, the equations of the two problems are identical, which implies that the solutions are also the same. It follows that the expressions of the relative perturbation $\delta G/G^0$ of the energy-release-rate are identical.[13] This justifies the use of the expression of $\delta G/G^0$ for the *symmetric* problem to discuss the *non-symmetric* problem of debonding of a thin film from a rigid substrate, as was done in subsubsection **Comparison with experiments**.

It is important to note that *this property of equivalence holds only for thin films*; for plates of finite thickness h, debonding of a plate from a rigid substrate is *not* equivalent to symmetric separation of identical plates. Indeed for a finite h, the treatment of such problems cannot be based on Love-Kirchhoff's theory of thin plates; it requires use of the full 3D theory of elasticity, which does not only involve the out-of-plane component $v \equiv u_y$ of the displacement, but also its in-plane components u_x and u_z. Now in the symmetric separation problem, u_x takes identical, but *nonzero* values on the upper and lower halves of the plate, and similarly for u_z; whereas in the non-symmetric debonding problem, u_x and u_z take nonzero values on the upper half, but are nil on the lower half. The lack of equivalence of the problems is thus clear.

Crack propagation along the interface between an incompressible semi-infinite body and a rigid substrate. The second case is that of an *incompressible* semi-infinite body bonded onto some rigid substrate (μ_+ arbitrary, $\nu_+ = 1/2$, $\mu_- = +\infty$, ν_- arbitrary with the notations of Sect. 3.9).

The fully general case of different elastic bodies with completely arbitrary elasticity coefficients was considered in Sect. 3.9. A priori, the expression of the perturbation $\delta G(z)$ of the energy-release-rate arising from a small perturbation $\phi(z)$ of a crack front must depend upon *three* dimensionless material constants, for instance μ_+/μ_-, ν_+ and ν_- with the notations of Sect. 3.9. However Eqs. (130) and (131) show that contrary to intuition, this variation in fact depends upon *two* dimensionless constants only, the bielastic constant ϵ and the equivalent Poisson ratio ν defined by equations (123). It follows that if, for some special combination of materials, these two constants take the same values as for a homogeneous material, that is $\epsilon = 0$ and $\nu = \nu_+$, then the expression of $\delta G(z)$ is the same as in the homogeneous case.

Now for a rigid substrate ($\mu_- = +\infty$), the expressions (123) of ϵ and $1 - \nu$ become, regardless of the value of ν_-:

$$\epsilon = \frac{1}{2\pi} \ln(3 - 4\nu_+) \quad ; \quad 1 - \nu = \frac{1 - \nu_+}{\cosh^2(\pi\epsilon)} .$$

If, in addition, material "+" is incompressible ($\nu_+ = 1/2$), these values become

[13] For a given local SIF, the local energy-release-rate for the symmetric problem is obviously twice that for the non-symmetric one; but since this true for both δG and G^0, their ratio remains the same.

$$\epsilon = 0 \quad ; \quad 1 - \nu = 1 - \nu_+ \quad \Rightarrow \quad \nu = \nu_+ = \frac{1}{2} \, .$$

These values are the same as for a homogeneous material. This entails, following the previous discussion, that it is admissible in this case to use the formula for $\delta G(z)$ for a semi-infinite crack in a *homogeneous* infinite body, and discuss crack propagation accordingly.

3.11 Concluding Summary

This section was devoted to *coplanar* perturbations of cracks in fully 3D situations. Although the loadings considered did not include only pure mode I, but also mixed mode I+II+III situations, the crack was assumed to propagate along its original plane, either because of symmetry reasons (pure mode I loading in a homogeneous material), or because of "channeling" of the crack along a weak plane (interface crack propagating between two different elastic materials).

As a prerequisite, Sect. 3.2, based on the works of Rice (1985, 1989), presented a re-formulation of Bueckner (1987)s theory of 3D weight functions, which permits to express the first-order variation of the displacement discontinuity across the crack surface resulting from some small but otherwise arbitrary in-plane perturbation of the front, in the form of a crack front integral. This integrand involves, in addition to the perturbation itself, the unperturbed SIFs and the *fundamental kernel* (FK) of the cracked geometry considered.

In Sect. 3.3, again based on the work of Rice (1989), it was shown how to deduce from there, in the case of a mode I loading but an arbitrary cracked geometry, general formulae for the first-order variations of the mode I SIF and FK. The remarkable point in these formulae is that they permit, in some cases, to determine the distributions of this SIF and FK along the crack front *without solving the entire 3D elasticity problem implied* (*special* method of solution).

Section 3.4 then provided fully explicit first- and second-order formulae for the perturbations of the mode I SIF and FK, in the special case of a semi-infinite tensile crack in an infinite body. The derivation was based on the results of Sect. 3.3, combined with the explicit knowledge of the FK for such a cracked geometry (in the unperturbed configuration) (Rice 1985, 1989).

The purpose of Sect. 3.5 was to illustrate the effect of the *finite dimensions of the crack*, by considering the case of a tensile slit-crack in some infinite body. Following the work of Leblond et al. (1996), we showed how the mode I FK (and consequently the perturbed mode I SIF) could be deduced from the general formula for the variation of the FK established in Sect. 3.3, by applying it to special motions of the front and rear parts of the crack front preserving the shape of the crack, though modifying its size and orientation.

These results were applied in Sect. 3.6, following again the work of Leblond et al. (1996), to a linear stability analysis of the geometry of the front of a slit-crack

propagating in some infinite body. A sinusoidal instability mode of the two parts of the front, symmetric with respect to the central line of the crack, was evidenced for values of the wavelength of the perturbation larger than some critical, characteristic value proportional to the half-width of the crack.

To illustrate the effect of the *finite dimensions of the body*, Sect. 3.7, based on the works of Legrand et al. (2011) and Vasoya et al. (2016b), considered the case of a mode I crack propagating along the mid-plane of a plate of finite thickness. Fully explicit first- and second-order formulae for the variation of the SIF along the front were derived. The first-order formula was obtained from Love-Kirchhoff's plate theory, rigorously applicable to plates of infinitesimal thickness, completed by finite element computations for finite values of this thickness. The second-order formula was obtained like for a semi-infinite crack in an infinite body, by using the general formulae for the first-order variations of the mode I SIF and FK of Sect. 3.3.

Following the work of Vasoya et al. (2016b), Sect. 3.8 applied the results of Sect. 3.7 to the calculation of the in-plane deformation of the front of a mode I crack, propagating along the mid-plane of a plate, and encountering a harder obstacle. The deformation predicted was successfully compared to that actually observed in some specific experiments of debonding of thin films from rigid substrates (Vasoya et al. 2016b).

Section 3.9, based on the works of Lazarus and Leblond (1998a, b) and Piccolroaz et al. (2007), considered the coplanar perturbation of a semi-infinite *interface* crack in a fully 3D, mixed mode I+II+III situation. The derivation of first-order expressions of the variations of the SIFs was essentially based on an extension of a formula of Sect. 3.2, for the variation of the displacement discontinuity across the crack surface in a homogenenous material, to the case of an interface crack; homogeneity properties of the FK were also used.

Finally the purpose of Sect. 3.10 was to compare experiments of *symmetric separation of two identical plates* on the one hand, and *non-symmetric debonding of a single plate from a rigid substrate* on the other hand. The difference between the two situations was duly noted in general. However it was shown, using the results of Sect. 3.7 and 3.9, that they are in fact equivalent, if the upper plate is either *very thin*, or *very thick and made of some incompressible material*. In these two special but important cases, this justifies use of formulae for the first-order variation of the SIF(s) applicable a priori only to symmetric situations, to interpret non-symmetric experiments of debonding of plates from rigid substrates.

4 3D Out-of-Plane Crack Perturbations

4.1 Introduction

In this final section, we shall consider *out-of-plane* perturbations of cracks loaded in mixed-mode I+II+III in fully 3D situations. There are two main applications. The first one pertains to the study and prediction of the *roughness* of the surface of cracks

loaded in mode I, and its consequences upon the global toughness, in materials with heterogeneous fracture properties. Although this important question was the topic of several interesting recent studies (see notably Lebihain 2019; Lebihain et al. 2020), we shall not consider it for space reasons, and concentrate instead on the second application. That application pertains to the fundamental problem of the theoretical explanation of the current observation that cracks loaded in mixed-mode I+III do not generally propagate along their original plane, but in the form of small, tilted facets growing out-of-plane—the wording *crack front segmentation* is currently used to designate the phenomenon. This issue raises a very difficult challenge, due to the breaking of the translatory invariance along the crack front; but it is our aim to show that important progress has been made on the topic in recent years, even though a number of questions still remain unresolved.

Just like in 2D, out-of-plane crack perturbations may be of Type I or Type II, in the terminology of the General Introduction: one may perturb either the sole vicinity of the crack front, through addition of some extension of small length (perturbation of Type I), or the entire crack surface (perturbation of Type II).

The papers reviewed here are more recent than those discussed in Sect. 3 on coplanar crack perturbations, because the topic is more difficult. They were published between 1998 and the present day. Two of them were devoted to the fundamental calculation of the SIFs along the front of a crack slightly perturbed out of its plane, under arbitrary loading. The others were devoted to the application of these basic papers to the tentative explanation of crack front segmentation in mixed-mode I+III or I+II+III. Note however that the *consequences* of segmentation upon the overall toughness are not envisaged in the present review (see for instance Lazarus et al. (2020) on this topic).

The two papers devoted to the basic calculation of the perturbed SIFs are due to Leblond (1999) and Movchan et al. (1998). In the first, the author extended the methods devised and the results obtained previously in the 2D case for perturbations of Type I (Leblond 1989; Amestoy and Leblond 1992) and summarized in Sect. 2.3 to 2.7 of Sect. 2, to the 3D case. Assuming the length—variable along the front—of the short added kinked and curved extension to be the product of some small parameter η and some known function, in the same manner as in Sect. 3, he determined the first two terms of the expansion of the SIFs in powers of this parameter, proportional to $\eta^0 = 1$ and $\eta^{1/2}$. He showed that the form of these two terms is exactly identical to that in the 2D case, except for the extra dependence upon the position of the point of observation of the SIFs along the crack front: they depend only on the local SIFs and non-singular stresses just before the kink, plus the local geometric parameters of the kinked and curved extension—there is no remote contribution of the entire crack front in these terms. (Such a remote contribution, in the form of an integral over the crack front, appears only in the third term of the expansion of the SIFs, proportional to $\eta^1 = \eta$, as shown in a further paper of Leblond et al. (1999); but this paper will not be commented further here).

There are some interesting applications to Leblond (1999)s results, notably the extension of Cotterell and Rice (1980)s original 2D directional stability criterion to the 3D case, see Leblond (1999) and Leblond and Lazarus (2015). However the

crack perturbations considered by Leblond (1999), being of Type I, do not permit to consider perturbations extending over the whole crack surface, such as needed for linear stability analyses of coplanar propagation of cracks loaded in mode I+III, which form the basis of theoretical studies of crack front segmentation in mode I+III, as will be seen.

The second basic paper devoted to the calculation of the perturbed SIFs is due to Movchan et al. (1998). In this paper the authors considered general—albeit small—out-of-plane perturbations of Type II, extending over the entire crack surface. (The same problem had been envisaged, with some errors of principle, in earlier papers not quoted here). They showed that the expressions of the perturbed SIFs along the front were the sum of three types of terms:

- *local* terms depending only on the constants characterizing the local stress field in the unperturbed configuration of the crack (SIFs, non-singular stresses...), and the parameters characterizing the local geometry of the perturbation;
- *semi-local* terms in the form of integrals over the unperturbed crack front, involving the SIFs and the perturbation all along this front;
- *non-local* terms in the form of integrals over the entire crack surface, involving the unperturbed stress field and the perturbation all over this surface.[14]

With regard now to the application to crack propagation in mode I+III, the instability of the coplanar configuration of a mode I+III crack is well-documented experimentally; see for instance the works of Sommer (1969), Knauss (1970), Palaniswamy and Knauss (1975), Hourlier and Pineau (1979), Pollard et al. (1982), Suresh and Tschegg (1987), Pollard and Aydin (1988), Yates and Miller (1989), Hull (1993), Hull (1995), Cooke and Pollard (1996), Lazarus (1997), Lazarus et al. (2001b), Lazarus et al. (2008), Lin et al. (2010), Goldstein and Osipenko (2012), Pham and Ravi-Chandar (2014). The front of cracks loaded in mode I+III is known to split (fragmentation), leading to formation of small facets inclined over the average plane of propagation so as to reduce the local mode III component of the stress field. Many materials have been used in experiments: glass (Sommer 1969; Pham and Ravi-Chandar 2014), steels (Hourlier and Pineau 1979; Yates and Miller 1989; Lazarus 1997), rocks (Pollard et al. 1982; Pollard and Aydin 1988; Cooke and Pollard 1996), alumina (Suresh and Tschegg 1987), PMMA (Lazarus et al. 2008), gypsum and even cheese! (Goldstein and Osipenko 2012). This suggests that the causes of crack front fragmentation are not rooted in microscopic, material-dependent mechanisms, so that the standard macroscopic theory of LEFM should be able to handle the problem.

The three main theoretical papers on the subject seem to be due to Leblond et al. (2011, 2018) and Vasudevan et al. (2019). They were inspired by some numerical simulations of Pons and Karma (2010), which evidenced out-of plane instability modes in which the crack front took the shape of a helix with exponentially growing size; these simulations were based on a phase-field model of Karma et al. (2001)

[14] Local and semi-local terms were also found in the work of Leblond (1999); but he could not get Movchan et al. (1998)s fully non-local terms since the perturbations he considered were confined to the immediate vicinity of the crack front.

equivalent—under certain conditions detailed in Hakim and Karma (2009) and satisfied in Pons and Karma (2010)s calculations—to LEFM, which again pointed to the potential usefulness of this theory to predict crack front fragmentation. The work of Leblond et al. (2011) consisted of a linear stability analysis of coplanar propagation in mode I+III, combining two main elements:

- first-order expressions of the perturbations of the SIFs arising from (i) the in-plane perturbation of the crack front (Gao and Rice 1986); (ii) the out-of-plane perturbation of the crack surface (Movchan et al. 1998);
- use of a double propagation criterion combining Griffith (1920)s energetic condition and Goldstein and Salganik (1974)s PLS.

With these elements, instability modes of the type found numerically by Pons and Karma (2010) were indeed discovered, for values of the unperturbed mixity ratio (ratio of the unperturbed mode III to mode I SIFs) exceeding some "threshold value" depending only on Poisson's ratio.

Although this result was quite appealing, it raised a major issue. Indeed for standard values of Poisson's ratio, the theoretical threshold is of the order of 0.5. But this value is generally much larger than that actually observed: although an exceptionally high value of 0.57 was reported by Eberlein et al. (2017) for an aluminium alloy, Sommer (1969)s estimate for glass amounted to a few percent only, and according to Pham and Ravi-Chandar (2014), there is even no threshold at all in both Homalite 100 and glass.

Although other explanations of the discrepancy (explained below) have been suggested, an appealing one was proposed by Leblond et al. (2018). These authors suggested to consider the critical-energy-release rate not as a constant along the front, but rather as a function of the local mixity ratio (ratio of the local mode III to mode I SIFs), as evidenced by some experimental results of Lin et al. (2010). They repeated Leblond et al. (2011)s linear stability analysis with this new hypothesis, and showed that an acceptable match of theoretical and experimental values of the threshold could then be obtained, with some reasonable value of the heuristic parameter characterizing the dependence of the critical-energy-release rate upon the mixity ratio.

Finally, very recently, these results were further extended by Vasudevan et al. (2019) to include the possible presence of some small mode II global loading component. The linear stability analysis was repeated again. The major output of the calculation was the discovery, in the presence of mode II, of a gradual *drift of instability modes along the front* as it propagates. This theoretical result opens interesting perspectives for the interpretation of some experiments where a drifting motion of facets was indeed observed (Lazarus et al. 2008; Lin et al. 2010).

The section is organized as follows:

- Section 4.2 first expounds Leblond (1999)s 3D extension of Leblond (1989); Amestoy and Leblond (1992)s works on crack kinking and curving in 2D. Two simple applications are presented.

- Then Sect. 4.3, essentially based on Movchan et al. (1998)s fundamental work on the first-order out-of-plane perturbation of a semi-infinite crack in some infinite body, presents the expressions of the SIFs along the front of such a crack, perturbed both within and out of its plane.
- We next present, in Sect. 4.4, Leblond et al. (2011)s linear stability analysis of coplanar crack propagation in mode I+III, leading to the conclusion of existence, when the unperturbed mixity ratio exceeds some threshold, of instability modes in which the crack front assumes the shape of a helix with size growing exponentially with the distance of propagation. The application of this result to the explanation of crack front segmentation is discussed.
- Following the work of Leblond and Lazarus (2015), Sect. 4.5 proposes a first, qualitative explanation of the discrepancy observed between theoretical and experimental values of the threshold. This explanation relies on a 3D extension, presented in Sect. 4.2, of Cotterell and Rice (1980)s analysis of directional stability of straight propagation in 2D.
- Section 4.6 expounds Leblond et al. (2018)s recent extension of Leblond et al. (2011)s linear stability analysis to the case where the local energy-release-rate is allowed to depend on the local mixity ratio. This leads to a much improved agreement of theoretical and experimental values of the threshold.
- Finally Sect. 4.7 expounds (Vasudevan et al. 2019) further extension to the case where the loading includes a small global mode II component, leading to the theoretical conclusion that for such a loading, instability modes must gradually drift along the crack front.

4.2 Crack Kinking in 3D

Hypotheses and notations. The geometric and mechanical situation is the exact analog, in 3D, of that depicted in Sect. 2.2 of Sect. 2 in the 2D case; it is schematized in Fig. 33, similar to Fig. 1 but in 3D. The hypotheses and notations are the same, except that (i) the tip O of the initial crack is replaced by some arbitrary point of curvilinear abscissa s along the crack front; (ii) the kink angle $\alpha(s)$ now depends on s; and (iii) the same is true of the length $\phi(s)$ of the crack extension, which is taken in the form (analogous to expression (41) of Sect. 3):

$$\phi(s) \equiv \eta\bar{\phi}(s) \tag{134}$$

where η is a small parameter and $\bar{\phi}(s)$ a given, fixed function.

The local shape of the crack extension, in the plane perpendicular to the local tangent to the front, is still schematized by Fig. 3 of Sect. 2, where $\alpha(s)$ is now a function of s, and the frames Oxy and $Ox'y'$ are those locally "adapted" to the crack and its extension in this plane: O coinciding with the point s of the initial front, Ox and Ox' parallel to the initial and new directions of propagation respectively, and Oy and Oy' parallel to the local normals to the initial crack and its extension,

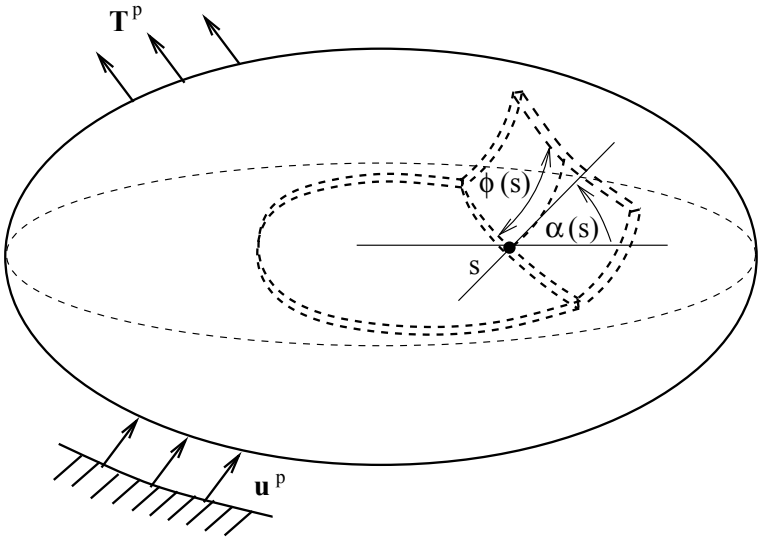

Fig. 33 A crack with a kinked and curved extension in 3D

respectively. The equation of the crack extension reads, in the frame $Ox'y'$:

$$y' = a^*(s)x'^{3/2} + O\left(x'^2\right), \tag{135}$$

which is analogous to equation (6) except for the dependence of the "pseudo-curvature parameter" $a^*(s)$ upon the position s along the front.

The loading is arbitrary, so that it generates all three SIFs $K_I^0(s)$, $K_{II}^0(s)$, $K_{III}^0(s)$ along the front of the original crack, and all three SIFs $K_I(\eta; s)$, $K_{II}(\eta; s)$, $K_{III}(\eta; s)$ along that of its extension of local length $\eta\bar{\phi}(s)$. Like in Sect. 2, we shall use "SIF-vectors" made from the mode I, II and III SIFs: for instance for the initial SIFs,

$$\mathbf{K}^0(s) \equiv \begin{pmatrix} K_I^0(s) \\ K_{II}^0(s) \\ K_{III}^0(s) \end{pmatrix} \tag{136}$$

and similarly for other triplets of SIFs. We shall consider the expansion of the SIF-vector $\mathbf{K}(\eta; s)$ on the front of the crack extension in powers of η:

$$\mathbf{K}(\eta; s) = \mathbf{K}^*(s) + \mathbf{K}^{(1/2)}(s)\sqrt{\eta} + ... \tag{137}$$

First and second terms of the expansion of the stress intensity factors. Using a relatively straightforward 3D extension of the method previously devised by Leblond (1989) in 2D, Leblond (1999) showed that the SIF-vector just after the kink is given by a formula completely analogous to that in 2D, Eq. (15):

$$\mathbf{K}^*(s) = \mathbf{F}(\alpha(s)).\mathbf{K}^0(s) \quad \Leftrightarrow \quad K_p^*(s) = F_{pq}(\alpha(s))K_q^0(s) \tag{138}$$

where $\mathbf{F}(\alpha) \equiv [F_{pq}(\alpha)]_{p,q=I,II,III}$ is a linear operator depending only on α (universality property).

The **F**-matrix is not full. Indeed, a symmetry with respect to the plane Oxy, applied to the local geometry and mechanical fields, leaves the mode I and II SIFs unchanged but changes the sign of the mode III SIFs, both before and after the kink. It follows that the components $F_{I,III}$, $F_{II,III}$, $F_{III,I}$ and $F_{III,II}$ must be zero, so that the **F**-matrix must be of the form

$$\mathbf{F}(\alpha) = \begin{pmatrix} F_{I,I}(\alpha) & F_{I,II}(\alpha) & 0 \\ F_{II,I}(\alpha) & F_{II,II}(\alpha) & 0 \\ 0 & 0 & F_{III,III}(\alpha) \end{pmatrix}. \tag{139}$$

The "in-plane" components $F_{I,I}(\alpha)$, $F_{I,II}(\alpha)$, $F_{II,I}(\alpha)$ and $F_{II,II}(\alpha)$ are of course identical to those found in 2D by considering a simple special case, see Sect. 2.5 of Sect. 2. The "out-of-plane" component $F_{III,III}(\alpha)$ may be evaluated using the same special case, but now with a mode III (antiplane) loading; the calculation is even entirely feasible analytically. The result reads (Sih 1965):

$$F_{III,III}(\alpha) = \left(\frac{1-m}{1+m}\right)^{m/2} \quad , \quad m \equiv \frac{\alpha}{\pi}. \tag{140}$$

From there, a reasoning based on the same elements as that in Sect. 2.7 of Sect. 2—but with an extra integration over the extended crack front, to express the derivative of the total potential energy $\mathcal{P}(\eta)$ of the body with respect to η—leads to an extended Irwin formula for a fully 3D kinked crack:

$$G^*(s) = \frac{1-\nu^2}{E}\left\{[K_I^*(s)]^2 + [K_{II}^*(s)]^2\right\} + \frac{1+\nu}{E}[K_{III}^*(s)]^2, \tag{141}$$

where $G^*(s)$, like in Sect. 2, represents the energy-release-rate just after the kink—the only novelty being that here it is a local quantity at the point s of the crack front, defined per unit length of this front.

In addition, Leblond (1999) showed that the second term of the expansion of the SIFs along the front of the extended crack, proportional to $\sqrt{\eta}$, is also analogous to that in 2D, Eq. (22):

$$\mathbf{K}^{(1/2)}(s) = \left[\mathbf{G}(\alpha(s)).\mathbf{T}^0(s) + a^*(s)\mathbf{H}(\alpha(s)).\mathbf{K}^0(s)\right]\sqrt{\tilde{\phi}(s)}$$

$$\Rightarrow \quad \mathbf{K}^{(1/2)}(s)\sqrt{\eta} = \left[\mathbf{G}(\alpha(s)).\mathbf{T}^0(s) + a^*(s)\mathbf{H}(\alpha(s)).\mathbf{K}^0(s)\right]\sqrt{\phi(s)}. \tag{142}$$

In this equation $\mathbf{G}(\alpha)$ and $\mathbf{H}(\alpha)$ are universal operators, and

$$\mathbf{T}^0(s) \equiv \begin{pmatrix} T_I^0(s) \\ T_{II}^0(s) \\ T_{III}^0(s) \end{pmatrix} \equiv \begin{pmatrix} T_{xx}^0(s) \\ T_{zz}^0(s) \\ T_{xz}^0(s) \end{pmatrix} \tag{143}$$

is the vector of non-singular stresses along the front of the original crack: $T_{xx}^0(s)$, $T_{zz}^0(s)$, $T_{xz}^0(s)$ represent uniform stress fields σ_{xx}, σ_{zz}, σ_{xz}.[15]

Just like the **F**-matrix, the **G**- and **H**-matrices are not full. Indeed a symmetry argument similar to that presented above permits to conclude that the components $G_{I,III}$, $G_{II,III}$ and $G_{III,I}$ of the **G**-matrix, and the components $H_{I,III}$, $H_{II,III}$, $H_{III,I}$ and $H_{III,II}$ of the **H**-matrix, must be zero. Furthermore it is obvious that a uniform stress field σ_{zz}, such as represented by the non-singular stress $T_{zz}^0(s) \equiv T_{II}^0(s)$, has no effect whatsoever on the stress singularity, on both the original and extended crack fronts; it follows that the components $G_{I,II}$, $G_{II,II}$ and $G_{III,II}$ of the **G**-matrix must also be zero. Hence the two matrices are necessarily of the form

$$\begin{cases} \mathbf{G}(\alpha) = \begin{pmatrix} G_{I,I}(\alpha) & 0 & 0 \\ G_{II,I}(\alpha) & 0 & 0 \\ 0 & 0 & G_{III,III}(\alpha) \end{pmatrix} \\ \mathbf{H}(\alpha) = \begin{pmatrix} H_{I,I}(\alpha) & H_{I,II}(\alpha) & 0 \\ H_{II,I}(\alpha) & H_{II,II}(\alpha) & 0 \\ 0 & 0 & H_{III,III}(\alpha) \end{pmatrix}. \end{cases} \tag{144}$$

Of course the functions $G_{I,I}(\alpha)$ and $G_{II,I}(\alpha)$ are identical to the functions $G_I(\alpha)$ and $G_{II}(\alpha)$ of the 2D case,[16] and the functions $H_{I,I}(\alpha)$, $H_{I,II}(\alpha)$, $H_{II,I}(\alpha)$ and $H_{II,II}(\alpha)$ to their 2D counterparts. Comments on all these functions were given in subsubsection **Second term of the expansion of the stress intensity factors** of Sect. 2. Finally the function $G_{III,III}(\alpha)$ was calculated analytically by Sih (1965) and the function $H_{III,III}(\alpha)$ by Leblond (1999), considering special cases with an antiplane loading. The results will not be needed here and therefore will not be given.

Two simple applications. As a first, simple application, one may wonder what the preceding results say about crack front fragmentation in mode I+III. The answer is simple: absolutely nothing! Indeed let us adopt, following the discussion in Sect. 2.9 of Sect. 2, the PLS to predict the value of the kink angle. Assume that $K_I^0(s)$ and $K_{III}^0(s)$ are nonzero, but $K_{II}^0(s) = 0$. Since $K_{III}^0(s)$ has no effect upon $K_{II}^*(s)$ (see Eq. (139)), the expression of $K_{II}^*(s)$ is exactly the same as in pure mode I, and therefore *the predicted kink angle is zero*. (For $\alpha(s) = 0$, $K_{II}^*(s) = K_{II}^0(s) = 0$). This prediction is inconclusive: it is not incompatible with the possible formation of inclined facets, because even in the absence of a kink, the crack extension may be curved in the direction of propagation. But it says nothing about this possibility.

---

[15] In the work of Leblond (1999), the notations $T_{II}^0(s) \equiv T_{xz}^0(s)$, $T_{III}^0(s) \equiv T_{zz}^0(s)$ were used instead of $T_{II}^0(s) \equiv T_{zz}^0(s)$, $T_{III}^0(s) \equiv T_{xz}^0(s)$. The present notations lead to a more natural-looking **G**-matrix, see Eq. $(144)_1$ below.

[16] The sole, purely formal difference lies in the absence of a second index in the 2D functions; this index was unnecessary in the 2D case since there was only one non-singular stress then.

As a more interesting application, let us turn to the 3D extension of Cotterell and Rice (1980)s directional stability criterion, presented in the 2D case in subsubsection **Application to the problem of directional stability** of Sect. 2. With the same hypotheses as in this subsubsection—except for the 3D geometry—the expansion of the SIF $K_{II}(\eta; s)$ of mode II, for a small kink angle $\alpha(s)$, is the exact 3D equivalent of the expression (36) of the 2D case:

$$K_{II}(\eta; s) = K^0_{II}(s) + \frac{\alpha(s)}{2} K^0_I(s) + \left[\frac{3}{4} a^*(s) K^0_I(s) - 2\sqrt{\frac{2}{\pi}}\, \alpha(s) T^0_{xx}(s) \right] \sqrt{\phi(s)} + O(\eta)\,. \tag{145}$$

The rest of Cotterell and Rice (1980)s reasoning follows without any change, and leads to the same conclusion: *crack propagation in mode I is locally directionally stable if, and only if, the local non-singular stress* $T^0_{xx}(s)$ *is negative*.

4.3 First-Order In-Plane and Out-of-Plane Perturbation of a Semi-infinite Crack in an Infinite Body

The basic explanation of the failure of Leblond (1999)s work to predict crack front segmentation in mode I+III lies in the fact that he considered only perturbations of Type I. Such perturbations, being confined to the immediate vicinity of the crack front, cannot account for a possible instability of coplanar propagation induced by small, accidental out-of-plane perturbations *extending far behind this front*. It thus becomes necessary to consider such perturbations of Type II.

This subsection is essentially based on the fundamental work of Movchan et al. (1998) on a first-order analysis of some arbitrary Type II, out-of-plane perturbation of a semi-infinite crack in some infinite body. We shall not attempt to describe the very elaborate method employed by these authors, based on Betti's theorem and some integral identity, but merely state the results obtained.

We consider a semi-infinite crack embedded within an infinite isotropic elastic body. In a first, unperturbed configuration (Fig. 34), the crack is planar and its front is straight. A Cartesian frame $Oxyz$, with origin O somewhere on the crack plane and axes Ox, Oy, Oz oriented according to the standard convention, is introduced. The crack is loaded under general mixed-mode I+II+III conditions, through some system of forces independent of the coordinate z, so that the unperturbed SIFs K^0_I, K^0_{II}, K^0_{III} are constant along the front. We also disregard, for simplicity, the variation of these SIFs with the position x of the crack front within the crack plane.

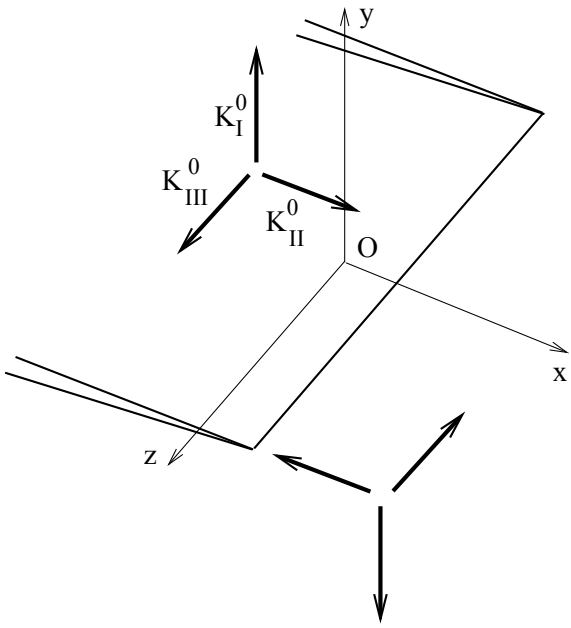

Fig. 34 Unperturbed semi-infinite crack in an infinite body loaded in mode I+II+III

In the second, slightly perturbed configuration, the front of the crack is displaced in the direction x of propagation by a small distance $\phi_x(x, z)$ (Fig. 35), and its surface is displaced in the direction y normal to the crack plane by a small distance $\phi_y(x, z)$ (Fig. 36). Note that in Fig. 36 the perturbation is limited to the immediate vicinity of the crack front for legibility, but can in fact extend over the entire crack surface.

The perturbation of the p-th SIF ($p = I, II, III$) due to the in-plane perturbation $\phi_x(x, z)$ is denoted $\delta_x K_p(x, z)$, and that due to the out-of-plane perturbation $\phi_y(x, z)$ is denoted $\delta_y K_p(x, z)$. To first order in the pair (ϕ_x, ϕ_y), these perturbations are additive so that the total perturbation of the p-th SIF is simply

$$\delta K_p(x, z) = \delta_x K_p(x, z) + \delta_y K_p(x, z) \quad (p = I, II, III). \tag{146}$$

We apply the results of Gao and Rice (1986) on the perturbations of the SIFs, $\delta_x K_p(x, z)$, due to $\phi_x(x, z)$ (extending those of Rice (1985) in pure mode I to fully general mode I+II+III conditions), and those of Movchan et al. (1998) on the perturbations $\delta_y K_p(x, z)$ of the SIFs due to $\phi_y(x, z)$. We introduce the assumption that the characteristic length defined by the loading (in the absence of any length scale defined by the infinite geometry) is much larger than the typical distances of variation of the perturbations $\phi_x(x, z)$ and $\phi_y(x, z)$.[17] One can then retain only these terms, in Gao and Rice (1986)s and Movchan et al. (1998)s formulae, which involve the

[17] This assumption was already implicit in the disregard of the variation of the unperturbed SIFs with the position of the unperturbed front within the crack plane.

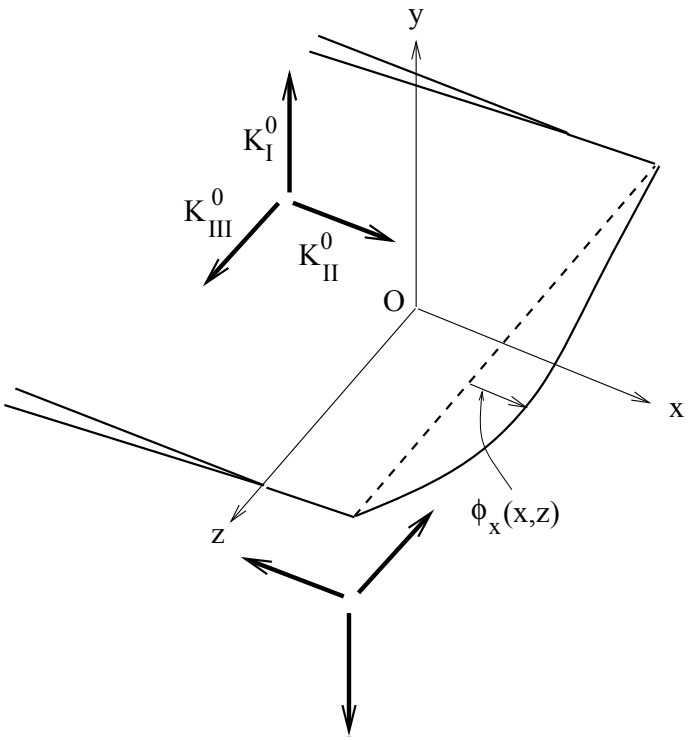

Fig. 35 In-plane perturbation of the crack front of a semi-infinite crack

unperturbed SIFs, and discard those involving the unperturbed non-singular stresses and higher-order constants characterizing the initial stress field near the unperturbed crack front. Gao and Rice (1986)s formulae then read:

$$\begin{cases} \delta_x K_I(x,z) &= \dfrac{K_I^0}{2\pi}\, PV \displaystyle\int_{-\infty}^{+\infty} \frac{\phi_x(x,z') - \phi_x(x,z)}{(z'-z)^2}\, dz' \\ \delta_x K_{II}(x,z) &= -\dfrac{2}{2-\nu} K_{III}^0 \dfrac{\partial \phi_x}{\partial z}(x,z) \\ &\quad + \dfrac{2-3\nu}{2-\nu} \dfrac{K_{II}^0}{2\pi}\, PV \displaystyle\int_{-\infty}^{+\infty} \frac{\phi_x(x,z') - \phi_x(x,z)}{(z'-z)^2}\, dz' \\ \delta_x K_{III}(x,z) &= \dfrac{2(1-\nu)}{2-\nu} K_{II}^0 \dfrac{\partial \phi_x}{\partial z}(x,z) \\ &\quad + \dfrac{2+\nu}{2-\nu} \dfrac{K_{III}^0}{2\pi}\, PV \displaystyle\int_{-\infty}^{+\infty} \frac{\phi_x(x,z') - \phi_x(x,z)}{(z'-z)^2}\, dz' \end{cases} \tag{147}$$

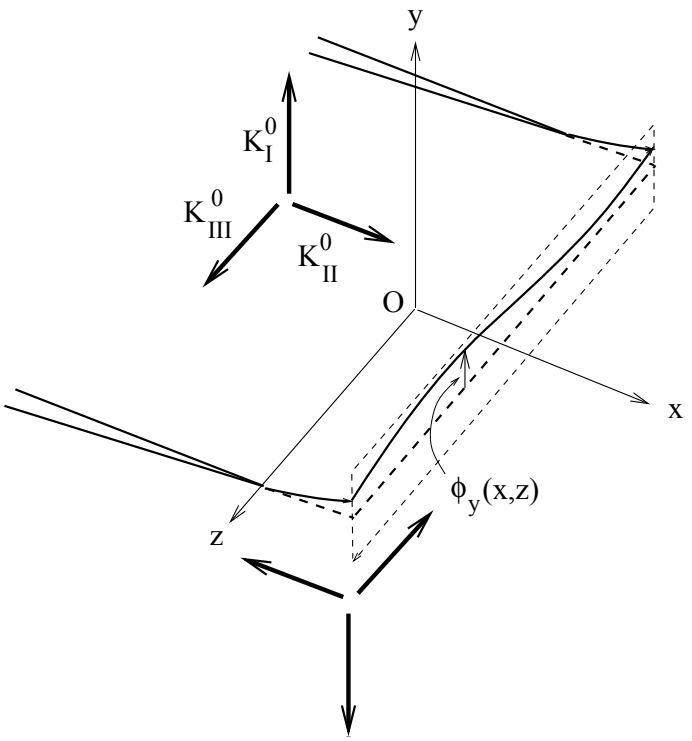

Fig. 36 Out-of-plane perturbation of the crack surface of a semi-infinite crack

where ν denotes Poisson's ratio and the symbol PV a Cauchy Principal Value. In addition Movchan et al. (1998)s formulae read:

$$\begin{cases} \delta_y K_I(x,z) &= -\dfrac{3}{2} K_{II}^0 \dfrac{\partial \phi_y}{\partial x}(x,z) - 2K_{III}^0 \dfrac{\partial \phi_y}{\partial z}(x,z) \\ &\quad -\dfrac{K_{II}^0}{2\pi}\, PV \int_{-\infty}^{+\infty} \dfrac{\phi_y(x,z') - \phi_y(x,z)}{(z'-z)^2}\, dz' + \delta_y K_I^{\text{skew}}(x,z) \\ \delta_y K_{II}(x,z) &= \dfrac{K_I^0}{2} \dfrac{\partial \phi_y}{\partial x}(x,z) \\ &\quad -\dfrac{2-3\nu}{2-\nu} \dfrac{K_I^0}{2\pi}\, PV \int_{-\infty}^{+\infty} \dfrac{\phi_y(x,z') - \phi_y(x,z)}{(z'-z)^2}\, dz' \\ \delta_y K_{III}(x,z) &= \dfrac{2(1-\nu)^2}{2-\nu} K_I^0 \dfrac{\partial \phi_y}{\partial z}(x,z). \end{cases} \tag{148}$$

In the expression of $\delta_y K_I(x,z)$ here, the quantity $\delta_y K_I^{\text{skew}}(x,z)$ is connected to Bueckner (1987)s *skew-symmetric* (whence the notation) crack face weight functions. Movchan et al. (1998) calculated this term only for a perturbation $\phi_y(x,z)$ independent of x. Their calculation was extended to an arbitrary perturbation $\phi_y(x,z)$ by Leblond et al. (2011), with the following result:

$$\delta_y K_I^{\text{skew}}(x,z) = \frac{\sqrt{2}}{4\pi}\,\frac{1-2\nu}{1-\nu}\,\text{Re}\left\{\int_{-\infty}^{x} dx' \int_{-\infty}^{+\infty} \frac{[K_{III}^0 - i(1-\nu)K_{II}^0](\partial\phi_y/\partial z)(x',z')}{(x-x')^{1/2}\,[x-x'+i(z-z')]^{3/2}}\,dz'\right\} \tag{149}$$

where the cut of the complex power function is along the half-line of negative real numbers.

The presence of local, semi-local and non-local terms, in the sense defined in Sect. 4.1, is conspicuous in equations (148) and (149). Note however that $\delta_y K_I^{\text{skew}}(x,z)$ is the only term of truly non-local nature.[18]

4.4 *Linear Stability Analysis of a Semi-infinite Crack Loaded in Mixed-Mode I+III*

Preliminaries. This subsection is based on the work of Leblond et al. (2011). We consider the geometric and mechanical situation depicted in Sect. 4.3, with the additional assumption that the unperturbed SIF K_{II}^0 of mode II is zero, so that the crack is globally loaded in mode I+III. Without any loss of generality, we may assume K_{III}^0 to be positive like K_I^0.

The prediction of the crack path will be based on a double propagation criterion, enforced at all points of the crack front and all instants, consisting of

- Griffith (1920)s condition $G(x,z) = G_c$ where $G(x,z)$ denotes the local energy-release-rate, and G_c its critical value;
- Goldstein and Salganik (1974)s PLS, which states that the local SIF $K_{II}(x,z)$ of mode II must be zero.

In a first approach, the critical energy-release-rate G_c will be supposed to be a constant along the front, independent of the stress state prevailing locally, that is of the local mixity ratio $K_{III}(x,z)/K_I(x,z)$.

The analysis will be based on consideration of instability modes of the form

$$\begin{cases} \phi_x(x,z) = e^{\lambda x}\,\psi_x(z) \\ \phi_y(x,z) = e^{\lambda x}\,\psi_y(z) \end{cases} \tag{150}$$

[18] There were other non-local terms in Movchan et al. (1998)s original formulae, connected to the unperturbed non-singular stresses and higher-order constants characterizing the initial stress field, which are disregarded here.

where λ is an unknown positive parameter homogeneous to the inverse of a length, characterizing the *growth rate* of the mode in the direction x of propagation, and $\psi_x(z)$, $\psi_y(z)$ unknown functions characterizing the *shape* of the deformed crack front.

Use will be made of Fourier transforms in the direction z of the crack front; the definition adopted here for the Fourier transform $\widehat{\chi}(k)$ of an arbitrary function $\chi(z)$ is the same as in Sect. 3, Eq. (69). Also, we define the "normalized growth rate" ξ of the instability mode in the direction x by the formula

$$\xi \equiv \frac{\lambda}{|k|} \quad (> 0); \tag{151}$$

this dimensionless parameter compares the growth rate λ of the instability mode in the direction x of propagation, to the wavenumber $|k|$ of the Fourier component considered in the direction z of the crack front.

Application of the double criterion. The first task is to calculate the Fourier transforms $\widehat{\delta K_p}$ of the variations δK_p ($p = I, II, III$) of the SIFs. One gets after some lengthy calculations (Leblond et al. 2011):

$$\left\{\begin{array}{ll}
\widehat{\delta K_I}(x,k) & = e^{\lambda x}\left\{-K_I^0\dfrac{|k|}{2}\widehat{\psi_x}(k)\right. \\
& \quad \left. +iK_{III}^0\left[-2+\dfrac{1-2\nu}{\sqrt{2}(1-\nu)}F(\xi)\right]k\widehat{\psi_y}(k)\right\} \\
\widehat{\delta K_{II}}(x,k) & = e^{\lambda x}\left\{-iK_{III}^0\dfrac{2}{2-\nu}k\widehat{\psi_x}(k)\right. \\
& \quad \left. +K_I^0\left[\dfrac{2-3\nu}{2(2-\nu)}|k|+\dfrac{\lambda}{2}\right]\widehat{\psi_y}(k)\right\} \\
\widehat{\delta K_{III}}(x,k) & = e^{\lambda x}\left\{-K_{III}^0\dfrac{2+\nu}{2(2-\nu)}|k|\widehat{\psi_x}(k)+iK_I^0\dfrac{2(1-\nu)^2}{2-\nu}k\widehat{\psi_y}(k)\right\} \\
F(\xi) & \equiv \dfrac{1}{\sqrt{1+\xi}}\,.
\end{array}\right. \tag{152}$$

The PLS in "Fourier's form", $\widehat{\delta K_{II}}(x,k) = 0$, then yields, with $\mathrm{sgn}(x)$ denoting the sign of x:

$$\widehat{\psi_y}(k) = \frac{4i}{2-3\nu+(2-\nu)\xi}\,\rho^0\,\mathrm{sgn}(k)\widehat{\psi_x}(k) \quad , \quad \rho^0 \equiv \frac{K_{III}^0}{K_I^0}\,; \tag{153}$$

the quantity ρ^0 here is the unperturbed mode mixity ratio.

Using this expression to eliminate the Fourier transform $\widehat{\psi_y}$ of the out-of-plane perturbation, plus Irwin's formula, one can get the Fourier transform $\widehat{\delta G}$ of the perturbation of the energy-release-rate, as a function of the Fourier transform $\widehat{\psi_x}$ of the sole in-plane perturbation. One thus gets, again after some lengthy calculations

(Leblond et al. 2011):

$$\frac{\widehat{\delta G}(x,k)}{G^0} = -e^{\lambda x} f(\rho^0;\xi)\,|k|\widehat{\psi_x}(k), \tag{154}$$

where

$$G^0 \equiv \frac{1-\nu^2}{E}(K_I^0)^2 + \frac{1+\nu}{E}(K_{III}^0)^2 \tag{155}$$

is the unperturbed energy-release-rate, and f the function defined by:

$$f(\rho;\xi) \equiv \frac{1-\nu}{1-\nu+\rho^2}\left\{1 - \frac{3(2-\nu) - 4\sqrt{2}(1-2\nu)F(\xi) - (2+\nu)\xi}{(1-\nu)\,[2-3\nu+(2-\nu)\xi]}\,\rho^2\right\}. \tag{156}$$

Griffith (1920)s criterion in "Fourier's form", $\widehat{\delta G}(x,k) = 0$, then yields at the different orders in the pair (ϕ_x, ϕ_y):

- At order 0:

$$G^0 = G_c. \tag{157}$$

  This condition specifies the intensity of the loading inducing crack propagation.
- At order 1:

$$f(\rho^0;\xi)\,|k|\widehat{\psi_x}(k) = 0 \quad (\forall k).$$

  There are then two possibilities for each nonzero value of the wavenumber k: either the Fourier component $\widehat{\psi_x}(k)$ is zero and this relation is trivially satisfied; or $\widehat{\psi_x}(k)$ is not zero and then necessarily

$$f(\rho^0;\xi) = 0. \tag{158}$$

  This condition specifies the value of the normalized growth rate $\xi = \lambda/|k|$ of the instability mode, as a function of the unperturbed mode mixity ratio $\rho^0 = K_{III}^0/K_I^0$.

Growth rate of the instability modes and critical mode mixity ratio. Equation (158) may be formally solved with respect to ξ by artificially considering the quantity $F(\xi)$ as known. One thus gets:

$$\xi = \frac{N(\rho^0;\xi)}{D(\rho^0)} \quad , \quad \begin{cases} N(\rho;\xi) \equiv -(1-\nu)(2-3\nu) \\ \qquad\qquad + \left[3(2-\nu) - 4\sqrt{2}(1-2\nu)F(\xi)\right]\rho^2 \\ D(\rho) \quad \equiv (1-\nu)(2-\nu) + (2+\nu)\rho^2\,. \end{cases} \tag{159}$$

Equation (159) is in a form convenient for a mathematical analysis, presented in full detail in Leblond et al. (2011). The following conclusions were reached there:

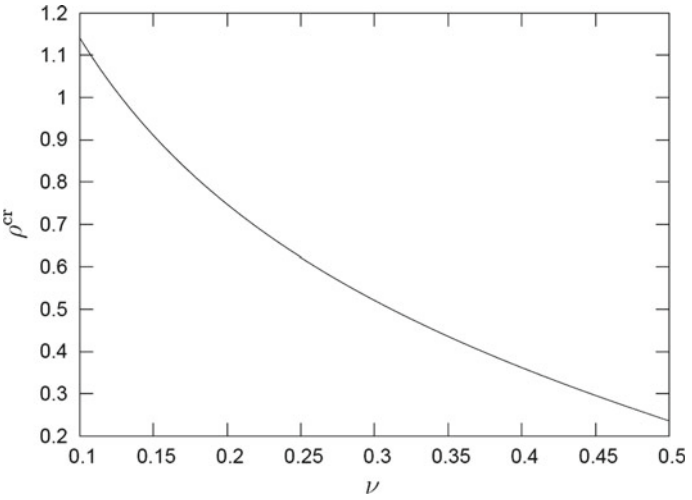

Fig. 37 Plot of the critical mixity ratio versus Poisson's ratio, for a mode I+III loading

- The equation $N(\rho^0; 0) = 0$ (corresponding to $\xi = 0$ in Eq. (159)) admits a unique positive solution ρ^{cr}, given by

$$\rho^{cr} = \sqrt{\frac{(1-\nu)(2-3\nu)}{3(2-\nu) - 4\sqrt{2}\,(1-2\nu)}}\,. \tag{160}$$

  This solution represents the "critical value" of the unperturbed mixity ratio ρ^0 for which a neutrally stable mode (having $\xi = 0$) exists. This critical value is plotted as a function of Poisson's ratio in Fig. 37.
- For values of ρ^0 larger than ρ^{cr}, Eq. (159) on ξ admits a unique positive solution. Hence an instability mode exists.
- For values of ρ^0 smaller than ρ^{cr}, equation (159) on ξ does not admit any positive solution (except in the case where ν is very close to zero, which is of little practical interest). Hence there is no instability mode.

These results mean that *the critical value* ρ^{cr} *of the unperturbed mixity ratio* ρ^0 *represents a threshold above which an instability occurs*.

Because the term $3(2-\nu) - 4\sqrt{2}(1-2\nu)F(\xi)$ in $N(\rho; \xi)$ varies modestly with ξ, equation (159) is also in a form convenient for the numerical calculation of ξ as a function of ρ^0, by a simple fixed-point method. Examples for various values of ν are provided in the work of Leblond et al. (2011).

Geometry of the instability modes. To discuss instability modes, we consider a positive value of the wavenumber k, and an in-plane perturbation of the crack front of the form

$$\psi_x(z) \equiv A_x \cos(kz + \theta) = \frac{A_x}{2}\left[e^{i(kz+\theta)} + e^{-i(kz+\theta)}\right] \tag{161}$$

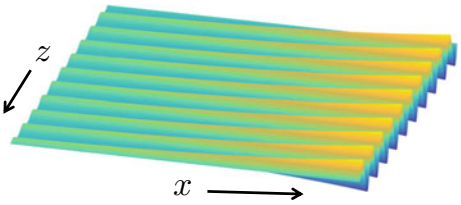

Fig. 38 Instability mode for a mode I+III loading: geometry of perturbed surface

where A_x and θ are real numbers, with Fourier transform

$$\widehat{\psi_x}(k') = \frac{A_x}{2}\left[e^{i\theta}\,\delta(k'-k) + e^{-i\theta}\,\delta(k'+k)\right]. \tag{162}$$

Then by Eq. (153), the Fourier transform of the out-of-plane perturbation of the crack surface is given by

$$\widehat{\psi_y}(k') = \frac{4i}{2-3\nu+(2-\nu)\xi}\,\rho^0\,\frac{A_x}{2}\left[e^{i\theta}\,\delta(k'-k) - e^{-i\theta}\,\delta(k'+k)\right],$$

and it follows that

$$\begin{aligned}\psi_y(z) &= \frac{4i}{2-3\nu+(2-\nu)\xi}\,\rho^0\,\frac{A_x}{2}\left[e^{i(kz+\theta)} - e^{-i(kz+\theta)}\right]\\ &= -\frac{4}{2-3\nu+(2-\nu)\xi}\,\rho^0 A_x\sin(kz+\theta).\end{aligned} \tag{163}$$

From there and equations (150), one gets the components of the instability mode:

$$\begin{cases}\phi_x(x,z) = A_x e^{\xi kx}\cos(kz+\theta)\\ \phi_y(x,z) = A_y e^{\xi kx}\sin(kz+\theta)\end{cases},\quad A_y = -\frac{4\rho^0}{2-3\nu+(2-\nu)\lambda/k}\,A_x. \tag{164}$$

Equation (164) specifies the geometry of the instability mode: the perturbed crack front assumes the shape of *an elliptic helix, of central axis coinciding with the present unperturbed crack front, and semi-axes in the directions x and y growing in proportion and exponentially with the distance of propagation*. Figures 38 and 39 represent schematically the geometries of the deformed surface and front of the crack.

Discussion. The results of subsubsection **Geometry of the instability modes** are appealing in that the instability modes found correspond closely to those observed in Pons and Karma (2010)s numerical simulations, based on Karma et al. (2001)s phase-field model. Even the precise value of the threshold predicted by equation (160) was confirmed, with a reasonable accuracy, by Chen et al. (2015)s more recent, very thorough numerical study.

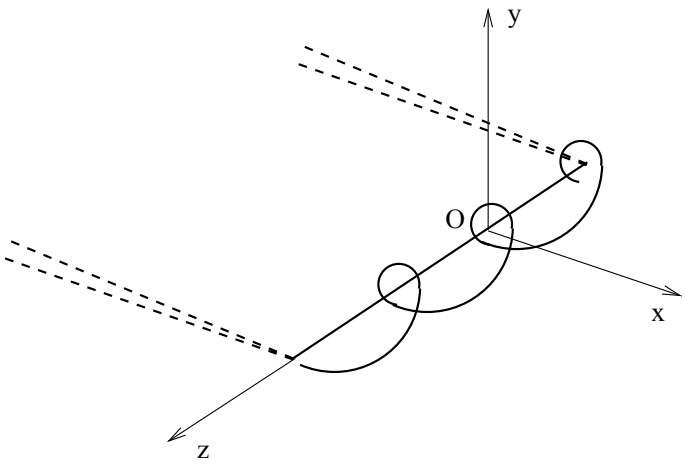

Fig. 39 Instability mode for a mode I+III loading: geometry of perturbed front

Equation (160) however raises a serious problem, in that as already mentioned in Sect. 4.1, the threshold values it predicts are generally much larger than those actually observed. Another problem is that the theoretical threshold depends only on Poisson's ratio, so that it varies modestly from one material to another; whereas, as mentioned in Sect. 4.1, widely different thresholds have been observed in different materials. This experimental observation suggests that the threshold may depend in reality on additional material parameters.

4.5 Application of Cotterell and Rice (1980)s Directional Stability Criterion to Cracks Propagating in Mode I+III

Context. The gap between theoretical and experimental values of the threshold could perhaps be explained by a strong destabilizing influence, well below the theoretical threshold, of imperfections of the crack front geometry and/or the loading upon the fundamental coplanar configuration of the crack. Such a strong influence is to be expected if the bifurcation accompanying the instability of coplanar crack propagation is of subcritical nature. This idea was explored by Chen et al. (2015), using numerical simulations analogous to, and extending those of Pons and Karma (2010), based on Karma et al. (2001)s phase-field model. The results clearly pointed to a strongly subcritical character of the bifurcation, implying an important influence of imperfections below the theoretical threshold.

In this subsection, based on the work of Leblond and Lazarus (2015), we present a theoretical complement to Chen et al. (2015)s simulations, in the form of a qualitative directional stability analysis, based on the 3D extension of Cotterell and Rice (1980)s stability criterion presented in subsubsection **Two simple applications**. But this

analysis also stands as complement to the work of Gao and Rice (1986). These authors noted that for a mode I+III crack slightly perturbed within its plane, the mode III loading component must generate nonzero and opposite local mode II SIFs on the two sides of a local protrusion of the front; thus the crack will tend to extend out of its original plane in opposite directions on these two sides, giving birth to an incipient non-coplanar facet. We shall show here that in addition, Cotterell and Rice (1980)s directional stability criterion may be violated, because of a locally positive non-singular stress in the direction of crack propagation; so that the deviation of this facet from the original crack plane may increase upon propagation, even in the absence of a true bifurcation.

First-order variation of the non-singular stresses for a semi-infinite crack slightly perturbed within its plane. Following Gao and Rice (1986)s line of thought, we consider the situation where the mode I+III crack already exhibits slight imperfections, in the form of small in-plane undulations of its front, due for instance to some slight spatial variations of toughness. According to Gao and Rice (1986)s analysis, fracture facets, implying out-of-plane deviations of the crack, must then form; but they have not started to do so yet. We wish to use Cotterell and Rice (1980)s criterion to analyze the directional stability of coplanar crack propagation, and for this we need to know the distribution of the non-singular stresses along the coplanarly perturbed crack front.

We thus consider a situation analogous to that in Sect. 4.3, but now with a crack perturbation confined to the original crack plane: $\phi_x(z) \neq 0$, $\phi_y(z) \equiv 0$ (Fig. 35). Like in Sect. 4.3, we assume the crack to be loaded by some system of forces independent of the coordinate z, so that the unperturbed SIFs K_I^0, K_{II}^0, K_{III}^0[19] as well as the unperturbed non-singular stresses T_{xx}^0, T_{zz}^0, T_{xz}^0 are constant along the crack front. We also again disregard the variation of these unperturbed SIFs and non-singular stresses with the position x of the front within the crack plane. (This permits to omit various indications of dependence upon this coordinate in the sequel).

The first-order variations $\delta_x T_{xx}(z)$, $\delta_x T_{zz}(z)$, $\delta_x T_{xz}(z)$ of the non-singular stresses along the front may be obtained from Rice (1985, 1989)s equation (49) of Chap. 3, providing the variation $\delta_x u_i(M)$ of the displacement at some arbitrary point M in the body. The procedure, detailed in Leblond and Lazarus (2015), is basically analogous to, but somewhat more elaborate than that for the variations of the SIFs; it may be summarized as follows:

1. Apply equation (49) on the faces $y = 0^{\pm}$ of the crack surface, to get the variations $\delta_x u_x$, $\delta_x u_z$ of the in-plane components of the displacement there.
2. Differentiate with respect to x and z, to get the variations $\delta\epsilon_{xx}$, $\delta\epsilon_{zz}$, $\delta\epsilon_{xz}$ of the in-plane components of the strain tensor on the faces of the crack.
3. Apply the elasticity operator in *plane stress* (since $\sigma_{yy} = 0$ by the boundary conditions), to get the variations $\delta\sigma_{xx}$, $\delta\sigma_{zz}$, $\delta\sigma_{xz}$ of the in-plane components of the stress tensor on these faces.

[19] The unperturbed SIF K_{II}^0 may harmlessly be assumed to be nonzero; this has no impact upon the results of this subsubsection.

4. Deduce from there the variations $\delta_x T_{xx}(z)$, $\delta_x T_{zz}(z)$, $\delta_x T_{xz}(z)$ of the non-singular stresses. This is easily done; indeed there is a direct connection between the stress components σ_{xx}, σ_{zz}, σ_{xz} on the crack faces and the non-singular stresses.

   The results read as follows Leblond and Lazarus (2015):

$$\left\{\begin{array}{l}
\delta_x T_{xx}(z) = -2T^0_{xz}\dfrac{d\phi_x}{dz}(z) \\
\qquad\qquad -\dfrac{1-2\nu}{4\sqrt{2\pi}}K^0_I\displaystyle\int_{-\infty}^{+\infty}\left[\frac{d\phi_x}{dz}(z')-\frac{d\phi_x}{dz}(z)\right]\frac{\mathrm{sgn}(z'-z)}{|z'-z|^{3/2}}\,dz'; \\
\delta_x T_{zz}(z) = 2T^0_{xz}\dfrac{d\phi_x}{dz}(z) \\
\qquad\qquad +\dfrac{1-2\nu}{4\sqrt{2\pi}}K^0_I\displaystyle\int_{-\infty}^{+\infty}\left[\frac{d\phi_x}{dz}(z')-\frac{d\phi_x}{dz}(z)\right]\frac{\mathrm{sgn}(z'-z)}{|z'-z|^{3/2}}\,dz'; \\
\delta_x T_{xz}(z) = \left(T^0_{xx}-T^0_{zz}\right)\dfrac{d\phi_x}{dz}(z) \\
\qquad\qquad -\dfrac{1-2\nu}{4\sqrt{2\pi}}K^0_I\displaystyle\int_{-\infty}^{+\infty}\left[\frac{d\phi_x}{dz}(z')-\frac{d\phi_x}{dz}(z)\right]\frac{dz'}{|z'-z|^{3/2}}\,.
\end{array}\right. \tag{165}$$

Note that the SIFs K^0_{II} and K^0_{III} nowhere appear in these formulae. This property could be anticipated from some symmetry argument: the perturbed non-singular stresses T_{xx}, T_{zz}, T_{xz}, being invariant in a symmetry with respect to the plane Oxz, cannot depend upon K^0_{II} and K^0_{III} which change sign upon such a symmetry.

It should also be noted that formulae (165) were obtained, albeit in Fourier's form rather than in the physical space, by Gao (1992) much before Leblond and Lazarus (2015)s work. The derivation was however incomplete and relied on unnecessarily strong hypotheses; on this point see the discussion in Leblond and Lazarus (2015).

Application to stability of in-plane propagation of a mixed-mode I+III crack. We now assume the crack to be loaded in mode I+III ($K^0_{II}=0$), and the in-plane undulations of its front to be for instance sinusoidal, of (small) amplitude A, (positive) wavenumber k and phase θ:

$$\phi_x(z) = A\cos(kz+\theta). \tag{166}$$

This situation is depicted schematically in Fig. 40. Note that in this figure the more advanced zones of the perturbed crack front, having $\cos(kz+\theta)>0$, are indicated with a symbol A, and the less advanced ones, having $\cos(kz+\theta)<0$, with a symbol B.[20] The amplitude A is assumed to be much smaller than the wavelength $\lambda = 2\pi/k$ of the perturbation $\phi_x(z)$, in order for the first-order expressions of the variations of the SIFs and non-singular stresses to be applicable.

[20] This now widely adopted terminology was first suggested by Hourlier and Pineau (1979).

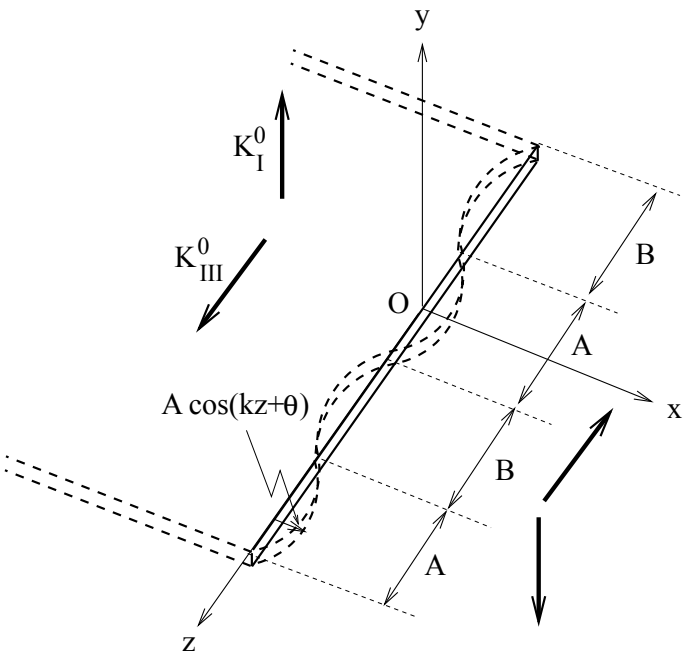

Fig. 40 In-plane sinusoidal perturbation of a semi-infinite crack loaded in mode I+III

We shall need the expressions of the SIF $K_{II}(z)$ and the non-singular stress $T_{xx}(z)$ along the perturbed crack front. That of $K_{II}(z)$ is a straightforward consequence of Gao and Rice (1986)s formula $(147)_2$:

$$K_{II}(z) = K_{II}^0 + \delta K_{II}(z) = \frac{2}{2-\nu} K_{III}^0 kA \sin(kz+\theta). \tag{167}$$

To evaluate the expression of the variation $\delta T_{xx}(z)$, we assume, like in Sect. 4.3, that the characteristic length L defined by the loading is much larger than the wavelength λ of the perturbation $\phi_x(z)$. Then the term proportional to T_{xz}^0 in the expression $(165)_1$ of $\delta T_{xx}(z)$, of order $\frac{K_I^0}{\sqrt{L}} \frac{A}{\lambda}$, is negligible compared to the integral term, of order $K_I^0 \frac{A}{\lambda^{3/2}}$; and calculation of the latter term yields (Leblond and Lazarus 2015):

$$\delta T_{xx}(z) \simeq \left(\frac{1}{2} - \nu\right) K_I^0 k^{3/2} A \cos(kz+\theta). \tag{168}$$

We finally introduce the extra assumption that *the amplitude A of the in-plane perturbation is much larger than* $\lambda^{3/2} L^{-1/2} = \lambda \sqrt{\frac{\lambda}{L}}$. (This hypothesis is compatible with the condition $A \ll \lambda$, since $\frac{\lambda}{L} \ll 1$). With this assumption, the initial non-

singular stress T^0_{xx}, of order $\frac{K^0_I}{\sqrt{L}}$, is much smaller than its variation $\delta T_{xx}(z)$, of order $K^0_I \frac{A}{\lambda^{3/2}}$, so that the value of the perturbed non-singular stress is

$$T_{xx}(z) = T^0_{xx} + \delta T_{xx}(z) \simeq \left(\frac{1}{2} - \nu\right) K^0_I k^{3/2} A \cos(kz + \theta). \tag{169}$$

All elements are now at hand for a discussion of the formation and directional stability of incipient facets.

- *Formation of facets*. Following Gao and Rice (1986), we note that according to equation (167), $K_{II}(z)$ takes opposite values on the two sides of a type A (advanced) or type B (retarded) zone of the crack front. Then, according to equation (37) extended to the 3D case, that is with $\alpha(z)$, $K_I(z)$, $K_{II}(z)$ instead of α, K^0_I, K^0_{II}, the local resulting kink angle $\theta(z)$ will also take opposite values on these two sides. This implies formation of an incipient non-coplanar facet, originating from the zone of type A or B considered, and gradually rotating about the direction x of crack propagation. Facets of type A and B rotate in opposite directions.
- *Directional stability of facets*. According to equation (169), on a type A zone, the non-singular stress $T_{xx}(z)$ is positive so that Cotterell and Rice (1980)s directional stability criterion is violated, implying directional instability; conversely, on a type B zone, $T_{xx}(z)$ is negative and Cotterell and Rice (1980)s criterion is met, implying directional stability. Thus, type A (advanced) facets tend to gradually deviate more and more from the original crack plane, whereas type B (retarded) facets tend to come back to it. This lends support to the intuitive idea that the crack would ideally prefer to develop only along unstable, tilted facets of type A; stable facets of type B being present only because they are "geometric necessary". Note that these qualitative tendencies are independent of the value of the ratio K^0_{III}/K^0_I as soon as $K^0_{III} \neq 0$ (which is a necessary condition for out-of-plane deviations of the crack to appear). Thus development of tilted facets of type A, generated for instance by in-plane fluctuations of the fracture toughness of sufficient amplitude, are probable because of a Cotterell and Rice (1980)-type instability, even for values of this ratio well below Leblond et al. (2011)s theoretical threshold (equation (160)).

To analyze in more detail Cotterell and Rice (1980)s instability as a function of the wavelength $\lambda = 2\pi/k$ of the initial coplanar perturbation $\phi_x(z)$, one must examine the value of the pseudo-curvature parameter $a^*(z)$ of the incipient facets. Combining the PLS with equations (145), (167) and (169), one gets

$$a^*(z) = -\frac{16}{3}\sqrt{\frac{2}{\pi}}\,\frac{1-2\nu}{2-\nu}\,\frac{K^0_{III}}{K^0_I}\,k^{5/2}A^2 \sin(kz+\theta)\cos(kz+\theta). \tag{170}$$

This expression shows that the pseudo-curvature parameter $a^*(z)$ depends on the (square of the) amplitude A of the in-plane perturbation. Therefore, to examine the influence of the wavelength of the perturbation, it is necessary to fix this amplitude in some way or other. A natural way of doing so is to consider "homothetical" per-

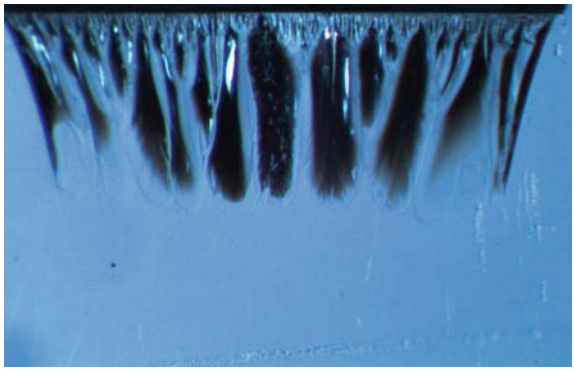

Fig. 41 Photograph of a mode I+III fracture surface, showing facets of gradually increasing size (after Leblond and Lazarus (2015))

turbations (differing in size but identical in shape), having $A/\lambda = \text{Cst.}$ or $kA = \text{Cst.}$ Then, according to equation (170), $a^*(z)$ is proportional to $(kA)^2\sqrt{k}$, that is to $\sqrt{k}$ or $1/\sqrt{\lambda}$ for a given value of kA. Therefore, the smaller λ, the larger $|a^*(z)|$: in other words, *the smaller the wavelength of the initial in-plane perturbation, the more directionally unstable/stable the incipient facets of type A/B it generates*. This theoretical conclusion seems compatible with the experimental observation that incipient facets are generally of tiny initial wavelength, apparently limited in smallness only by the microstructure. This is illustrated in Fig. 41, which shows a photograph of a fracture surface resulting from top-to-bottom propagation of a crack loaded in mode I+III in a glass specimen.[21]

4.6 Extension of the Stability Analysis to the Case of a Mode-Dependent Critical Energy-release-rate

Preliminaries. Although previous conclusions about the strong influence of imperfections upon stability of coplanar crack propagation in mode I+III were appealing, the analysis was not free of shortcomings. Indeed, although it might explain why actually observed values of the threshold value ρ^{cr} of the mixity ratio $\rho^0 = K^0_{III}/K^0_I$ are generally so much smaller than the theoretical value given by equation (160), it did not supply any estimate of the "practical" threshold. In particular, it failed to provide any rationale for the high variability, mentioned in Sect. 4.1, of the actual threshold from one material to another.

The aim of this subsection, adapted from the work of Leblond et al. (2018), is to explore another possible explanation of the large gap between experimental and theoretical values of the threshold: namely, the idea that the fracture energy G_c might

[21] The facet wavelength does not, however, remain small when the crack propagates, due to some "coarsening" of facets resulting from several coalescence events. But this phenomenon is ignored in the present analysis limited to incipient facets.

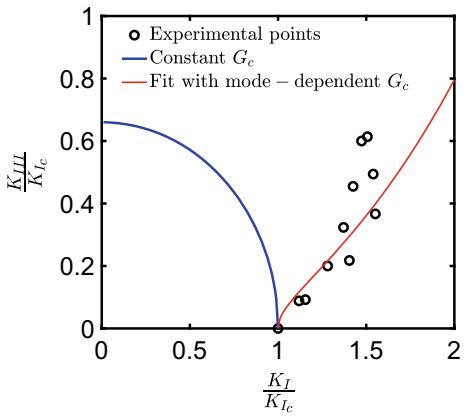

Fig. 42 Locus of the pairs $\left(\frac{K_I}{K_{Ic}}, \frac{K_{III}}{K_{Ic}}\right)$ for crack initiation under conditions of mixed mode I + III (after Lin et al. (2010), with permission)

not be a constant but depend upon the local mode mixity ratio

$$\rho(x, z) \equiv \frac{K_{III}(x, z)}{K_I(x, z}\,. \tag{171}$$

For interfacial fracture in mode I+II between distinct materials, the dependence of the critical energy-release-rate upon the ratio K_{II}/K_I is well documented; see for instance the work of Freund et al. (2003). For fracture under mixed-mode I+III conditions, an influence of $\rho = K_{III}/K_I$ upon G_c is in line with the general observation that crack propagation is more difficult than in pure mode I: the effect is illustrated in Fig. 42, borrowed from the work of Lin et al. (2010), which shows the experimental locus of the pairs $\left(\frac{K_I}{K_{Ic}}, \frac{K_{III}}{K_{Ic}}\right)$ leading to crack initiation under mixed-mode I + III conditions. The idea of a G_c depending on ρ *via* some material-dependent parameter is also indirectly supported by the observed variability of the threshold, which can hardly be ascribed to the rather modest variability of Poisson's ratio.

Possible physical mechanisms underlying the dependence of G_c upon $\rho = K_{III}/K_I$ were evoked in the work of Leblond et al. (2018). However our aim here is not to discuss such mechanisms, but merely to heuristically postulate the existence of such a dependence, and explore its consequences upon the linear stability analysis expounded above.

More specifically, we shall consider the function $G_c(\rho)$ to be of the form

$$G_c(\rho) \equiv G_c^{\text{mode I}}\,(1 + \gamma|\rho|^{\kappa})\,, \tag{172}$$

where $G_c^{\text{mode I}}$ denotes the critical energy-release-rate in pure mode I, and γ and κ positive dimensionless material parameters. The positivity of γ means that the presence of mode III *increases* the value of the critical energy-release-rate, in line with Lin et al. (2010)s observations. For the parameter κ, a value of 2 represents the most natural choice, since it is the smallest that simultaneously respects evenness

and smoothness of the function $G_c(\rho)$. But we keep it here as a free parameter, so as not to restrict generality of the stability analysis.

Theoretical analysis. We consider the same situation as in Sect. 4.4; in particular, the unperturbed crack is loaded under a combination of modes I and III ($K^0_{II} = 0$), with $K^0_{III} > 0$. The sole difference is that here G_c is supposed to depend on ρ according to equation (172).

Equations (152) for the Fourier transforms of the variations of the SIFs still hold. From there, and using equation (153) deduced from the PLS, one obtains not only equation (154) for the Fourier transform of the variation of the energy-release-rate, but also the following expression of the Fourier transform of the variation of the mixity ratio $\rho(x, z)$ (required for the application of Griffith (1920)s criterion):

$$\widehat{\delta\rho}(x, k) = -e^{\lambda x} g(\rho^0; \xi)\, |k| \widehat{\psi_x}(k) \tag{173}$$

where

$$g(\rho; \xi) \equiv \frac{\rho}{2 - 3\nu + (2 - \nu)\xi} \left\{ 4 - 5\nu + \nu\xi + 2 \left[4 - \sqrt{2}\, \frac{1 - 2\nu}{1 - \nu} F(\xi) \right] \rho^2 \right\}. \tag{174}$$

To now enforce Griffith (1920)s criterion $G(x, z) = G_c(x, z)$ for every x and z, we use the expressions of $G(x, z)$ and $G_c(x, z)$ expanded to first order in the pair (ϕ_x, ϕ_y):

$$\begin{cases} G(x, z) &= G^0 + \delta G(x, z) \\ G_c(x, z) &= G_c(\rho^0) + \dfrac{dG_c}{d\rho}(\rho^0)\, \delta\rho(x, z) \end{cases} \tag{175}$$

where δG and $\delta\rho$ are given, in Fourier's form, by Eqs. (154) and (173). One thus gets at the successive orders, like in Sect. 4.4:

- At order 0:

$$G^0 = G_c(\rho^0) \quad (= G_c^{\text{mode I}}[1 + \gamma(\rho^0)^\kappa]). \tag{176}$$

- At order 1:

$$\delta G(x, z) = \frac{dG_c}{d\rho}(\rho^0)\, \delta\rho(x, z) \quad \Rightarrow$$

$$G^0 e^{\lambda x} f(\rho^0; \xi)\, |k| \widehat{\psi_x}(k) = \frac{dG_c}{d\rho}(\rho^0)\, e^{\lambda x} g(\rho^0; \xi)\, |k| \widehat{\psi_x}(k) \quad (\forall k).$$

If the Fourier component $\widehat{\psi_x}(k)$ is nonzero, then necessarily

$$f(\rho^0; \xi) - \frac{d(\ln G_c)}{d\rho}(\rho^0)\, g(\rho^0; \xi) = 0 \tag{177}$$

where equation (176) has been used.

Just like in subsubsection **Growth rate of the instability modes and critical mode mixity ratio**, Eq. (177) on ξ may be put in the following form, convenient for both its mathematical analysis and its numerical solution:

$$\xi = \frac{N(\rho^0;\xi)}{D(\rho^0)}, \quad \begin{cases} N(\rho;\xi) \equiv -(1-\nu)(2-3\nu) \\ \quad + \left[3(2-\nu) - 4\sqrt{2}(1-2\nu)F(\xi)\right]\rho^2 \\ \quad + X(\rho)\left(1-\nu+\rho^2\right)\left\{4-5\nu+2\left[4-\sqrt{2}\dfrac{1-2\nu}{1-\nu}F(\xi)\right]\rho^2\right\} \\ D(\rho) \equiv (1-\nu)(2-\nu) + (2+\nu)\rho^2 - X(\rho)\nu\left(1-\nu+\rho^2\right) \\ X(\rho) \equiv \dfrac{\kappa\gamma\rho^\kappa}{1+\gamma\rho^\kappa}\,. \end{cases} \tag{178}$$

Equation (178) is analogous to equation (159) of Sect. 4.4, except for the more complex expressions of the numerator $N(\rho;\xi)$ and the denominator $D(\rho)$ arising from the terms proportional to $X(\rho)$, tied to the dependence of G_c upon ρ and hence to the material parameters γ and κ.

A thorough mathematical analysis of equation (178), presented in the work of Leblond et al. (2018), reveals the following features:

- The equation $N(\rho^0;0) = 0$ admits a unique positive solution ρ^{cr}, which again represents the critical value of the unperturbed mode mixity ratio ρ^0 for which a neutrally stable mode exists. But unlike in the case of a constant G_c, this critical value does not admit a simple analytic expression analogous to (160).
- Assume that $\kappa \leq 3$. Then for values of the unperturbed mode mixity ratio ρ^0 larger than ρ^{cr}, the equation $\xi = N(\rho^0;\xi)/D(\rho^0)$ on ξ admits a unique positive solution: an instability mode exists.
- Assume that $\kappa \leq 3$ and ν is not too close to 0.[22] Then for values of ρ^0 smaller than ρ^{cr}, the equation $\xi = N(\rho^0;\xi)/D(\rho^0)$ on ξ does not admit any positive solution: no instability mode exists.

Numerical illustrations. Figures 43 and 44 show the critical mode mixity ratio ρ^{cr}—obtained by numerically solving the equation $N(\rho^{\mathrm{cr}};0) = 0$—as a function of Poisson's ratio ν, for several values of the material parameters γ and κ. The dependence of G_c upon ρ is observed to have a major influence on the critical mode mixity ratio: the larger γ, the smaller ρ^{cr}, whereas the effect of κ is less straightforward and depends upon the value of ν.

Figure 44 makes it clear that $\rho^{\mathrm{cr}} \ll 1$ when $\gamma \gg 1$. This leads to an analytical estimate of ρ^{cr} in this case. Indeed when $\rho \ll 1$, the expression of $N(\rho;0)$ becomes, with the approximations $-(1-\nu)(2-3\nu) + [...]\rho^2 \simeq -(1-\nu)(2-3\nu)$, $1-\nu+\rho^2 \simeq 1-\nu$, $4-5\nu+2[...]\rho^2 \simeq 4-5\nu$:

[22] The precise minimum value of ν is given in Leblond et al. (2018).

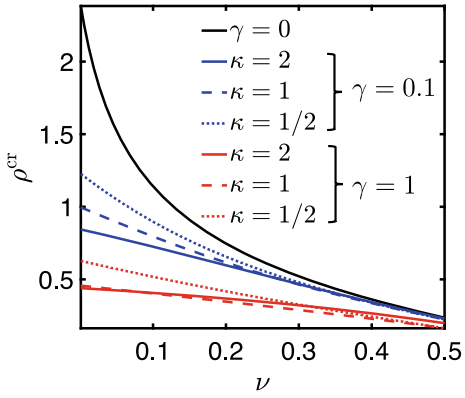

Fig. 43 Critical mode mixity ratio $\rho^{\rm cr}$ versus Poisson's ratio ν, for various values of the parameters γ and κ: small values of γ

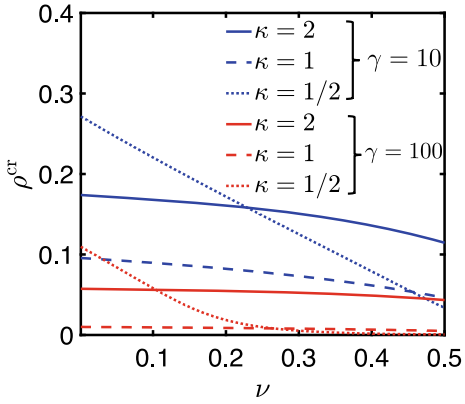

Fig. 44 Critical mode mixity ratio $\rho^{\rm cr}$ versus Poisson's ratio ν, for various values of the parameters γ and κ: large values of γ

$$N(\rho;0) \simeq -(1-\nu)(2-3\nu) + \frac{\kappa\gamma\rho^{\kappa}}{1+\gamma\rho^{\kappa}}(1-\nu)(4-5\nu).$$

It follows that the solution $\rho^{\rm cr}$ of the equation $N(\rho^0;0) = 0$ is

$$\rho^{\rm cr} \simeq \left\{ \frac{2-3\nu}{[(4-5\nu)\kappa - (2-3\nu)]\,\gamma} \right\}^{1/\kappa} \qquad (\gamma \gg 1). \tag{179}$$

Expression (179) applies provided that $(4-5\nu)\kappa - (2-3\nu) > 0$, which is true for $\kappa \geq 1/2$ (with $0 < \nu < 1/2$).

Figures 43 and 44 and equation (179) show that when a dependence of G_c upon ρ is introduced, with a sufficiently large value of the parameter γ, the critical mode mixity ratio $\rho^{\rm cr}$ greatly decreases, down to values compatible with the majority of experiments. In a more quantitative way, a tentative comparison may be attempted with the experimental observations of Lin et al. (2010). Adopting the simplest value of 2 for the parameter κ, one finds that the value $\gamma \simeq 25$ leads to the best theoretical fit (for small ρ) of Lin et al. (2010)s experimental crack initiation curve: see Fig. 42

which illustrates such a fit. For these parameters ρ^{cr} is of the order of 0.1, which is precisely in the range of ρ-values considered in the experiments—in which facetting of the crack surface was observed.

Finally, with regard to the geometry of instability modes, one may note that equation (153) of Sect. 4.4, connecting the in-plane and out-of-plane perturbations of the crack, applies without modification here, since it bears no relation to the critical energy-release-rate—being a mere consequence of the PLS. It follows that the geometry of instability modes is the same as for a constant G_c; it is still depicted by Figs. 38 and 39 of Sect. 4.4 and requires no new illustration.

4.7 Further Extension to General Mixed-Mode I+II +III Situations

Preliminaries. It is almost impossible experimentally not to generate all three modes simultaneously, even if one or two SIFs are close to zero. Therefore, for a more meaningful comparison with experiments, it is interesting, following Vasudevan et al. (2019), to repeat the preceding stability analysis with a small added contribution of mode II in the planar configuration of the crack ($K_{II}^0 \neq 0$). The presence of mode II will be seen to result in a dramatically new effect.

We consider the same situation as in Sect. 4.6, except for the presence of mode II; in particular G_c is assumed to depend upon $\rho = K_{III}/K_I$ according to the same expression (172).

The general mixed-mode I+II+III conditions considered make the evolution of the crack more complex than that resulting from a simpler mode I+III condition, because of the general kink of the crack induced by the mode II component of the loading. This kink is considered to occur only once the crack front has reached a certain position. More specifically, we consider an initially flat semi-infinite crack, obtained for instance through machining of the specimen, or crack propagation in mode I fatigue: Fig. 45. A load of sufficient magnitude, including mode II and III components, is applied henceforward. A general kink of the crack ensues, possibly with superimposed perturbations of the crack front and surface growing unstably: Fig. 46, where the full line represents the fundamental, kinked but unperturbed configuration, and the dotted line a kinked and perturbed configuration.

The SIFs in the initial planar configuration of the crack being as before denoted K_I^0, K_{II}^0, K_{III}^0 and assumed to be independent of the position x of the crack front, we introduce three dimensionless constant ratios:

$$\varphi^0 \equiv \frac{K_{II}^0}{K_I^0} \quad ; \quad \rho^0 \equiv \frac{K_{III}^0}{K_I^0} \quad ; \quad R^0 \equiv \frac{K_{II}^0}{K_{III}^0} \equiv \frac{\varphi^0}{\rho^0}. \tag{180}$$

Like in Sects. 4.4 and 4.6, one may harmlessly assume K_{III}^0 to be positive like K_I^0; ρ^0 is then positive. Note that this leaves the signs of φ^0 and R^0 arbitrary, although identical. *The quantities $|\varphi^0|$ and ρ^0 are both assumed to be much smaller than unity*, albeit for distinct reasons:

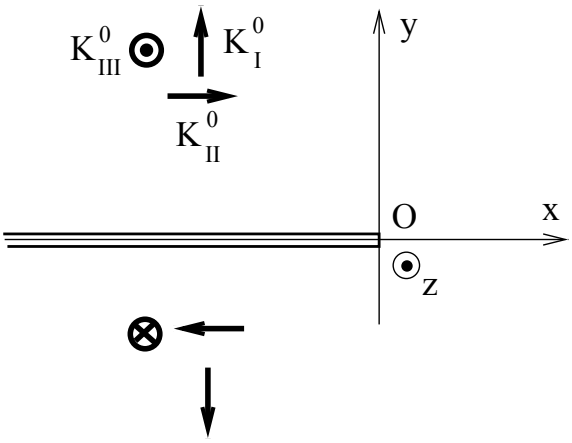

Fig. 45 Configurations of a crack loaded in mode I+II+III: prior to propagation

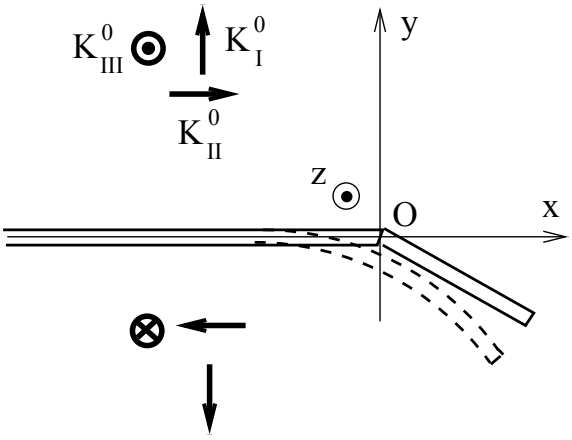

Fig. 46 Configurations of a crack loaded in mode I+II+III: during propagation

- the former because the mode II loading component generates a general kink angle proportional to φ^0 to first order; thus if $|\varphi^0|$ were large, the kink angle would also be large, and this would prohibit using Movchan et al. (1998)s and Leblond et al. (2011)s geometrically linearized formulae (148), (149);
- the latter because it greatly simplifies the calculation of the perturbed SIFs, as detailed in Vasudevan et al. (2019).

These hypotheses are not overly restrictive, since most experiments of mixed-mode I+III or I+II+III fracture discussed in the literature were performed under conditions of predominant mode I. Note that they do not imply anything regarding the magnitude of the ratio $R^0 = \varphi^0/\rho^0$.

The first thing to do is to determine the general kink induced by the mode II loading component. Using equation $(148)_2$ for a perturbation ϕ_y independent of z, combined with the PLS, one easily concludes that the value of this kink angle is

$\alpha = -2\frac{K_{II}^0}{K_I^0} = -2\varphi^0$. Thus the fundamental, kinked but unperturbed configuration of the crack consists of a semi-infinite crack occupying the half-plane $x < 0$, $y = 0$, endowed in the region $x \geq 0$ with an extension of equation $y = -2\varphi^0 x$ (Fig. 46, full line).

To study deviations from this fundamental configuration, the following change of function is introduced for the out-of-plane deviation of the crack:

$$\begin{cases} \phi_y(x,z) = \widetilde{\phi}_y(x,z) & \text{for } x < 0 \\ \phi_y(x,z) = -2\varphi^0 x + \widetilde{\phi}_y(x,z) & \text{for } x \geq 0. \end{cases} \tag{181}$$

The instability modes $(\phi_x, \widetilde{\phi}_y)$ are then taken in the following form:

- In the region $x \geq 0$:
$$\begin{cases} \phi_x(x,z) = \mathrm{Re}\left[e^{\lambda x}\psi_x(z)\right] \\ \widetilde{\phi}_y(x,z) = \mathrm{Re}\left[e^{\lambda x}\psi_y(z)\right] \end{cases} \tag{182}$$
where the growth rate λ of the mode and the functions $\psi_x(z)$, $\psi_y(z)$ are now all *complex*—indeed the analysis to follow will reveal that unlike in mode I+III, none of these quantities can remain real in the presence of global mode II ($K_{II}^0 \neq 0$). The normalized growth rate $\xi = \frac{\lambda}{|k|}$ will accordingly also be complex.
- In the region $x < 0$:
No specific assumption is introduced, other than the quick vanishing of $\widetilde{\phi}_y$ in the direction of negative x (initially flat crack).

Application of the double criterion. The calculation of the variations δK_p ($p = I, II, III$) of the SIFs is more difficult than in Sect. 4.4 on situations of mixed-mode I+III, because of the more complex expression (182) of the perturbations ϕ_x and $\widetilde{\phi}_y$. It is detailed in Vasudevan et al. (2019), and the results read at the first order in the pair (φ^0, ρ^0):

$$\begin{cases} \dfrac{K_I(x,z)}{K_I^0} = 1 - \mathrm{Re}\left\{ e^{\lambda x} \displaystyle\int_{-\infty}^{+\infty} \frac{|k|}{2}\, \widehat{\psi_x}(k) e^{ikz} dk \right\} \\ \dfrac{K_{II}(x,z)}{K_I^0} = \mathrm{Re}\left\{ e^{\lambda x} \displaystyle\int_{-\infty}^{+\infty} \left[-\left(\frac{2i}{2-\nu}\rho^0 k + \frac{2-3\nu}{2(2-\nu)}\varphi^0|k| \right) \widehat{\psi_x}(k) \right.\right. \\ \qquad \left.\left. + \left(\frac{\lambda}{2} + \frac{2-3\nu}{2(2-\nu)}|k| \right) \widehat{\psi_y}(k) \right] e^{ikz} dk \right\} \\ \dfrac{K_{III}(x,z)}{K_I^0} = \rho^0 + \mathrm{Re}\left\{ \frac{e^{\lambda x}}{2-\nu} \displaystyle\int_{-\infty}^{+\infty} \left[\left(2i(1-\nu)\varphi^0 k - \frac{2+\nu}{2}\rho^0|k| \right) \widehat{\psi_x}(k) \right.\right. \\ \qquad \left.\left. + 2i\,(1-\nu)^2 k \widehat{\psi_y}(k) \right] e^{ikz} dk \right\}. \end{cases} \tag{183}$$

Combination of equation $(183)_2$ and the PLS then yields the following condition:

$$\widehat{\psi_y}(k) = \frac{(2-3\nu)\varphi^0 + 4i\rho^0\,\mathrm{sgn}(k)}{2-3\nu+(2-\nu)\xi}\,\widehat{\psi_x}(k). \tag{184}$$

One observes that the factor connecting the Fourier transforms of the in-plane and out-of-plane perturbations is now no longer real but complex; the importance of such a property will be apparent in subsubsection **Drifting motion of instability modes along the crack front** below.

To now apply Griffith (1920)s criterion, one needs the following expression of the variation $\delta\rho(x,z)$ of the mixity ratio $\rho(x,z)$, obtained from equations $(183)_{1,2}$ and (184) after some tedious calculation:

$$\begin{aligned}&\delta\rho(x,z) = \\ &\mathrm{Re}\left\{e^{\lambda x}\int_{-\infty}^{+\infty}\frac{-(4-5\nu+\nu\frac{\lambda}{|k|})\rho^0 + 2(1-\nu)(2-3\nu+\frac{\lambda}{|k|})i\varphi^0\mathrm{sgn}(k)}{2-3\nu+(2-\nu)\frac{\lambda}{|k|}}\right. \\ &\qquad\left.\times|k|\widehat{\psi_x}(k)e^{ikz}dk\right\}.\end{aligned} \tag{185}$$

Application of Griffith (1920)s criterion then yields:

- At order 0 in the pair $(\phi_x, \widetilde{\phi_y})$, the same result as in the absence of mode II, Eq. (176).
- At order 1, the following relation, instead of (178):

$$\xi = \frac{N_1 + iN_2}{D_1 + iD_2}\quad,\quad \begin{cases} N_1 \equiv -2+3\nu+(4-5\nu)X \\ N_2 \equiv -2(1-\nu)(2-3\nu)XR^0\,\mathrm{sgn}(k) \\ D_1 \equiv 2-\nu-\nu X \\ D_2 \equiv 2(1-\nu)XR^0\,\mathrm{sgn}(k) \end{cases} \tag{186}$$

  where $X \equiv X(\rho^0)$ denotes the same quantity as in Eq. (178), and indications of dependence upon the parameters φ^0 and ρ^0 (or $R^0 = \varphi^0/\rho^0$) are omitted in order to keep notations reasonably light.[23] Note that unlike equations (178), (186) directly provides the value of the normalized growth rate ξ, since none of the quantities in the right-hand side depends on it. (A dependence of N_1 and N_2 upon ξ would appear if terms of order 2 and more in the pair $(\phi_x, \widetilde{\phi_y})$ were accounted for).

Influence of mode II upon the onset of configurational instability of the fundamental crack configuration. Equation (186) shows that in the presence of mode II, the normalized growth rate $\xi = \lambda/|k|$ of the perturbation is *complex:*

[23] Note that the comparison between equations (178) (without mode II) and (186) (with mode II) is not as simple as it may seem at first sight: it does not suffice to set $\varphi^0 = 0$ or $R^0 = 0$ in (186) to get (178), because the former equation was obtained for a small ρ^0 in contrast to the latter.

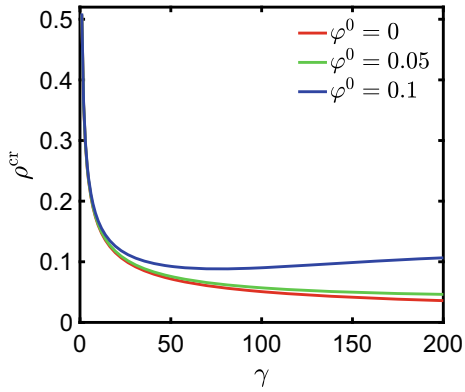

Fig. 47 Critical mode mixity ratio $\rho^{\rm cr}$ as a function of the material parameter γ, for various values of $\varphi^0 = K_{II}^0/K_I^0$ ($\nu = 0.38$, $\kappa = 2$)

$$\xi \equiv \xi_1 + i\xi_2 \quad , \quad \xi_1 \equiv \frac{N_1 D_1 + N_2 D_2}{D_1^2 + D_2^2} \quad , \quad \xi_2 \equiv \frac{N_2 D_1 - N_1 D_2}{D_1^2 + D_2^2} \, . \tag{187}$$

The condition for incipient instability of the fundamental configuration of the crack is

$$\xi_1 = 0 \quad \Leftrightarrow \quad N_1 D_1 + N_2 D_2 = 0 \quad \Leftrightarrow$$

$$[-2 + 3\nu + (4 - 5\nu)X]\,(2 - \nu - \nu X) - 4(1 - \nu)^2(2 - 3\nu)(R^0)^2 X^2 = 0. \tag{188}$$

Equation (188) (with X given by Eq. (178)$_4$) is equivalent to an algebraic equation of the second degree on the unknown $(\rho^0)^\kappa$, which determines the critical value $\rho^{\rm cr}$ of the mixity ratio ρ^0 leading to incipient instability.

The simplicity of equation (188) permits elementary analyses of some of its consequences:

- For $\rho^0 = 0$, $N_1 D_1 + N_2 D_2 = (-2 + 3\nu)(2 - \nu) < 0$ since $X = 0$. Thus ξ_1 is negative (implying configurational stability of the propagating crack) for small values of ρ^0. Now $\rho^{\rm cr}$ is by definition the *smallest* positive solution in ρ^0 of equation (188). Therefore ξ_1 is negative (stability) if $\rho^0 < \rho^{\rm cr}$, vanishes if $\rho^0 = \rho^{\rm cr}$ (neutral stability), and is positive (instability) if $\rho^0 > \rho^{\rm cr}$.
- The quantity $N_1 D_1 + N_2 D_2$ is negative for $0 \leq \rho^0 < \rho^{\rm cr}$, and decreases when $|R^0|$ increases for a given ρ^0. Hence when $|R^0|$ increases, the interval $\rho^0 \in [0, \rho^{\rm cr})$ over which $N_1 D_1 + N_2 D_2 < 0$ must become larger, implying that $\rho^{\rm cr}$ must increase: *presence of mode II increases the instability threshold, that is, favours stability*.

Figure 47 illustrates the second property, by showing the critical value $\rho^{\rm cr}$ of the mixity ratio ρ^0 versus the parameter γ characterizing the dependence of G_c upon ρ, for various values of the other mixity ratio $\varphi^0 = K_{II}^0/K_I^0$. This figure is drawn for the values $\nu = 0.38$ and $\kappa = 2$. The increase of $\rho^{\rm cr}$ arising from the presence of mode II is conspicuous, especially for large values of γ.

Drifting motion of instability modes along the crack front. The discussion of instability modes basically follows the same lines as in subsubsection **Geometry of the instability modes** of Sect. 4.4, with some slight complications arising from the complex nature of the functions $\psi_x(z)$ and $\psi_y(z)$. The function $\psi_x(z)$ is taken in the form

$$\psi_x(z) = A_x\, e^{i(kz+\theta)} \quad \Leftrightarrow \quad \widehat{\psi_x}(k') = A_x\, e^{i\theta}\delta(k'-k) \tag{189}$$

where k, A_x and θ are real, k being positive. The normalized growth rate ξ is determined by equation (186), the complex growth rate λ by $\lambda = \xi|k| = (\xi_1 + i\xi_2)k$, and the in-plane perturbation $\phi_x(x, z)$ by

$$\phi_x(x, z) = A_x\, e^{\xi_1 kx} \cos\left[k(z + \xi_2 x) + \theta\right]. \tag{190}$$

(see equation $(182)_1$).

To now calculate $\widetilde{\phi_y}$, write the ratio connecting $\widehat{\psi_x}$ and $\widehat{\psi_y}$ in Eq. (184) in the form

$$\frac{(2-3\nu)\varphi^0 + 4i\rho^0}{2-3\nu+(2-\nu)(\xi_1+i\xi_2)} \equiv p + iq \tag{191}$$

where p and q are real and of first order in the pair (φ^0, ρ^0)—and consequently small. (The precise expressions of these quantities do not matter). Then

$$\widehat{\psi_y}(k') = (p+iq)A_x\, e^{i\theta}\delta(k'-k) \quad \Leftrightarrow \quad \psi_y(z) = (p+iq)A_x\, e^{i(kz+\theta)}.$$

Then by Eq. $(182)_2$,

$$\begin{aligned}\widetilde{\phi_y}(x, z) &= \mathrm{Re}\left[e^{(\xi_1+i\xi_2)kx}(p+iq)A_x\, e^{i(kz+\theta)}\right] \\ &= A_x\, e^{\xi_1 kx}\Big\{p\,\cos\left[k(z+\xi_2 x)+\theta\right] - q\,\sin\left[k(z+\xi_2 x)+\theta\right]\Big\}.\end{aligned} \tag{192}$$

To geometrically interpret the instability mode defined by equations (190) and (192), introduce a new frame $(Ox'y'z)$ obtained by rotating the original one $(Oxyz)$ by a small angle ϵ about the axis Oz (Fig. 48).

The "perturbation vector" $\phi_x \mathbf{e}_x + \widetilde{\phi_y}\mathbf{e}_y$ may then be expressed, to first order in ϵ, as

$$\phi_x \mathbf{e}_x + \widetilde{\phi_y}\mathbf{e}_y = {\phi_x}'\mathbf{e}_{x'} + {\widetilde{\phi_y}}'\mathbf{e}_{y'} \quad , \quad \begin{cases} {\phi_x}'(x, z) = \phi_x(x, z) + \epsilon\widetilde{\phi_y}(x, z) \\ {\widetilde{\phi_y}}'(x, z) = -\epsilon\phi_x(x, z) + \widetilde{\phi_y}(x, z). \end{cases}$$

The cosine term in the expression (192) of $\widetilde{\phi_y}$ disappears in that of ${\widetilde{\phi_y}}'$, if the choice $\epsilon = p$ is made; the expressions of ${\phi_x}'$ and ${\widetilde{\phi_y}}'$ then become

$$\begin{cases} {\phi_x}'(x, z) = A_x\, e^{\xi_1 kx}\cos\left[k(z+\xi_2 x)+\theta\right] \\ {\widetilde{\phi_y}}'(x, z) = A_y\, e^{\xi_1 kx}\sin\left[k(z+\xi_2 x)+\theta\right] \end{cases} \quad \text{where} \quad A_y \equiv -qA_x. \tag{193}$$

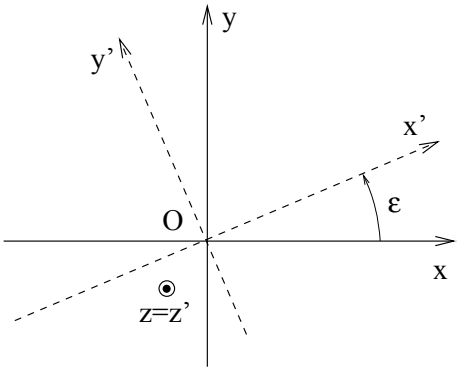

Fig. 48 Change of frame in the plane Oxy orthogonal to the unperturbed crack front

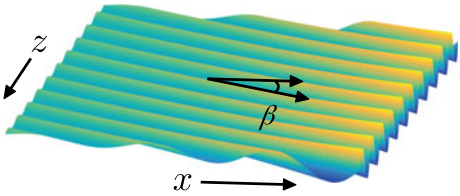

Fig. 49 Instability mode for a mode I+II+III loading: geometry of perturbed surface

The instability modes defined by equation (193) differ from those in the absence of mode II, Eq. (164), through the following two features:

- Because of the presence of mode II, the principal axes of the ellipse (projection of the helix onto the plane Oxy) rotate—by a small angle of p radians—about the direction z of the unperturbed crack front.
- More spectacularly, the helix no longer moves in the general direction x of crack propagation, but drifts along the front as it propagates. Its "drift velocity" dz/dx is given by

$$\frac{dz}{dx} \equiv -\xi_2 = \frac{N_1 D_2 - N_2 D_1}{D_1^2 + D_2^2} = \frac{2(1-\nu)^2[2-3\nu+(4-3\nu)X]XR^0}{(2-\nu-\nu X)^2 + 4(1-\nu)^2 X^2 (R^0)^2} \quad (194)$$

  where the expression of $N_1 D_2 - N_2 D_1$ has been developed and rearranged. Note that this drift velocity depends on both mixity ratios $R^0 = K^0_{II}/K^0_{III}$ and $\rho^0 = K^0_{III}/K^0_I$ (through the parameter $X \equiv X(\rho^0)$).

Figure 49 schematically illustrates the geometry of the crack surface in some instability mode defined by equation (193). (There is no need to illustrate the geometry of the crack front which is the same as in the absence of global mode II, see Fig. 38). The drifting motion of the out-of-plane oscillations of the crack surface is conspicuous in Fig. 49. It is worth noting that according to equation (194), the sign of the "drift angle" $\beta = \arctan(dz/dx) = -\arctan(\xi_2)$ is the same of that of R^0 or K^0_{II} (for a positive K^0_{III}, as envisaged here).

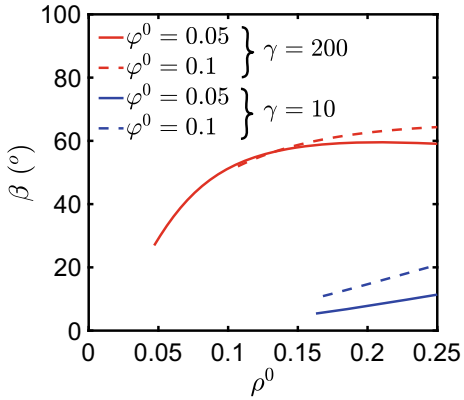

Fig. 50 Drift angle $\beta = \arctan(dz/dx)$ of an instability mode as a function of $\rho^0 = K^0_{III}/K^0_I$, for several values of $\varphi^0 = K^0_{II}/K^0_I$ and γ ($\nu = 0.38$, $\kappa = 2$)

Figure 50 illustrates the dependence of the drift angle $\beta = \arctan(dz/dx)$ of an instability mode upon the mixity ratio $\rho^0 = K^0_{III}/K^0_I$, for $\nu = 0.38$ and $\kappa = 2$, and two values of the other mixity ratio $\varphi^0 = K^0_{II}/K^0_I$; two values of the parameter γ are also considered: $\gamma = 10$, for a material with a modest dependence of G_c upon ρ, and $\gamma = 200$, for a material with a largely ρ-dependent G_c. (Results are displayed only for $\rho > \rho^{\rm cr}$ since there is no instability otherwise). One observes that β increases with both the amount of in-plane shear K^0_{II} and the parameter γ, and also with the amount of anti-plane shear K^0_{III} at least up to the value $\rho^0 = K^0_{III}/K^0_I \sim 0.15$.

Basically, the appearance of a drifting motion of instability modes for a general mixed-mode loading I+II+III is the result of a loss of symmetry properties:

- Starting from a mode I loading, introducing a mode III loading component destroys the symmetry of the problem with respect to the crack plane Oxz, but leaves intact its invariance in a rotation of 180° around the direction x of propagation. This prohibits any drifting motion, which would violate this invariance.
- Further adding a mode II component destroys the invariance in a rotation of 180° around the direction x, thus making a drifting motion possible.

However it is worth noting that in the present analysis, the existence of a drifting motion of instability modes is also a consequence of the dependence of the fracture energy $G_{\rm c}$ upon the mixity ratio $\rho = K_{III}/K_I$. Indeed according to equation (194), the drift velocity is zero when $X = 0$, that is when $\gamma = 0$ or equivalently when $G_{\rm c}$ is independent of ρ.[24]

Relation to experiments. According to the preceding theoretical analysis, the most dramatic consequence of presence of an additional mode II loading component during crack propagation in mode I+III concerns the resulting fracture pattern. In the

[24] A more refined analysis presented in Vasudevan et al. (2019) shows that in fact, a drifting motion of instability modes exits even when G_c is independent of ρ; this is due to terms of order 2 or more in the pair (φ^0, ρ^0), disregarded in the present analysis. But the corresponding drift velocity is much smaller than that calculated here for a ρ-dependent G_c.

presence of plane shear, above the instability threshold, the crests of the exponentially growing helical perturbations are predicted to drift along the front, thus leaving behind them ridges that are not parallel to the mean direction x of crack propagation. The value of the drift angle is determined by those of the mixity ratios K^0_{II}/K^0_I and K^0_{III}/K^0_I, plus the material parameter γ characterizing the dependence of the fracture energy G_c upon the ratio K_{III}/K_I. (In the absence of such a dependence, the drift angle is very small).

With regard to experiments, the drifting motion of facets was indeed observed in various studies of fracture in mode I+III (Lazarus et al. 2008; Baumberger et al. 2008; Sherman et al. 2008; Lin et al. 2010; Ronsin et al. 2014; Pham and Ravi-Chandar 2014; Kolvin et al. 2018). However, whether or not these observations may be ascribed to the presence of mode II during crack growth is not a priori obvious.

However the experiments of Lin et al. (2010) depicted in Fig. 51 are of special interest in this respect, in that the mode II loading component was *controlled* in the tests performed by these authors. Figure 51a illustrates the principle of the experiments, which consisted of using a three-point bending device to break beams containing a notch machined *obliquely*, so as to generate a mode III loading component.

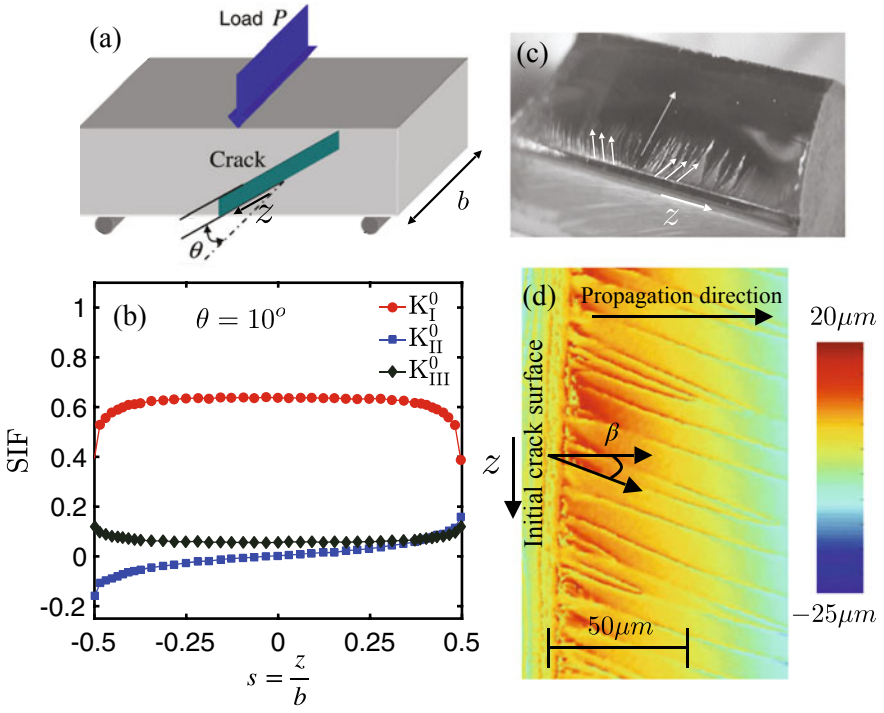

Fig. 51 Three-point-bending fracture tests of Lin et al. (2010) (with permission of the authors). **a** Experimental apparatus—**b** Calculated SIFs—**c** and **d** General and detailed views of the fracture surface

Figure 51b shows the distributions of the three SIFs along the crack front, as calculated by the finite element method: the mode II component changed sign halfway along the front, whereas the mode III component remained essentially uniform and positive. The resulting fracture pattern, displayed in Fig. 51c and d, exhibited facets which drifted in opposite directions in the two halves of the specimen: the drift angle $\beta = \arctan(dz/dx)$ was positive in the region $z > 0$ where K^0_{II} and K^0_{III} were of identical signs, and negative in the region $z < 0$ where these signs were opposite. All these features are in qualitative agreement with the predictions of the stability analysis presented above.

To make the comparison more quantitative, it is necessary to examine the magnitude of the drift. Characteristic relative values of the shear loading components in the initial planar configuration of the crack, at a point of the crack front located at some distance from the mid-plane $z = 0$, were $\varphi^0 = K^0_{II}/K^0_I \simeq 0.08$ and $\rho^0 = K^0_{III}/K^0_I \simeq 0.08$, implying that $R^0 = K^0_{II}/K^0_{III} \simeq 1$. For these parameters and the values $\nu \simeq 0.34$ (typical for Homalite, as employed in the experiments) and $\gamma \simeq 25$ (see subsubsection **Numerical illustrations** of Sect. 4.6), Eq. (194) yields $\beta \simeq 16°$, which is reasonably compatible with the experimental drift angle of 20 to 30° (see Figs. 6 and 7 of Lin et al. 2010).

More experiments and comparisons are obviously needed in order to definitively settle the question of the relevance of the theoretical analysis developed above.

4.8 Concluding Summary

In this final section, we considered out-of-plane perturbations of cracks in fully 3D situations, under mixed-mode I+III or fully general I+II+III loading conditions. With regard to practical aspects, although many applications could have been envisaged (for instance, to out-of-plane deviations of cracks due to encountering of harder obstacles, and their influence upon the overall toughness), it was decided to concentrate on a unique, but fundamental issue: explaining the phenomenon of *crack front segmentation* in mode I+III, that is, the fact that cracks loaded thus do not generally propagate in a coplanar manner, but in the form of small facets tilted about the direction of propagation. Such an explanation represents a very difficult challenge, because of the breaking of translatory invariance along the crack front implied by segmentation.

In a first step, Sect. 4.2 expounded Leblond (1999)s 3D extension of the works of Leblond (1989) and Amestoy and Leblond (1992) on crack kinking and curving in 2D (plane strain) situations. In this extension, like in the previous works, the crack was endowed with an extension of small length, but which could be arbitrarily kinked and curved. It was found that in the expansion of the SIFs in powers of the crack extension length, the fully 3D expressions of the first two terms were basically similar to their 2D counterparts, in particular in their purely local character—in the sense that the geometric and mechanical parameters involved were just those at the point of observation considered on the crack front, without any non-local contribution of other

points of this front. With regard to applications, these results permitted to extend Cotterell and Rice (1980)s directional stability analysis of a mode I crack—expounded in Sect. 2.10 of Sect. 2—to fully 3D situations, with an essentially identical conclusion. They did not, however, lead to any definite conclusion concerning crack front segmentation in mixed-mode I+III conditions.

Then Sect. 4.3 provided the first-order expressions of the variations of the SIFs along the front of a semi-infinite crack, slightly perturbed both within and out of its plane. It was based on the work of Gao and Rice (1986) for the in-plane perturbation problem, and the paper of Movchan et al. (1998) (as completed by Leblond et al. (2011)) for the out-of-plane perturbation problem. Unlike the perturbations (of type I) studied by Leblond (1999), those (of type II) considered by Movchan et al. (1998) were not confined to the vicinity of the crack front, but could extend back indefinitely in the direction opposite to that of propagation, as required for the subsequent stability analyses of coplanar propagation in mode I+III. (As a counterpart, the slope of the perturbed crack surface with respect to the original crack plane had to be small in all directions of this plane, unlike in the work of Leblond (1999)).

As a first application of the results presented in Sects. 4.3, 4.4 presented Leblond et al. (2011)s linear stability analysis of coplanar propagation of a semi-infinite crack in an infinite body under mixed mode I+III loading conditions, based on Griffith (1920)s energetic criterion combined with Goldstein and Salganik (1974)s PLS. This analysis led to the remarkable conclusion of existence of instability modes above some critical value of the unperturbed "mixity ratio" (ratio of the unperturbed mode III to mode I SIFs), depending only on Poisson's ratio. In these instability modes, the crack front was found to assume a helical shape of size growing exponentially with the distance of propagation. Unfortunately this result seemed to solve an issue only to raise a new one, in that the instability threshold was, for usual values of Poisson's ratio, much too high compared to the majority of those actually observed.

The rest of the section was devoted to tentative explanations of this puzzling discrepancy. First Sect. 4.5, following the work of Leblond and Lazarus (2015), expounded a qualitative study of the influence of imperfections—in the form of accidental undulations of the crack front within the crack plane—upon the bifurcation accompanying the loss of stability of the coplanar configuration of the crack. This study was based on the 3D extension—presented in Sect. 4.2—of Cotterell and Rice (1980)s 2D directional stability criterion. The results exhibited a large destabilizing influence of in-plane undulations of the crack front of sufficient amplitude upon the coplanar configuration of the crack; this provided evidence for a strongly subcritical character of the bifurcation, fully in line with Chen et al. (2015)s conclusions deduced from numerical simulations based on a phase-field model.

Section 4.6, based on the recent work of Leblond et al. (2018), explored another possibility in the form of a renewed linear stability analysis, based on the heuristic hypothesis of a mode-dependent fracture energy. This idea was suggested by the well-documented mode-dependence of this energy in mixed-mode interfacial fracture. It was found that such a dependence may, if large enough, lead to a very significant decrease of the theoretical instability threshold, down to values agreeing reasonably well with experimental ones.

Finally Sect. 4.7 presented Vasudevan et al. (2019)s very recent further extension of Leblond et al. (2011)s and Leblond et al. (2018)s works, to fully general mode I+II+III loading conditions. The major conclusion of this study was that presence of a small mode II loading component, in the initial planar configuration of the crack, must result in a gradual drifting motion of the instability modes along the crack front, as the crack propagates. This theoretical conclusion found some qualitative, and even reasonably quantitative support in some experimental observations of Lin et al. (2010). It was clear, however, that further experiments and comparisons with the stability analysis were required, in order to conclude in a definitive way about the relevance of the theory developed for the interpretation of the often observed "crab-like" motion of fracture facets.

5 General Conclusion

This review was devoted to analytical perturbation studies of cracks and their applications to some problems of LEFM, as developed in the last few decades by various authors. A limited choice of papers, admittedly dictated more by the author's personal taste than objective reasons, was made in the large body of literature available.

A possible option would have been to classify crack perturbations according to their "type": I for perturbations confined to the immediate vicinity of the crack front, II for perturbations extending over the entire crack surface. However it was decided, for pedagogical reasons, to rather classify papers by increasing degree of geometric complexity: perturbations of cracks in 2D (plane strain) situations, then in-plane perturbations of cracks in general 3D situations, and finally out-of-plane perturbations of 3D cracks.

Section 2 first considered crack perturbations in 2D. Among all papers cited in this review, those pertaining to this topic were the oldest, ranging roughly from the 70s to the 90s. The essential aim of perturbation studies of this type was to formulate a physical criterion providing the direction of future crack growth, in 2D (mode I+II) situations. Necessary ingredients to achieve this aim were formulae of general applicability for the stress intensity factors and the energy-release-rate just after an abrupt change of direction of the crack; these formulae were provided by Amestoy (1987), Leblond (1989) and Amestoy and Leblond (1992) for the stress intensity factors, and Ichikawa and Tanaka (1982) for the energy-release-rate. Following a detailed presentation of these works, the review expounded an original discussion of various propagation criteria proposed in the literature. This discussion led to the firm conclusion that combination of Griffith (1920)s energetic criterion and Goldstein and Salganik (1974)s *principle of local symmetry* represents the "best" possible option to predict crack paths in 2D, notwithstanding the fact that the direction of crack extension satisfying the principle of local symmetry does not exactly coincide with that maximizing the energy-release-rate.

Section 3 was devoted to *coplanar* perturbations of cracks in fully 3D situations. The exploration of this domain started with a seminal paper of Rice (1985), devoted

to the in-plane perturbation of a semi-infinite crack in an infinite body under pure mode I loading conditions. This work was extended to more general geometric and mechanical situations (and notably to general mixed-mode loading conditions) by various authors. It also generated a large body of literature—especially from authors of physical background—devoted to the analytical or numerical study of coplanar propagation of mode I cracks in media having heterogeneous fracture properties. In this review, we first presented Rice (1985, 1989)s re-formulation of Bueckner (1987)s 3D weight function theory, which later served as a basis in the vast majority of theoretical works on in-plane perturbations of cracks. We then expounded Rice (1985)s work on coplanar perturbation of a semi-infinite mode I crack in an infinite body. This was followed by a presentation of several of the most significant extensions of Rice (1985)s solution; the aim here was to provide more complex solutions for less idealized situations, corresponding better to those of actual experiments. The utility of such extensions was clearly illustrated through comparison of their predictions with some experimental results of Vasoya et al. (2016b), pertaining to peeling of a thin film bonded onto some rigid substrate.

Section 4 was finally devoted to *out-of-plane* perturbations of cracks in 3D situations. Studies of such perturbations were initiated by a fundamental paper of Movchan et al. (1998), which—as completed by Leblond et al. (2011)—provided the first correct and comprehensive solution to the problem of out-of-plane perturbation of a semi-infinite crack in an infinite body, under general loading conditions. Potential applications of Movchan et al. (1998)s work are multiple (though largely unexplored yet). It was nevertheless decided to concentrate on the single issue of *crack front fragmentation* in mode I+III: that is, the commonly observed fact that crack fronts loaded in mixed-mode I+III conditions tend to split into small facets tilted around the direction of propagation. After having presented Movchan et al. (1998)s results (completed by those of Gao and Rice (1986) for the in-plane perturbation of a semi-infinite crack), we expounded Leblond et al. (2011)s and Leblond et al. (2018)s linear stability analyses of coplanar propagation of a mode I+III crack. These studies led to a reasonable qualitative and quantitative interpretation of crack front fragmentation, provided the fracture energy was allowed to depend upon mode mixity. The section was closed by a presentation of Vasudevan et al. (2019)s further extension of Leblond et al. (2011, 2018)s works to general mode I+II+III conditions, leading to the prediction of a gradual drifting motion of instability modes along the crack front in the presence of an additional mode II loading component.

Many extensions of the works reviewed are possible in various directions. To conclude, we shall sketch just a few of these extensions, again without any claim to completeness. The presentation will be made clearer by distinguishing between the *physical nature* of the phenomena considered, and the *methods of solution* envisaged for their study.

- *Physical phenomena*
  - From a theoretical viewpoint, the issue of crack front segmentation is still far from fully resolved, in spite of the recent advances recently made on the topic, some of which were expounded above. Further progress could notably be made

on the prediction of the geometric features of the fracture facets, like their initial width and spacing, and their tilt angle around the direction of propagation. It would also be nice to provide a theoretical explanation to the phenomenon of coarsening of facets through repeated coalescence events, apparent in Fig. 41. Some steps in these directions were very recently made by Lazarus et al. (2020).

- Many analytical, semi-analytical or numerical works have been devoted to the estimation of the "overall toughness" of materials having heterogeneous fracture properties; but these works almost invariably made the hypothesis of coplanar crack propagation. However, allowing cracks to circumvent harder obstacles through out-of-plane excursions is bound to considerably change the picture, and result in a significant reduction of the overall toughness, by preventing total "locking" of crack fronts around hard inclusions. A powerful semi-analytical method was very recently devised by Lebihain et al. (2020) to tackle this problem and similar ones, with promising first results.
- All the works discussed in this review were based on the classical theory of LEFM, which is well fit to describe crack *propagation* but precludes *initiation*. But many experimental fracture tests cited above, notably those involving mixed-mode I+III loading conditions, were in fact initiation experiments. The most powerful theoretical approach of initiation, in the author's view, is Leguillon (2002)s *finite theory of fracture*, based on a "double" fracture criterion involving both the fracture energy and some critical "strength" (stress). Combining this approach and the kind of stability analyses depicted above could be very fruitful for the understanding of crack initiation in mode I+III.

- *Methods of solution*
  - *Analytical methods* were extensively developed in the 70's—80's for the solution of crack perturbation problems in 2D situations; they will probably not be used so much in this geometric context in the future, except perhaps to incorporate Leguillon (2002)s double criterion approach within stability studies. For coplanar perturbations of cracks in 3D, Rice (1985, 1989)s re-formulation of Bueckner (1987)s weight function theory offers a powerful and convenient way of developing solutions of new crack perturbation problems; some of these solutions were presented above but a lot remains to be done, especially with regard to second-order solutions. For out-of-plane perturbations of cracks in 3D, an extension of Movchan et al. (1998)s first-order solution to the second order would be of very considerable interest, notably for the study of the stability of coplanar crack propagation in mode I+III. The formidable technical difficulties of such an extension might however reveal insurmountable.
  - The limitations of analytical methods have already led to a considerable development of *numerical methods* for the solution of crack perturbation problems, especially in 3D. The finite element method, applied to the classical equations of LEFM, is not so popular for numerical solutions of this type, because of the difficulties associated to the repeated operations of re-meshing required when the crack is made to propagate. But finite element or finite difference methods have proved very efficient when combined with phase-field models, see for

instance (Pons and Karma 2010); the reason being that the material degradation resulting from development of a crack is then incorporated into the material behaviour itself, rather than in geometric changes, which permits to circumvent the need for re-meshing. Such methods are bound to undergo a considerable development in the future.

– Even modern numerical techniques do not permit to deal with problems involving a large number of cracks and/or material inhomogeneities. But *hydrid analytical/numerical methods*, based on combination of analytical solutions and partial discretization of the geometry, offer an interesting alternative for the solution of such problems, in spite of their limitations—generally the restriction to semi-infinite cracks and infinite bodies. The prototype of such an approach is Lebihain et al. (2020)s method of solution for non-coplanar propagation of a semi-infinite crack, in some infinite medium with homogeneous elastic properties but heterogeneous fracture toughness. This very recent method is based on combination of the theoretical results of Leblond (1999) and Movchan et al. (1998), and meshing of the sole *front* of the crack. It is expected that the powerfulness of Lebihain et al. (2020)s method will inspire the development of other similar approaches.

In conclusion, although crack perturbations have been a "hot topic" for some decades now, they may be expected to remain so for quite some time in the future, in view of the theoretical and practical importance of the problems implied!

References

Amestoy M (1987) Propagation de fissures en élasticité plane. Université Pierre et Marie Curie (UPMC), Thèse de Doctorat d'Etat

Amestoy M, Leblond JB (1992) Crack paths in plane situations - II: detailed form of the expansion of the stress intensity factors. Int J Solids Struct 29:465–501

Autesserre P (1995) Simulation numérique de trajets de propagation de fissures en mécanique linéaire bidimensionnelle de la rupture. Université Pierre et Marie Curie (UPMC), Thèse de Doctorat

Baumberger T, Caroli C, Martina D, Ronsin O (2008) Magic angles and cross-hatching instability in hydrogel fracture. Phys Rev Lett 100:178303

Bilby B, Cardew GE (1975) The crack with a kinked tip. Int J Fract 11:708–712

Bower AF, Ortiz M (1990) Solution of three-dimensional crack problems by a finite perturbation method. J Mech Phys Solids 38:443–480

Bueckner HF (1987) Weight functions and fundamental fields for the penny-shaped and the half-plane crack in three-space. Int J Solids Struct 23:57–93

Bui HD (1978) Mécanique de la rupture fragile. Masson

Chatterjee SN (1975) The stress field in the neighborhood of a branched crack in an infinite elastic sheet. Int J Solids Struct 11:521–538

Chen CH, Cambonie T, Lazarus V, Nicoli M, Pons A, Karma A (2015) Crack front segmentation and facet coarsening in mixed-mode fracture. Phys Rev Lett 115:265503

Chopin J, Prevost A, Boudaoud A, Adda-Bedia M (2011) Crack front dynamics across a single heterogeneity. Phys Rev Lett 107:144301

Cooke ML, Pollard DD (1996) Fracture propagation paths under mixed mode loading within rectangular blocks of polymethyl methacrylate. J Geophys Res 101:3387–3400
Cotterell B, Rice JR (1980) Slightly curved or kinked cracks. Int J Fract 16:155–169
Dudukalenko VV, Romalis NB (1973) Direction of crack growth under plane stress state conditions. Izw An SSSR MTT 8:129–136
Eberlein A, Richard HA, Kullmer G (2017) Facet formation at the crack front under combined crack opening and anti-plane shear loading. Engng Fract Mech 174:21–29
Erdogan F, Sih GC (1963) On the crack extension in plates under plane loading and transverse shear. ASME J Basic Eng 85:519–527
Favier E, Lazarus V, Leblond JB (2006) Coplanar propagation paths of 3D cracks in infinite bodies loaded in shear. Int J Solids Struct 43:2091–2109
Feulvarch E, Fontaine M, Bergheau JM (2013) XFEM investigation of a crack path in residual stresses resulting from quenching. Finite Elem Anal Des 75:62–70
Freund LB, Suresh S (2003) Thin film materials. Cambridge University Press
Gao H (1988) Nearly circular shear mode cracks. Int J Solids Struct 24:177–193
Gao H (1992) Variation of elastic T-stresses along slightly wavy 3D crack fronts. Int J Fract 58:241–257
Gao H, Rice JR (1986) Shear stress intensity factors for planar crack with slightly curved front. ASME J Appl Mech 53:774–778
Gao H, Rice JR (1987) Somewhat circular tensile cracks. Int J Fract 33:155–174
Gao H, Rice JR (1987) Nearly circular connections of elastic half-spaces. ASME J Appl Mech 54:627–634
Goldstein RV, Osipenko NM (2012) Fracture structure near a longitudinal shear macrorupture. Mech Solids 47:505–516
Goldstein RV, Salganik RL (1974) Brittle fracture of solids with arbitrary cracks. Int J Fract 10:507–523
Gradshteyn IS, Ryzhik IM (1980) Table of integrals, series, and products. Academic Press
Griffith A (1920) The phenomena of rupture and flow in solids. Philos Trans Roy Soc Lond Ser A 221:163–198
Hakim V, Karma A (2009) Laws of crack motion and phase-field models of fracture. J Mech Phys Solids 57:342–368
Hourlier F, Pineau A (1979) Fissuration par fatigue sous sollicitations polymodales (mode I ondulé + mode III permanent) d'un acier pour rotors 26NCDV14. Mémoires Scientifiques de la Revue de Métallurgie 76:175–185
Hull D (1993) Tilting cracks: the evolution of fracture surface topology in brittle solids. Int J Fract 62:119–138
Hull D (1995) The effect of mixed mode I/III on crack evolution in brittle solids. Int J Fract 70:59–79
Hussain MA, Pu SL, Underwood J (1974) Strain energy release rate for a crack under combined mode I and mode II. In: Fracture analysis, proceedings of the 1973 national symposium on fracture mechanics. American Society for Testing and Materials STP 560, Part II, pp 2–28
Hutchinson JW, Mear ME, Rice JR (1987) Crack paralleling an interface between dissimilar materials. ASME J Appl Mech 54:828–832
Ichikawa M, Tanaka S (1982) A critical analysis of the relationship between the energy-release-rate and the stress intensity factors for non-coplanar crack extension under combined mode loading. Int J Fract 18:19–28
Irwin G (1958) Fracture. Handbuch der Physik, vol VI. Springer, Berlin, pp 551–590
Karihaloo BL, Keer LM, Nemat-Nasser S, Oranratnachai A (l981) Approximate description of crack kinking and curving. ASME J Appl Mech 48:515–519
Karma A, Kessler DA, Levine H (2001) Phase-field model of mode III dynamic fracture. Phys Rev Lett 87:045501
Knauss WG (1970) An observation of crack propagation in anti-plane shear. Int J Fract 6:183–187
Kolvin I, Cohen G, Fineberg J (2018) Topological defects govern crack front motion and facet formation on broken surfaces. Nat Mater 17:140–144

Lazarus V (1997) Quelques problèmes tridimensionnels de mécanique de la rupture fragile. Ph.D. Thesis, Université Pierre et Marie Curie (UPMC)
Lazarus V (2003) Brittle fracture and fatigue propagation paths of 3D plane cracks under uniform remote tensile loading. Int J Fract 122:23–46
Lazarus V, Buchholz FG, Fulland M, Wiebesiek J (2008) Comparison of predictions by mode II or mode III criteria on crack front twisting in three- or four-point bending experiments. Int J Fract 153:141–151
Lazarus V, Leblond JB (1998) Three-dimensional crack-face weight functions for the semi-infinite interface crack. I. Variation of the stress intensity factors due to some small perturbation of the crack front. J Mech Phys Solids 46:489–511
Lazarus V, Leblond JB (1998) Three-dimensional crack-face weight functions for the semi-infinite interface crack. II. Integro-differential equations on the weight functions and resolution. J Mech Phys Solids 46:513–536
Lazarus V, Leblond JB (2002) In-plane perturbation of the tunnel-crack under shear loading. I: bifurcation and stability of the straight configuration of the front. Int J Solids Struct 39:4421–4436
Lazarus V, Leblond JB (2002) In-plane perturbation of the tunnel-crack under shear loading. II: determination of the fundamental kernel. Int J Solids Struct 39:4437–4455
Lazarus V, Leblond JB, Mouchrif SE (2001) Crack front rotation and segmentation in mixed mode I+III or I+II+III - part II: comparison with experiments. J Mech Phys Solids 49:1421–1443
Lazarus V, Prabel B, Cambonie T, Leblond JB (2020) Mode I+III multiscale cohesive zone model with facet coarsening and overlap: solutions and applications to facet orientation and toughening. J Mech Phys Solids 141:104007
Lebihain M (2019) Large-scale crack propagation in heterogeneous brittle materials: an insight on the homogenization of brittle fracture properties. Ph.D. Thesis, Sorbonne Université
Lebihain M, Leblond JB, Ponson L (2020) Effective toughness of periodic heterogeneous materials: the effect of out-of-plane excursions of cracks. J Mech Phys Solids 137:103876
Leblond JB (1989) Crack paths in plane situations - I: general form of the expansion of the stress intensity factors. Int J Solids Struct 25:1311–1325
Leblond JB (1999) Crack paths in three-dimensional solids. I: two-term expansion of the stress intensity factors - application to crack path stability in hydraulic fracturing. Int J Solids Struct 36:79–103
Leblond JB, Karma A, Lazarus V (2011) Theoretical analysis of crack front instability in mode I+III. J Mech Phys Solids 59:1872–1887
Leblond JB, Karma A, Ponson L, Vasudevan A (2018) Configurational stability of a crack propagating in a material with mode-dependent fracture energy - Part I: mixed-mode I+III. J Mech Phys Solids 126:187–203
Leblond JB, Lazarus V (2015) On the strong influence of imperfections upon the quick deviation of a mode I+III crack from coplanarity. J Mech Mater Struct Special Issue Memoriam: Huy Dong Bui 10:299–316
Leblond JB, Lazarus V, Mouchrif SE (1999) Crack paths in three-dimensional solids. II: three-term expansion of the stress intensity factors - applications and perspectives. Int J Solids Struct 36:105–142
Leblond JB, Mouchrif SE, Perrin G (1996) The tensile tunnel-crack with a slightly wavy front. Int J Solids Struct 33:1995–2022
Leblond JB, Patinet S, Frelat J, Lazarus V (2012) Second-order coplanar perturbation of a semi-infinite crack in an infinite body. Eng Fract Mech 90:129–142
Legrand L, Leblond JB (2010) In-plane perturbation of a system of two coplanar slit-cracks - II: case of close inner crack fronts or distant outer ones. Int J Solids Struct 47:3504–3512
Legrand L, Patinet S, Leblond JB, Frelat J, Lazarus V, Vandembroucq D (2011) Coplanar perturbation of a crack lying on the mid-plane of a plate. Int J Fract 170:67–82
Leguillon D (1990) Comportement asymptotique du taux de restitution de l'énergie en fin de fracture. Comptes Rendus Acad Sci Paris II 310:155–160

Leguillon D (1993) Asymptotic and numerical analysis of crack branching in non-isotropic materials. Eur J Mech A/Solids 12:33–51
Leguillon D (2002) Strength or toughness? A criterion for crack onset at a notch. Eur J Mech A/Solids 21:61–72
Lin B, Mear ME, Ravi-Chandar K (2010) Criterion for initiation of cracks under mixed-mode I+III loading. Int J Fract 165:175–188
Moës N, Dolbow J, Belytschko T (1999) A finite element method for crack growth without remeshing. Int J Numer Method Eng 46:131–150
Mouchrif SE (1994) Trajets de propagation de fissures en mécanique linéaire tridimensionnelle de la rupture fragile. Ph.D. Thesis, Université Pierre et Marie Curie (UPMC)
Movchan AB, Gao H, Willis JR (1998) On perturbations of plane cracks. Int J Solids Struct 35:3419–3453
Muskhelishvili NI (1953) Some basic problems of the mathematical theory of elasticity. Noordhoff, Groningen
Neuber H (1934) Ein neuer Ansatz zur Lösung räumlicher Probleme der Elastizitätstheorie. J Appl Math Mech 14:203–212
Palaniswamy K, Knauss WG (1975) Crack extension in brittle solids. In: Nemat-Nasser Ed (ed) Mechanics today, vol 4. Pergamon Press, pp 87–148
Papkovich PF (1932) Solution générale des équations différentielles fondamentales d'élasticité exprimée par trois fonctions harmoniques. C R Acad Sci Paris 195:513–515
Pham KH, Ravi-Chandar K (2014) Further examination of the criterion for crack initiation under mixed-mode I+III loading. Int J Fract 189:121–138
Piccolroaz A, Mishuris G, Movchan AB (2007) Evaluation of the Lazarus-Leblond constants in the asymptotic model of the interfacial wavy crack. J Mech Phys Solids 55:1575–1600
Pindra N, Lazarus V, Leblond JB (2008) The deformation of the front of a 3D interface crack propagating quasistatically in a medium with random fracture properties. J Mech Phys Solids 56:1269–1295
Pindra N, Lazarus V, Leblond JB (2010) In-plane perturbation of a system of two coplanar slit-cracks - I: case of arbitrarily spaced crack fronts. Int J Solids Struct 47:3489–3503
Pollard DD, Aydin A (1988) Progress in understanding jointing over the past century. Geol Soc Am Bull 100:1181–1204
Pollard DD, Segall P, Delaney PT (1982) Formation and interpretation of dilatant echelon cracks. Geol Soc Am Bull 93:1291–1303
Pons AJ, Karma A (2010) Helical crack-front instability in mixed-mode fracture. Nature 464:85–89
Ponson L, Shabir Z, Abdulmajid M, Van der Giessen E, Simone A (2020) A unified scenario for the morphology of crack paths in two-dimensional disordered solids. Submitted to Phys Rev E
Rice JR (1968) A path-independent integral and the approximate analysis of strain concentration by notches and cracks. ASME J Appl Mech 35:379–386
Rice JR (1985) First-order variation in elastic fields due to variation in location of a planar crack front. ASME J Appl Mech 52:571–579
Rice JR (1989) Weight function theory for three-dimensional elastic crack analysis. In: Wei and Gangloff (eds), Fracture mechanics: perspectives and directions (twentieth symposium). American Society for Testing and Materials STP 1020, Philadelphia, pp 29–57
Ronsin O, Caroli C, Baumberger T (2014) Crack front echelon instability in mixed mode fracture of a strongly nonlinear elastic solid. Europhys Lett 105:34001
Sherman D, Markovitz M, Barka O (2008) Dynamic instabilities in 1 1 1 silicon. J Mech Phys Solids 56:376–387
Sih G (1965) Stress distribution near internal crack tips for longitudinal shear problems. ASME J Appl Mech 32:51–58
Sommer E (1969) Formation of fracture "lances" in glass. Eng Fract Mech 1:539–546
Sumi Y (1986) A note on the first-order perturbation solution of a straight crack with slightly branched and curved extension under a general geometric and loading condition. Tech Note Enq Fract Mech 24:479–481

Sumi Y (1992) A second-order perturbation solution of a non-collinear crack and its application to crack path prediction of brittle fracture in weldment. Nav Architect Ocean Eng 28:143–156
Sumi Y, Nemat-Nasser S, Keer LM (1983) On crack branching and kinking in a finite body. Int J Fract 21:67–79. Erratum in Int J Fract 24:159
Suresh S, Tschegg EK (1987) Combined mode I - mode III fracture of fatigue-precracked alumina. J Am Ceramic Soc 70:726–733
Vasoya M, Lazarus V, Ponson L (2016a) Bridging micro- to macroscale fracture properties in highly heterogeneous brittle solids: weak pinning versus fingering. J Mech Phys Solids 95:755–773
Vasoya M, Leblond JB, Ponson L (2013) A geometrically nonlinear analysis of coplanar crack propagation in some heterogeneous medium. Int J Solids Struct 50:371–378
Vasoya M, Unni AB, Leblond JB, Lazarus V, Ponson L (2016b) Finite size and geometrical nonlinear effects during crack pinning by heterogeneities: an analytical and experimental study. J Mech Phys Solids 89:211–230
Vasudevan A, Ponson L, Karma A, Leblond JB (2019) Configurational stability of a crack propagating in a material with mode-dependent fracture energy - part II: drift of fracture facets in mixed-mode I+II+III. J Mech Phys Solids 137:103894
Wu CH (1978) Elasticity problems of a slender Z-crack. J Elast 8:183–205
Yates JR, Miller KJ (1989) Mixed-mode (I+III) fatigue thresholds in a forging steel. Fatigue Fract Eng Mater Struct 12:259–270

Fracture Mechanics of Heterogeneous Materials: Effective Toughness and Fluctuations

Laurent Ponson

Abstract This chapter explores the basic mechanisms underlying crack propagation in brittle heterogeneous materials and introduces tools that allow for the prediction of their effective failure properties from their microscale features. The second part of this chapter explores two fascinating features of the failure behavior of disordered materials, namely the intermittent dynamics of cracks and the roughening processes leading to the fractal structure of fracture surfaces.

1 Introduction

Crack propagation is the central mechanism leading to material failure under tensile loading conditions. However, crack growth phenomena are far from being fully understood. A major challenge underlying tensile fracture problems relates to its multiscale nature: The macroscopic failure behavior of materials is largely governed by microstructural features and processes localized in the crack tip vicinity. Cracks that are efficient stress concentrators exacerbate their impact that can be felt on macroscopic quantities like toughness and crack speed. This renders the prediction of the *effective fracture properties* of heterogeneous solids a challenging task. In the following, we will address this problem in the context of the brittle failure of materials embedding a heterogeneous distribution of toughness, as discussed by Xia et al. (2012, 2015), Vasoya et al. (2013, 2016a, b), Démery et al. (2014), Hossain et al. (2014), Patinet (2013), Leblond and Ponson (2016), Chopin et al. (2018) and Albertini et al. (2021) while the effect of elastic heterogeneities, that is not addressed here, is studied for example by Xia et al. (2013) and Wang and Xia (2017). We will see that homogenization in brittle failure requires dedicated theoretical tools that are

L. Ponson (✉)
Institut Jean Le Rond d'Alembert, CNRS - Sorbonne Université, Paris, France
e-mail: laurent.ponson@sorbonne-universite.fr

L. Ponson (ed.), *Mechanics and Physics of Fracture*, CISM International Centre for Mechanical Sciences 608,
https://doi.org/10.1007/978-3-031-18340-9_3

fundamentally different from the ones classically used in micromechanics. Another consequence of the multi-scale nature of fracture problems is the predominance of *fluctuations* in the failure behavior of materials. We will see that they provide rich insights on the basic mechanisms at play during the propagation of cracks. And as such, they can be used to characterize the failure properties of materials like their toughness.

This chapter is organized in two parts. In the first one, I discuss the question of the *effective toughness* of heterogeneous brittle solids. The basic mechanism at play is that cracks are locally slowed down or even trapped when encountering tougher material regions. The induced front deformations result in a selection of local toughness values that reflect at larger scale on the overall material resistance. I will present some theoretical tools that describe crack pinning by tough obstacles and allow for the prediction of the effective toughness in the limit of weakly heterogeneous materials. The effective toughness of strongly heterogeneous solids will be discussed through higher order perturbation theory and through numerical simulations. Finally, I will illustrate how these theoretical paves the way for the design of materials with improved failure performances.

The second chapter is devoted to the *fluctuations* observed during failure of disordered materials, an issue formerly discussed by Bonamy (2009), Zapperi (2012) and Ponson (2016). Once deciphered, the statistical properties of such fluctuations provide rich insights on the basic processes underlying crack growth in heterogeneous solids. It also suggests a unified paradigm for understanding fracture in a large range of a priori very different materials. The Sects. 2.7 and 3.3 that conclude each part of this chapter discuss some promising research directions for future investigations in the field of fracture mechanics of heterogeneous solids.

2 Effective Toughness of Heterogeneous Brittle Materials

2.1 Homogenization Procedure

Consider a solid body containing a crack and made of a brittle material with homogeneous elastic constants E and ν, but heterogeneous fracture toughness $G_c(M)$.[1] We assume pure mode I tensile loading and denote $G(M)$ the energy release rate defined locally at a point M along the crack front $\mathcal{F}$. The crack evolution is governed by the Griffith's criterion:

$$\begin{cases} G(M) < G_c(M) & \Rightarrow \quad \text{no crack advance} \\ G(M) = G_c(M) & \Rightarrow \quad \text{crack propagation} \end{cases} \tag{1}$$

[1] With some abuse of terminology, we will refer in the following to G_c as the material toughness that, strictly speaking, corresponds to the fracture energy.

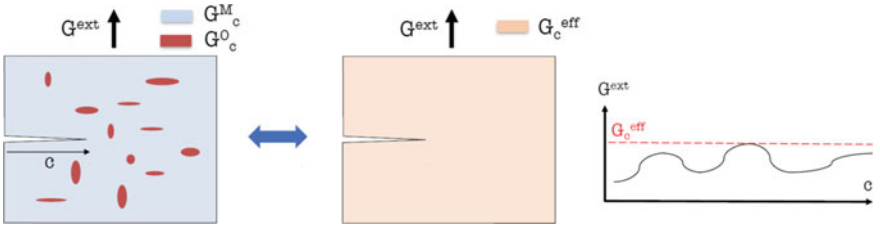

Fig. 1 Homogenization procedure for the effective toughness of a brittle material with heterogeneous distribution of toughness $G_c(M)$: the Griffith's local criterion $G(M) \leq G_c(M)$ enforced along the front is replaced at the specimen scale by $G^{\text{ext}} \leq G_c^{\text{eff}}$ where the G^{ext} is the macroscopic energy release rate defined in Eq. (1.2) and G_c^{eff} is the homogenized toughness. It corresponds to the minimum value of G^{ext} that ensures a propagation of the crack over the whole specimen width, and so corresponds to the maximum value of G^{ext} along the crack path

Homogenization consists in replacing the heterogeneous solid presented in Fig. 1 by an equivalent homogeneous solid with the same effective fracture properties. For this, we propose to replace Griffith's local criterion of Eq. (1) by a global criterion $G^{\text{ext}} \leq G_{\text{c}}^{\text{eff}}$, the macroscopic energy release rate $G_{\text{c}}^{\text{eff}}$ being given by

$$G^{\text{ext}} = \frac{\int_{\mathcal{F}} G(M)\delta c(M) ds(M)}{\int_{\mathcal{F}} \delta c(M) ds(M)} \tag{2}$$

where δc(M) is the normal distance between $\mathcal{F}$ and an infinitesimally close subsequent position of the crack front. With this definition, the homogenized toughness $G_{\text{c}}^{\text{eff}}$ corresponds to the minimum value of G^{ext} that ensures a propagation of the crack over the whole specimen. As a result, it corresponds to the maximum value of $G^{\text{ext}}(c)$ along the crack path (see Fig. 1). Using the concept introduced by Hossain et al. (2014), $G_{\text{c}}^{\text{eff}}$ is the maximum value of the *instantaneous fracture energy* $G_{\text{c}}(c) = G^{\text{ext}}(c)$ corresponding to the energy dissipated by fracture for the crack length c.

We now consider weakly heterogeneous materials for which the toughness field follows

$$G_{\text{c}}(M) = G_{c0} + C\, \delta G_{\text{c}}(M) \tag{3}$$

where $G_{c0} = \langle G_{\text{c}}(M) \rangle_M$ is the average material toughness and $C \ll 1$ is the toughness contrast considered small in the following. As detailed in the following section, the increment of crack advance can also be decomposed as

$$\delta c(M) = \delta c_m + C\delta c(M) \tag{4}$$

where $\delta c_m = \langle \delta c(M) \rangle_M$ is proportional to the average crack velocity. Using Eqs. (3) and (4) into the expression (2), and assuming $G(M) = G_{\text{c}}(M)$ along the crack front, one obtains the macroscopic elastic energy release rate

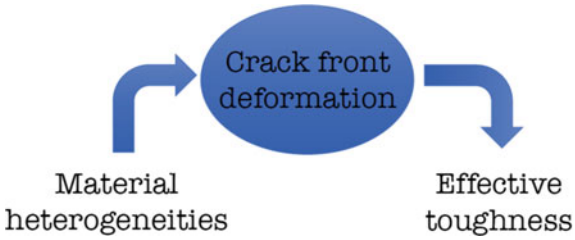

Fig. 2 The front deformation induced by the heterogeneities of toughness must be determined prior to the effective toughness

$$G^{\text{ext}} = \langle G_{\text{c}}(M) \rangle_{\mathcal{F}}. \tag{5}$$

This expression is valid for weakly heterogeneous solid for which only linear terms in the contrast C are relevant. It also corresponds to the so-called *weak pinning* situation where the Griffith condition is satisfied all along the front (see Roux et al. (2003) and Roux and Hild (2008)).

This implies that the instantaneous fracture energy corresponds to the average of the local toughness field *along the crack front*: the front, as it deforms under the effect of material heterogeneities, visits some material regions of local toughness $G_{\text{c}}(M \in \mathcal{F})$ that ultimately controls the overall macroscopic toughness. As schematized in Fig. 2, the front configuration that is not known a priori has first to be determined in order to predict the material toughness. The question of the front deformation and its evolution under the effect of heterogeneities is addressed in the following section.

2.2 Crack Evolution in Weakly Heterogeneous Brittle Solids

We limit our analysis to *planar* crack propagation under tension and imposed displacement conditions.[2] An interfacial crack of length $c(z, t)$ propagates through a specimen that is loaded at a constant opening rate v_{ext}. We assume here that all the characteristic length scales of the sample (crack length, thickness...) are much larger than both the perturbations along the crack front and the characteristic size of the heterogeneities. Another important assumption is that all the dissipative processes located near the crack tip (for example bond breaking, plasticity, microcracking) are confined in a zone much smaller than the typical heterogeneity size. Then, the problem of planar crack propagation within a 3D brittle solid can be reduced to a 2D problem where an interface, the crack front, is driven within a plane with heterogeneous fracture properties, as represented schematically in Fig. 3 (See Rice (1985), Gao and Rice (1989), and Ponson and Bonamy (2010)). The central question is how to predict the geometry of this interface and its evolution.

[2] The case of cracks that can meander out of the mean fracture plane is discussed in perspectives in Sect. 2.7.

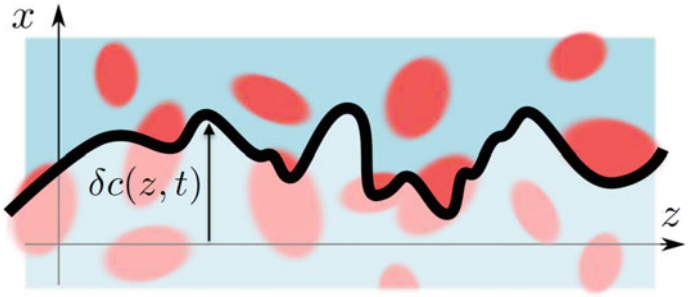

Fig. 3 Schematic view of the crack front propagating through a heterogeneous field of toughness

To address this question, we derive an evolution equation for the interface in three steps (Rice 1985; Bonamy et al. 2008; Ponson et al. 2006):

- First, the field of driving force along the crack front, i.e. the elastic energy release rate $G(z, t)$, is written as a function of the front configuration $c(z, t)$.
- The material disorder is described through a random field of fracture energy $G_c(x, z)$ that is drawn from a statistical distribution.
- These two previous expressions are used into a kinetic law where the local crack speed increases linearly with the net driving force, $\dfrac{\partial c}{\partial t} \sim G(z, t) - G_c(z, x = c(z, t))$.

We now provide the detailed derivation of each of these steps.

Elastic energy release rate Material heterogeneities distort the crack line, resulting in a heterogeneous distribution of driving force. To calculate this distribution from the geometrical perturbations of the front, consider first a reference straight configuration $c(z, t) = c_0$ that corresponds to the homogeneous distribution of elastic energy release rate $G(c_0, \delta)$ at the imposed displacement δ. While keeping δ constant, then perturb the crack front within the average crack plane, assuming an infinitely large homogeneous elastic solid under tensile loading conditions. At first order in the front perturbation $\delta c(z) = c(z, t) - c_0$ where the amplitude C of the variations of toughness is small with respect to one, the elastic energy release rate follows (Rice (1985))

$$\begin{aligned} G(z,t) \quad = \quad & G(c_0,\delta) + \frac{\partial G}{\partial c}\Big|_{c_0,\delta} \delta c(z,t) \\ & + \frac{G(c_0,\delta)}{\pi} PV \int_{-\infty}^{+\infty} \frac{\delta c(\tilde{z}) - \delta c(z)}{(\tilde{z}-z)^2} d\tilde{z} \end{aligned} \tag{6}$$

where the Principal Value (PV) ensures the convergence of the integral.[3] We now take care of the driving resulting from the imposed loading conditions. As the displacement δ of the lower plate is increased, the driving $G(c_0, \delta)$ increases too. As a result, the three terms on the right-hand side of Eq. (1.6) must be updated. However, two of them are already linear in the front perturbation, so we only need to update the first one that is the only one to bring a first order contribution. Limiting this analysis to short propagation distance, the opening displacement $\delta = \delta_0 + v_{\text{ext}}t$ can be expressed as the sum of the initial opening with a small variation $v_{\text{ext}}t \ll \delta_0$ that increases linearly with time where v_{ext} is the opening rate imposed by the test machine. This leads to $G(c_0, \delta) = G(c_0, \delta_0) + \left.\dfrac{\partial G}{\partial \delta}\right|_{c_0,\delta_0} v_{\text{ext}}t$ while the two other terms depending on δ in Eq. (6) are replaced by $\partial G/\partial c|_{c_0,\delta_0}$ and $G(c_0, \delta_0)$.

For a *stable* fracture test geometry, i.e. when the external driving $G(c_0, \delta)$ *decreases* with the crack length, $\partial G/\partial c|_{c_0,\delta_0}$ is negative. Introducing the structural length $\mathcal{L} = -\dfrac{G(c_0, \delta_0)}{\partial G/\partial c|_{c_0,\delta_0}}$ and the normalized variations of the driving force

$$g(z, t) = \frac{G(z, t) - G(c_0, \delta_0)}{G(c_0, \delta_0)} \tag{7}$$

the Eq. (6) can be rewritten as

$$g(z, t) = \frac{v_m t - \delta c(z, t)}{\mathcal{L}} + \frac{PV}{\pi} \int_{-\infty}^{+\infty} \frac{\delta c(\tilde{z}, t) - \delta c(z, t)}{(\tilde{z} - z)^2} d\tilde{z} \tag{8}$$

where we have introduced the velocity $v_m = -\dfrac{\partial G/\partial \delta|_{c_0,\delta_0}}{\partial G/\partial c|_{c_0,\delta_0}} v_{\text{ext}}$ t imposed by the loading machine to the crack.

Equation (8) calls for a few comments. The constant opening rate imposed to the fracturing specimen turns out to be equivalent to pull on the crack line with an array of springs of effective stiffness $1/\mathcal{L}$ driven at the velocity v_m. Thus, this amounts to consider that the crack line is trapped in a potential well moving at some constant velocity, as classically considered in disorder elastic interface problems (Rice 1985; Måløy and Schmittbuhl 2001). The non-local term in Eq. (8) describes the interactions along the front. This effective line elasticity will compete with the effect of the disorder, as it tends to straighten the crack front.

Fracture energy We now turn to the description of the material fracture properties and introduce the normalized variations of the toughness field

$$C\, g_c(z, x) = \frac{G_c(z, x) - \langle G_c \rangle}{\langle G_c \rangle} \tag{9}$$

[3] The non-local part of the elastic energy release rate can be conveniently written in the Fourier space as $\delta\tilde{G}(q) = -|q|G(c_0, \delta)\delta\tilde{c}(q)$.

where $C \ll 1$ is the toughness contrast that we assume to be small. The variations of g_c are of order one with zero spatial average $\langle g_c(M)\rangle_M = 0$. The toughness field reflects the material microstructure that can be either periodic for engineered materials (Sect. 2.3) or disordered for natural materials (Sect. 2.5).

Kinetic crack growth law To predict the evolution of the crack, its local speed is generally assumed to vary linearly with the local net driving force $v \sim G - G_c$ (Gao and Rice 1989; Ramanathan et al. 1997; Katzav and Adda-Bedia 2006; Bonamy et al. 2008). Here, we justify this linear kinetic law from the Griffith's equilibrium condition $G = G_c(v)$ where the dependence of the fracture energy with the crack speed v is taken into account (Kolvin et al. 2015; Ponson 2016). Indeed, the linearization of the fracture energy $G_c(v) = G_c(v_m) + dG_c/dv|_{v_m}(v - v_m)$ near the average crack speed gives

$$\frac{v - v_m}{v_0} = \frac{G - G_c(v_m)}{G_c(v_m)} \tag{10}$$

where the characteristic velocity $v_0 = \dfrac{G_c(v_m)}{dG_c/dv|_{v_m}}$ follows from the fracture properties of the interface. We will show in the next section that this equation of motion captures successfully the relaxation dynamics of a crack depinning from a single obstacle.

Evolution equation The derivation of an evolution equation for the crack is now in order, as it suffices to insert the expressions (8) and (9) of the elastic energy release rate and the fracture energy into the kinetic law of Eq. (10). Considering small enough crack perturbations $\delta c \ll c_0$, one can decouple the zeroth order equation $G(c_0, \delta_0) = \langle G_c(v_m)\rangle$ from the first order one $\dfrac{\partial\delta c/\partial t - v_m}{v_0} = g(z,t) - C\, g_c(z, x = \delta c(z,t))$ where all terms are linear in contrast $C \ll 1$.

Using the expressions (8) and (9) into the previous equation, one obtains

$$\frac{\partial\delta c/\partial t - v_m}{v_0} = \frac{v_m\, t - \delta c}{\mathcal{L}} + \frac{PV}{\pi}\int_{-\infty}^{+\infty} \frac{\delta c(\tilde{z}) - \delta c(z)}{(\tilde{z} - z)^2} d\tilde{z} - C\, g_c(z, f). \tag{11}$$

This evolution equation provides a powerful tool to make predictions on the crack front geometry and its evolution, as we now show through the comparison with experiments.

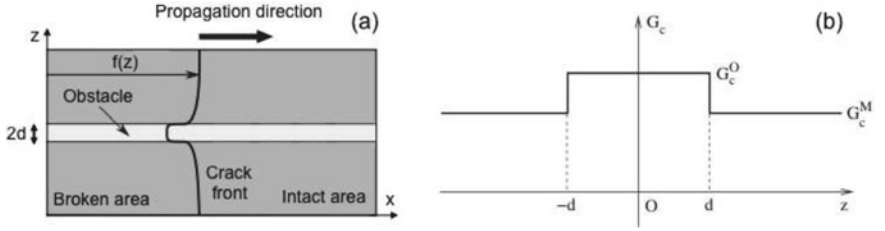

Fig. 4 **a** Pinning of a crack by an isolated obstacle. **b** The landscape of fracture energy varies as a step function along the front and is characterized by the toughness contrast $C = \dfrac{G_c^O - G_c^M}{G_c^M} = \dfrac{G_c^O - \bar{G}_c}{\bar{G}_c}$ where the normalized toughness variation $g_c(z)$ introduced in Eq. (12) is equal to one within the defect and zero elsewhere

2.3 *Comparison with Experiments: Crack Pinning by a Single Obstacle*

We now confront the proposed theory with experimental observations made in simple configurations: (i) the stationary deformed shape taken by a front when pinned by a single obstacle and (ii) its dynamics as it relaxes toward a straight configuration after depinning from an obstacle.

Stationary shape of a crack pinned by an obstacle An emblematic example of crack pinning phenomenon is the case of a crack trapped by a single obstacle that is infinitely elongated along the propagation direction, as shown in Fig. 4a. The field of fracture energy is invariant along the propagation direction x, and varies along the crack front direction z according to the step function represented in Fig. 4b. Under such a hypothesis, this problem reduces to

$$g[\delta c(z)] = C\, g_c(z, v_m) \tag{12}$$

as the crack speed is constant along the front. This equation can be conveniently solved in the Fourier space, as

$$\delta\tilde{c}(q) = \frac{C\, \tilde{g}_c(q)}{1/\mathcal{L} + |q|}. \tag{13}$$

where $\mathcal{L}$ is the structural length introduced previously. We then need to calculate the inverse Fourier transform $\delta c(z) = \dfrac{1}{2\pi}\displaystyle\int_{-\infty}^{+\infty} \delta\tilde{c}(q) e^{iqz} dq$ to obtain the front deformation[4]

[4] The convergence of this integral is ensured under the condition $dG_0/dc_0 < 0 \Leftrightarrow \mathcal{L} > 0$. In fact, the limiting case $dG_0/dc_0 \to 0 \Leftrightarrow \mathcal{L} \to +\infty$, admits also a solution as long as these front perturbations

$$\delta c(z) - \delta c(0) = \frac{Cd}{\pi}[(1 + z/d)\log(|1 + z/d|) + (1 - z/d)\log(|1 - z/d|)]. \quad (14)$$

in the limit $\mathcal{L} \to +\infty$ (Vasoya et al. 2013). A striking feature of the process of pinning by a single obstacle is that the front perturbation increases logarithmically as $\delta c(z) \simeq 2Cd/\pi \log(|z|/d)$ for $z \gg d$ far away from the defect. This behavior is reminiscent of the long-range elasticity of the crack front.[5]

We now study the effect of large toughness contrasts, leading subsequently to large front deformations. This can be assessed by calculating the second order term in the development of the elastic energy release rate with respect to $\delta c(z)$

$$G[f(z)] = G_0(c_0) + \delta G^{(1)}[\delta c(z)] + \delta G^{(2)}[\delta c(z)] \quad (15)$$

where the first order term $\delta G^{(1)}$, linear in the perturbation $\delta c(z)$, is given in Eq. (6), and the second order term, proportional to the square of the perturbation, follows

$$\delta G^{(2)}[\delta c](z) = \frac{1}{2}\frac{d^2 G_0}{dc_0^2}[\delta c(z)]^2 + \frac{1}{2\pi}\frac{dG_0}{dc_0}\int_{-\infty}^{+\infty}\frac{\delta c'(z')(\delta c(z) + \delta c(z'))}{z' - z}dz' + \mathcal{G}[\delta c](z) \quad (16)$$

with

$$\mathcal{G}[\delta c(z)](z) = \frac{G_0}{4\pi^2}\int\int_{-\infty}^{+\infty} dz'dz''\frac{\delta c(z') + \delta c(z)}{(z' - z)^2)}\times \left[\frac{\delta c(z'') + \delta c(z)}{(z'' - z)^2} + \delta c'(z')\left(\frac{1}{z' - z} + \frac{2}{z' - z''}\right) + \frac{2\delta c(z')}{z'' - z}\left(\frac{1}{z' - z} - \frac{1}{z - z''}\right)\right]. \quad (17)$$

The details of the calculation of this second order term are provided in Vasoya et al. (2016a). It relies on two formulas derived by Rice (1989) using the weight functions theory of Bueckner (1970).[6]

---

are calculated from the reference configuration $\delta c(0)$. In physical terms, it means that the structural length $\mathcal{L}$ is much larger than the obstacle width d.

[5] The logarithmic evolution of the perturbation obtained for a crack pinned by a single heterogeneity can be inferred more directly by considering the application of a point force on the front that reflects the toughness distribution $g_c \sim \delta(z)$ where δ is the Dirac function. The application of the equilibrium condition Eq. (13) in the limit $\mathcal{L} \to 0$ gives $\delta\tilde{c} \sim 1/|q|$ that results in the logarithmic behavior $\delta c(z) \sim \log(|z|)$.

[6] The second order term calculated by this procedure takes a more compact form in Fourier space

$$\delta\tilde{G}^{(2)}[\delta\tilde{c}](q) = \int_{-\infty}^{+\infty}\mathcal{Q}(q', q - q')\delta\tilde{c}(q')\delta\tilde{c}(q - q')dq' \quad (18)$$

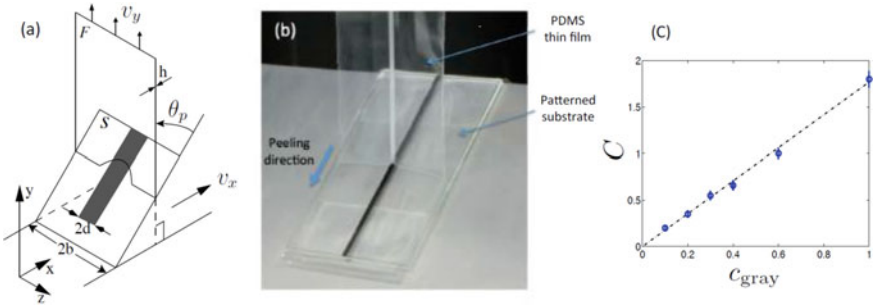

Fig. 5 Experimental setup for studying the front shape pinned by a single obstacle: **a** Schematic representation of the peeling test. The substrate is moved horizontally in order to maintain a constant peeling angle. **b** Snapshot of the experiment. **c** Relationship between the contrast C of adhesion energy as a function of the level of gray c_{gray} used to print the obstacle

We apply now Eq. (19) to predict the shape of a planar crack pinned by a single obstacle. We look for the front shape up to second order in the toughness contrast

$$c(z) = c_0 + \delta c(z) \quad \text{with} \quad \delta c(z) = C\delta c^{(1)}(z) + C^2\delta c^{(2)}(z) \tag{20}$$

The Fourier transform of the front shape is used in the expression (15) of the elastic energy release rate leading to

$$\begin{aligned}\tilde{G}(q) = G_0(c_0)\delta(q) + C\delta\tilde{G}^{(1)}(q)[\delta\tilde{c}^{(1)}(q)] \\ + C^2\left(\delta\tilde{G}^{(1)}(q)[\delta\tilde{c}^{(2)}(q)] + \delta\tilde{G}^{(2)}(q)[\delta\tilde{c}^{(1)}(q)]\right)\end{aligned} \tag{21}$$

where terms of higher order have been neglected. Comparing with the expression (12) of the toughness field that does not contain terms proportional to C^2, we conclude that the second order term between bracket in the former expression equals to zero, leading to $\delta\tilde{G}^{(1)}\left[\tilde{\delta c}^{(2)}\right](q) = -\delta\tilde{G}^{(2)}\left[\delta\tilde{c}^{(1)}\right](q)$ which provides, using Eqs. (14) and (16), the second order term of the front shape

---

where the kernel $\mathcal{Q}$ follows the form

$$\begin{aligned}\mathcal{Q}(q',\tilde{q}) = \frac{1}{2}\frac{d^2G_0}{dc_0^2} - \frac{1}{4}\frac{dG_0}{dc_0}[|q'+\tilde{q}| + |q'| + |\tilde{q}|] + \\ \frac{G_0}{8}\left[\text{sign}(q'\tilde{q})(q'+\tilde{q})^2 + [\text{sign}(q') - \text{sign}(\tilde{q})]\,|q'+\tilde{q}|(k'-\tilde{q}) - (|q'| - |\tilde{q}|)^2\right].\end{aligned} \tag{19}$$

.

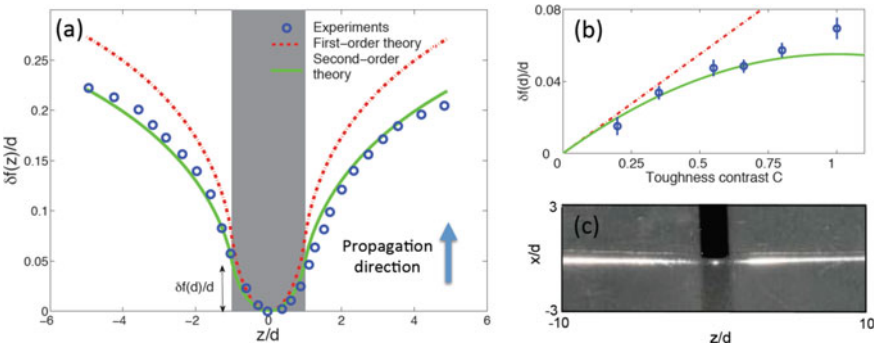

Fig. 6 Stationary shape of a peeling front pinned by a single obstacle of contrast $C = 0.65 \pm 0.06$, and comparison with the first- and second-order theoretical predictions (Eqs. (14) and (22)). **b** Variations of the normalized amplitude $\delta c(d)/d$ of the crack front deformation as a function of the contrast, and comparison with the predictions of the first- and second-order theories. **c** Typical snapshot of the peeling front pinned by the obstacle

$$\delta c^{(2)}(z) = \begin{cases} -\dfrac{d}{2\pi}[(1+z/d)\ln(1+z/d) + (1-z/d)\ln(1-z/d)] & \text{if} \quad |z/d| \le 1 \\ -\dfrac{d}{2\pi}\left[(|z/d|-1)\ln\left(\dfrac{|z/d|+1}{|z/d|-1}\right) + 2\ln 2\right] & \text{if} \quad |z/d| \ge 1. \end{cases} \tag{22}$$

This term brings a correction to the first order solution given in Eq. (14). A striking feature is that the second order correction *decreases* the total front deformation, indicating that the front *stiffens* under the effect of a tough heterogeneity, as reflected by the negative sign of the second order term.

These effects are now brought out experimentally in the context of thin film peeling from heterogeneous substrate, using the setup presented in Fig. 5. The local fracture properties of the interface are fully controlled by printing obstacles on a commercial transparency, taking advantage of the high adhesion energy of the printed regions compared to the neat one (see Fig. 5c). In particular, this allows to control and tune the toughness contrast that has been measured separately as a function of the grey level used for the obstacle. The relevance of the previous theory to describe the deformation of the peeling front is justified in Vasoya et al. (2016a). It relies on the fact that the previous analysis remains also valid for a crack lying at the interface between two thin elastic plates. It so occurs that the replacement of the bottom elastic plate by a rigid one does not affect the calculation, as long as the limit $h/d \to 0$ where h is the plate thickness is considered.[7]

Figure 6a shows the stationary shape of a peeling front separating the bonded from the unbonded domain of an adhesive peeled from a substrate patterned with a

[7] Note however that the expressions (6) and (16) of the perturbed elastic energy release rate are multiplied by a factor 4 for infinitely thin plates $h/d \to 0$. As a result, the expression of the front deformation given in Eqs. (14) and (22) are simply divided by a factor of 4.

defect of controlled toughness contrast $C = 0.65$. The experimental front compares well with the theoretical predictions, when both the first order and second order terms are used, while the first order term used alone slightly overestimates the perturbations amplitude. These non-linear effects are also visible in Fig. 6b that shows the front perturbations amplitude versus the toughness contrast: The amplitude $\delta c(d)/d$ increases more slowly with C than the linear prediction of the first order theory. Here, the theoretical expressions (14) and (22) of the front perturbations derived in an infinite medium have been divided by a factor four to take into account that $\delta G^{(1)}$ and $\delta G^{(2)}$ are four times larger for a peeling front than for a crack front, resulting in a front deformation four times smaller in the peeling geometry for a same value of contrast (Xia et al. 2012, 2015; Vasoya et al. 2016a).

Depinning dynamics We now go beyond the stationary behavior of crack fronts, and test further the proposed theory by exploring the dynamics of the crack as it recovers a straight configuration after depinning from a tough obstacle. The experimental setup is presented in Fig. 7a: a PMMA plate (Young's modulus $E = 1.5$ MPa) is detached from a thick PDMS elastomer block ($E = 1.8$ GPa and $\nu \simeq 0.5$) through the application of a vertical upward point like force exerted at the extremity of the plate. We then track the full spatio-temporal evolution of the front as it escapes from a rectangular obstacle and relaxes towards a straight configuration (Fig. 7b and c). This experimental setup is thus designed to explore the crack front behavior in response to a step driving over a region of extent 2d along the front Here, both parameters can be varied thanks to our patterning technique that allows to print obstacles of controlled size and strength. It turns out that this fracture test geometry is amenable to a proper comparison with the theory proposed in Sect. 2.2. The reason is that the first order expression (6) of the perturbed elastic energy release rate remains valid for an interfacial crack too for the particular case considered here where one of the plate is rigid while the other one is incompressible.

From a theoretical point of view, the dynamics of the front during depinning is addressed by considering the motion equation (11) derived in Sect. 2.2 but with a homogeneous toughness field $g_c = 0$. The initial front geometry at the onset of depinning corresponds to the stationary shape derived previously for a front pinned by an isolated obstacle of width $2d$ and is given in Eq. (14). The resolution of the relaxation dynamics is detailed in Chopin et al. (2018) where the expression of the front shape evolution $\delta c(z,t)$ is also provided. The velocity field follows

$$\frac{\partial \delta \dot{c}}{\partial t}(z,t) = C v_0 \left[1 - \frac{1}{\pi} \left(\arctan\left(\frac{v_0 t}{d+z} \right) + \arctan\left(\frac{v_0 t}{d-z} \right) \right) \right] \tag{23}$$

for small defects $d \ll \mathcal{L}$ compared to the structural length introduced previously. It provides a simple physical interpretation of the characteristic velocity v_0 introduced in the crack front evolution equation, as v_0 sets the initial velocity $v_{\text{dep}} = \partial c/\partial t(|z| < d, 0) = C v_0$ at the onset of depinning. As the fracture toughness is found to increase as $G_c v_m^{\gamma}$ with the crack speed v_m where $\gamma = 0.35 \pm 0.05$, we

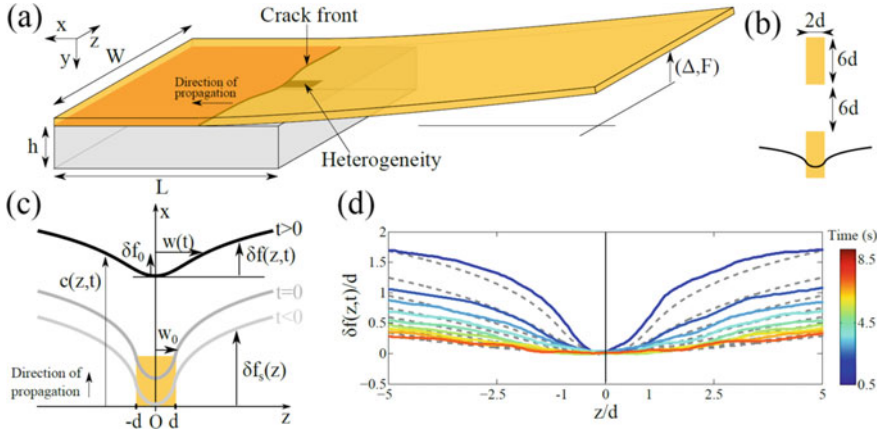

Fig. 7 **a** Schematics of the experimental setup showing a interfacial crack front pinned by an heterogeneity. **b** Geometry of the rectangular obstacles of larger toughness. **c** Crack front positions $c(z, t)$ in the stationary regime ($t < 0$), at the onset of depinning ($t = 0$) and during relaxation ($t > 0$). $\delta c(z, t) = c(z, t)c(0, t)$ describes the crack front geometry at time t. **d** Sequence of crack profiles after depinning from an obstacle ($d = 140\ \mu$m, $C = 1.2$, $v_m = 24\ \mu$m/s). The dotted lines correspond to the model prediction using the depinning velocity $v_{\text{dep}} = 76\ \mu$m/s as a unique fitting parameter

expect $v_0 = G_c(v_m)/G_c'(v_m) = v_m/\gamma$ to be proportional to the average crack speed v_m.

The comparison of the predicted front shapes with the sequence of crack profiles measured experimentally are presented in Fig. 7d. The unique fitting parameter is the depinning velocity v_{dep}. v_{dep} obtained for several experiments performed at different average crack speeds v_m and contrasts C are presented in Fig. 8. It increases linearly with the mean speed and the contrast, in agreement with the theoretical prediction $v_{\text{dep}} = Cv_0 = Cv_m/\gamma$. The slope $v_{\text{dep}}/(Cv_m) \simeq 3.1$ is compatible with the measurement of the exponent $\gamma = 0.35$.

Interestingly, this shows that depinning dynamics is not controlled by inertia but instead by the rate dependency of the dissipative mechanisms taking place within the fracture process zone. This confirms that the crack speed v can be predicted from an overdamped equation of motion $(v - v_m)/v_0 = G - G_c$ where v_m is the mean speed and $v_0 = G_c(v_m)/G_c(v_m)'$ is a characteristic velocity of the material emerging from the variations of the fracture energy with the crack speed.

2.4 *Application: Failure by Design*

The experimentally validated theoretical framework for crack propagation in heterogeneous materials can be used as a tool to design materials with new and improved

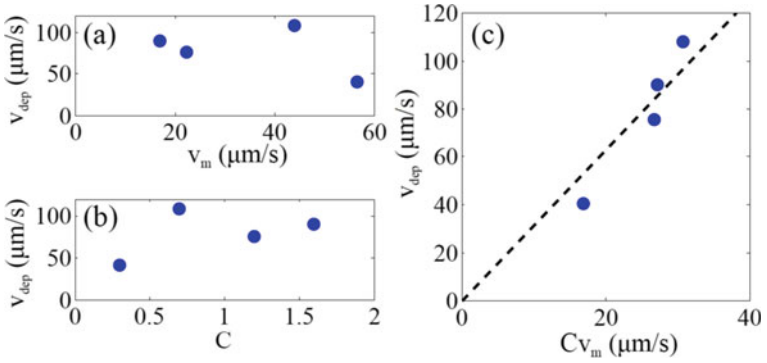

Fig. 8 **a** and **b** Depinning velocity v_{dep} defined as the jump in crack speed as the front escapes from an obstacle of toughness contrast C. **c** After normalization by C, v_{dep} increases linearly with the mean speed v_{m} with a slope $1/\gamma = 3.1$, in agreement with the theoretical prediction $v_{\mathrm{dep}} = C v_0$ where $v_0 = v_{\mathrm{m}}/\gamma$ is the characteristic velocity involved in the crack evolution equation (see Sect. 2.2)

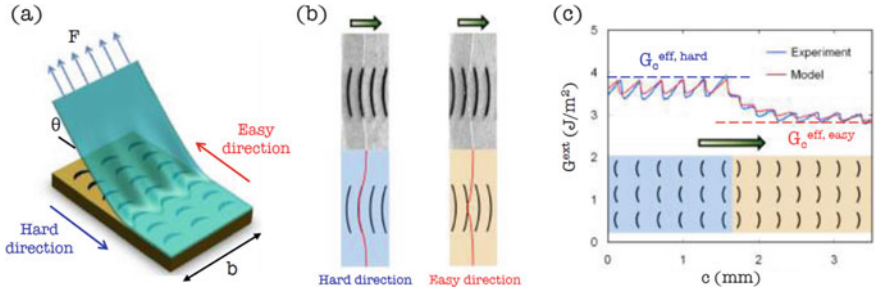

Fig. 9 **a** Peeling of adhesive tape adhesive heterogeneities. **b** The peeling front is distorted as it negotiates regions of enhanced or diminished adhesion energy. Top halves show the experimental observations while the bottom halves show the results of the theory. The arc features have a constant line thickness of 100 μm and a vertical span of 4 mm. **c** The measured elastic energy release rate to peel a film from a patterned substrate: note that the force in the forward-facing region is higher than that in the backward-facing region

failure properties. Indeed, designed obstacles introduced at small scale with an appropriate shape can produce dramatic effect at large scale by changing the overall material toughness. We illustrate this concept of *failure by design* in the context of thin film adhesives. We consider heterogeneous adhesives with the arc pattern shown in Fig. 9a. We create two regions with the pattern pointing in opposite directions. This allows us to examine the adhesive strength in both directions in a single test and remove artifacts resulting from variations in sample preparation and loading. As we peel the film, the peel force oscillates as it passes each column of arc-shaped regions of higher adhesion energy. More importantly, the effective adhesive strength in the forward region (front first touching the convex portion of the arc) is 25% higher than that in the backward region. As the front propagates in the forward region, it first encounters the curved convex portion of the arc. As a result, it deforms following the

arc shape imposed by the obstacle until it sees it as a significant obstacle that requires a large peeling force to overcome (Fig. 9b). On the other hand, as the front propagates in the backward region, it first encounters the narrow arms of the arc. As a result, the front does not deform much and sees these as smaller obstacles. The evolution equation (11) derived in Sect. 2.2 is used to model quantitatively this phenomenon. The computed front shape as well as the peel forces are also shown in Fig. 9b and c and agree with the experimental observations.

In order to achieve stronger asymmetry, we can optimize the pattern geometry. Using an algorithm developed in the context of elastic manifolds driven in random media (Rosso and Krauth 2001a), the asymmetric factor $\alpha = G_c^{\text{eff,hard}}/G_c^{\text{eff,easy}}$ is computed efficiently allowing the exploration of a large range of geometrical parameters and strength contrast. The most asymmetric adhesives are made of obstacles with very thin arms. An asymmetric factor as large as the toughness contrast $\alpha \leq C \simeq G_c^O/G_c^M$ can be reached. This corresponds to a situation where the effective toughness is entirely governed by the toughness G_c^O of the obstacle in the hard direction, while it is set by the matrix toughness G_c^M in the opposite one.

More generally, it can be shown that the minimum value of the local toughness field constitutes a lower bound for the effective toughness while the maximum value corresponds to an upper bound, leading to

$$\min_M G_c(M) \leq G_c^{\text{eff}} \leq \max_M G_c(M). \tag{24}$$

2.5 *Effective Toughness of Disordered Solids*

A question of broad interest is the effective failure properties of brittle solids with random distributions of obstacles, as most materials display disordered microstructures. The challenge is to determine the deformed configuration $c(z,t)$ of the front and its evolution, that informs about the visited region of the toughness landscape allowing to compute the effective toughness $G^{ext}(t) = \langle G_c(z, x = c(z,t))\rangle_z$ (see Sect. 2.1). Note that the evolution equation (11) is strongly nonlinear and cannot be solved analytically in that case, since the front configuration c(z, t) is argument of the disorder term $G_c\,(z, x = c(z,t))$. We consider here a fracture plane embedding a disordered arrangement of weak obstacles (see Fig. 3), the toughness of which is drawn from a statistical distribution (Gaussian, bivalued, exponential..). The toughness field is then characterized by a correlation length ξ that corresponds to the typical obstacle size and the relative fracture energy fluctuations $\sigma = \langle g_c^2(M)\rangle_M$ that quantifies the strength of the disorder. Dèmery et al (2014) used a numerical procedure based on the fast determination of the *critical* configuration of the crack that corresponds to the maximum of $G^{ext}(c)$.

This study shows that the effective toughness is systematically *larger* than the average value of the toughness field

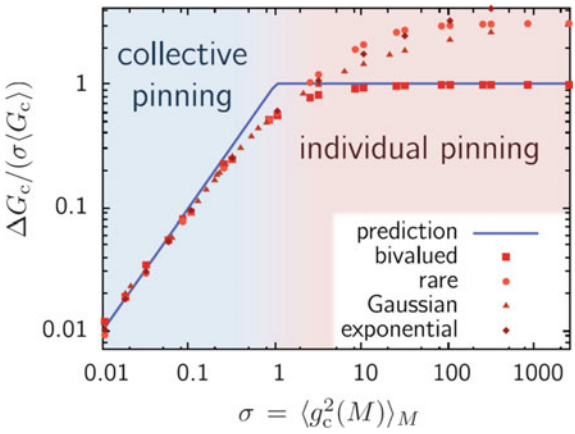

Fig. 10 Phase diagram of the crack behavior as a function of the toughness map: **a** Weak pinning versus **b** strong pinning

$$G_c^{\text{eff}} = \langle G_c \rangle + \Delta G_c. \tag{25}$$

The toughening induced by the disorder is studied in detail in Fig. 10 that shows $\Delta G_c/(\langle G_c \rangle)$ normalized by σ as a function of the level of disorder σ. It reveals two regimes. In the so-called collective pinning regime ($\sigma \ll 1$), the effective toughness can be expressed as a function of σ only, irrespective of the actual distribution of obstacle strength. This is at odd with the individual pinning regime ($\sigma \gg 1$) where the passage from micro to macroscale is more subtle and the full distribution of local toughness is required to be predictive. The scaling of the toughening $\Delta G_c \sim \sigma^2$ in the collective pinning regime can be understood from arguments proposed by Larkin and Ovchinnikov (1979) in the context of pinning of vortexes in superconductors. A key idea is the concept of Larkin length $L_{\text{Larkin}} = \xi/\sigma^2$ that separates a small scale regime $\delta z \ll L_{\text{Larkin}}$ governed by elasticity from a large scale regime $\delta z \gg L_{\text{Larkin}}$ governed by disorder. In the so-called Larkin regime $\delta r \ll L_{\text{Larkin}}$, also referred to as the weak pinning regime, the assumption $G(M) = G_c(M)$ is satisfied. L_{Larkin} corresponds to the scale at which the front geometrical perturbations $\Delta c(\delta z = L_{\text{Larkin}}) \simeq \xi$ becomes of the order of the correlation length of the toughness field. The comparison of the Larkin length with the correlation length ξ provides explanation for the transition from the collective regime ($L_{\text{Larkin}} \gg \xi$) to the individual pinning ($L_{\text{Larkin}} \ll \xi$). Such a rationalization of the disorder induced toughening in brittle failure opens interesting perspectives for the design of tougher solids embedding randomly distributed inclusions. The extension of this approach to fully 3D crack propagation problems where the front can meander out of the mean fracture plane has been recently addressed in Lebihain et al. (2021) and will be discussed in the conclusion Sect. 2.7.

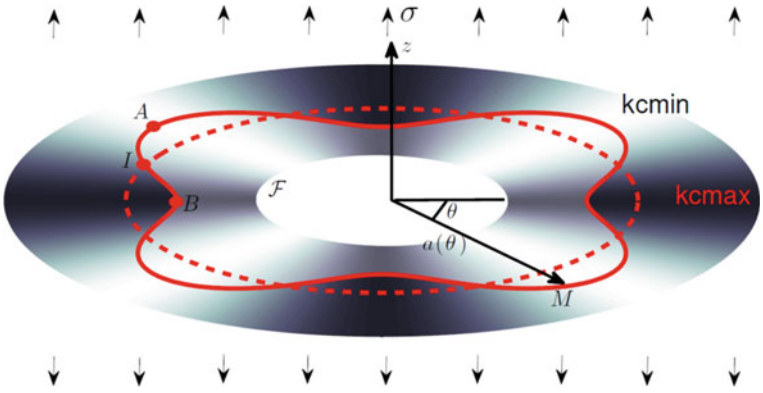

Fig. 11 Penny-shape crack under traction pinned by a periodic array of k tough obtacles schematized here for $k = 4$

2.6 *Effective Toughness of Penny-Shaped Cracks: From Pinning to Fingering*

Until now, we have considered *stable* loading conditions, corresponding to an elastic energy release rate under fixed applied loading that *decreases* with the crack length a_0 $\left(\partial G_0/\partial a_0|_{\delta,\sigma} < 0\right)$. Here, we study the effect of unstable loading conditions $\left(\partial G_0/\partial a_0|_{\delta,\sigma} > 0\right)$ on both the deformation of the front under the effect of tough obstacles and the resulting effective toughness (Vasoya et al. 2016b).

As an example of unstable loading condition, we consider a penny-shape crack embedded in an infinite elastic medium submitted remotely to the tensile stress σ (see Fig. 11). The unperturbed elastic energy release rate follows $G_0 = \frac{4}{\pi}\frac{\sigma^2}{E}a_0$. We assume a planar propagation within a plane constituted of k tough obstacles of contrast C that we describe through the toughness map,

$$G_c^M = \langle G_c \rangle (1 + 2C\cos(k\,\theta)). \tag{26}$$

where $g_c(\theta) = cos(k\theta)$ are the normalized toughness variations with respect to the average toughness $\langle G_c \rangle$. In this way, the toughness depends on the position through the polar angle θ only so that the toughness is invariant along the propagation direction. We note $\lambda = 2a/k$ the obstacle width, where $a = \sqrt{S/\pi}$ is the apparent radius of the deformed crack of area S.

To predict the crack evolution, we use an iterative numerical procedure that allows to update the local elastic energy release rate $G(M)$ after each increment. It provides the crack evolution in both weakly ($C \to 0$) and strongly ($C \to 1$) heterogeneous toughness fields (see Vasoya et al. 2016b for details). As a result, this method allows to investigate the failure behavior of highly heterogeneous materials beyond the limit of the linear theory presented in Sect. 2.2.

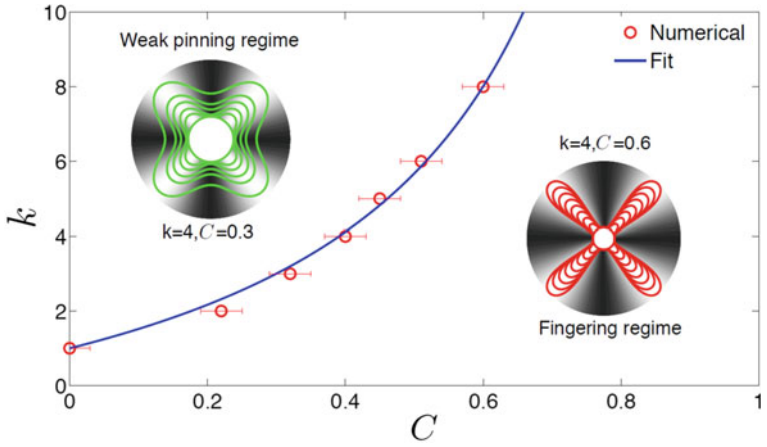

Fig. 12 Phase diagram of the crack behavior as a function of the toughness map: Weak pinning versus strong pinning

The systematic study of the evolution of the crack front deformation as a function of the number k of obstacles and their strength C allows us to define two separated regions in the (k, Δ) parameters space of Fig. 12, that associate with two distinct growth regimes:

- A weak pinning regime taking place for small obstacle strengths $C < C_c(k)$ where, after an initial transient, the front reaches a stationary shape characterized by a finite petal size.
- A fingering strong pinning regime taking place for large obstacle strengths $C > C_c(k)$) where localized regions of the front remain trapped by the obstacles while the other ones propagate in-between forming elongated fingers. In that regime, the crack shape never becomes stationary and looks like a flower with infinitely growing petals. Despite different underlying mechanisms, this morphology is not without reminding the digital instability emerging in soft elastic films when used as joints between relatively rigid bodies (Ghatak et al. 2000; Saintyves et al. 2013) or the fingers destabilizing the interface between two immiscible fluids of different viscosity (Saffman and Taylor 1958).

To understand this behavior, we explore further the response of the front in the pinning stable regime as it is trapped by an obstacle. Figure 13 shows the normalized front deformation amplitude $\Delta a/\lambda = (a(A) - a(B))/\lambda$ as a function of the toughness contrast C of the obstacle—see Fig. 11 for the definition of the points A and B located on the front. Interestingly, the front amplitude normalized by the obstacle width increases faster than linearly, implying that the front *softens* as it deforms. This response is antagonist to the response characterizing semi-infinite cracks under

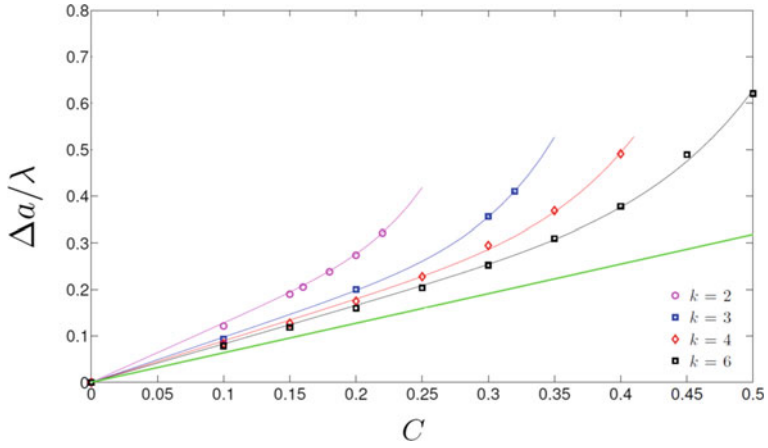

Fig. 13 Amplitude $\Delta a = a(A) - a(B)$ of the front deformation normalized by the obstacle width λ as a function of the obstacle strength C. The *softening* of the crack at high contrast values reflects the *unstable* loading conditions imposed to the penny-shaped crack represented in Fig. 11. This response is antagonist to the one of a semi-infinite crack under stable loading conditions that *stiffens* under the effect of very tough obstacles. The straight green line $\Delta a/\lambda = \frac{2}{\pi}C$ corresponds to the response of a penny-shaped crack in the limit $k \to \infty$ of very small obstacles compared to the structural length $\mathcal{L} = G_0/|dG_0/dc| = a$ introduced in Sect. 2.2 (Vasoya et al. (2016b)). The same behavior is obtained for a semi-infinite crack too, as long as the limit $\lambda/\mathcal{L} \to 0$ is also considered (see footnote 8)

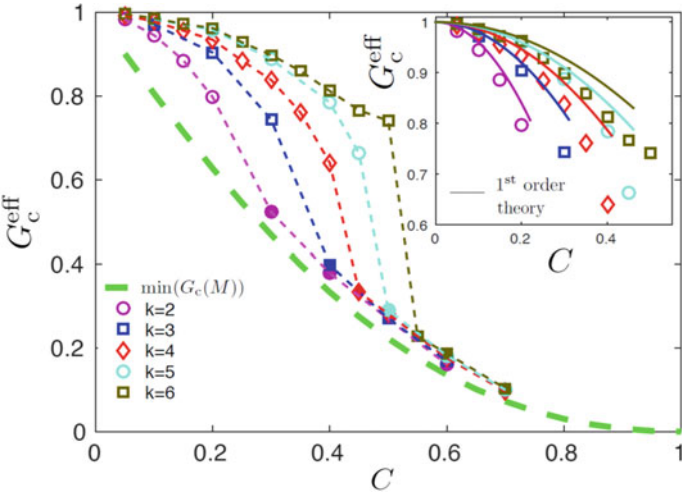

Fig. 14 Effective toughness as a function of the toughness contrast of the obstacles. Note the sudden drop of effective toughness beyond some critical toughness contrast $C_c(k)$ reminiscent of the fingering instability. The inset compares the prediction of the first order theory with the numerical results for the weak-pinning regime ($C \ll 1$)

stable loading conditions studied in Sect. 2.3, and that *stiffens* when submitted to large deformations (see the Fig. 6b and compare it to Fig. 13).[8]

What are the consequences of this behavior on the overall failure behavior of heterogeneous solids? First, the non-linear softening response of crack fronts to tough defects is at the origin of the bifurcation towards a fingering fracture mode, as it induces that beyond some critical contrast, the problem $g[a(\theta)] = C g_c(\theta)$ has no solution.[9] Second, the growth of the cracks thought elongated petals have dramatic consequences on the overall fracture toughness of the material, that is shown in Fig. 14 as a function of the value of toughness. For weak obstacles $C < C_c(k)$, the effective toughness slightly decays with C, but remains close to the average value $[\langle G_c \rangle]$ of the toughness field.[10] While above some critical contrast value $C_c(k)$, the effective toughness suddenly drops to follow another branch corresponding to the minimal value $\min[G_c(M)]$ of the toughness field. This reflects the deformation process of the crack front through very large petals that visit only the weaker regions of the fracture plane.

The discontinuous evolution of the effective fracture energy with the obstacle strength C brings interesting insights on the problem of homogenization in failure of heterogeneous solids. Since the effective fracture properties reflects the (long-time) configuration reached by the crack after its evolution through the heterogeneous fracture plane, a small variation in the material features at small scale may result in large variations in the effective resistance at large scale.

2.7 Conclusion and Perspectives

What are the main insights drawn from the study of the effective toughness of heterogeneous brittle solids? First, the comparison of the results obtained for a semi-infinite

[8] Note the interesting asymptotic case $k \to \infty$ showing a linear behavior (green line in Fig. 8). This case actually corresponds to the behavior of a semi-infinite crack pinned by a sinusoidal distribution of tough obstacles $g_c = 2C\cos(kz)$ that can be solved using Eq. (13) for $C \ll 1$. One obtains sinusoidal front deformations $\delta a(z) = 2C/k\cos(kz)$ of amplitude $\Delta a/\lambda = 2C/\pi$, in agreement with the amplitude of the front perturbations of a penny-shape crack in the limit $\lambda/a \to 0$ of very small obstacles with respect to the crack radius. As the last result is valid for any contrast, this suggests that it may also apply to the semi-infinite crack for any value of C. Ultimately, this suggests that the stiffening behavior observed in Fig. 6 and the softening behavior observed in Fig. 13 for large contrast vanish when the front deformations are negligible with respect to the structural length $\mathcal{L}$.

[9] Roughly speaking, the determination of the stationnary front configuration solving the equation $g(a(\theta)) = C g_c(\theta)$ consists in determining the front deformation amplitude $\Delta a/\lambda(C)$ corresponding to the imposed contrast C (see Fig. 13). However, as the contrast increases, we expect the curves in Fig. 13 to display a vertical asymptote for the critical contrast $C_c(k)$ shown in Fig. 12. This implies that the problem has no solution for $C > C_c(k)$, explaining the continously growing petals observed in the fingering regime.

[10] The slight decrease of the effective toughness with the contrast in this regime can actually be explained quantitatively using the first order theory of Gao and Rice (1987). It allows to capture that a larger section of the front visits the weaker region of the fracture plane where the crack deforms further, leading to $\frac{G_c^{\text{eff}}}{\langle G_c \rangle} = 1 - \frac{4}{k-1}C^2$.

crack under stable loading conditions (Sect. 2.4) and the ones derived for a penny-shaped crack under unstable loading conditions (Sect. 2.6) shows that the effective toughness may not be an intrinsic material property, as it may also depend on some structural parameters, like the variations of the unperturbed elastic energy release rate G_0 with the crack length that strongly affect the way the deforms and interacts with obstacles. This behavior reflects the fact that by essence, fracture problems are structural problems that challenge the possibility to decouple the response related to the material behavior from the one related to the specimen geometry and the loading conditions, as it is classically achieved in other homogenization problems of micromechanics.

However, as one considers the limit $d/\mathcal{L} \to 0$ where $\mathcal{L}$ is a structural length characterizing the variations of the loading conditions with the crack length and d is the characteristic heterogeneity size, this decoupling becomes actually possible. Indeed, when such a clear scale separation between the characteristic microstructural length and the characteristic structural length is achieved, the front deformation under the effect of an obstacle of size d follows the linear behavior $\Delta a/d \sim C$ presented in Fig. 13 at all orders in the front deformation, and for both stable and unstable loading conditions. In this limit, the effective toughness is an intrinsic material property, independent of the loading conditions and the specimen geometry.

One also conclude that the effective toughness can reach any value within the admissible range $\min_M[G_c(M)] \leq G_c^{\text{eff}} \leq \max_M[G_c(M)]$. The upper bound can be approached for fracture processes dominated by pinning, as the front gets trapped by the toughest material region while the lower bond is approached when the crack growth process gives rise to fingering that allows the front to visit only the weakest material regions of the fracture plane.

Going further requires the exploration the effective failure properties of heterogeneous brittle solids in a *fully 3D configuration* where the crack can meander out of the mean fracture plane. A key mechanism is the by-passing of obstacles by the crack that allows the front to visit weaker material regions than if it was confined to a plane (see Fig. 15). This mechanism is however at the expense of an increased loading as the front gets around the obstacle, and so takes place only for sufficiently tough obstacles with respect to the surrounding matrix. The competition between the crossing and the by-passing of obstacles during pinning in 3D crack propagation problems plays a central role in the selection of the local failure properties that ultimately set the effective material toughness. This issue that relates to the competition between trans- to inter-granular failure has been recently revisited in Lebihain et al. (2021). This work builds on the description of cracks perturbed both in and out of the mean fracture plane using the tools detailed in the second chapter of this book. For a disordered distribution of inclusions (like e.g. in Fig. 15), the competition between the crossing and the by-passing of obstacles must be handled by taking into account the collective pinning of the front, as discussed in the previous Sect. 2.5. This can elegantly be done by reducing a fully 3D crack propagation problem to the issue of a co-planar crack propagating in an effective heterogeneous field of toughness, see Lebihain et al. (2021). The predictions given in Sect. 2.5 that provide the effective

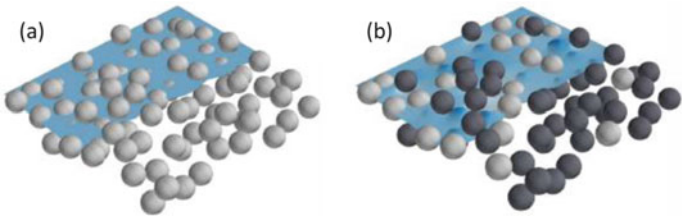

Fig. 15 Comparison between **a** planar and **b** fully 3D propagation crack propagation in a brittle materials with a random distribution of tough inclusions, as obtained from numerical simulations based on Eq. (11) extended to out-of plane perturbations. The inclusions in white are crossed by the crack front while the inclusion in black are by-passed

toughness of a disordered fracture plane can then be readily applied to predict the effective toughness of the overall 3D solid. Overall, the tools presented in Lebihain et al. (2021) constitutes a powerful homogenization framework for brittle fracture problems that paves the way for the rational design of optimized brittle composites with tailored fracture properties, see for example Lebihain (2021).

Interestingly, models of crack propagation in 3D heterogeneous solids provide rich insights on the origin of the roughness of fracture surfaces. This issue, together with the intermittent dynamics of cracks, is addressed in the next part dedicated to fluctuations in crack growth phenomena.

3 Statistics of Fluctuations During the Tensile Failure of the Disordered Materials

Extracting meaningful information from fluctuations has been a preferred line of research in various domains, including the physics of condensed matter. As a result, the approaches and concepts developed in these fields have been largely borrowed and applied to fracture problems (Alava et al. 2006; Bonamy 2009). A major output of these works has been to establish a connection between the failure of disordered materials and critical phenomena. Near a critical point, fluctuations dominate the system behavior, as they can be much larger than average quantities. In addition, they become strongly non-Gaussian and are characterized by power laws that emerge from the interplay between disorder and elastic interactions. In the context of material failure, the observed power laws emerge from the competition between the microstructural disorder and elasticity, often influenced by damage processes. In the following, we give sense to the scaling behaviors of the fluctuations observed experimentally by showing that they are signature of some elementary crack growth mechanisms. This will lead us to propose a unified description of crack growth phenomena in a large range of disordered materials. In the following, we focus on two

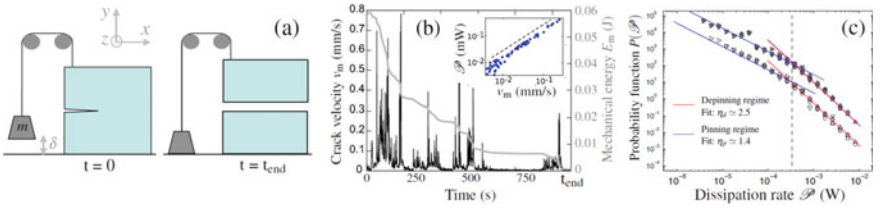

Fig. 16 **a** Isolated system of total energy $E_{tot} = E_m(t) + E_f(t)$ constituted of a notched specimen under dead weight loading conditions. Before failure, the energy is stored as potential energy $E_{tot} = E_m(0)$ that has been fully dissipated in fracture energy $E_{tot} = E_f(t_{end})$ after failure. **b** Experiments in heterogeneous solids show that this transfer from mechanical into fracture energy proceeds through bursts that can be studied through the variations of the crack velocity v_m that is proportional to the dissipation rate $\mathcal{P} = -dE_m/dt = dE_f/dt$ as shown in inset. **c** Density probability of the dissipation rate. The different symbols correspond to different experimental sampling rates, while both curves correspond to two average crack growth velocities. [Courtesy of Barés et al. (2013)]

central quantities in failure problems, the crack speed and its fluctuations in Sect. 3.1 and the crack path and its fluctuations in Sect. 3.2.

3.1 Fluctuations in the Dynamics of Cracks

Experimental observations We start by reviewing some important experimental results on the dynamics of cracks in disordered solids. Here, the emphasis is put on the fluctuations of crack speed that can either be investigated at the local scale, i.e at some location along the crack front, or at the global scale, through the evolution of the average crack position. Interestingly, studying this second quantity amounts to investigate the rate of dissipated energy through failure. To establish this connection, one considers the isolated system depicted in Fig. 16a made of a notched specimen and a dead load pulling on its upper face through frictionless pulleys. The total energy $E_{tot} = E_m + E_f$ can be partitioned into *mechanical* and *fracture* energy. The process of failure proceeds through a transfer of the first contribution into the second one.

In the example depicted in Fig. 16, the initial condition corresponds to a state of the system where the energy is entirely stored in mechanical energy with $\{E_m^0 = E_{tot}, E_f^0 = 0\}$ at $t = 0$. On the contrary, once the sample is broken, all the mechanical energy initially available has been dissipated into fracture so that $\{E_m^{end} = 0, E_f^{end} = E_{tot}\}$ at t_{end}. In practice, for more general loading conditions, the total dissipated energy corresponds to the work of the force applied to the sample during the test that reduces well to the potential energy $E_m^0 = mg\delta$ of the dead load m displaced over the height δ in the specific example considered here.

To describe this energy transfer, we introduce the elastic energy release rate $G(z, t)$ that measures the decrease $dE_m(t) = -\int_0^b G(z, t)\delta c(z, t)dz$ of mechanical energy for an incremental crack advance $\delta c(z, t)$, where $c(z, t)$ provides the crack length

in z at time t. Wherever the crack propagates, G(z, t) is equal to the rate of energy dissipated or fracture energy G_c, so that the mechanical energy released compensates the energy dissipated $dE_f(t) = \int_0^b G(z,t)\delta c(z,t)dz$. It follows that the transfer rate

$$\mathcal{P}(t) = \frac{dE_s}{dt} = -\frac{dE_m}{dt} = \int_0^b G(z,t)\frac{\delta c}{\delta t}dz = b\,G_c(t)v_m(t) \simeq b\,G_c^{\text{eff}}v_m(t) \quad (27)$$

is proportional to the average crack speed v_m.[11] This linear relation has been tested experimentally by Barés et al. (2013) and is shown in the inset of Fig. 16b. The proportionality constant is close to the material fracture energy G_c.[12]

Interestingly, in disordered solids, the dissipation rate is far from being constant in time. Instead, it displays a strong intermittency characterized by bursts of failure activities, as exemplified in Fig. 16b for an artificial rock made of sintered PMMA beads. This observation contrasts with the smooth variation of the displacement imposed to the fracturing specimen that produces a smoothly varying rate dW/dt of mechanical energy injected into the system. To reconcile these two different dynamics, we separate the mechanical energy $E_m = W + E_{el}$ into the work of the external force that varies smoothly with time and the elastic energy stored in the sample from which emerges these strong fluctuations. The elastic solid, by storing potential energy and suddenly releasing it through $avalanches$, acts as a complex filter that drains intermittently the energy flux from the external loading to the crack tip. This stick-slip dynamics is a direct consequence of the disorder nature of the fracturing material.

The velocity signal $v_m(t)$, or equivalently the dissipation rate $\mathcal{P} \sim v_m$, are natural candidates to disentangle this complex dynamics. Their statistics is investigated in Fig. 16c that shows the density probability function of $\mathcal{P}$. The experiments of Barés et al. (2013) show two regimes characterized by power law behaviors with the exponents $\eta_p \simeq 1.4$ and $\eta_d \simeq 2.5$ at small and large dissipation rates, respectively. The presence of two distinct regimes reflects the unique dynamics of cracks in disordered materials that is dominated by rare peaks of activity where the dissipation rate is exceptionally large, separated by almost silent periods where the crack speed and so the dissipation rate is much lower.

To identify the physical processes behind these puzzling observations, it is fruitful to observe the motion of the crack at the local scale, where the front interacts with the material microstructure. Figure 17a shows an experimental setup designed by Maloy et al. (2001) at Oslo's university to explore the local dynamics of crack fronts in disordered solids. In this experiment, the crack front is confined at the weak interface between two transparent PMMA plates where toughness heterogeneities

[11] b denotes the sample width along the z-axis.

[12] Strictly speaking, the effective fracture energy G_c^{eff} corresponds to the maximum of the instantaneous fracture energy $G_c(t)$ while our calculation predicts here that the proportionality constant corresponds to its time-average $\langle G_c(t)\rangle_t$.

have been introduced by sandblasting one of the two plates before sintering them together. The complex evolution of the crack recorded at the micrometer scale using a fast camera is illustrated in Fig. 17b that shows in grey scale the time spent by the front in the different regions of the fracture plane. The intermittency evidenced at the large scale in Fig. 16b is also obvious at the local scale: The black lines visible in Fig. 17b that correspond to long waiting time indicate front configurations that have remained trapped by the material strongest heterogeneities. The white regions on the contrary are reminiscent of micro-instabilities during which the front goes rapidly from one stable configuration to another. The coexistence of two antagonistic behaviors is clearly evidenced in the statistics of local crack velocity shown in Fig. 17c. Their density probability shows two distinct regimes where the small speeds $v < \langle v \rangle$ provides the time spent by the front before escaping from a pinned configuration while the large speeds $v > \langle v \rangle$ characterizes the front dynamics during the so-called *avalanches* right after depinning and before it gets pinned again in another configuration. Interestingly, the power law behavior observed at the local scale in the depinning regime is characterized by the exponent $\eta_d \simeq 2.5$ also measured at the global scale in the experiments of Bares et al. Bonamy et al. (2006) presented in Fig. 16. This implies that the fluctuations resulting from the pinning of the front by heterogeneities introduced at small scale produces speed variations measurable at the sample scale. This survival of the power law statistics with exponent $\eta_d \simeq 2.5$ to upscaling has been explained in Tallakstad et al. (2013): The central limit theorem that generally ensures Gaussian fluctuations of global velocities breaks down here since for large exponents $\eta > 2$, the variance of the local crack speed probability diverges.

We now depict in Fig. 17d the experimental setup build at ∂'Alembert at Sorbonne University where a crack is driven between a transparent PDMS block and a stiff thin plate patterned with randomly located defects of controlled strength and density. This system has been used earlier in Sect. 2.3 to investigate the behavior of cracks pinned by a single obstacle. Similarly to Maloy (1992)'s observations (Fig. 17b), the front dynamics is also very intermittent, as illustrated by the map of Fig. 17e of the front waiting times. However, the scaling behavior of the density probability of local crack speed is characterized by an exponent $\eta_d \simeq 1.9$ significantly lower, as shown in Fig. 17f. We will see in the next section devoted to the comparison with the theoretical predictions that this difference reveals two fundamentally different crack growth mechanisms.

Beyond the density probability of speeds fluctuations, the spatial structure of the velocity field can provide rich insights on the crack growth process in heterogeneous solids. Using Oslo's experimental setup, Tallakstad et al. (2011) explored the correlations between speed fluctuations $\delta v^{front}(z,t) = v^{front}(z,t) - v_m$ by using

$$C(\delta t) = \frac{\langle \delta v^{\text{front}}(z, t+\delta t) \times \delta v^{\text{front}}(z,t) \rangle_{z,t}}{\langle \delta v^{\text{front}}(z,t)^2 \rangle_{z,t}} \tag{28}$$

that provides how the velocity fluctuations at time t correlates with the velocity fluctuations at time $t + \delta t$ for a fixed position z along the front. Figure 2.3a shows

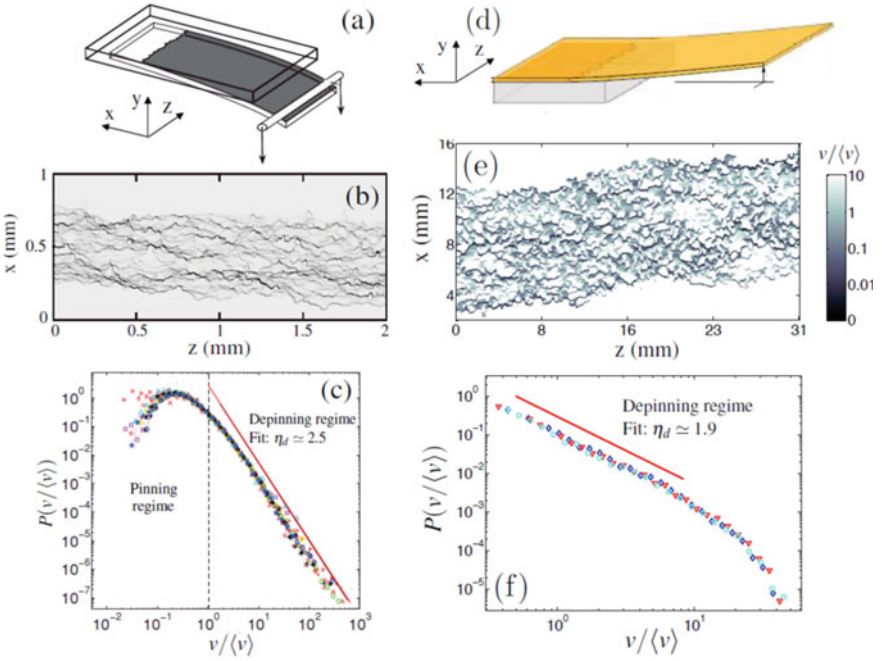

Fig. 17 **a** Sketch of Oslo's experimental setup: Two PMMA plates are sintered together, creating a weak plane for the fracture to propagate. **b** Time spent by the front in the different regions of the fracture plane. The dark lines correspond to long waiting times and thus low velocities while the white domains correspond to micro-instabilities and so fast velocities. **c** Distribution of local crack growth velocities [Courtesy of Måløy et al. (2006)]. **d** Sketch of ∂'Alembert's experimental setup: A thin rigid cantilever is detached from a thick PDMS specimen. The interface where the crack propagates is patterned with randomly distributed obstacles of controlled strength and size. **e** Intermittent dynamics of the crack front in the fracture plane. The dark regions correspond to long waiting times and thus a low velocity while the bright regions correspond to avalanches and so fast velocities. **f** Distribution of local crack growth velocities

the correlation function $C(v)$ for different speeds $0.03\,\mu\,\mathrm{m.s}^{-1} \leq v_m \leq 140\,\mu\,\mathrm{m.s}^{-1}$. After normalization by the time scale δ^*, all the curves collapse on a single master curve. This characteristic time is found to vary as $\delta t^* = l_0/v_m$ and provides the range of time scales $\delta t < \delta t^*$ over which the local speeds are correlated.[13]

In other words, δt^* provides the duration of the coordinated motions of the front that characterize the crack dynamics in disordered materials. We will see in the following section that the divergence of the correlation time of the speed fluctuations in the limit $v_m \to 0$ is signature of the critical nature of the failure of disordered solids, and the exponent characterizing this divergence (here one as $\delta t^* \sim v_m^{-1}$) tells us about the nature of this critical transition.

[13] The length scale $l_0 \approx 8\,\mu\mathrm{m}$ involved in the variations of the correlation time δt^* with v_m is found to be of the order of one tenth of the characteristic size of the heterogeneities.

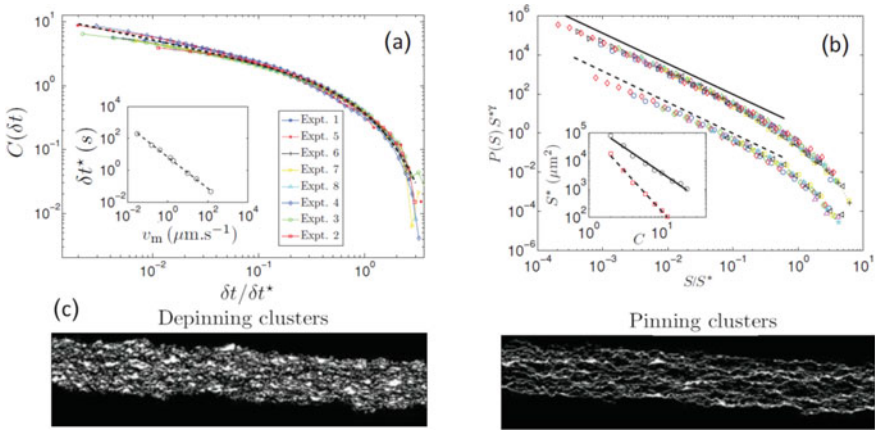

Fig. 18 Characterization of the local crack front dynamics in Oslo's experiment: **a** Correlations between the velocity fluctuations at time t and at time $t + \delta t$ for a fixed position z along the front, as defined in Eq. (28). Curves corresponding to different speeds v_m collapse on a single master curve after renormalization by the correlation time δ^* that is represented in inset as a function of v_m. **b** Distributions of cluster's size both in the depinning regime (top) and the pinning one (bottom). They follow. power law with exponent $\gamma = 1.56 \pm 0.04$. The inset shows the variations of the largest clusters S^* with the value of C used to threshold the velocity matrix. **c** Threshold velocity matrices: for the depinning case, the white clusters correspond to rapid advances of the front, while for the pinning case, they correspond to front positions at arrest for some time. [Courtesy of Tallakstad et al. (2011)]

Finally, the intermittency in the crack evolution illustrated at the *global scale* by the evolution of the mean crack speed (Fig. 16b) is now characterized at the *local scale*. The following procedure proposed in Måløy et al. (2006) is subsequently used: The fracture plane is divided in regular grid using pixels of size $2 \times 2\ \mu\text{m}^2$. The time spent by the front in each of these pixels is recorded, giving rise to the maps shown in Figs. 17b that is referred to as the waiting time matrix. The dark lines in this diagram correspond to long waiting times and thus low velocities while the white domains correspond to micro-instabilities and so fast velocities. The inversion of each individual element of the waiting time matrix gives the so-called velocity matrix V that is then thresholded following

- depinning regime

$$V_d^{\text{thres}} = \begin{cases} 1 & \text{if} \quad v_{i,j} \geq C\, v_m \\ 0 & \text{if} \quad v_{i,j} < C\, v_m \end{cases} \tag{29}$$

- pinning regime

$$V_d^{\text{thres}} = \begin{cases} 1 & \text{if} \quad v_{i,j} \leq v_m / C. \\ 0 & \text{if} \quad v_{i,j} > v_m / C. \end{cases} \tag{30}$$

Figure 18c shows a typical thresholded velocity matrix in each regime. The white depinning clusters revealed by this procedure and shown on the left correspond to regions of the fracture plane that have been rapidly crossed by the front while the white pinning clusters shown on the right reflect configurations of the front trapped by heterogeneities. The distributions $P(S)$ of the cluster sizes is shown in Fig. 18b in both regimes. It shows a power law behavior with an exponent $\gamma = 1.56 \pm 0.04$ for both depinning and pinning.

Theoretical interpretation: crack pinning versus damage coalescence We now interpret these experimental observations by comparing them to the predictions of the model of crack propagation in weakly heterogeneous brittle solids derived in Sect. 2.2. We remind that in this model, damage processes taking place at the crack tip vicinity are assumed to be localized in a process zone of size l_{pz} small with respect to the heterogeneity size ξ, as illustrated in Fig. 20. This assumption justifies the description of failure processes at a continuum scale through Linear Elastic Fracture Mechanics (LEFM). The crack front evolution Eq. (11) as derived from LEFM is particularized to disordered solids by modeling the toughness field by a quenched noise. For pedagogical purposes, we introduce the dimensionless quantities $f(z,t) = \delta c(z,t)/\mathcal{L}$, $u = z/\mathcal{L}$, $w = x/\mathcal{L}$ and $\tau = v_0/\mathcal{L} \times t + 1$ that gives

$$\frac{\partial f}{\partial \tau} = \frac{v_m}{v_0}\tau - f + \frac{PV}{\pi}\int_{-\infty}^{+\infty} \frac{f(\tilde{u}) - f(u)}{(\tilde{u}-u)^2} d\tilde{u} - \eta_c(u, f). \tag{31}$$

This expression reveals that three parameters control the crack front evolution: the normalized mean crack speed v_m/v_0, the ratio of the correlation length over the structural length $\xi/\mathcal{L}$ and the disorder strength $\sigma = \langle \sqrt{\eta_c(u,w)^2} \rangle_{u,w}^{\frac{1}{2}} = \langle \sqrt{G_c(z,x)^2} \rangle_{u,w}^{\frac{1}{2}}$.[14] Since the evolution equation (1) is strongly nonlinear due to the presence of the front perturbation f as an argument of the disorder term η_c, predicting analytically the detailed statistical properties of the crack dynamics remains a very challenging task.[15] To compare our model with the experiments, this equation is thus solved numerically following the procedure described in Ponson and Pindra (2017) for values of the parameters in agreement with the experimental values used in Oslo's experiments. In particular, we choose $\xi/\mathcal{L} = 10^{-3}$ and $\sigma = 1$ of the same order than the experimental values, while v_m/v_0 is varied to mimic the experimental procedure used by Tallakstad et al. (2011).[16]

[14] Higher order momentum of the distribution of toughness do not play any role in the collective regime considered subsequently, as illustrated by the study of the effective toughness of disordered solids presented in Sect. 2.5.

[15] See Wiese and Le Doussal (2007) for a review of the appropriate analytical methods based on the Functional Renormalization Group theory. Note however that they provide only approximated solutions, strictly valid at the critical dimension d_c, where d is the interface dimension with $d_c = 2$ while $d = 1$ for crack propagation problems.

[16] A fit of the experimental data of Lengliné et al. (2011) with the law $G_c \sim (1 + v_m/v_c)^\gamma$ allows for an estimation of the characteristic velocity $v_0 \simeq 140\ \mu$ m.s^{-1} over the experimentally investigated

Let us note that evolution equations similar to Eq. (31) are involved in various physical situations where an interface is driven in a random medium and is known to give rise to the so-called *depinning transition*: under *force* controlled loading conditions, the front is pinned by the disorder and remains stable up to some critical value G_c^{eff} of the applied elastic energy release rate. As in classical critical transitions, the order parameter, the macroscopic velocity of the interface, is then expected to increase as a power law $v_m \sim (G^{\text{ext}} - G_c^{\text{eff}})^{\theta}$ of the distance to the critical point, i.e. the difference between the applied elastic energy release rate G^{eff} and the effective toughness G_c^{eff}, with an exponent $\theta^{the} \simeq 0.625 \pm 0.005$ (Kardar 1998; Ertas and Kardar 1994; Overvelde and Bertoldi 2014; Leschhorn et al. 1997; Duemmer and Krauth 2007). In addition, power law distributed fluctuations are expected to emerge from the front behavior, involving length and time scales that diverge at the depinning threshold. In crack propagation problems, many of these features were evidenced in experiments and shown to compare qualitatively, and to some extent quantitatively, with the predictions derived using the concept of depinning transition (Bonamy and Bouchaud 2011; Bonamy 2009).

However, in most experimental situations like the one considered in Fig. 17 crack growth is achieved under *displacement* controlled conditions. It can be shown that as the driving velocity v_m goes to zero, the net applied force G^{ext} tends to its critical value G_c^{eff}. In other words, under displacement controlled conditions, the driving velocity plays the role of the control parameter and defines the distance to the critical point. In the evolution equation (31), it corresponds to the parameter v_m/v_0.

We start the comparison between theory and experiments through the velocity correlation function introduced in Eq. (28) that we compute for four velocities v_m. As shown in Fig. 19a, the correlation function $C(\delta t)$ predicted from our simulations shows an exponential decay with a characteristic time δt^* that decreases with v_m, as shown in inset. We observe that δt^* is inversely proportional to v_m, and hence

$$C(\delta t) \simeq e^{-\delta t/\delta t^*} \quad \text{with} \quad \delta t^* \simeq \frac{l_0}{v_m} \tag{32}$$

where $l_0 \approx 0.2\xi$. This behavior is in excellent agreement with the experimental observations of Fig. 18a where a similar variation of the velocity correlation function with $l_0 \approx 0.1 \times \xi$ was observed. The divergence of δt^* in the limit $v_m \to 0$ makes perfectly sense from a theoretical perspective: as the system is driven closer and closer to the critical point, the correlation time of the crack motion increases.

But how to interpret quantitatively the scaling $\delta t^* \sim 1/v_m$? As reminded previously, the driving velocity controls the distance to the critical point in the depinning transition. Therefore, as v_m decreases, the size and duration of the largest avalanches increase, and in particular their depth $\xi_{av,x}$. To relate $\xi_{av,x}$ to v_m, we predict first the scaling of the avalanche lateral extent $\xi_{av} \sim v_m^{-\nu/\theta}$ using the velocity exponent θ and the correlation length exponent ν that describes the diver-

range of crack speeds $0.4\,\mu\ \text{m.s}^{-1} \leq v_m \leq 40\,\mu\ \text{m.s}^{-1}$, using the fitting parameters $v_c = 5\,\mu\ \text{m.s}^{-1}$ and $\gamma \simeq 0.07$.

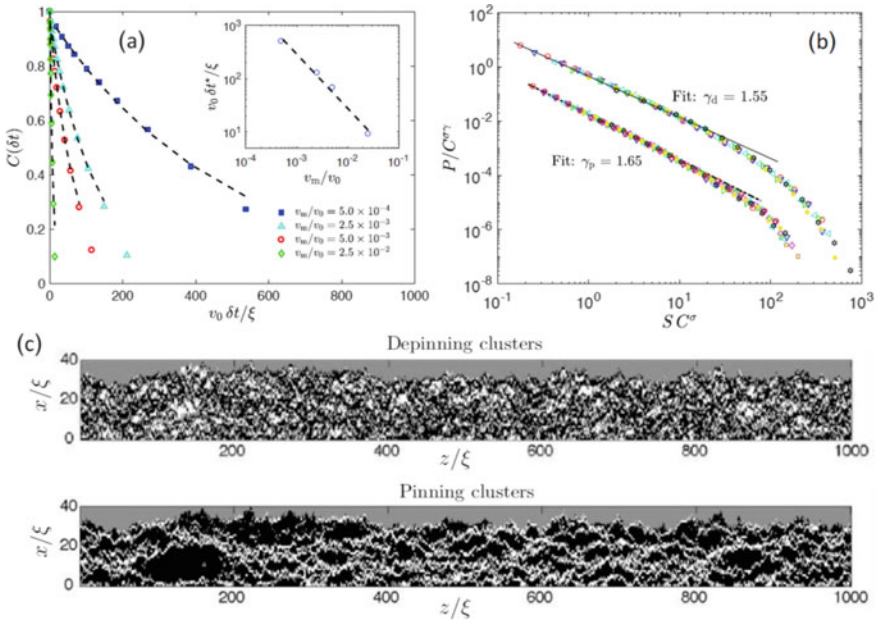

Fig. 19 Local crack front dynamics as predicted from the LEFM-based model of Eq. (2.3) [xi]: **a** Correlation function of the velocity fluctuations as defined in Eq. (28) computed for different average speeds v_m. The exponential decay of Eq. (32) defines the correlation time δt^* that is represented in inset as a function of v_m. **b** Collapse of the distributions of cluster sizes in the depinning regime (top) and the pinning one (bottom) corresponding to different values of the threshold C. Both families of distributions are well described by the power law behavior of Eq. (33) with exponents $\gamma_d = 1.55 \pm 0.05$ and $\gamma_d = 1.65 \pm 0.10$ that are compatible with Oslo's experimental findings (Tallakstad et al. 2011). On the contrary, the scaling of the cut-offs $S_d^* \sim C^{-\sigma_d}$ and $S_p^* \sim C^{-\sigma_p}$ lead to $\sigma_d = 3.8 \pm 0.2$ and $\sigma_p = 1.3 \pm 0.1$, in disagreement with the values measured experimentally. **c** Threshold velocity matrices V_d^{thres} and V_p^{thres}. For the depinning case, white clusters correspond to rapid advances of the front, while for the pinning case, the thin lines correspond to front positions at arrest for some time

gence $\xi_{av} = (G^{\text{ext}} - G_c^{\text{eff}})^{-\nu}$ of the avalanche size close to the depinning threshold. The avalanche depth $\xi_{av,x} \sim \xi_{av}^{\zeta} \sim v_m^{-\zeta\nu/\theta}$ then follows using the roughness exponent ζ that characterizes not only the crack roughness, but also the aspect ratio of avalanches (Barabási and Stanley (1995)). We can then determine the time $\delta t^* = \xi_{av,x}/v_0 \sim v_m^{-\zeta\nu/\theta}$ required to the front to cross the largest cluster that corresponds to the correlation time of the velocity fluctuations. The predicted exponent takes the simplified form $\zeta\nu/\theta = \beta/(1-\beta)$ after using the scaling relation $\theta = \nu(z-\zeta)$ (Nattermann et al. 1992) that involves the dynamic exponent $z = \zeta/\beta$. It takes a value $\beta^{\text{the}}/(1-\beta^{\text{the}}) \simeq 0.98 \pm 0.02$ close to unity using the numerically determined value of the growth exponent $\beta^{\text{the}} \simeq 0.495 \pm 0.005$ (Duemmer

and Krauth 2007).[17] To summarize, the correlation time δt^* relates directly to the *avalanche depth* that both diverge as $1/v_m$ in agreement with the predictions derived from the theory of depinning transition.

We confront further our model with experiments through the distribution of cluster sizes. Depinning and pinning clusters are defined from the velocity matrix that is thresholded at different speeds $C\, v_m$ as detailed in the previous section. This procedure reveals the avalanche like structure of the front dynamics that is shown in Fig. 19c for our simulations. The size distribution of pinning and depinning clusters obtained for different values of the threshold C is shown in Fig. 19b. They follow

$$\begin{cases} P(S_d) \sim S_d^{\gamma_d} e^{-S_d/S_d^*} & \text{with} \quad S_d^* \sim C^{-\sigma_d} \\ P(S_p) \sim S_p^{\gamma_p} e^{-S_p/S_p^*} & \text{with} \quad S_p^* \sim C^{-\sigma_p}. \end{cases} \tag{33}$$

Optimizing the collapse of distributions with different C values give the exponents $\gamma_d = 1.55 \pm 0.05$ for the depinning clusters and $\gamma_p = 1.65 \pm 0.10$ for the pinning clusters. This behavior is compatible with the experimental findings made in Oslo's experiment where $\gamma_d^{\text{exp}} \simeq \gamma_p^{\text{exp}} \simeq 1.56 \pm 0.04$ were measured (Tallakstad et al. 2011). On the contrary, the theoretical exponents $\sigma_d = 3.8 \pm 0.2$ and $\sigma_p = 1.3 \pm 0.1$ obtained from our simulations that characterize the variations of the cut-off sizes S_d^* and S_p^* with the threshold C do not match the experimental values $\sigma_d = 1.77 \pm 0.16$ and $\sigma_p^{\text{ext}} = 2.81 \pm 0.23$.

Before getting to the origin of this discrepancy, we provide the physical meaning of the exponent σ_d. Consider the size S_{av}^* of the largest avalanches as we drive the crack at finite but small velocity v_m. It follows $S_{av}^* \sim \xi^{1+\zeta}$ where ξ is the correlation length along the crack line. Since the correlation length diverges as $\xi \sim v_m^{-\nu/\theta}$ when the driving velocity vanishes, the typical size of the largest avalanches diverges too, following the scaling behavior $S_{av}^* \sim v_m^{-\theta_d^{av}} \sim v_m^{-(1+\zeta)\nu/\theta}$. From the relations between critical exponents and the numerical values $\beta \simeq 0.495$ and $\zeta \simeq 0.388$ (Duemmer and Krauth 2007; Rosso and Krauth 2001b), one obtains $\theta_d^{av} - (1/\zeta + 1)/(1/\beta - 1) \simeq 3.58 \pm 0.02$ that is very close to the value $\sigma_d \simeq 3.8$ measured in our simulations. This calls for the following comment: in our analysis, we considered a fixed velocity v_m of the front, and characterized the distribution of depinning clusters defined from the regions where the local velocity was larger than $v_{\text{thres}} = C\, v_m$. We observed that the smaller the threshold, the larger the size of the depinning clusters, and we could evidence the following scaling $S_d^* \sim v_{\text{thres}}^{-\sigma_d}$. We believe that this procedure reveals the depinning clusters as they would be observed if the driving velocity was actually equal to v_{thres}. σ_d and then characterizes the divergence of the size of the largest

[17] Two important assumptions have been made here. First, the depth of the largest cluster has been approximated by the depth of the total avalanche. According to our numerical observations and the one made in Lawn and Marshall (1998), this looks like a fair assumption that relies on the anisotropic spatial structure of the avalanches that extend along the front direction rather than along the propagation direction. Second, we have assumed that the velocity during the propagation of the crack over *one cluster* is set by the velocity v_0, as observed during the depinning from a single obstacle (see Sect. 2.3).

depinning cluster or avalanche when the driving velocity goes to zero.[18] Overall, this suggests that thresholding the velocity field at different levels $v_{\text{thres}} = C\, v_m$ allows to explore how quantities of interest like the avalanche size diverges with the distance to the critical point.

We can now come back to the comparison between experiment and theory: in our simulations, both the avalanche depth (studied through the time correlation of the velocity field) and the avalanche size (studied for the threshold velocity matrix) diverge as $v_m \to 0$ following scalings consistent with the theory of depinning transition. But the study of the local crack front dynamics in Oslo's experiments delivers a different picture: both quantities do diverge as $v_m \to 0$, but only the avalanche depth follows the expected scaling. This discrepancy suggests that the *spatial structure* of avalanches in Oslo's experiment is not compatible with the predictions of the depinning model. As discussed further in the following, a physical ingredient may be missing in our model of crack growth in disordered solids to fully capture the intermittent dynamics observed in Oslo's experiment.

The now turn to the study of the distribution of local crack speeds. The distribution predicted by our model is shown in Fig. 21. Similarly to the experimental observations, it shows two different regimes with a pinning regime for $v < \langle v \rangle$ corresponding to pinned crack configurations characterized by a power law with exponent $\eta_p \simeq 1.6$ and a depinning regime for $v > \langle v \rangle$ characterized by $\eta_d \simeq 2.0$. Note that the slopes of the distribution represented in Fig. 21 are actually $\eta_d - 1$ and $\eta_p - 1$, since the velocities have been defined from the waiting times of the crack front following the procedure proposed in Tallakstad et al. (2011). The correspondence between the theoretically predicted and the experimentally measured exponents of Figs. 17c and f is not clear.

To disentangle the scaling behavior of the velocity distribution, it is useful to explore the dynamics of the crack in a simpler situation. Consider the relaxation of a crack front as it recovers a straight configuration after depinning from a single obstacle, as studied in detail in Sect. 2.3. The velocity field follows Eq. (23), and after a short transient $t \gg d/v_0$, it decays as $\partial \delta c / \partial t \sim 1/t$. One deduces from it the scaling behavior of the velocity distribution $P(v) \sim 1/v^{\sim 2}$ during the micro-instability produced by the depinning of the front from a single obstacle.

Avalanches observed during the propagation of a crack through a disordered interface result from the depinning from several obstacles. However, our numerical simulations show that the scaling of the velocity distribution remains unchanged and follows $P(v) \sim 1/v^2$ irrespective of the avalanche size and so the number of obstacles involved in the depinning process. An interpretation of the scaling behavior of the local velocity distribution is now in order. In the direct simulations of the crack growth equation, the power law statistics $P(v) \sim 1/v^2$ observed in the depinning regime is the signature of the relaxation mechanisms when the front detaches from obstacles. This is consistent with the observation in Fig. 17f of a similar scaling in

[18] Note that we need to assume here that the largest avalanche size S^*_{av} is proportional to the largest cluster size S^*_d. This was indeed observed by Laurson et al. (2010) who found $S_d \sim S_{av}$ for the largest events.

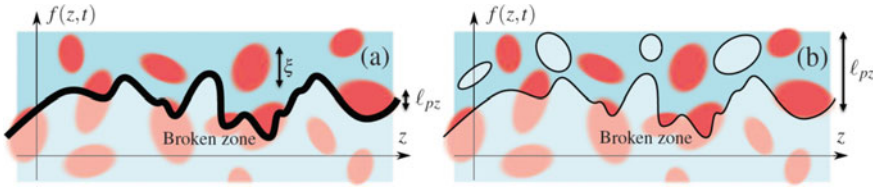

Fig. 20 Brittle vs quasi-brittle failure of heterogeneous materials. **a** For *brittle* failure, the progress zone l_{pz} is much smaller than the characteristic microstructural length ξ of the material. The crack growth process is well described by the motion of a sharp interface $f(z,t)$ separating the broken from the unbroken domain of the fracture plane. **b** For *quasi-brittle*, $l_{pz} \gg \xi$ so crack propagation is dominated by the processes of damage nucleation, growh and percolation

∂'Alembert's experiment. Indeed, for that particular experimental setup, the process zone size is of the order of a few tenth of nanometers (Ciccotti and Creton 2016), much lower than the patterned heterogeneities introduced at the micrometer scale, guaranteeing that the hypothesis of *brittle* crack growth illustrated in Fig. 20 a is satisfied.

The agreement between the LEFM based model and ∂'Alembert's experimental findings raises the question of the origin of the large exponent $\eta_d \simeq 2.5$ characterizing the depinning regime in Oslo's experiments (Fig. 17c). This deviation to the LEFM prediction can be understood by investigating the local crack front dynamics using a discrete model of fracture that goes beyond brittle fracture. Gjerden et al. (2014) investigated the propagation of a crack through a disordered interface separating two blocks connected by an array of parallel brittle fibers. When the force applied to one of the fiber exceeds its failure threshold, the fiber breaks and tensile forces are redistributed through the intact region of the interface assuming that blocks behave elastically. This redistribution mechanism produces cascades of failure events, qualitatively similar to the avalanche dynamics described by the LEFM based model of Eq. (23). For a weakly disordered interface, the simulation even recovers quantitatively the predictions of the depinning models like for example the value of the roughness exponent $\zeta \simeq 0.4$ predicted from LEFM. But a more interesting regime takes place for strongly disordered interfaces. Indeed, in that regime, the front dynamics is not governed by the competition between the elasticity of the crack line and the disorder, but instead by the coalescence of regions of broken fiber located ahead of the crack with the advancing crack itself, as illustrated in Fig. 20b. Interestingly, this transition from brittle to quasi-brittle crack growth also reflects on the velocity distribution: When the process of damage coalescence dominates, it follows another scaling behavior $P(v) \simeq v^{-\eta_d}$ with $\eta_d \simeq 2.5$ as shown in Fig. 21b, in excellent agreement with Oslo's experimental findings shown in Fig. 20c.

The comparison between coalescence model and experiments suggests that crack growth in Oslo's experiments is dominated by damage coalescence. This could also explain why our LEFM-based model do not capture *all* the statistical features of the local front dynamics, and in particular the divergence of the avalanche size S^* as $v_m \to 0$ while the other experimental observations are consistent with the model of

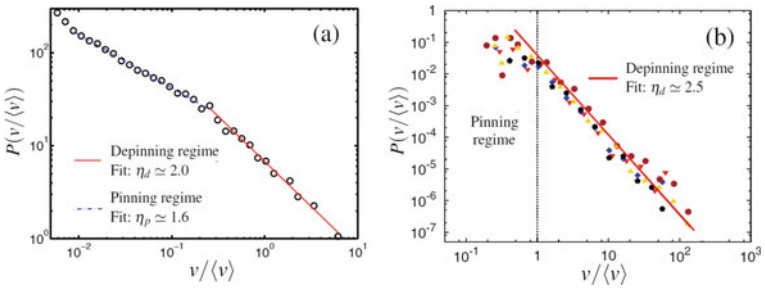

Fig. 21 Distribution of local crack growth velocities as predicted from **a** the LEFM-based model proposed in Sect. 2.2 and illustrated in Fig. 20a; **b** the damage percolation model proposed by Gjerden et al. (2014) and illustrated in Fig. 20b. In both cases, the velocity distribution shows two regimes: The low velocity or pinning regime is reminiscent of zones of the front that are trapped by material heterogeneities while the large velocity or depinning regime describes the crack dynamics within avalanches. Note that the exponents involved in the depinning regimes are different in both models and captures well the difference also observed in the experiments (see Fig. 17c and f)

brittle failure (see Figs. 18 and 19). Confirming this scenario would certainly require further experimental investigations using Oslo's experimental setup.[19] Note also that more recently, an alternative scenario relying on the fully non-linear kinetic law $v \sim \mathcal{F}(G - G_c)$ relating the crack speed with the driving force for creep fracture was proposed in Vincent-Dospital et al. (2021) to explain the difference between the (linearized) LEFM based predictions of the statistics of speed fluctuations and the experimental observations.

To conclude, we have shown that the proposed model of brittle crack growth in disordered solids allows for an interpretation of most of the statistical features of the speed fluctuations from the concept of depinning transition. For example, it makes sense of the divergence of the correlation time as the average crack speed vanishes and it also accounts for the power law distributions of local avalanches and local speeds. The few but significant discrepancies between theory and experiment in Oslo's setup turned out to be enlightening, as they could be used to reveal a mechanism of crack growth not included in our original model and based on damage coalescence. We now move to the study of fracture surfaces statistics that also provide a rich information on the elementary mechanisms of crack growth in disordered solids.

[19] The existence of two distinct scaling regimes with exponent $\eta_d \simeq 2.0$ for brittle failure and $\eta_d \simeq 2.5$ for quasi-brittle crack growth also invites to discuss Barés et al. (2013)s experimental results presented in Fig. 16c. Here, a scaling law with $\eta_d \simeq 2.5$ was reported in the depinning regime. Since such scaling actually does survive to upscaling Tallakstad et al. (2011), it is tempting to interpret this observation in terms of microscopic failure mechanism, and conjecture that microcracking does take place at a scale comparable to the grain size $\xi \simeq 500\ \mu$m of the sintered materials used in these experiments.

3.2 Statistics of Fluctuations in the Trajectory of Cracks

Fracture surfaces have often been considered as the Holy Grail for models of crack propagation in disordered materials, as they have been extensively used as a benchmark to compare and discriminate competing approaches (Bouchaud et al. 1993; Hansen and Schmittbuhl 2003; Ponson et al. 2006; Nukala et al. 2010). Here, we would like to illustrate how to take advantage of the dialogue between theory and experiment to identify basic crack growth mechanisms from the statistics of fracture surfaces. And propose fracture surface geometry as a paradigm for understanding failure phenomena in disordered materials.

Crack path in thin sheets To isolate the basic mechanisms underlying crack path selection in heterogeneous media, it is instructive to consider first crack growth in 2D thin sheets. By thin sheets, we mean structures with a small thickness compared to their thickness and length, but also smaller than or comparable to the characteristic microstructural feature of the material.

Figure 22a and c show fracture profiles in a paper sheet and in a panel of expanded polystyrene made of $d \simeq 2$ mm size beads, respectively. After digitizing the crack paths $h(x)$, their geometry can be characterized through their height-height correlation function

$$\Delta h(\delta x) = \langle [h(x + \delta x) - h(x)]^2 \rangle_x^{1/2}. \tag{34}$$

where Δh is the height difference between two points along the crack path $h(x)$ separated by the distance δx along the average crack line x. Δh is also averaged over several samples of the same material broken under the same loading conditions to obtain a smooth variation with δx. Figure 22b and d show the crack correlation functions thus obtained for the polystyrene panel and the three types of paper sheet. They both follow a power law $\Delta h \simeq \delta x^H$ which is reminiscent of self-affine properties. However, the value of the characteristic exponent, also referred to as the Hurst exponent, differs significantly with $H = 0.48 \pm 0.05$ in polystyrene panels (Chopin et al. 2018) and $H = 0.67 \pm 0.05$ in paper sheets (Bouchaud and Ponson 2022). This last result is consistent with various studies devoted to crack path in thin sheets that reported exponents in the range $H \simeq 0.65 - 0.70$ (Salminen et al. 2003; Kertesz et al. 1993; Lockner et al. 1991; Engøy et al. 1994; Morel et al. 2004).

This finding indicates two fundamentally different fracture behaviors. Cracks in polystyrene panels with $H \simeq 1/2$ follow trajectories close to a directed random walk: At any time during failure, the crack has the same probability to propagate upward as downward, irrespective of the prior propagation direction. As clear from Fig. 22b where the axes have been normalized by the bead size, the random walk behavior starts at a scale $\delta x \simeq d$ up to a cutoff length $\delta x \simeq 100d$. Since the self-affine crack geometry reflects the random microstructure of the material, the elementary microstructural feature sets the lower bound of the scale invariant regime. The upper bound has a different origin: It emerges from the finite size of the specimen, as

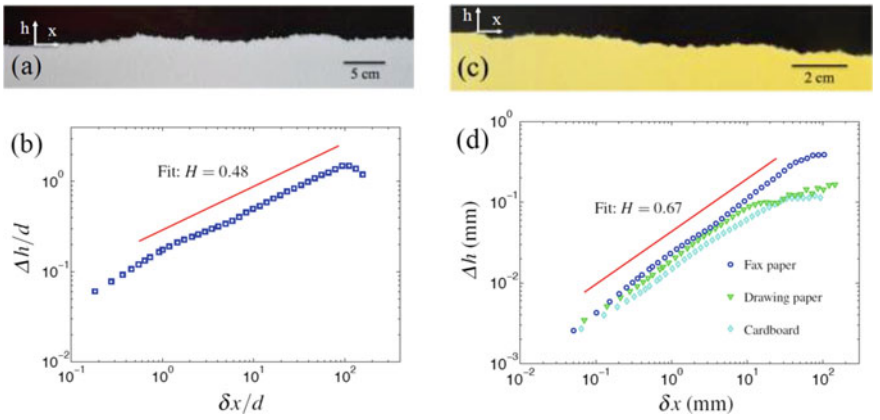

Fig. 22 **a** Fracture profile in a thin panel of expanded polystyrene made of beads of size $d \approx$ 2 mm Ponson et al. (2021). **b** Logarithmic representation of the height-height correlation function of the fracture profiles. At scales larger than the bead size d, crack roughness is self-affine with an exponent $H = 0.48 \pm 0.05$. **c** Fracture profile in a sheet of drawing paper Bouchaud and Ponson (2022). **d** Logarithmic representation of the height-height correlation of fracture profiles in three different types of paper. The fracture roughness shows a self-affine behavior characterized by an exponent $H = 0.67 \pm 0.05$ that do not vary significantly from one type of paper to another

shown by studying the effect of the sample dimensions on the fracture surface scaling properties (Ponson et al. 2007).

For fractures in paper sheets that display exponents $H \simeq 0.7$ than 1/2, the crack follows a persistent random walk. Crack deflections towards the upper $h'(x) > 0$ (resp. lower h'(x) < 0) direction will be more likely followed by a positive (resp. negative) subsequent deflection. The lower bound of the self affine regime is less clear for paper sheets than for polystyrene panels, and we will explain this observation later. The upper bound however, as for polystyrene panels, can be shown to emerge from the finite size of the specimen.

To make sense to these observations, the geometry of cracks in brittle materials with disordered fracture properties is explored theoretically. The model proposed here relies on the assumption that the crack follows the direction in which the shear component of the loading cancels out (Gol'dstein and Salganik 1974). Using this so-called principle of local symmetry actually amounts to assume that the process zone size l_{pz} is much smaller than the size of the microstructural features at the origin of the crack deflection, so that LEFM can be safely applied. We will see that this hypothesis plays a central role in the interpretation of the two roughening behaviors observed experimentally. From the principle of local symmetry and the expression of the local stress intensity factors in tension $k_I\{h(x)\}$ and shear $k_{II}\{h(x)\}$ for slightly perturbed crack trajectory, one derives the following path equation

$$\frac{dh}{dx} = -\frac{1}{\sqrt{\mathcal{L}_1}} \int_{-\infty}^{x} \frac{h'(\tilde{x})}{\sqrt{x-\tilde{x}}} d\tilde{x} - \frac{h(x)}{\mathcal{L}_2} + \eta(x) \tag{35}$$

that is valid in the limit of small crack deflections $h'(x) \ll 1$. Note that contrary to Katzav et al. (2007), the material elastic heterogeneities are not taken into account, resulting in a simplified version of the path equation that they derived. The term $\eta(x)$ is a quenched noise that describes the effect of the toughness variations and anisotropy resulting from the disordered material microstructure. Its value change randomly over $\eta_0 \leq \eta \leq \eta_0$ each time the crack propagates over a distance of the order of the characteristic microstructural size. The lengths $\mathcal{L}_1 \simeq (T/K_I)^2$ and $\mathcal{L}_2 \simeq A_I/K_I$ involved in the path equation (2.7) relates to the values of the coefficients K_I, T and A_I in the Williams' development of then stress field in the tip vicinity of the unperturbed straight crack. In particular, n the T-stress, negative in the experiments described here, plays an important rolenon the stability of the crack trajectory (Cotterell and Rice 1980). The calculation of these lengths for the actual fracture tests shown in Fig. 22 a and c gives $\mathcal{L}_1 \simeq \mathcal{L}_1 \simeq 100d$ for the polystyrene panels and $\mathcal{L}_1 \simeq \mathcal{L}_1 \simeq 10$ cm m for the paper sheets: They are of the order of the specimen in-plane dimension and much larger than the characteristic size of the microstructural features. Under these conditions, the first two terms in the path equation that scale as $\sim 1/\sqrt{\mathcal{L}_1}$ and $\sim 1/\mathcal{L}_2$ become negligible. The approximated path equation $dh/dx \simeq \eta(x)$ thus obtained is characteristic of a directed random walk. It predicts self-affine crack profiles with an exponent $H = 1/2$.

This theoretical analysis of the crack paths in 2D disordered brittle solids captures the observations made in Fig. 22 for polystyrene panels, namely uncorrelated crack deflections reflected by the random walk exponent $H \simeq 0.5$. This agreement lies in the peculiar failure mechanism of expanded polystyrene: As the crack meanders through its poorly consolidated granular structure, the actual dissipative failure mechanisms taking place in the crack tip vicinity are confined in a process zone of size l_{pz} much smaller than the size d of the polystyrene beads. Therefore, the crack deflection mechanism in this material is fairly well described under the assumption of a brittle crack growth (Vasoya et al. 2016a).

The behavior of cracks in paper sheets with $H > 1/2$ indicate another roughening mechanism. Here, the characteristic scale of the microstructure, namely fibers of length $d \simeq 0.1 - 1$mm (Ververis et al. 2004), compares with the characteristic scale of damage processes. A closer look at the failure mechanisms in paper indeed reveal that macroscopic cracks propagate through the nucleation and growth of mm scale microcracks that subsequently coalesce with it. This discontinuous growth process results in jumps of the crack tip from one position to another that can be evidenced using a fast camera or through the acoustic bursts emitted during failure (Stojanova et al. 2014).

These local failure mechanisms reflect on the crack roughness at the large scale. As shown in Ben-Dayan et al. (2006), crack propagation by damage nucleation and coalescence produces persistent self-affine crack trajectories characterized by a Hurst exponent larger than 1/2, equal to $H \simeq 0.55$ in their specific model. Roughly

speaking, the positive correlations that build along the crack path emerges from the attraction exerted by the microcrack on the main crack through the following mechanism: As the level of tensile stress is maximum along the current crack propagation direction, microcracks are likely to nucleate in this direction. Once damage nucleation takes place, microcrack and crack attract each other, so the main crack is now more likely to propagate in its current propagation direction. Such a roughening mechanism was also observed through simulations of crack propagation by damage growth and coalescence in ductile materials (Ponson et al. 2013; Srivastava et al. 2014; Osovski et al. 2015). The roughness exponent $H \simeq 0.55$ characterizing the fracture surfaces in these simulations is lower than the one found by Ben-Dayan et al. (2006), however significantly larger than 1/2 to indicate persistency in the crack trajectory.

The link between failure mechanisms and roughness properties in thin sheets is clear from the experiments and the models: Brittle crack growth in the limit of large specimens leads to uncorrelated random fracture profiles ($H \simeq 0.55$) while crack propagation through damage nucleation results in positive correlations between successive crack growth increments ($H > 1/2$). The comparison between two length scales, namely the characteristic size d of the elementary microstructural feature and the characteristic size l_{pz} of the damage processes, is proposed as a criterion to discriminate both mechanisms. We now move to the study of the fracture surfaces of fully three-dimensional materials that does reveal the competing roughening mechanisms evidenced in thin sheets, although involving a different selection process.

Roughness of two-dimensional fracture surfaces We now consider fracture in specimens with a large dimension along the crack front direction compared to the characteristic microstructural size of the material. In that situation, the crack leaves behind it a 2D fracture map as the ones shown in Fig. 23. Three materials are considered, namely an aluminum allow, a mortar and a ceramic, with a priori three different failure behaviors to elicit roughness properties common to a large range of materials. The topography $h(z, x)$ of the fracture surface of each of these materials is measured through an adapted profilometric technique as detailed by Pouchou et al. (2002), Morel et al. (2008) and Ponson et al. (2006), respectively.

The standard approach to characterize the geometry of fracture surfaces is to compute their height-height correlation function, as defined in Eq. (34), either along the propagation direction x or the perpendicular one z. A more complete characterization consists in computing their 2D correlation function $\Delta h(\delta\vec{x}) = \langle[\delta h(\vec{x}+\delta\vec{x}) - h(\vec{x})]^2\rangle_{\vec{x}}^{1/2}$ that allows for the description of their anisotropic scaling properties (Ponson et al. 2006). Previous works have shown that fracture surfaces are self-affine, namely that their correlation function follows a power law $\Delta h \sim \delta z^{\zeta}$ with an exponent $\zeta \simeq 0.75$ that was conjectured to be universal (Bouchaud et al. 1990; Måløy et al. 1992). However, more recently, another roughness behavior was reported on brittle rocks with a lower roughness exponent $\zeta \simeq 0.45$ (Boffa et al. 1998; Ponson et al. 2006). Following the work of Santucci et al. (2007), we would like here to take a step back from the scaling properties of fracture surfaces and investigate the

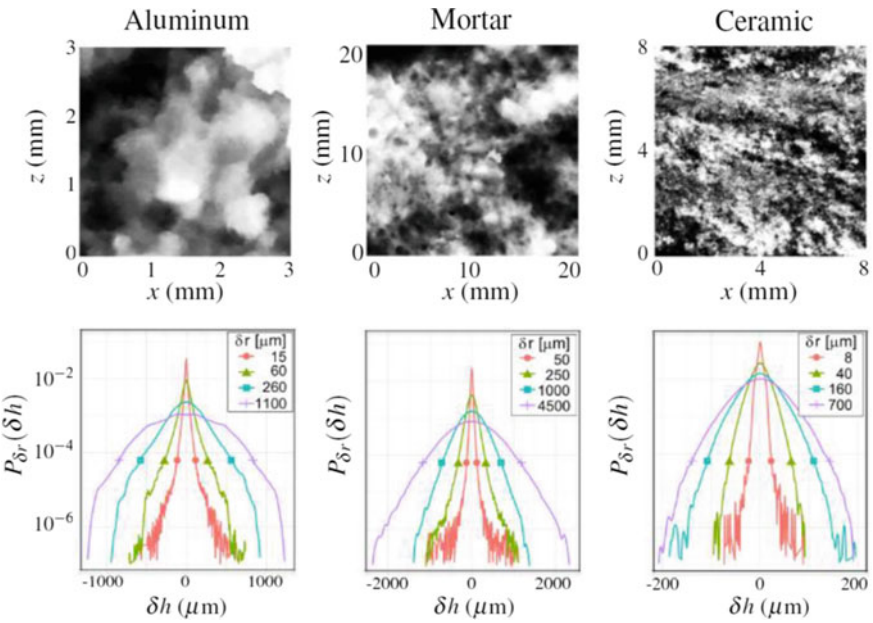

Fig. 23 Height maps $h(x)$ of fracture surfaces of aluminium, mortar and ceramic. Their distributions of height variations computed at different scales $\delta r = |x|$ show a Gaussian behavior at large scales $\delta r \gg \xi$ against fat tail behavior at small scales $\delta r \ll \xi$ where ξ is a material dependent length scale measured in Fig. 24 (Vernède et al. 2015)

underlying statistics of height fluctuations to reveal the range of length scales over which roughness shows meaningful correlations.

Figure 2.8 shows the distribution $P_{\delta r}$ of height variations $\delta h(\vec{x} + \delta\vec{x}) - h(\vec{x})$ where the sampling is done on all admissible $\vec{x}$ and $\delta\vec{x}$ such as $\delta r - |\delta\vec{x}|$. In other words, we focus on the height variations at different scales δr and treat fracture surfaces as isotropic maps. An interesting property of the family of distributions P_{δ_r} is that they follow a Gaussian behavior at large length scales $\delta r \gg \xi$ while they exhibit fat tail statistics at small length scales $\delta r \ll \xi$ as evidenced from the comparison with parabolas characteristic of Gaussian distributions in the semi-logarithmic representation of Fig. 23. To measure the crossover length scale ξ between fat tail and Gaussian statistics, we introduce the following operator.

$$\omega(\vec{x}) = \frac{1}{2}\log\left(\langle \delta h(\vec{x}, \delta\vec{x})^2 \rangle_{|\delta\vec{x}|=\epsilon}\right) - \Omega_\epsilon. \tag{36}$$

It transforms the original height map $h(\vec{x})$ into a map $\omega(\vec{x})$ of the local roughness level that is defined from an average of the height variations over a circle of radius ϵ centered in $\vec{x}$.[20]. The fields ω computed for the three fracture surfaces considered

[20] The constant Ω_c involved in Eq. (2.8) is chosen such that the average of $\omega(\vec{x})$ over all $\vec{x}$ is zero.

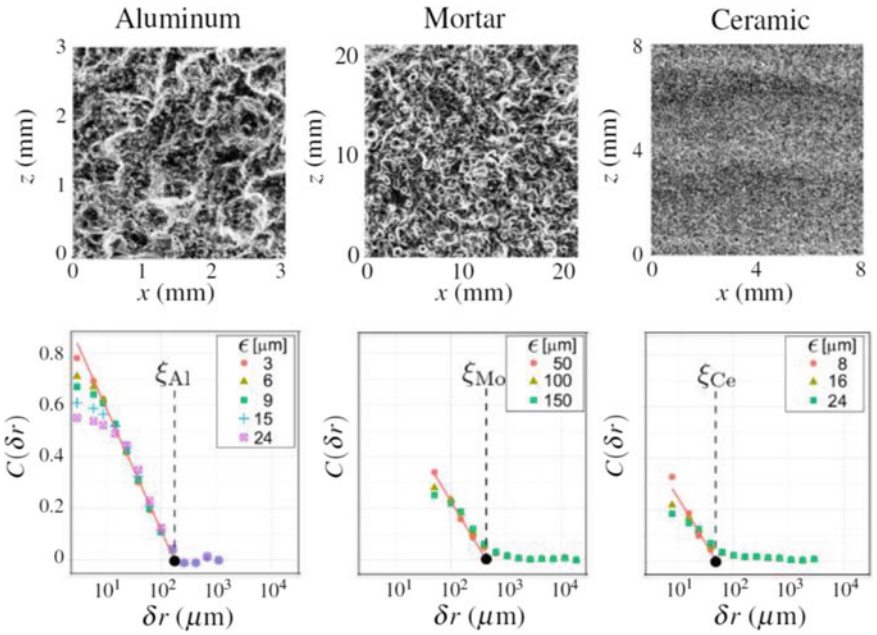

Fig. 24 Fracture surfaces shown in Fig. 23 processed through Eq. (36) to highlight the steepest cliffs that are shown in white. The characteristic size ξ of the patterns visible on these maps is obtained from the variations of their correlation function $C(\delta r) \sim log(\delta r/\xi)$ and gives $\xi = 170\,\mu$m, $430\,\mu$m and 170μm for the aluminium, the mortar and the ceramics fracture surface, respectively Vernède et al. (2015)

are shown in Fig. 24. The patterns that emerge on the fracture surface through this transformation correspond to steep cliffs and reveal complex correlations of the height variations. Their characteristic size is reminiscent of the length scale ξ evidenced from the variations of P_{δ_r} with δr. Indeed, first write the height variation computed at a scale δr as the sum of several height variations computed at a finer scale $\epsilon \ll \delta r$,[21] and then use the central limit theorem: If the fluctuations at the scale ϵ are uncorrelated, then $P_{\delta_r \gg \epsilon}$ is a Gaussian. Conversely, if the distribution $P_{\delta_r \gg \epsilon}$ is non-Gaussian, this indicates spatial correlations of height variations at a scale δr or smaller. As a result, the crossover length identified from the transition from fat tail to Gaussian statistics does correspond to the correlation length of the ω-maps, and we note both length scales ξ in the following.

The correlations of ω are studied through the function $C(\delta r) = \langle \omega(\mathbf{x})\omega(\mathbf{x} + \delta\mathbf{x})\rangle_{\mathbf{x},|\delta\mathbf{x}|=\delta r}$ shown in Fig. 24 as a function of the distance δr for different values of ϵ; $C(\delta r)$ is in fact independent of ϵ whenever $\delta r \gg \epsilon$. For the three materials considered, we observe two regimes: at small scales, $C(\delta r) \sim \log(\delta r/\xi)$ and extrapolates

[21] The actual decomposition of the height variation computed as a scale δr into the sum of height variations computed at a finer scale $\epsilon = \delta r/n$ where n is an integer writes as $\delta h(\vec{x}, \delta\vec{x}) = h(\vec{x} + \delta\vec{x}) - h(\vec{x}) = \sum_{k=1}^{n} h(\vec{x} + \frac{k}{n}\delta\vec{x}) - h(\vec{x} + \frac{k-1}{n}\delta\vec{x}) = \sum_{k=1}^{n} \delta h(\vec{x} + \frac{k-1}{n}\delta\vec{x}, \frac{\delta\vec{x}}{n})$.

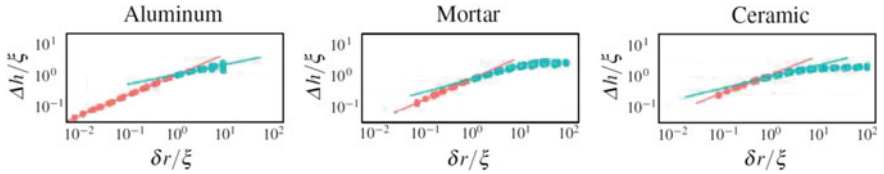

Fig. 25 Correlation function of the three fracture surfaces considered. The power law fits are performed below and above the length ξ determined in Fig. 24 and give $\xi = 0.42 \pm 0.07$ at large scale (Vernède et al. 2015)

to zero for $\delta r = \xi$. For larger distances, these correlations are zero within statistical noise. ξ corresponds to the characteristics size of the patterns of the ω-fields shown in Fig. 24.

The presence of two distinct ranges of length scales with fundamentally different statistical features on the fracture surfaces of these materials is clear: At small scales $\delta r \ll \xi$, the height fluctuations are strongly correlated and display non-Gaussian statistics while at large scales $\delta r \gg \xi$, the roughness follows a Gaussian behavior with no spatial correlation of the ω-fields. We would like now to come back on the self-affine properties of the fracture surface and determine the value of the roughness exponent in these both regimes.

Figure 25 shows the correlation function $\Delta h(\delta r)$ of the three fracture surfaces following the definition of Eq. (34) after averaging over all the possible directions such that $\delta r = |\delta \vec{x}|$. The two ranges of length scales determined previously are indicated by two different colors. They do show two different scaling behaviors: At small scales $\delta r < \xi$, the correlation function follows $\Delta h \sim \delta r^{\zeta}$ with a roughness exponent $\zeta \simeq 0.75 \pm 0.05$, irrespective of the material considered. At larger scales $\delta r > \xi$, the roughness is characterized by a lower exponent $\zeta = 0.45 \pm 0.05$ here also robust and independent on the material. As a result, the presence of two regimes evidenced in the statistics of height fluctuations is also clear from the self-affine

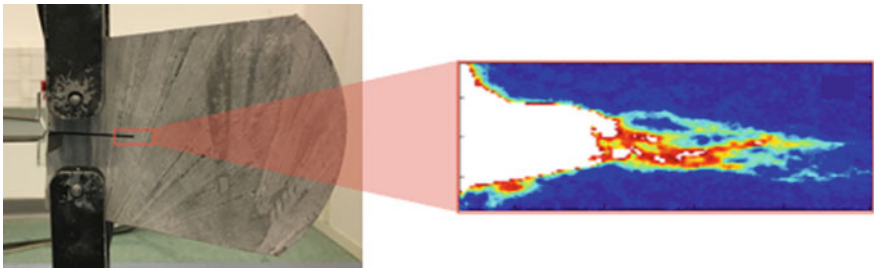

Fig. 26 Dissipative mechanisms during material failure are localized at the crack tip vicinity in a process zone of characteristic size l_{pz}. The fracture surfaces of aluminum, mortar and ceramics reflects this phenomenon as they display two distinct statistical behaviors at small $\delta r > \xi$ and large $\delta r > \xi$ length scales, reminiscent of damage coalescence and brittle crack growth, respectively

properties of the height fracture maps that show a persistent behavior $\zeta > 1/2$ at small scales $\delta r < \xi$ and an anti-persistent one $\zeta < 1/2$ at large scales $\delta r > \xi$. The following section addresses the physical origin of these two regimes.

The roughness statistics as a paradigm for the failure of materials? The analysis of Sect. 3.2 of the fracture profiles in 2D thin specimens gives indication on the mechanisms underlying the roughness properties observed for 3D solids. In 2D solids, persistency ($H > 1/2$) of fracture profiles is reminiscent of crack growth governed by damage coalescence processes while pure random walk behavior $H = 1/2$ results from brittle fracture. Theoretical analyses of crack propagation in *brittle* media reveal that the major difference between 2D and 3D situations lies in the effective elasticity of the crack line that opposes to out-of-plane crack excursions (Larralde and Ball 1995; Ramanathan et al. 1997; Movchan et al. 1998). This effect was argued to explain the anti-persistent roughness ($\zeta \simeq 0.45$) reported in porous brittle rocks (Ponson et al. 2006; Bonamy et al. 2006) and the logarithmic ($\zeta = 0$) height correlations reported for phase-separated glasses (Dalmas et al. 2008). Therefore, the anti-persistent roughness regime $\zeta \simeq 0$ observed at *large* scale $\delta r > \xi$ on the three materials considered here is interpreted as the result of *brittle* crack growth. At these length scales, the material can indeed be identified as a coarse-grained equivalent linear elastic medium and LEFM can safely be applied.

A quantitative understanding of the *small* scale $\delta r < \xi$ roughness regime is still missing. However, the patterns present on the volatility maps computed at these scales (see Fig. 24) display remarkably robust features (Vernède et al. 2015), like e.g. a fractal geometry with dimension $D = 1.70 \pm 0.05$ irrespective of the material considered. This suggest a common underlying mechanism. Inspired by the study (Guerra et al. 2012) of the marks let by microcracks on PMMA fracture surfaces, it was conjectured that the steep cliffs evidenced on the volatility maps of a large range of materials like aluminum, mortar and ceramics are the footprints of damage coalescence (see Fig. 26). The particularity of PMMA compared to these three materials is that microcracking processes take place at a much larger scale than the microstructural features, leaving on fracture surfaces conic marks characteristic of the interaction between two microcracks in a *homogeneous* material. On the contrary, the interplay between material disorder and damage coalescence may result in the complex entangled lines evidenced in the volatility fields of Fig. 24.

What are the physical implications of the fracture surface properties revealed by this study? As a matter of fact, the picture drawn from this work recovers the traditional text-book picture of Fig. 26 of crack propagation phenomena where dissipative failure mechanisms are confined at the crack tip vicinity in the so-called process zone while LEFM applies at larger distances $r \gg l_{pz}$ from the crack tip where the material recovers a linear elastic behavior (Irwin 1958). However, it goes beyond this classical description as the complex structure of the fracture surfaces evidenced at small scales does display universal features independent of the material investigated. This is an important observation as it suggests that at small scales too, within the process zone, a common description that does survive to variations of failure mechanisms from one material to another is possible.

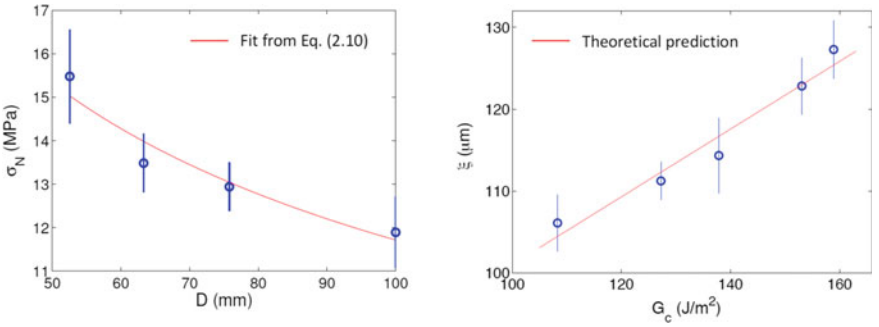

Fig. 27 **a** Tensile strength of the Botucatu sandstone as measured through Brazilian tests (Carneiro 1943) as a function of the specimen diameter. The extrapolation down to the mean grain size $d \simeq 170$ μm provides an estimate of the cohesive stress $\sigma_c = 140$MPa involved in the cohesive zone model of Eq. (37). **b** Relationship between the length scale ξ measured from the fracture surface using the statistical analysis described in Sect. 3.2 and patented in Vernède and Ponson (2017) as a function of the toughness G_c in Sandstone specimens broken at different crack speeds. The linear variation is consistent with Eq. (37) and the hypothesis that ξ provides an estimate of the extent of the fracture process zone l_{pz}

3.3 Conclusion and Perspectives

To conclude, we would like to discuss the application of this research to quantitative fractography and the *post-mortem* determination of material properties from the analysis of their fracture surface (Vernède and Ponson 2017). From our observations, it is rather natural to interpret the length scale ξ emerging from the fracture surface statistics as a measure of the fracture process zone size l_{pz}. Measuring l_{pz} from the analysis of the fracture surface would then pave the way for the determination of the material toughness G_c, as both quantities linearly related to each other. The observation made in Srivastava et al. (2014) of a linear relationship between the length scale ξ extracted from the crack roughness and the fracture toughness G_c in simulations of ductile crack growth in heterogeneous solids does support this idea.

In brittle solids, cohesive zone models (Barenblatt 1962) also predict a linear variation

$$G_c = \alpha\, l_{pz} \quad \text{with} \quad \alpha = \frac{8}{\pi}\frac{\sigma_c^2}{E} \tag{37}$$

between the toughness and the process zone size, the proportionality constant being set by the cohesive stress σ_c and the Young's modulus E. As a result, one may also expect a linear relationship between the length scale $\xi \simeq l_{pz}$ extracted from fracture surfaces and the material toughness G_c.

This idea is tested in Fig. 27 using specimens of Botucatu sandstone. First, the cohesive stress σ_c is measured using Brazilian tests where cylindrical specimens of different diameters D are submitted to a uniaxial compression until failure. The

tensile strength σ_N represented as a function of D in Fig. 27a is then extrapolated down to the mean grain size $d \simeq 170\ \mu$m using Weibull's prediction

$$\sigma_N \sim D^{-1/m} \tag{38}$$

for the size effect on the brittle failure strength where $m = 2.6$, the so-called Weibull's modulus, is fitted from our data. The extrapolated value $\sigma_c = 140$MPa provides an estimate of the cohesive stress that can be interpreted as the cohesive strength between neighboring grains. The relationship between G_c and ξ is finally explored by performing fracture tests at different crack speeds v_m leading to variations in the values of toughness within the range $110 J.m^{-2} \leq G_c \leq 160 J.m^{-2}$ (Ponson 2009). The resulting fracture surfaces are scanned using an optical profilometer and the values of ξ are extracted from the fracture height maps following the statistical analysis described in Sect. 3.2 and patented in Vernède and Ponson (2017). The variations of ξ extracted from the fracture surfaces with the toughness value measured from the fracture tests are shown in Fig. 27b. First, we recover a linear relationship consistent with Eq. (37) and the assumption that ξ provides a measurement of the process zone size. In addition, the proportionality constant measured experimentally is close to the expected theoretical value $\alpha = \frac{8}{\pi}\frac{\sigma_c^2}{E}$ using the cohesive stress extrapolated in Eq. (38) and the experimental Young's modulus $E = 25$ GPa suggesting that ξ may actually be close to the process zone size l_{pz} as defined in cohesive zone models, at least for the Botucatu sandstone used for this study.

Further investigations of the relationship between ξ extracted from fracture surface and the fracture toughness are currently on-going. Preliminary observations are very encouraging, and we are closer than ever to confirm the conjecture proposed 30 years ago by Mandelbrot et al. (1984) regarding a quantitative link between toughness and roughness.[22] If it was confirmed, the statistical analysis of fracture surfaces, referred to as statistical fractography, could become a powerful engineering technique that provides the mechanical properties of materials from the scan and the analysis of their fracture surface. It will also provide a mean to determine afterwards the load applied to a structure when it failed, thus helping failure experts to determining the root causes of catastrophic structural failures and preventing future accidents.

Acknowledgements The author would like to dedicate this chapter to my younger collaborators, Aditya Vasudevan, Ashwij Mayya, Estelle Berthier, Guillaume de Luca, Julien Chopin, Manish Vasoya, Thiago Grabois and Vincent Démery without who this research would not have been possible. A special thank to Guillaume de Luca who provided a precious help in the editing of this book.

[22] Note however that the original idea of Mandelbrot et al. (1984) was to establish a correlation of the material toughness with the *roughness exponent*, and not with a crossover length scale between two self-affine regimes as discussed here.

References

Alava MJ, Nukala PK, Zapperi S (2006) Statistical models of fracture. Adv Phys 55:349–476

Albertini G, Lebihain M, Hild F, Ponson L, Kammer DS (2021) Effective toughness of heterogeneous materials with rate-dependent fracture energy. Phys Rev Lett 127:035501

Barabási AL, Stanley HE (1995) Fractal concepts in surface growth. Cambridge University Press

Barenblatt GI (1962) The mathematical theory of equilibrium cracks in brittle fracture. Adv Appl Mech 7:55–129

Barés J, Barbier L, Bonamy D (2013) Crackling versus continuumlike dynamics in brittle failure. Phys Rev Lett 111:054301

Ben-Dayan I, Bouchbinder E, Procaccia I (2006) Random and correlated roughening in slow fracture by damage nucleation. Phys Rev E 74:046102

Boffa JM, Allain C, Hulin JP (1998) Experimental analysis of fracture rugosity in granular and compact rocks. Eur Phys J Appl Phys 2:281–289

Bonamy D (2009) Intermittency and roughening in the failure of brittle heterogeneous materials. J Phys D: Appl Phys 42:214014

Bonamy D, Bouchaud E (2011) Failure of heterogeneous materials: a dynamic phase transition? Phys Rep 498:1–44

Bonamy D, Ponson L, Prades S, Bouchaud E, Guillot C (2006) Scaling exponents for fracture surfaces in homogeneous glass and glassy ceramics. Phys Rev Lett 97:135504

Bonamy D, Santucci S, Ponson L (2008) Crackling dynamics in material failure as the signature of a self-organized dynamic phase transition. Phys Rev Lett 101:045501

Bouchaud E, Ponson L (2022) Fracture mechanics of heterogeneous materials. Wiley, Hoboken, in preparation

Bouchaud E, Lapasset G, Plan'es J (1990) Fractal dimension of fractured surfaces: a universal value? Europhys Lett 13:73–79

Bouchaud JP, Bouchaud E, Lapasset G, Plan'es J (1993) Models of fractal cracks. Phys Rev Lett 71:2240–2243

Bueckner HF (1970) A novel principle for the computation of stress intensity factors. ZAMM 50:529–546

Carneiro FLLB (1943) A new method to determine the tensile strength of concrete. In: Proceedings of the 5th meeting of the Brazilian association for technical rules, pp 126–129

Chopin J, Bhaskar A, Jog A, Ponson L (2018) Depinning dynamics of crack fronts. Phys Rev E 121:235501

Ciccotti M, Creton C (2016) Fracture and adhesion of soft materials: a review. Rep Prog Phys 79:0466601

Cotterell B, Rice JR (1980) Slightly curved or kinked cracks. Int J Fract 16:155–169

Dalmas D, Lelarge A, Vandembroucq D (2008) Crack propagation through phase-separated glasses: effect of the characteristic size of disorder. Phys Rev Lett 101:255501

Démery V, Rosso A, Ponson L (2014) From microstructural features to effective toughness in disordered brittle solids. EPL 105:34003

Duemmer O, Krauth W (2007) Depinning exponents of the driven longrange elastic string. J Stat Mech 1:01019

Engøy T, Måløy KJ, Hansen A, Roux S (1994) Roughness of twodimensional cracks in wood. Phys Rev Lett 73:834–837

Ertas D, Kardar M (1994) Critical dynamics of contact line depinning. Phys Rev E 49:R2532

Gao H, Rice JR (1987) Somewhat circular tensile cracks. Int J Fract 33:155–174

Gao H, Rice JR (1989) A first-order perturbation analysis of crack trapping by arrays of obstacles. J Appl Mech 56:828–836

Ghatak A, Chaudhury MK, Shenoy V, Sharma A (2000) Meniscus instability in a thin elastic film. Phys Rev Lett 85:4329–4332

Gjerden KG, Stormo A, Hansen A (2014) Local dynamics of a randomly pinned crack front: a numerical study. Front Phys 2:66

Gol'dstein RV, Salganik RL (1974) Brittle fracture of solids with arbitrary cracks. Int J Fract 10:507–523
Guerra C, Scheibert J, Bonamy D, Dalmas D (2012) Understanding fast macroscale fracture from microcrack post mortem patterns. Proc Natl Acad Sci 109:390–394
Hansen A, Schmittbuhl J (2003) Origin of the universal roughness exponent of brittle fracture surfaces: stress weighted percolation in the damage zone. Phys Rev Lett 90:045504
Hossain MZ, Hsueh CJ, Bourdin B, Bhattacharya K (2014) Effective toughness of heterogeneous media. J Mech Phys Solids 71:15–32
Irwin GR (1958) Fracture. In: Handbuch der Physik, vol 6. Springer, Berlin, p 551
Kardar M (1998) Nonequilibrium dynamics of interfaces and lines. Phys Rep 301:85–112
Katzav E, Adda-Bedia M (2006) Roughness of tensile crack fronts in heterogeneous materials. EPL 76:450–456
Katzav E, Adda-Bedia M, Derrida B (2007) Fracture surfaces of heterogeneous materials: a 2D solvable model. EPL 78:46006
Kertesz J, Horvath V, Weber F (1993) Self-affine rupture lines in paper sheet. Fractals 1:67–74
Kolvin I, Cohen G, Fineberg J (2015) Crack front dynamics: the interplay of singular geometry and crack instability. Phys Rev Lett 114:175501
Larralde H, Ball RC (1995) The shape of slowly growing cracks. Europhys Lett 30:87–92
Larkin A, Ovchinnikov Y (1979) Pinning in type II superconductors. J Low Temp Phys 34:409–428
Laurson L, Santucci S, Zapperi S (2010) Avalanches and clusters in planar crack front propagation. Phys Rev E 81:046116
Lawn BR, Marshall DB (1998) Nonlinear stress-strain curves for solids containing closed cracks with friction. J Mech Phys Solids 46:85–113
Lebihain M (2021) Towards brittle materials with tailored fracture properties: the decisive influence of the material disorder and its microstructure. Int J Frac 230:99–114
Lebihain M, Leblond JB, Ponson L (2020) Effective toughness of periodic heterogeneous materials: the effect of out-of-plane excursions of cracks. J Mech Phys Solids 137:103876
Lebihain M, Ponson L, Kondo D, Leblond JB (2021) Effective toughness of disordered brittle solids: a homogenization framework. J Mech Phys Solids 153:104463
Leblond JB, Ponson L (2016) Out-of-plane deviation of a mode I+III crack encountering a tougher obstacle. C R Mécanique 344:521–531
Lengliné O, Toussaint R, Schmittbuhl J, Elkhoury JE, Ampuero JP, Tallakstad KT, Santucci S, Måløy KJ (2011) Average crack-front velocity during subcritical fracture propagation in a heterogeneous medium. Phys Rev E 84:036104
Leschhorn H, Nattermann T, Stepanow S, Tang LH (1997) Driven interface depinning in a disordered medium. Ann Phys 6:1–34
Lockner DA, Byerlee JB, Kiksenko V, Ponomarev A, Sidorin A (1991) Quasi-static fault growth and shear fracture energy in granite. Nature 350:39–42
Måløy KJ, Schmittbuhl J (2001) Dynamical event during slow crack propagation. Phys Rev Lett 87:105502
Måløy KJ, Hansen A, Hinrichsen EL, Roux S (1992) Experimental measurements of the roughness of brittle cracks. Phys Rev Lett 68:213–215
Måløy KJ, Santucci S, Schmittbuhl J, Toussaint R (2006) Local waiting time fluctuations along a randomly pinned crack front. Phys Rev Lett 96:045501
Mandelbrot BB, Passoja DE, Paullay AJ (1984) Fractal character of fracture surfaces of metals. Nature 308:721–722
Morel S, Lubet T, Pouchou JL, Olive JM (2004) Roughness analysis of the cracked surfaces of a face centered cubic alloy. Phys Rev Lett 93:065504
Morel S, Bonamy D, Ponson L, Bouchaud E (2008) Transient damage spreading and anomalous scaling in mortar crack surfaces. Phys Rev E 78:016112
Movchan AB, Gao H, Willis JR (1998) On perturbations of plane cracks. Int J Solids Struct 35:3419–3453

Nattermann T, Stepanow S, Tang LH, Leschhorn H (1992) Dynamics of interface depinning in a disordered medium. J Phys II Franc 2:1483–1488
Nukala PKVV, Barai P, Zapperi S, Alava M, Simunovic S (2010) Fracture roughness in three-dimensional beam lattice systems. Phys Rev E 82:026103
Osovski S, Sristava A, Ponson L, Bouchaud E, Tvergaard V, Ravi-Chandar K, Needleman A (2015) The effect of loading rate on ductile fracture toughness and fracture surface roughness. J Mech Phys Solids 76:20–46
Overvelde JTB, Bertoldi K (2014) Relating pore shape to the nonlinear response of periodic elastomeric structures. J Mech Phys Solids 64:351–366
Patinet S, Vandembroucq D, Roux S (2013) Quantitative prediction of effective toughness at random heterogeneous interfaces. Phys Rev Lett 110:165507
Ponson L (2009) Depinning transition in the failure of inhomogeneous brittle materials, Phys Rev Lett 103:055501
Ponson L (2016) Statistical aspects in crack growth phenomena: how the fluctuations reveal the failure mechanisms. Int J Fract 201:11–27
Ponson L, Bonamy D (2010) Crack propagation in brittle heterogeneous solids: material disorder and crack dynamics. Int J Fract 162:21–31
Ponson L, Pindra N (2017) Crack propagation through disordered materials as a depinning transition: a critical test of the theory. Phys Rev E 95:053004
Ponson L, Bonamy D, Bouchaud E (2006) Two-dimensional scaling properties of experimental fracture surfaces. Phys Rev Lett 96:035506
Ponson L, Bonamy D, Auradou H, Mourot G, Morel S, Bouchaud E, Guillot C, Hulin JP (2006) Anisotropic self-affine properties of experimental fracture surfaces. Int J Fract 140:27–36
Ponson L, Auradou H, Vié P, Hulin JP (2006) Low self-affine exponents of fractured glass ceramics surfaces. Phys Rev Lett 97:125501
Ponson L, Auradou H, Pessel M, Lazarus V, Hulin J-P (2007) Failure mechanisms and surface roughness statistics of fractured fontainebleau sandstone. Phys Rev E 76:036108
Ponson L, Cao Y, Bouchaud E, Tvergaard V, Needleman A (2013) Statistics of ductile fracture surfaces: the effect of material parameters. Int J Fract 184:137–149
Ponson L, Shabir Z, Van der Giessen E, Simone A (2021) Unified scenario for the morphology of crack paths in two-dimensional disordered solids. Phys Rev E 104:055003
Poon B, Ponson L, Zhao J, Ravichandran G (2011) Damage accumulation and hysteretic behavior of max phase materials. J Mech Phys Solids 59:2238–2257
Pouchou JL, Boivin D, Beauchêne P, Le Besnerais G, Vignon F (2002) 3D reconstruction of rough surfaces by SEM stereo imaging. Microchimica Acta 139:135–144
Ramanathan S, Ertas D, Fisher DS (1997) Quasistatic crack propagation in heterogeneous media. Phys Rev Lett 79:873–876
Rice JR (1989) Weight function theory for three-dimensional elastic crack analysis. In: Wei, Gangloff (eds) Fracture mechanics: perspectives and directions, ASTM STP 1020. American Society for Testing and Materials, pp 29–57
Rice JR (1985) First-order variation in elastic fields due to variation in location of a planar crack front. J Appl Mech 52:571–579
Rosso A, Krauth W (2001) Monte carlo dynamics of driven elastic strings in disordered media. Phys Rev B 65:012202
Rosso A, Krauth W (2001) Origin of the roughness exponent in elastic strings at the depinning threshold. Phys Rev Lett 87:187002
Roux S, Vandembroucq D, Hild F (2003) Effective toughness of heterogeneous brittle materials. Eur. J. Mech. A Solids 22:743–749
Roux S, Hild F (2008) Self-consistent scheme for toughness homogenization. Int J Fract 154:159–166
Saffman PG, Taylor GI (1958) The penetration of a fluid into a porous medium of hele-shaw cell containing a more viscous liquid. Proc R Soc Lond A 245:312

Saintyves B, Dauchot O, Bouchaud E (2013) Bulk elastic fingering instability in hele-shaw cells. Phys Rev Lett 111:047801
Salminen LI, Alava M, Niskanen KJ (2003) Analysis of long crack lines in paper webs. Eur Phys J B 32:369–374
Santucci S, Måløy KJ, Delaplace A, Mathiesen J, Hansen A, Bakke J, Schmittbuhl J, Vanel L, Ray P (2007) Statistics of fracture surfaces. Phys Rev E 75:016104
Srivastava A, Ponson L, Osovski S, Bouchaud E, V Tvergaard, Needleman A (2014) Effect of inclusion density on ductile fracture toughness and roughness. J Mech Phys Solids 63:62–79
Stojanova M, Santucci S, Vanel L, Ramos O (2014) High frequency monitoring reveals aftershocks in subcritical crack growth. Phys Rev Lett 112:115502
Tallakstad KT, Toussaint R, Santucci S, Schmittbuhl J, Måløy KJ (2011) Local dynamics of a randomly pinned crack front during creep and forced propagation: an experimental study. Phys Rev E 83:046108
Tallakstad KT, Toussaint R, Santucci S, Måløy KJ (2013) Non-gaussian nature of fracture and the survival of fat-tail exponents. Phys Rev Lett 110:145501
Vasoya M, Leblond JB, Ponson L (2013) A geometrically nonlinear analysis of coplanar crack propagation in some heterogeneous medium. Int J Solids Struct 50:371–378
Vasoya M, Unni AB, Leblond JB, Lazarus V, Ponson L (2016) Finite size and non-linear effects during crack pinning by heterogeneities: an analytical and experimental study. J Mech Phys Sol 89:211
Vasoya M, Lazarus V, Ponson L (2016) Bridging micro to macroscale fracture properties in highly heterogeneous brittle solids: weak pinning versus fingering. J Mech Phys Solids 95:755–773
Vernède S, Ponson L, Bouchaud J-P (2015) Turbulent fracture surfaces: a footprint of damage percolation? Phys Rev Lett 141:215501
Vernède S, Ponson L (2017) Method for characterizing the cracking mechanism of a material from the fracture surfaces thereof. French patent 1459525 (2014), European, US and Chinese patent
Ververis C, Georghiou K, Christodoulakis N, Santas P, Santas R (2004) Fiber dimensions, lignin and cellulose content of various plant materials and their suitability for paper production. Ind Crop Prod 19:245–254
Vincent-Dospital T, Cochard A, Santucci S, Maloy KJ, Toussaint R (2021) Thermallu activated intermittent dynamics of creeping crack fronts along disordered interfaces. Sci Rep 11:20418
Wang N, Xia S (2017) Cohesive fracture of elastically heterogeneous materials: an integrative modeling and experimental study. J Mech Phys Solids 98:87–105
Wiese K, Le Doussal P (2007) Functional renormalization for disordered systems. Basic recipes and gourmet dishes. In: Markov processes and related fields, vol 13. Polymath, pp 777–818
Xia S, Ponson L, Ravichandran G, Bhattacharya K (2012) Toughening and asymmetry in peeling of heterogeneous adhesives. Phys Rev Lett 108:196101
Xia S, Ponson L, Ravichandran G, Bhattacharya K (2013) Adhesion of heterogeneous thin. I: elastic heterogeneity. J Mech Phys Solids 61:838–851
Xia S, Ponson L, Ravichandran G, Bhattacharya K (2015) Adhesion of heterogeneous thin. II: adhesive heterogeneity. J Mech Phys Solids 83:88–103
Zapperi S (2012) Current challenges for statistical physics in fracture and plasticity. Eur Phys J B 85:829

The Fracture Mechanics of Biological Materials

Francois Barthelat

Abstract Biological materials such as skins, bones, teeth or seashells boast remarkable structures and mechanisms, many of them unmatched by engineering materials. In these materials, fracture toughness is key to achieve high strength, reliability, robustness, damage tolerance and notch performance, and to fulfil critical structural functions in the organism. In this chapter, we review and discuss some of the main strategies found in biological materials to resist the propagation of cracks and to reach high toughness. We discuss six major groups of natural materials through specific examples: a uniaxial fiber composite (tendon), a laminated composite (fish scales), a natural elastomer (skin), a mineralized brick and mortar composite (nacre), three-dimensional mineralized cross plies (conch shells, tooth enamel) and a complex hierarchical material (bone). The composition, architecture, mechanics of deformation and fracture, and overall performance is reviewed for each of these materials. The chapter concludes with a summary of the broad strategies deployed in biological materials to manage damage and prevent crack propagation. These lessons are now inspiring the next generation of structural materials.

1 Introduction

Improving the performance of materials is critical to technological advances as demonstrated through history (bronze age, iron age…) and by modern technology (aerospace, biotechnology, computing) (Ashby 2010). In particular, improving the strength and toughness of materials by manipulating their composition and structure of structural materials has been a focus for thousands of years. As early as the 3rd millennium BC, builders in the Indus valley incorporated straw into mud bricks as fiber reinforcements to increase their fracture toughness, strength and reliability (Lemmen and Khan 2012; Binici et al. 2007). Modern material engineering deals with

F. Barthelat (✉)
Department of Mechanical Engineering, University of Colorado Boulder,
427 UCB, 1111 Engineering Dr, Boulder 80309, USA
e-mail: francois.barthelat@colorado.edu

L. Ponson (ed.), *Mechanics and Physics of Fracture*, CISM International Centre for Mechanical Sciences 608,
https://doi.org/10.1007/978-3-031-18340-9_4

critical issues related to resistance to fatigue cracks, stable crack propagation, toughening mechanisms, damage tolerance, notch performance and reliability (Ashby 2010; Lawn 1993; Anderson 2005). When exploited and optimized systematically, these concepts have enabled strong, tough and light materials for aerospace, transportation, construction, and energy applications. Despite these impressive advances, nature is well ahead of engineers in making materials (Fratzl and Weinkamer 2007; Barthelat 2015). The materials of trees, skeletons, teeth or protective shells are subject to stringent mechanical requirements. Just like many of our engineering materials, they must fulfil a variety of functions that include structural support, transfer of static, dynamic or cyclic forces, and protection against impact. Nature mainly uses four elements (C, H, O, N), a few building blocks (amino acids, polysaccharides, biominerals), and does not use metals for structural functions except for a few rare exceptions (Lichtenegger et al. 2003). In addition, natural materials are generally processed and fabricated in ambient, "normal" conditions, a severe limitation which contrasts with the extreme temperatures, pressures and chemistries that are common in metallurgy, and ceramic or polymer making. In terms of absolute strength and toughness, biological materials are inferior to our modern steels, largely because of constraints in raw materials. When these limitations in raw materials and processing conditions are taken into account, it is clear that nature is way ahead of engineers and materials scientists in terms of making "more with less".

Figure 1 shows an Ashby material property map of toughness versus stiffness for a variety of biological materials. The five biological materials that will be discussed in more details in this chapter are highlighted in red on the chart (a sixth material—tendon—is so tough that no data on fracture toughness is available). Biological materials span 4–5 orders of magnitudes in terms of toughness and stiffness, despite of the narrow range of composition range described above. Soft proteinaceous materials such as skin are soft but extremely tough, while at the other extreme biominerals (calcite, calcium phosphate) are very stiff but also very brittle. Between these two extremes one finds a large number of biological materials with intermediate stiffness and toughness, and interestingly most of these materials display high combinations of these properties. For example, bone, teeth (dentine, enamel) and mollusc shell incorporate proteins and minerals and achieve simultaneous toughness and stiffness. The chart also highlights that nature "amplifies" the properties of raw materials to levels which are not seen yet in engineering materials. For example, nacre from mollusk shell is made of 95% vol. of aragonite (a brittle mineral which is similar to calcite), but its architecture is so well adapted to resist fracture that it is three orders of magnitude tougher (in energy terms).

For comparison the properties of a steel alloy (4340 steel: $E \sim 200$ GPa, $J_c \sim 10$ kJ/m^2) are also shown on the chart. The strongest and toughness of biological material cannot match our engineering materials, largely because of constraints in raw materials and processing.However, the "amplification" of toughness and stiffness that hard biological achieve from their fragile ingredients (biominerals, proteins) is not matched to this day by any engineering materials. Nature is developing these original solutions through natural selection and evolution, and while whether the

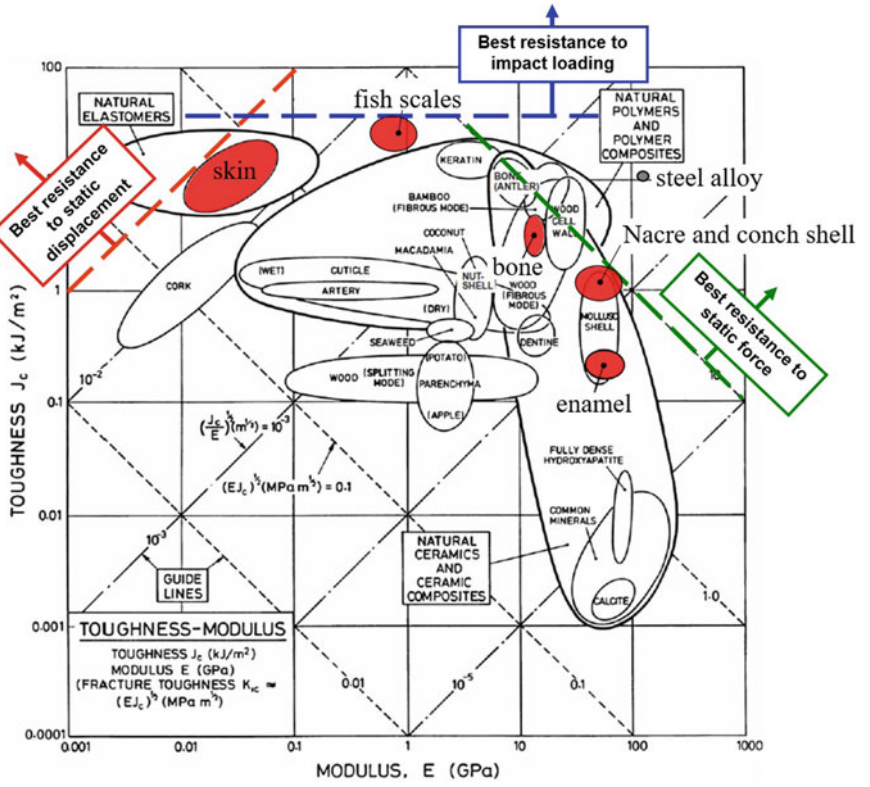

Fig. 1 Material property chart for modulus-toughness in biological materials (adapted from (?)). Guidelines show the best materials to resist large displacement, static force and impact. The specific materials discussed in this chapter (skin, fish scales, bone and nacre) are highlighted

structure of these materials is "optimum" is debatable, there is no question that their properties—including fracture toughness—are remarkably well adapted to their function. The toughness J_C is the energy required to generate new fracture areas in the material. Alternately, J_C can be interpreted as the amount of mechanical energy the material can absorb without fracturing, and therefore J_C can be used as a measure of the impact resistance of the material. By this measure, skin, fish scales, and bone antlers are the most adapted biological materials, which correlates with the function of these materials to resist impact loading without fracturing. In terms of resisting static forces and static stresses, the critical stress-intensity factor provides a better measure of resistance to crack propagation. This criterion maximizes $(EJ_C)^{1/2}$ on the chart, and nacre, conch shell, and bone are the materials which are the most adapted to resist static forces without fracturing. Finally, we examine the materials which can withstand large deformations without fracture, in other words those that maximize σ_s/E, where σ_s is strength. These materials therefore maximize $(J_C/E)^{1/2}$, and in this case natural elastomers such as skin are clearly the best biological materials

to resist large deformations without fracturing. While considering structure-property relationships in biological materials, it is important to also consider function, since the structure and properties of biological materials have evolved for specific functions.

The mechanical properties of biological materials have been of sustained interest for a long time, mainly for construction materials but also for biomechanics. For example the mechanical properties of wood have been of interest for a long time because wood is a construction material (Forest Products 1974). The mechanical properties of bone, cartilage, tendon, skin, and other connective tissues in the human body have also been of interest for biomedical applications, for example to guide optimum therapies, surgical treatments or rehabilitation strategies in orthopedics (Fung 2004).

Over last three decades there has been a renewed and vigorous effort towards understanding the mechanics of biological materials using the modern tools of materials science and mechanics. These powerful approaches let us probe the structure and mechanics of biological materials down to the nanoscale (Rabiei et al. 2010) (Gupta et al. 2005). Powerful computer models can now predict how a slight genetic mutation of the collagen structure at the molecular scale translates into crippling bone diseases (Gautieri et al. 2009). This "biological material science" (Meyers et al. 2008) is now largely motivated by bioinspiration and biomimetics (Barthelat 2007; Vincent et al. 2006). This transfer of technology from biology to engineering requires a precise understanding of structure-properties relationships and property-relationships in natural materials (Meyers et al. 2008), and this effort also includes fracture mechanics: Nature has evolved interesting architectures and mechanisms to prevent and control the propagation of cracks, and duplicating some of these ideas is a powerful approach that could overcome the inherent brittleness of glasses and ceramics (Wegst et al. 2015; Barthelat 2007; Espinosa et al. 2009), thereby expanding their range of applications.

2 Some General Construction Rules for Biological Materials

The range of compositions in biological materials is remarkably narrow considering the breadth of mechanical properties that can be achieved. In contrast with engineering materials, which make full use of most of the elements in the periodic tables, only four are prominent in nature: carbon, hydrogen, oxygen and nitrogen (C, H, O, N) account for 95% of the mass of biological organisms on earth. Proteins and polysaccharides are the "building blocks" of animals and plants. For example, proteins represent about 17% wt. of the human body, where they perform a wide variety of functions. The molecular building blocks for proteins are amino acids, small organic compounds with an amino group, a carboxyl (acid) group, and a radical group (*R*-group). The *R*-group varies in composition and size depending on the

amino acid, and only 21 amino acids are found in nature. Sequences of amino acids are assembled by condensation, which can be interpreted as polymerization where the amino acids form long polymeric chains with a strong covalent backbone. The process of transcription of DNA into RNA, and translation into a protein chain, is the fundamental fabrication mechanisms for proteins. This process is precise and governs the exact sequence of amino acids along the protein chain (also called primary structure) with high fidelity. Once the primary structure is formed, side groups along the proteins promote the formation of hydrogen bonds which can induce the folding of the protein chain into specific configurations. The exact sequence and size of the side groups will produce repeatable and robust folding patterns which lead to complex three-dimensional configurations called secondary structures. Common secondary structures in structural proteins are coiling (alpha helix) and crystallization (beta sheets). In terms of structural behavior, proteins can be interpreted as a precise coiling of a strong covalent backbone which is stabilized by weaker hydrogen bonds. Under the action of a mechanical pull, individual proteins can unfold as the hydrogen bonds are broken, which produces large elongations. Structural proteins such as keratin, elastin, and collagen are critical for the stiffness, deformability, strength and toughness of skin, nails, tendons, and bones. To illustrate the construction of a structural protein, we take the example of collagen, which represents about 25% wt. of all proteins in the human body. Collagen is critical for the mechanical performance of bones, tendons, skin, and eye cornea. Collagen is therefore a "Universal protein" found across various structural tissues in the human body, and also across the animal kingdom (all mammals, fish scales, anemones, sea cucumbers). Collagen is made of up to 20 different amino acids, the exact composition varying across about 20 types. The main collagen types are type I (in most human tissues), type II (cartilage), type III (in blood vessels and repair sites). Here we focus the discussion on collagen type I. Proteinaceous collagen chains assemble into tropocollagen, which consists of three left-handed alpha chains twisted in a right-handed triple helix stabilized by hydrogen bonds. Alternating between a left and right handed assembly is critical for the stability of the molecule, just like alternating the twisting direction in multi-stranded ropes is important to prevent the unraveling of the strands. Every third R-group along these chains is glycine, the smallest residue in amino acids. This residue faces the inner side of the coil, making the tropocollagen helix very tight. Individual tropocollagen molecules are 300 nm long for a diameter of about 1.5 nm. They have a head and a tail with distinct functionalities, and they tend to assemble so "head" bonds assemble with a "tail". This feature leads to the self-assemblies of tropocollagen molecules into three-dimensional periodic bundles called fibrils (Fratzl et al. 1998), which contain a periodic gaps and a 67 nm periodicity along the fibril. The resulting fibril is 20–200 nm thick, and can reach tens of millimeters in length. This fiber is large enough to be mechanically isolated, handled and tested in tension, using MEMS based actuators (Eppell et al. 2006) or capacitor-based devices (Poissant and Barthelat 2012). These tests reveal a relatively stiff fiber ($E = 1$ GPa), which is strong (strength >200 MPa) yet deformable (strain at failure >10 %). As depicted on Fig. 2, this formidable fiber serves as a basis to form random networks (skin), uniaxial composites (tendons, ligaments) or crossplies (fish scales). To add stiffness, these

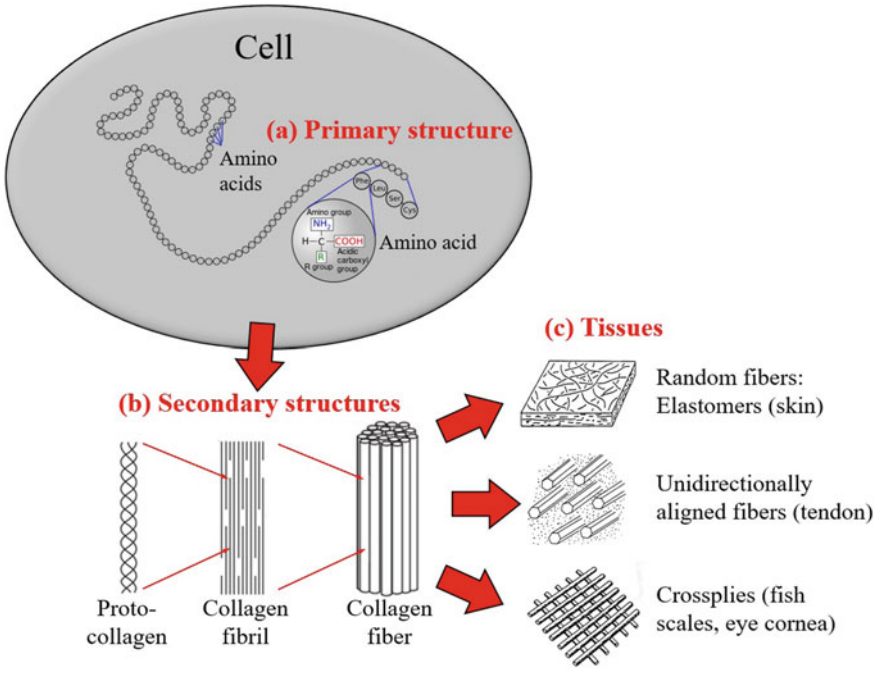

Fig. 2 Overview of the construction of collagenous tissues, which is typical of biological materials: **a** cells produce a sequence of amino acid that reflects DNA's blueprint; **b** these primary structures assemble into more complex, 3D "secondary" structures: protocollagen molecule, collagen fibrils, collagen fibers; **c** these fibers are deposited in various ways to form biological tissue with a broad range of structural properties

proteins may be mineralized, as seen in mineralized tendons (low mineralization), bone, nacre, and enamel (high mineralization). At the molecular scale, individual collagen molecules (tropocollagen) bond via coordinated hydrogen bonds (Buehler 2006) and self-assemble into fibrils (Fig. 3a). Specific covalent crosslinks at the ends of the collagen molecules (telopeptide regions) provide cohesion and mechanical stability to the fibrils, and govern complex unraveling nano-mechanisms as the fibril is stretched (Uzel and Buehler 2011). While cellulose is the main structural protein for many animals (mammals, reptile, fish), polysaccharides are the main construction materials for insects (chitin) and plants (cellulose). These fiber-like materials follow the same broad construction rules of collagen: strong molecular backbones, weaker intermolecular interaction, self-assembly into fibrils and fibers.

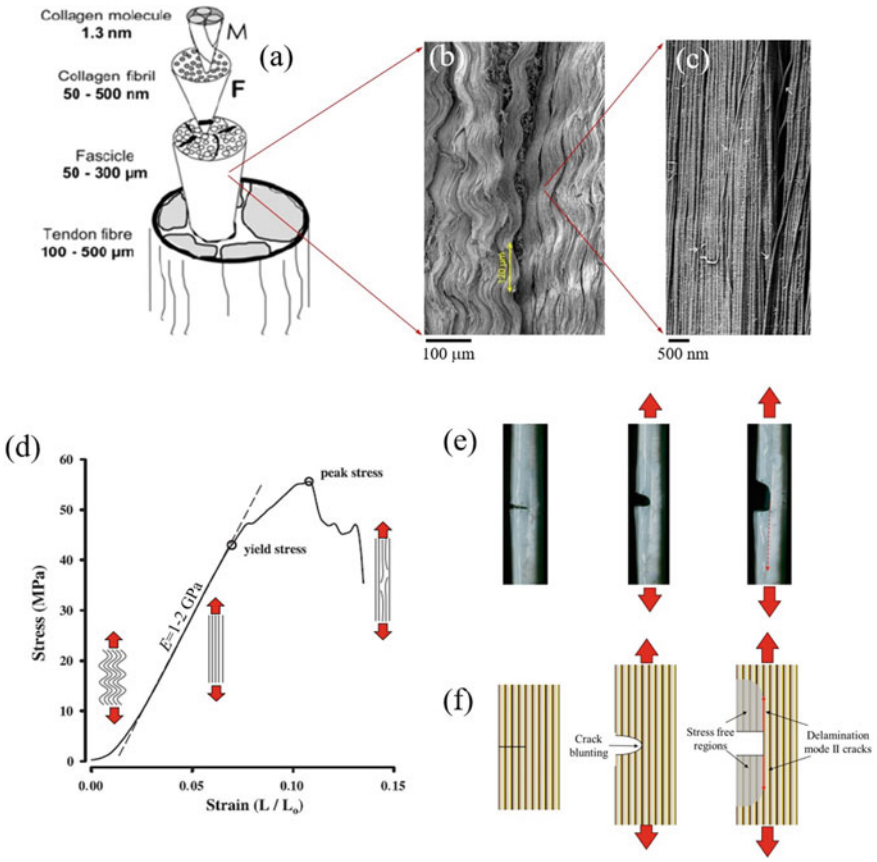

Fig. 3 The structure and mechanics of tendon: **a** Hierarchical bundles of collagen molecules, fibrils and fibers (Fratzl 2003); **b** Sinusoidal crimps (Scanning electron micrograph, Herod et al. 2016); **c** the fibrils in tendon are extremely long and may span the entire length of the tissue (Scanning electron micrograph, (Provenzano and Vanderby 2006); **d** typical tensile stress-stain curve of tendon (Haraldsson et al. 2005); **e** notch performance of tendon, adapted from Ker (2007) (tendon is so tough that crack propagation through its section is not possible); **f** schematic showing the mechanisms of crack blunting and delamination

3 A Uniaxial Fiber Composite: Tendon

The simplest way to arrange fibers and to make the most of their high performance in tension is to arrange them in parallel bundles, as in tendons. Tendons are highly specialized tissues whose function is to carry and transfer tensile forces between muscle and bone. Tendons must therefore be stiff in order to accurately and rapidly convert muscle action into skeletal motion, and strong in order to carry high tensile forces without failing. Tendons are also used as mechanical energy storage that, for example, improves the efficiency of running. They are made of collagen type I

(60–90% dry weight), elastin (5%) and other extra-collagenous proteins (Shen et al. 2008). Collagen fibrils bundle into parallel fibers or fascicles about 50–300 μ in diameter (Fig. 3a). The fibrils are held by a much softer extra-collagenous matrix, whose shear modulus is three orders of magnitude lower than the modulus of the fibers (Ker 2007). At rest, the fibers are not completely straight and display wavy patterns called crimps (Fig. 3b). Mechanical models and in-situ X-ray images suggest that the collagen fibrils have a finite length, which enables them to glide on one another when tensile forces are applied on the tendon (Puxkandl et al. 2002). However, direct observations on tendons show individual fibrils with no apparent ends, which suggests that fibers in fact span the entire length of the tendon (Provenzano and Vanderby 2006; Svensson et al. 2017) (Fig. 3a).

Figure 3d shows the tensile response of tendon (tensile stress-strain curve Haraldsson et al. 2005). The "toe" and "heel" region of low stress corresponds to an initial regime where the crimps in the collagen fibers are straightened. This process requires little tensile force, but once the crimps are straightened the material is much stiffer. In the linear region, the fibers are straight and aligned along the direction of pulling, and the strong and stiff covalent backbones of the collagen molecules carry an increasing amount of tensile stress. He linear region is therefore relatively stiff (E =1–2 GPa). At tensile stress of about 50–100 MPa the material reaches its maximum carrying capability and strength. The tendon softens because of defibrillation and progressive rupture of the fibers (Fung et al. 2009). In uniaxial tension, tendons are among the stiffest and strongest non-mineralized biological materials. Figure 3e shows a tendon containing a deep cut and subjected to tension (Ker 2007). The initial deformability of tendon blunts the tip of the cut, turning the sharp slit into a rounded notch with the direct effect of reducing the stress concentration. In addition, since the shear modulus of the fascicle interfaces is much lower that the fibers, large shear deformations take place along these interfaces. The interfaces then fail in shear and channel "delamination" mode II cracks along the direction of pulling. This mechanism blunts the crack further into a Cook-Gordon type configuration (Cook et al. 1964), further preventing propagation into the fibers. The delamination of the fibers has also two effects: (i) behind the crack tip a large volume of material becomes stress free (Fig. 3f); (ii) In front of the crack tip, the tensile stresses become uniformly distributed. In the laboratory test, the mode II crack reach the grips of the loading machine before the ligament fails in tension (Ker 2007). This powerful mechanism therefore turns tendon into a notch insensitive material. The cut decreases the strength because of the reduction in nominal cross section, but the stress concentration at the tip of the cut is completely suppressed. Instead, the delaminating crack proceeds into the grips of the machine. In this configuration it is therefore impossible to propagate a crack in model I across the fibers, and therefore estimates for the fracture toughness of tendon are not available (Szczesny et al. 2015). Interestingly, the construction and mechanisms of tendon are identical to the design guidelines for modern fiber reinforced engineering composites: High concentration of stiff and strong fibers in a weaker matrix to provide high combinations of stiffness and strength. The strength of the interface between matrix and fibers is critical: The interfaces must be strong enough to provide cohesion to the material, yet weak enough to interact with propagating cracks in order to trigger pow-

erful toughening mechanisms (Zok 2006) (Cook-Gordon blunting mechanism, crack deflection, crack bridging). The construction of tendon is perfectly adapted to carry large tensile forces, even in the presence of partial tears or local damage. However, it is a highly specialized tissue that can provide stiffness and stress along only one direction (tendons are very weak in the transverse direction). The next two examples discuss collagen fibrils in crossplies (fish scales) or random networks (skin). These different architectures produce different mechanisms and properties, but when stress concentrations are present fibers align locally, generating a "tendon-like" barriers to crack propagation.

4 A Natural Composite Laminate: Fish Scale

Tendons are rope-like tissues specialized in carrying tensile forces along a single direction. For other structural elements where biaxial stiffness and strength are required, crossply architectures are more adapted. In crossplies, the alignment of the fibers is uniform only within one layer (or "ply") of the material, and adjacent layers have a rotated arrangement. Simple cross plies have a (0–90) degree arrangement, while more complex crossplies such as the Bouligand structure of arthropod cuticles (the hard shell of insects and crustaceans) only vary by a few degrees from one layer to the next (Raabe et al. 2005). The immediate benefit of cross plies is that the tensile strength and stiffness of individual fibers are available along different pulling direction within the plane of the plies. In effect, crossplies increase the isotropy of fibrous material, the main drawback being that along each of these directions the stiffness and the strength is reduced compared to the uniaxial composite (Nikolov et al. 2010). Cross plies are well adapted for hydrostatic skeletons, which are essentially pressurized reservoirs: the body of sea anemones, soft-shelled turtles (Scheyer et al. 2007), and human annulus fibrosus (?). In arthropod shells (cuticles) and fish scale, crossplies are well adapted to resist multiaxial stresses from sharp contacts (impacts, attacks from predators). For example, localized surface forces generate flexural stresses in the shell, which must be resisted along direction in the plane of the shell.

The structure and mechanics of natural scaled skin, and more particularly fish scales, have recently been the subject of several studies (Yang et al. 2013a, b; Bruet et al. 2008; Ikoma et al. 2003; Garrano et al. 2012; Lin et al. 2011; Meyers et al. 2012; Zhu et al. 2013; Browning et al. 2013; Zimmermann et al. 2013; Vernerey and Barthelat 2010). Figure 4 shows the hierarchical features of fish scales. At the macroscopic level, the scales are staggered and cover most of the body of the fish, providing a continuous barrier from penetration combined with flexural compliance. At the mesoscale level, individual scales are polygonal thin plates composed of type-I collagen fibrils partially mineralized with hydroxyapatite (16–59% mineral content in weight (Ikoma et al. 2003; Liu et al. 2008; Torres et al. 2008; Schonborner et al. 1979; Seshaiya et al. 1963). The outer layer of the scale is significantly more mineralized and often referred to as the "bony layer". Bony and collagen layers

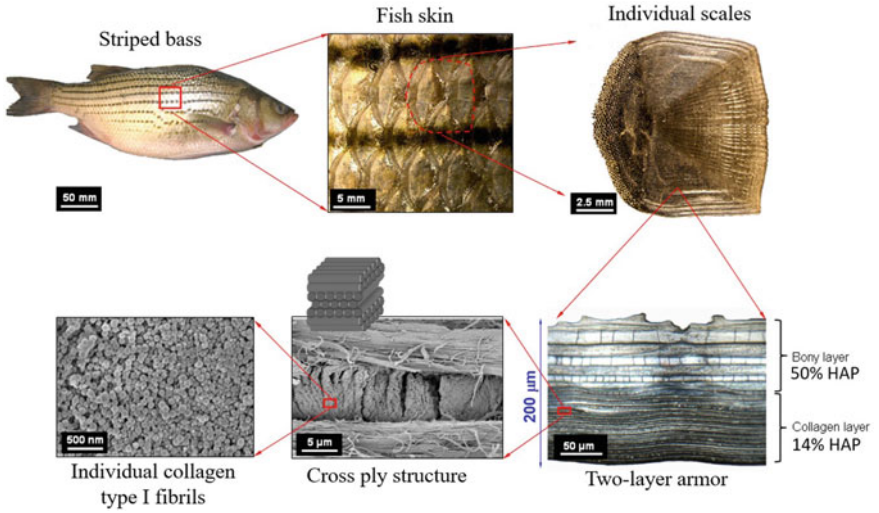

Fig. 4 The hierarchical structure of typical teleost fish scales (shown here for a striped bass Zhu et al. 2012)

have approximately the same thickness (~100μm). These layers are both cross-ply layered composites, each ply being made of parallel collagen fibrils rotated across layers by angles that can vary across species (Bigi et al. 2001; Meunier 1984; Zylberberg et al. 1988; Meunier and Castanet 1982; Meunier 1981). The scales of striped bass, consist of a basal layer formed of 20–25 plies about 4–5 μm thick each (Fig. 4d), where the collagen fibrils are rotated by 90 °C from one ply to the next (Fig. 4e, f). Natural scaled skins have remarkable mechanical properties: compliance, resistance to penetration, lightweight, and ultra-thin structure (Yang et al. 2013a). Tensile tests on natural teleost fish scales confirmed the scale as a stiff, strong, and tough material with extensive inelastic deformation and energy dissipation including pullout, defibrillation, sliding and ply rotation (Ikoma et al. 2003; Garrano et al. 2012; Lin et al. 2011; Zhu et al. 2012; Zimmermann et al. 2013). Fracture toughness is a critical property to resist puncture or lacerations from predators or collisions with other fish or obstacles. Early tests revealed that fish scales are so tough that they could not be fractured, even after immersion in liquid nitrogen (Currey 1999). Figure 5a,b show a set of tensile test results on plain and notched scales. The curves have a bell shape, with an initial linear response followed by large tensile strains and tremendous energy absorption. As expected, the notched samples were weaker than the intact samples because of the presence of the notch and the associated reduction in the nominal cross section (i.e. minimum load bearing cross section). However, when the nominal stresses are calculated, the stress strain curves for the notched and intact scales are nearly identical. Individual fish scales from *Morone saxatilis* are therefore notch insensitive. At the early stage of loading, the bony and collagen layer delaminated because of the mismatch between their mechanical

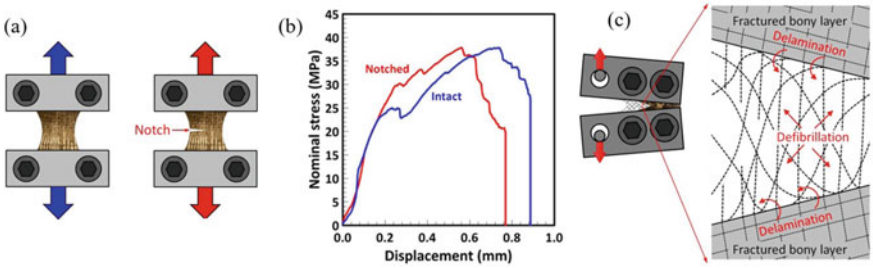

Fig. 5 Mechanical tests on individual scales: **a** tensile tests on intact and notched samples with **b** resulting nominal stress-displacement curves; **c** Fracture involves extensive delamination and bridging by collagen fibers (adapted from Dastjerdi and Barthelat 2015)

properties (Zhu et al. 2012) (Fig. 5b). Further increase of loading resulted in the fracture of the bony layer while the collagen layer was still deforming, with extensive defibrillation of the collagen cross plies up to the ultimate failure at around 0.8 mm displacement. The notched sample also showed crack blunting (Fig. 5b, 3c), a potent toughening mechanism for metals and polymeric materials. Instrumented fracture tests on individual fish scales are extremely difficult because of their small size and very high toughness. Recently a new miniature setup was used to measure the toughness of the scales along three crack propagation orientations (Dastjerdi and Barthelat 2015). Crack propagation was always stable, and the results confirmed that fish scales are among the toughest biological materials (work of fracture $\sim 40 \mathrm{J/m^2}$, Fig. 1). Fracture models suggest that inelastic deformations of the collagen fibrils, which operate over regions on the order of 1–2 mm around the crack tip is the main contributor to toughness (Dastjerdi and Barthelat 2015), a process similar to nacre (Barthelat and Rabiei 2011) and to advanced engineering polymers (Evans et al. 1986). The fibers also rotate towards the direction of pulling (Yang et al. 2014), providing a local "tendon" like structure to resist crack propagation. Delamination of the collagen fibers also produces a small bridging stress across the crack faces, but this mechanism can operate over large crack openings so that its contribution to toughness is not negligible (Dastjerdi and Barthelat 2015). For these mechanisms the interfaces between the fibers and the plies must be much weaker than the fibers. Delamination experiments indicated that these interface are indeed 400 times weaker than fish scale as a whole (Dastjerdi and Barthelat 2015).

5 A Rubber-Like Material: Skin

Human skin is the largest organ in the body. A thin, deformable and tough layer, skin fulfills a wide range of critical functions that include protection against mechanical threats, pathogens or water loss, but also temperature regulation, sensing and excretion (sweat) (Fung 2004). Skin is composed of several layers: stratum corneum

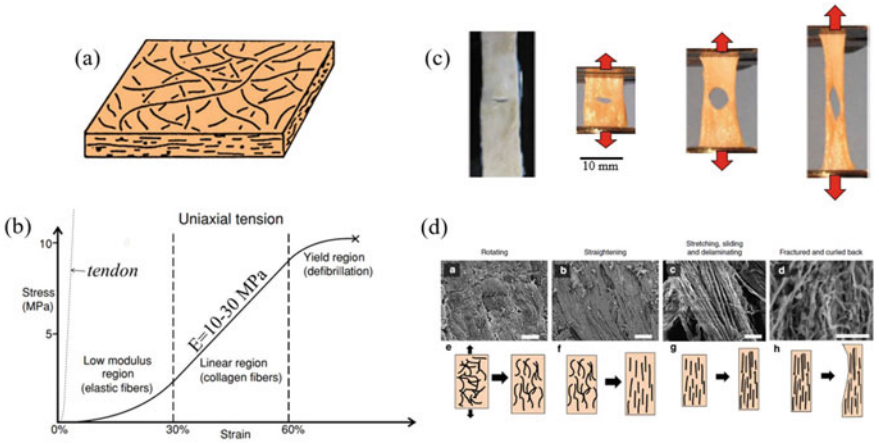

Fig. 6 Overview of skin structure and mechanics: **a** Schematic of the network of collagen fibrils in the dermis; **b** tensile stress strain curve of human skin (Silver et al. 2003); **c** Notch performance of skin in tension. Rounding of the crack tip suppresses stress concentrations (Yang et al. 2015); **d** at the crack tip the collagen fibrils align along the direction of loading, forming a "tendon-like" barrier to crack propagation (Yang et al. 2015)

(outermost layer), epidermis, dermis, subcutaneous tissue (innermost skin layer) (Silver et al. 2003). The dermis layer is the thickest layer, and it is also the layer that governs the mechanical response of skin (Oxlund et al. 1988). The dermis is a three-dimensional network of cross-linked collagen and elastin fibers embedded in proteoglycans (Silver et al. 2003). The network of collagen fibrils largely dominates the mechanical response of the dermis, elastin providing recoil and "elasticity" to the skin once it is unloaded (Oxlund et al. 1988). Individual collagen fibers within the network are primarily parallel to the surface of skin (Fung 2004) (Fig. 6a). Within the plane of the dermis, the fibers follow a mostly random orientation, although preferred orientations are observed locally along lines which were first mapped by Langer (Ridge and Wright 1966a). Skin tends to be stiffer and stronger along these Langer lines (Ridge and Wright 1966a, b), and wounds or cuts that disrupt these lines can take longer to heal (surgeons favor incision parallel to these lines). The dermis shares many attributes with rubbers and other engineering elastomers in terms of structure, mechanics and properties (including fracture properties). Both are made of a random network of cross-linked fibers or molecules, and the elasticity of both can be captured with entropy-based elastic models (Fung 2004; Bischoff et al. 2000). Both materials are very soft and can undergo large deformations in tension. The high level of hydration of skin maintains the high mobility of the elastin and collagen components. Figure 6b shows a typical stress-strain curve of skin in tension. Up to about 30% strain, the collagen network offers only a small resistance to deformation as entropic elastic dominates. At larger strains skin enter a much stiffer, linear region where the collagen network progressively aligns and stiffens along stretch direction. Eventually the cross links break, fibers slip, and the overall collagenous

network weakens which generate a "yield point" on the curve. Complete defibrillation follows with progressive tear of the skin. Skin provides a mechanical barrier to bites, scratches and small tears, so that fracture toughness is critical. Tear fracture tests reveal toughness in the order of 10 kJ/m^2 (Purslow 1983), which is towards the high end for biological materials (Fig. 1). Figure 6c shows a strip of skin containing a through cut in tension. Skin is easily deformed at low stresses, so that the initial slit immediately turns into a rounded ellipse as a tensile force is applied, which suppresses the stress singularity at the tip of the notch. In addition, the alignment of the collagen fibers in these deformed regions form a region of aligned collagen fibers which are transverse to the direction of crack propagation (Fig. 6d). Skin therefore "recruits" random collagen fibers with high deformations, to toughen the material locally with fiber reinforcements in a "tendon-like" material.

6 A Densely Mineralized Brick and Mortar Composite: Nacre

Minerals are widely used by living organisms for structural purposes, mainly for increasing the stiffness and hardness of otherwise relatively soft proteins. The tensile modulus of collagen, the most common structural protein, in a unidirectional material such as tendon is 1–2 GPa. This is relatively stiff for a protein, but too soft to fulfill skeletal functions or heavier protection. Structural biological materials therefore often incorporate stiff minerals to increase stiffness and hardness. Calcium carbonate (mollusk shells) or hydroxyapatite (human bone, teeth) are the most common minerals found in natural materials, although there are many others (Weiner and Addadi 1997). The general strategy for incorporating these minerals is for the organism to grow a scaffold of proteinaceous materials first, which is then mineralized over time. This process is highly regulated by complex biochemical processes combined with physical confinement to control the deposition sites, shape, size, and growth rate of mineral crystals (Weiner and Addadi 1997; Mann 2000). As a general rule, the minerals are in the form of nanograins (Rousseau et al. 2005), or in the form of mesocrystals (Colfen and Antonietti 2005): large crystals made of nanograins with uniform texture and bonded by organic materials. Therefore all mineralized tissues in nature are composite materials, even seemingly pure biominerals such as urchin spines (Seto et al. 2012). In general, stiff materials are also hard (Ashby 2010), and therefore incorporating minerals into soft matrices increases both stiffness and hardness. However, the deformability of the material also decreases and their fracture toughness also decreases in general, so that this "conflict" between strength and toughness is prominent in engineering materials (Ritchie 2011). Interestingly, natural materials alleviate this limitation by remarkable architectures and mechanisms which ensure high stiffness, hardness and fracture toughness.

Mollusk shells provide remarkable examples of highly mineralized natural materials. The shells are mostly made of minerals (at least 95% volume) and contain only

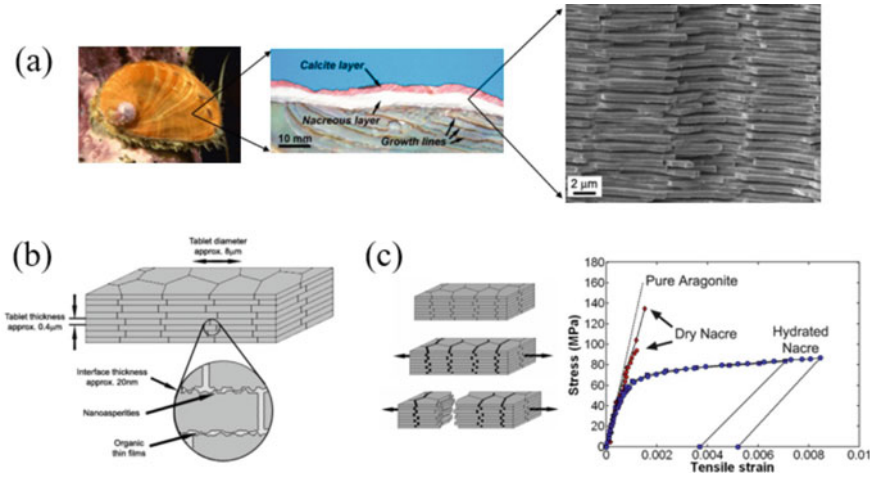

Fig. 7 Overview of the structure and mechanics of nacre: **a** Nacre has a three dimensional brick and mortar structure and is part of a two layer hard shell in mollusks (Barthelat et al. 2007); **b** schematic with dimensions. 20–30 nm thick layers of organic materials bond the microscopic tablets together; **c** when tension is applied along the direction of the tablets they slide on one another over large volumes. This behavior generates large strain, turning a brittle biomineral into a tough composite (Barthelat et al. 2007)

a small fraction (at most 5% volume) of organic materials (Currey and Taylor 1974). Among the different microstructures found in mollusk shells, nacre is the strongest and toughest (Currey and Taylor 1974). Nacre displays complex micro-mechanisms of deformation and fracture which generate high stiffness (70–80 GPa), high tensile strength (70–100 MPa) and a remarkably high fracture toughness (4–10 MPa.m1/2) (Currey 1977; Jackson et al. 1988; Wang et al. 2001). Nacre has a relatively simple, brick-wall-like architecture composed of mesocrystals of minerals in the shape of polygonal tablets (0.2–1 μ thick, 5–10 μ in diameter, Fig. 7a, b). In tension, the tablets can slide on one another, which generates relatively large deformations (up to almost 1% strain) accompanied with energy dissipation (Barthelat et al. 2007; Jackson et al. 1988; Wang et al. 2001), Fig. 7c. The sliding and pullout of the tablets are mediated by the thin (20–40 nm) interfaces between the tablets, which are rich in organic materials (Levi-Kalisman et al. 2001). The relatively large inelastic deformations and the energy dissipated at the interface translate into a material that can absorb deformations, deform to reduce the effects of stress concentrations, tolerate damage and absorb mechanical energy from impact. Figure 8a shows crack resistance curves obtained from four-point bending tests on single edge notched bend samples of nacre, prepared so a crack propagates across the tablets. In this configuration crack propagation in nacre is stable, and the curves display a very strong "R-curve" behavior, with a resistance to crack propagation (measured in kJ/m^2) that is initially low (low initiation toughness) but which increases significantly as the crack advances. This behavior, a characteristic of advanced structural materials, imparts the materials with tolerance

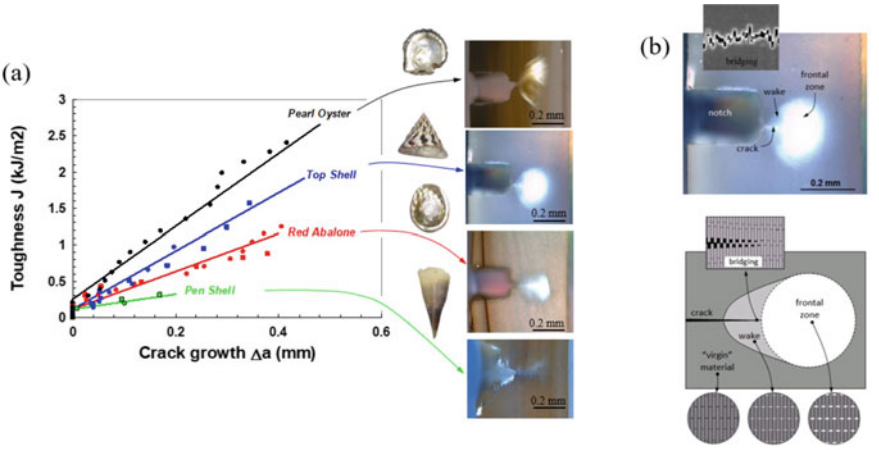

Fig. 8 The fracture mechanics of nacre: **a** Experimental crack resistance curves for four types of nacre, together with in-situ optical images. The whitening regions are an indication of tablet sliding at the microscale (Rabiei et al. 2010); **b** Schematic showing the main toughening mechanisms (Barthelat and Rabiei 2011)

to defects and stable crack propagation. This behavior also indicates that powerful toughening mechanisms are triggered by the stresses ahead of the advancing crack. The main two toughening mechanisms are both associated with the sliding of the micro tablets. If the cracks do not penetrate into the tablets, the intrinsic cohesion of nacre is provided by the interfaces. These interfaces are very weak, with a measured mode I fracture toughness of only about $10\,J/m^{-2}$ (Currey 1977; Mayer 2005; Dastjerdi et al. 2013), which is about 100 times lower than the toughness of nacre across the direction of the tablets (Rabiei et al. 2010). As noted previously for tendon and fish scales, weak interfaces are a requirement for the interfaces to deflect and guide incoming cracks. Mechanical tests on demineralized nacre confirm that the organic materials have low strength but high deformability (Dastjerdi et al. 2013; Lopez et al. 2014). The low toughness of the interfaces is amplified by two micro-mechanisms, both associated with tablet sliding (Fig. 8b). A first amplification of the toughness of the interfaces is provided by crack bridging, with tablets interacting behind the main crack tip. A second amplification of toughness is more powerful and provided by the inelastic process zone that develops in front of the advancing crack. The high tensile stress in this region triggers tablet sliding in a relatively large region, millimeters in size. As the crack propagates into that inelastic region, the material on either side of the newly created crack faces unloads, leaving a wake of permanently deformed material with residual strains. The process of propagating a crack in nacre therefore involves the loading and unloading of a large volume of material, which dissipates a large amount of energy. Process zone toughening (Barthelat and Rabiei 2011) make nacre several orders of magnitude tougher than aragonite (Rabiei et al. 2010; Barthelat 2007; Wang et al. 2001). This critical mechanism is supported by experiments:

nacres with small process zones have a low toughness (Fig. 8a). It is also supported by models, that show that transient process toughening can generate extremely large or even unbounded toughening (Barthelat and Rabiei 2011). High extensibility is critical to develop inelastic mechanisms over large volumes and generate toughness at the macroscale (Barthelat et al. 2007). Among other properties for the interfaces in nacre, it has been suggested that extensibility is the most important for the overall toughness of nacre (Nabavi et al. 2014). The properties of the interfaces appear to be fine-tuned to achieve high performance for the material (Nabavi et al. 2014).

7 A Mineralized Cross-Ply: Tooth Enamel

Tooth enamel is a very hard tissue that covers the surface of teeth. Its extremely high level of mineralization (∼96% vol.) makes it the hardest tissue in the human body (Nanci and Ten Cate 2013). Surface hardness is a critical property for the functionality of teeth, to ensure efficient crushing and cutting food particles. Biting forces can be relatively large (100–1000 N), which involves very high and localized contact stresses involving teeth and food particles (Yahyazadehfar et al. 2014). Specific architectures and mechanisms are therefore required to resist surface cracking. The microstructure of enamel is made of mineral rods about 5 μ in diameter, which start at the surface of the tooth and end at the junction between enamel and the underlying dentin (the dentine-enamel junction, Fig. 9a). Individual rods are made of nano-crystallites of the mineral hydroxyapatite (Habelitz et al. 2001). The thin interface between the rods is rich in proteins. While the rods are perpendicular to the surface of the tooth near the surface (in the outer enamel region), in deeper regions (inner enamel region) they crisscross complex three-dimensional decussation patterns (Macho et al. 2003). Cracks emanating from the surface of the tooth are channeled away from the surface and along the parallel rods, preventing chipping of the enamel surface. Deeper within enamel, the decussation pattern impedes further crack growth (Yahyazadehfar et al. 2013) by a series of crack deflection and crack bridging (Bajaj et al. 2010) (Fig. 9a, b). The powerful toughening mechanisms at work in the inner region can be quantified by propagating a crack from the outer layer to the inner layer (Bajaj and Arola 2009). In this "forward" direction (Fig. 9c), the toughness remains about constant in the outer layer, and the crack is mostly channeled by the proteinaceous interfaces. When the crack enters the decussated region in inner enamel, the toughness rapidly increases as crack bridging takes place, up to four times the initial fracture toughness. Through-cracks in enamel are therefore very stable and are actually considered a normal aging process for teeth (Lin and Douglas 1994; Bechtle et al. 2010; Espinosa et al. 2011). More severe stresses may propagate the crack through the enamel layer where they meet another line of defense: the dentine-enamel junction (Imbeni et al. 2005) and underlying dentin (Kruzic et al. 2003). In contrast, cracks propagated in the "reverse" direction (from inner to outer enamel) are unstable and propagate more easily (Bajaj and Arola 2009) (Fig. 10c). Similar mechanisms are found in the shell of conch, another example of a highly mineralized biological material (>99% vol.).

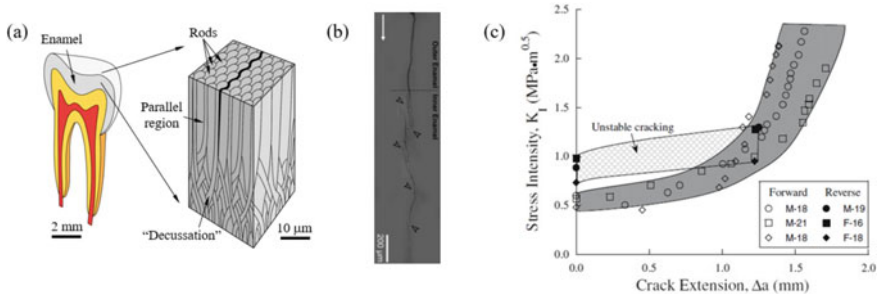

Fig. 9 Tooth enamel: **a** microstructure and interaction with a surface crack (Mirkhalaf et al. 2014); **b** Scanning electron micrograph of a crack propagated form the outer region (straight rods) to the inner region (decussated rods) (Bajaj et al. 2010); **c** Crack resistance curve for tooth enamel in the "forward" direction shows a pronounced rise in local toughness when the crack enters the decussation region. In the "reverse" direction the toughness is lower and the crack is unstable (Bajaj and Arola 2009)

In the outer layers of the shell, mineral plies are perpendicular to the surface, and proteinaceous interfaces between the plies channel multiple cracks in periodic arrays (Kamat et al. 2000, 2004). In the middle layer, the layers form a $\pm 45°$ crossply, which creates large scale crack bridging and amplifies the toughness by two to three orders of magnitude (Kamat et al. 2000, 2004). In tooth enamel and conch shell the weaker organic interfaces only represent 1–5 wt%, but they are crucial to the toughness of these biological ceramics (Yahyazadehfar and Arola 2015).

8 A Complex Hierarchical Composite: Bone

Bone is a high-performance material which fulfills a variety of functions, the primary of which is mechanical support (Currey 2002). Bone must therefore be stiff and hard, but it is also surprisingly tough (Wegst and Ashby 2004) considering its contents of brittle minerals and soft proteins. Bone density and mineral content have traditionally served as the only predictors of bone strength, but these measures have limitations (Hui et al. 1988). More recent research has considered the material bone as a composite material in which minerals, collagen and extracollagenous proteins contribute to its mechanical performance (Burr 2002; Ritchie et al. 2009). Figure 10 shows the structure of cortical bone, which is the dense, outer layer of long bones (femur, tibia). The material bone is composed of approximately 60% weight of mineral (calcium and phosphate), 10–20% water and 20–30% of proteins. About 90% of the protein content is collagen type I, the remaining 10% non-collagenous proteins including fibronectin, osteonectin, sialoprotein, osteocalcin and osteopontin (Young 2003).

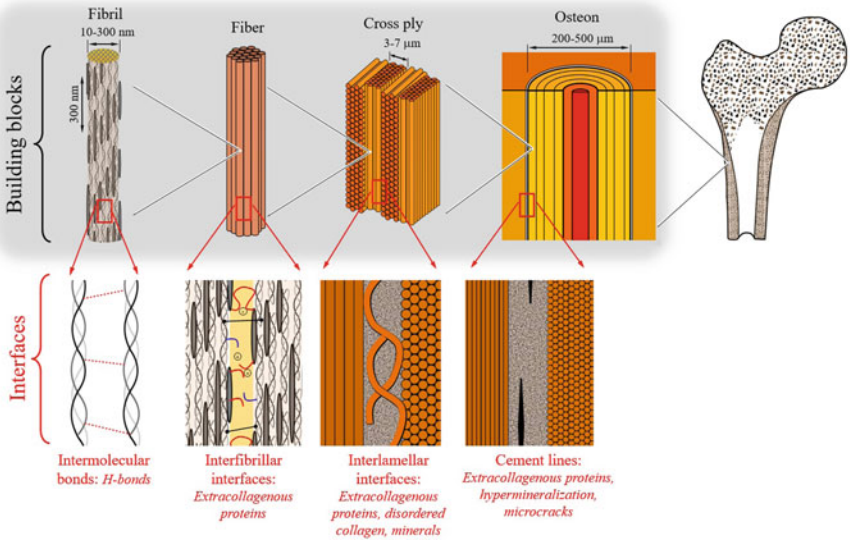

Fig. 10 The hierarchical building blocks that form the structure of cortical (dense bone). The building blocks are joined by interfaces which are critical to deformation and fracture mechanisms (Barthelat et al. 2016)

The collagen fibrils in bone they are reinforced by nanocrystals of hydroxyapatite (Weiner and Wagner 1998; Hassenkam et al. 2004; Buehler 2007). The fibrils bundle into fibers, which form the building block of bone at the next hierarchical level. Fibers arrange into cross plies and lamellae at the microscopic scale (Fig. 10), and the lamellae wrap around the Haversian canals concentrically to form the osteons, which are the microscopic building blocks of mature cortical bone. The deformation and fracture of bone is complex and involves mechanisms at each of these length scales (Ritchie et al. 2009; Launey et al. 2022; Ural and Vashishth 2014; Ritchie et al. 2005). This description of the structure and mechanics of bone, based on hierarchical building blocks (Weiner and Wagner 1998; Rho et al. 1998), has dominated our conception of this material over the last 20 years. More recently however, the interfaces between these building blocks have been examined in more depth (Fig. 10), especially in the context of deformation and fracture (Barthelat et al. 2016; Buehler 2007; Thurner and Katsamenis 2014; Zimmermann et al. 2011; Taylor et al. 2007; Gupta et al. 2006; Fantner et al. 2005; Dunlop et al. 2011). For example, fibrils are held together by a 1–2 nm thick layer of non-collagenous interfibrillar matrix which contains a variety of proteins including osteocalcin and osteopontin (Ural and Vashishth 2014). This mixture of proteins is more compliant and weaker than the stiff mineralized and aligned collagen fibrils as demonstrated by cleavage and fracture surfaces of lamellar bone at the microscale (Fantner et al. 2005). The proteins at the interfaces are highly deformable, however, and separating the collagen fibrils in bone forms ligaments in the interfaces (Fantner et al. 2005) which are similar to observations

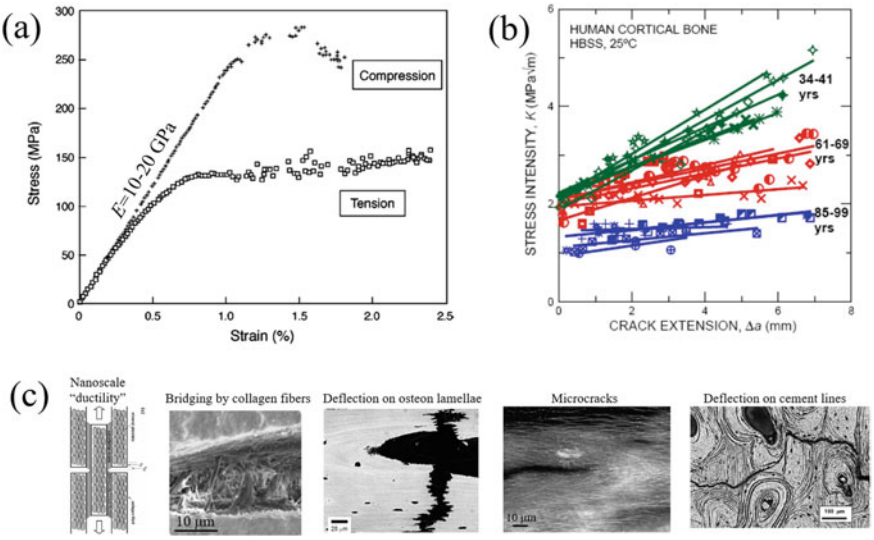

Fig. 11 Mechanics of deformation and fracture in cortical bone: **a** Stress strain curves in tension and compression along the axial direction of a bovine femur (Mercer et al. 2006); **b** crack resistance curve obtained from mode I fracture tests across the longitudinal direction of human humeri (Nalla et al. 2006); **c** Multiscale toughening mechanisms in cortical bone: Nanoscale "ductility" (Gupta et al. 2006), bridging by collagen fibers, (Fantner et al. 2006) deflection on osteon lamellae (Peterlik et al. 2006), microcracks (Vashishth 2007), deflection on cement lines (Zioupos et al. 2008)

on nacre. Figure 11a shows the stress-strain curve of bone. The modulus is in the range of 10–20 GPa and the tensile strength is about 100 MPa, which is about 10 times stiffer and two times stronger than tendon (respectively), a direct effect of the mineralization of bone. Beyond a "yield point" bone displays inelastic deformations and it can fail at strains in the order of 1–2%. The inelastic deformation of bone is critical to its ability to absorb impact energy without fracturing. The multiscale micromechanics governing this deformation includes the inelastic deformation of individual collagen fibrils (Tang et al. 2010), the sliding of minerals relative to collagen (Mercer et al. 2006), the sliding of fibrils on one another (Gupta et al. 2006), the accumulation of diffuse damage (Zioupos 1998), the development of dilatational bands at the nanoscale (Poundarik et al. 2012; Schwiedrzik et al. 2014), and shearing of the cement lines (Ascenzi and Bonucci 1972). While these inelastic deformations develop, bone must resist the propagation of large cracks emanating from bone's heterogeneities and microcracks (Zioupos 1998). This competition between deformation and fracture is what makes the ductility of bone possible. It requires not only high toughness for the material bone, but also a rising crack resistance curve that would promote crack stability.

Figure 11b shows a set of experimental crack resistance curves for cortical bone, for a mode I crack propagating across the longitudinal direction of long bones (human

humeri Nalla et al. 2006). The overall toughness (K_{IC}) of bone is on par with fish scale and nacre, and among the toughness natural materials (Fig. 1). Bone is also about 10 times tougher than skin and the pure hydroxyapatite mineral (in K_{IC} terms). Fracture toughness also increases significantly as the crack advances, an indication of powerful toughening mechanisms taking place. The ductility of the material bone at the tip of cracks generates a process zone toughening mechanism similar to nacre. Microcrack toughening was also suggested as a similar mechanism (Vashishth et al. 2003). Propagating a crack in bone also involves the pullout of individual fibers and fibrils out of the crack faces (Nalla et al. 2003; Fantner et al. 2004), crack bridging and added toughness for bone. Upon opening or shearing of the interface, these electrostatic sacrificial bonds can break and release 'hidden lengths' along the molecule, generating large deformations and energy dissipation at the molecular scale (Fantner et al. 2005). Tensile experiments on bovine cortical bone using stepwise changes in strain rates confirmed that the activation enthalpy associated to nonlinear deformation in bone corresponds to the disruption of electrostatic bonds (Gupta et al. 2007). A larger scales, mature cortical bone can therefore be interpreted as a unidirectional fiber reinforced composite, where the osteons are the fibers and the interstitial bone is the matrix (Burr et al. 1988). In a similar way that an interface of carbon or glass fibres in synthetic composites can deflect cracks and generate toughness by pullout, cracks can deflect or twist along the weaker cement lines (Launey et al. 2022; Koester et al. 2008). These powerful mechanisms make cortical bone five times tougher in the transverse direction compared to the longitudinal 'splitting' direction (Ritchie et al. 2005). To deflect incoming cracks, the cement line must be significantly weaker than both osteons and interstitial bone. Push-out tests on individual osteons have verified the low shear strength of the cement lines (8 MPa) (Ascenzi and Bonucci 1972; Bigley et al. 2006), about 10 times smaller than the surrounding interlamellar interfaces (73 MPa) (Dong et al. 2005). Once the cement line has broken, frictional pullout ensues (Bigley et al. 2006), a mechanism which is also observed and exploited in synthetic fibers used in engineering composites. The fracture toughness of cement lines can be estimated from the toughness of cortical bone in the splitting direction, because the crack mostly propagates along the cement lines in that orientation. By this measure, the toughness of the cement line is 1–2 $MPa^{1/2}$, which is 10 times lower than the toughness of bone in the transverse direction (Koester et al. 2008). These experiments confirm the strong contrast of strength between cement lines and the surrounding bone material, which can be explained by differences in composition and structure. The main toughening mechanisms associated with the cement line are crack deflection and twisting (Ritchie et al. 2009; Koester et al. 2008; Ager et al. 2006), although debonding followed by frictional pullout has also been suggested as an important toughening mechanism associated with osteons (Piekarsk 1970; Hiller et al. 2003). Disrupting the finely tuned structure and mechanisms of these interfaces in bone can have a profound impact on overall performance. For example, suppressing key interface proteins such as osteopontin has immediate and dramatic consequences on the overall toughness (Poundarik et al. 2012; Thurner et al. 2010), and recent studies have shown that the decrease of the mechanical properties of bone with age can be explained by excess of stiff and brittle covalent cross links at the

nano-interfaces (Zimmermann et al. 2011), with direct effects on the toughening mechanisms (Fig. 11b). These results make it clear that bone must be understood as an integration of structural building blocks connected by interfaces.

9 Summary and Overview of Toughening Mechanisms in Natural Materials

The examples discussed in this chapter show how natural materials can control deformation and prevent crack propagation by specific mechanisms and architectures. Tendon, fish scales, skin, nacre, tooth enamel, and bone display different types of architectures with a broad variety of toughening mechanisms. The loose organization of the collagen fibrils in skin allows for large deformations, crack tip rounding, and local re-orientation of the collagen fibrils. In more organized architectures like fish scales, bone, tooth enamel, and bone, crack deflection is prominent, and it is possible only if the interface is significantly weaker than the rest of the material (He and Hutchinson 1989). The inter-fibrillar interfaces in tendon must be much weaker than the collagen fibrils, the thin proteinaceous interfaces in nacre must be weaker than the mineral tablets, the thin cement lines in cortical bone must be weaker than the osteons. Weak interfaces are therefore a requirement for high toughness, a somewhat counterintuitive rule prevalent in fiber-reinforced composites (Evans 1989) and multilayered ceramics (Clegg et al. 1990). Weak interfaces are an universal theme in biological materials is the result of the adaptation and specialization of biological materials for specific functions. More isotropic structures are less specialized, and show less extreme mechanical properties (Nikolov et al. 2010). Crack deflection can trigger further toughening mechanisms such as crack bridging as seen in fish scales, tooth enamel, nacre or bone. The most powerful toughening mechanisms are associated with process zone toughening and inelastic deformations. This type of mechanism relies on volumetric dilation of the inelastic region and residual strains to generate toughness as the crack advances. In addition to spending energy to generate new surfaces, the material dissipates energy by the loading of the material ahead of the crack and unloading it behind the crack. Process zone toughening is the main toughening mechanisms in fish scales (Dastjerdi and Barthelat 2015) and nacre (Barthelat and Rabiei 2011). In these hard yet tough materials, inelastic deformations over large volumes near cracks cannot be dissociated from, and are critical to toughening mechanisms in ways similar to metals (Anderson 2005), phase transforming ceramics (Evans 1990) and reinforced epoxies (Evans et al. 1986). The amount of precision and effectiveness of toughening mechanisms in natural materials, as well as its controlled occurrence over multiple length scales, will continue to fascinate materials scientists and inspire new engineering materials in years to come. Other remarkable features such as self-healing to repair fatigue microcrack to remodeling to adapt to local stresses are unique to biological materials, but will perhaps also be used in the engineering materials of tomorrow.

Acknowledgements This chapter is based on lecture notes from a CISM school on "Mechanics and Physics of Fracture: Multi-scale modeling of the failure behavior of solids" held September 26–30, 2016. FB would like to acknowledge the contribution of Will Pro to the final preparation steps of this chapter.

References

Ager JW, Balooch G, Ritchie RO (2006) Fracture, aging, and disease in bone. J Mater Res 21:1878–92

Anderson TL (2005) Fracture mechanics: fundamentals and applications. Taylor & Francis, Boca Raton, FL

Ascenzi A, Bonucci E (1972) Shearing properties of single osteons. Anat Rec 172:499–510

Ashby M (2010) Materials selection in mechanical design. 4th Revised edition ed. Butterworth-Heinemann Ltd., Oxford

Bajaj D, Arola D (2009) Role of prism decussation on fatigue crack growth and fracture of human enamel. Acta Biomater 5:3045–56

Bajaj D, Park S, Quinn GD, Arola D (2010) Fracture processes and mechanisms of crack growth resistance in human enamel. Jom 62:76–82

Barthelat F (2007) Biomimetics for next generation materials. Philos Trans R Soc A-Math Phys Eng Sci 365:2907–19

Barthelat F (2015) Architectured materials in engineering and biology: fabrication, structure, mechanics and performance. Int Mater Rev 60:413–30

Barthelat F, Rabiei R (2011) Toughness amplification in natural composites. J Mech Phys Solids 59:829–40

Barthelat F, Tang H, Zavattieri PD, Li CM, Espinosa HD (2007) On the mechanics of mother-of-pearl: a key feature in the material hierarchical structure. J Mech Phys Solids 55:225–444

Barthelat F, Yin Z, Buehler MJ (2016) Structure and mechanics of interfaces in biological materials. Nat Rev Mater 1

Bass EC, Ashford FA, Segal MR, Lotz JC (2004) Biaxial testing of human annulus fibrosus and its implications for a constitutive formulation. Ann Biomed Eng 32:1231–42

Bechtle S, Fett T, Rizzi G, Habelitz S, Klocke A, Schneider GA (2010) Crack arrest within teeth at the dentinoenamel junction caused by elastic modulus mismatch. Biomaterials 31:4238–47

Bigi A, Burghammer M, Falconi R, Koch MHJ, Panzavolta S, Riekel C (2001) Twisted plywood pattern of collagen fibrils in teleost scales: an X-ray diffraction investigation. J Struct Biol 136:137–43

Bigley RF, Griffin LV, Christensen L, Vandenbosch R (2006) Osteon interfacial strength and histomorphometry of equine cortical bone. J Biomech 39:1629–40

Binici H, Aksogan O, Bodur MN, Akca E, Kapur S (2007) Thermal isolation and mechanical properties of fibre reinforced mud bricks as wall materials. Constr Build Mater 21:901–6

Bischoff JE, Arruda EM, Grosh K (2000) Finite element modeling of human skin using an isotropic, nonlinear elastic constitutive model. J Biomech 33:645–52

Browning A, Ortiz C, Boyce MC (2013) Mechanics of composite elasmoid fish scale assemblies and their bioinspired analogues. J Mech Behav Biomed Mater 19:75–86

Bruet BJF, Song JH, Boyce MC, Ortiz C (2008) Materials design principles of ancient fish armour. Nat Mater 7:748–56

Buehler MJ (2007) Molecular nanomechanics of nascent bone: fibrillar toughening by mineralization. Nanotechnology 18

Buehler MJ (2006) Nature designs tough collagen: explaining the nanostructure of collagen fibrils. Proc Natl Acad Sci USA 103:12285–90

Burr DB (2002) The contribution of the organic matrix to bone's material properties. Bone 31:8–11

Burr DB, Schaffler MB, Frederickson RG (1988) Composition of the cement line and its possible mechanical role as a local interface inhuman compact-bone. J Biomech 21:939–945
Clegg WJ, Kendall K, Alford NM, Button TW, Birchall JD (1990) A simple way to make tough ceramics. Nature 347:455–7
Colfen H, Antonietti M (2005) Mesocrystals: inorganic superstructures made by highly parallel crystallization and controlled alignment. Angew Chem-Int Ed 44:5576–91
Cook J, Gordon JE, Evans CC, Marsh DM (1964) A mechanism for the control of crack propagation in all-brittle systems. Proc R Soc Lond A 282:508–20
Currey JD (1977) Mechanical properties of mother of pearl in tension. Proc R Soc Lond B 196:443–63
Currey JD (1999) The design of mineralised hard tissues for their mechanical functions. J Exp Biol 202:3285–94
Currey JD (2002) Bones: structure and mechanics. Princeton University Press, Princeton, NJ
Currey JD, Taylor JD (1974) The mechanical behavior of some molluscan hard tissues. J Zool (Lond) 173:395–406
Dastjerdi AK, Barthelat F (2015) Teleost fish scales amongst the toughest collagenous materials. J Mech Behav Biomed Mater 52:95–107
Dastjerdi AK, Rabiei R, Barthelat F (2013) The weak interfaces within tough natural composites: experiments on three types of nacre. J Mech Behav Biomed Mater 19:50–60
Dong XN, Zhang X, Guo XE (2005) Interfacial strength of cement lines in human cortical bone. Mech Chem Biosyst: MCB 2:63–8
Dunlop JWC, Weinkamer R, Fratzl P (2011) Artful interfaces within biological materials. Mater Today 14:70–8
Eppell SJ, Smith BN, Kahn H, Ballarini R (2006) Nano measurements with micro-devices: mechanical properties of hydrated collagen fibrils. J R Soc Interface 3:117–21
Espinosa HD, Juster AL, Latourte FJ, Loh OY, Gregoire D, Zavattieri PD (2011) Tablet-level origin of toughening in abalone shells and translation to synthetic composite materials. Nat Commun 2
Espinosa HD, Rim JE, Barthelat F, Buehler MJ (2009) Merger of structure and material in nacre and bone - perspectives on de novo biomimetic materials. Prog Mater Sci 54:1059–100
Evans AG (1989) The mechanical performance of fiber-reinforced ceramic matrix composites. Mater Sci Eng A 107:227–39
Evans AG (1990) Perspective on the development of high-toughness ceramics. J Am Ceram Soc 73:187–206
Evans AG, Ahmad ZB, Gilbert DG, Beaumont PWR (1986) Mechanisms of toughening in rubber toughened polymers. Acta Metall 34:79–87
Fantner GE, Birkedal H, Kindt JH, Hassenkam T, Weaver JC, Cutroni JA et al (2004) Influence of the degradation of the organic matrix on the microscopic fracture behavior of trabecular bone. Bone 35:1013–22
Fantner GE, Hassenkam T, Kindt JH, Weaver JC, Birkedal H, Pechenik L et al (2005) Sacrificial bonds and hidden length dissipate energy as mineralized fibrils separate during bone fracture. Nat Mater 4:612–6
Fantner GE, Rabinovych O, Schitter G, Thurner P, Kindt JH, Finch MM et al (2006) Hierarchical interconnections in the nano-composite material bone: fibrillar cross-links resist fracture on several length scales. Compos Sci Technol 66:1205–11
Forest Products Laboratory. Wood handbook: wood as an engineering material. [Madison]; Washington: The Laboratory; For sale by the Supt. of Docs., U.S. Govt. Print. Off.; 1974
Fratzl P (2003) Cellulose and collagen: from fibres to tissues. Curr Opin Colloid Interface Sci 8:32–9
Fratzl P, Weinkamer R (2007) Nature's hierarchical materials. Prog Mater Sci 52:1263–334
Fratzl P, Misof K, Zizak I, Rapp G, Amenitsch H, Bernstorff S (1998) Fibrillar structure and mechanical properties of collagen. J Struct Biol 122:119–22
Fung YC (2004) Biomechanics: mechanical properties of living tissues. Springer, New York

Fung DT, Wang VM, Laudier DM, Shine JH, Basta-Pljakic J, Jepsen KJ et al (2009) Subrupture tendon fatigue damage. J Orthop Res 27:264–73
Garrano AMC, La Rosa G, Zhang D, Niu LN, Tay FR, Majd H et al (2012) On the mechanical behavior of scales from Cyprinus carpio. J Mech Behav Biomed Mater 7:17–29
Gautieri A, Uzel S, Vesentini S, Redaelli A, Buehler MJ (2009) Molecular and mesoscale mechanisms of osteogenesis imperfecta disease in collagen fibrils. Biophys J 97:857–65
Gupta HS, Wagermaier W, Zickler GA, Aroush DRB, Funari SS, Roschger P et al (2005) Nanoscale deformation mechanisms in bone. Nano Lett 5:2108–11
Gupta HS, Wagermaier W, Zickler GA, Hartmann J, Funari SS, Roschger P et al (2006) Fibrillar level fracture in bone beyond the yield point. Int J Fract 139:425–36
Gupta HS, Seto J, Wagermaier W, Zaslansky P, Boesecke P, Fratzl P (2006) Cooperative deformation of mineral and collagen in bone at the nanoscale. Proc Natl Acad Sci USA 103:17741–6
Gupta HS, Fratzl P, Kerschnitzki M, Benecke G, Wagermaier W, Kirchner HOK (2007) Evidence for an elementary process in bone plasticity with an activation enthalpy of 1 eV. J R Soc Interface 4:277–82
Habelitz S, Marshall SJ, Marshall GW, Balooch M (2001) Mechanical properties of human dental enamel on the nanometre scale. Arch Oral Biol 46:173–83
Haraldsson BT, Aagaard P, Krogsgaard M, Alkjaer T, Kjaer M, Magnusson SP (2005) Region-specific mechanical properties of the human patella tendon. J Appl Physiol 98:1006–12
Hassenkam T, Fantner GE, Cutroni JA, Weaver JC, Morse DE, Hansma PK (2004) High-resolution AFM imaging of intact and fractured trabecular bone. Bone 35:4–10
He MY, Hutchinson JW (1989) Crack deflection at an interface between dissimilar elastic materials. Int J Solids Struct 25:1053–67
Herod TW, Chambers NC, Veres SP (2016) Collagen fibrils in functionally distinct tendons have differing structural responses to tendon rupture and fatigue loading. Acta Biomater 42:296–307
Hiller LP, Stover SM, Gibson VA, Gibeling JC, Prater CS, Hazelwood SJ et al (2003) Osteon pullout in the equine third metacarpal bone: effects of ex vivo fatigue. J Orthop Res 21:481–488
Hui SL, Slemenda CW, Johnston CC (1988) Age and bone mass as predictors of fracture in a prospective-study. J Clin Investig 81:1804–9
Ikoma T, Kobayashi H, Tanaka J, Walsh D, Mann S (2003) Microstructure, mechanical, and biomimetic properties of fish scales from Pagrus major. J Struct Biol 142:327–33
Imbeni V, Kruzic JJ, Marshall GW, Marshall SJ, Ritchie RO (2005) The dentin-enamel junction and the fracture of human teeth. Nat Mater 4:229–32
Jackson AP, Vincent JFV, Turner RM (1988) The mechanical design of nacre. Proc R Soc Lond B 234:415–40
Kamat S, Su X, Ballarini R, Heuer AH (2000) Structural basis for the fracture toughness of the shell of the conch Strombus gigas. Nat Mater 405:1036–40
Kamat S, Kessler H, Ballarini R, Nassirou M, Heuer AH (2004) Fracture mechanisms of the Strombus gigas conch shell: II-micromechanics analyses of multiple cracking and large-scale crack bridging. Acta Mater 52:2395–406
Ker RF (2007) Mechanics of tendon, from an engineering perspective. Int J Fatigue 29:1001–9
Koester KJ, Ager JW III, Ritchie RO (2008) The true toughness of human cortical bone measured with realistically short cracks. Nat Mater 7:672–7
Kruzic J, Nalla RK, Kinney JH, Ritchie RO (2003) Crack blunting, crack bridging and resistance-curve fracture mechanics in dentin: effect of hydration. Biomaterials 24:5209–21
Launey ME, Buehler MJ, Ritchie RO (2022) On the mechanistic origins of toughness in bone. In: Clarke DR, Ruhle M, Zok F (eds) Annual review of materials research, vol 402010, pp 25–53
Lawn BR (1993) Fracture of brittle solids, 2nd edn. Cambridge University Press, New York
Lemmen C, Khan A (2012) A simulation of the neolithic transition in the indus valley. In: Giosan L, Fuller DQ, Nicoll K, Flad RK, Clift PD (eds) Climates, Landscapes, and Civilizations, pp 107-114
Levi-Kalisman Y, Falini G, Addadi L, Weiner S (2001) Structure of the nacreous organic matrix of a bivalve mollusk shell examined in the hydrated state using Cryo-TEM. J Struct Biol 135:8–17

Lichtenegger HC, Schoberl T, Ruokolainen JT, Cross JO, Heald SM, Birkedal H et al (2003) Zinc and mechanical prowess in the jaws of Nereis, a marine worm. Proc Natl Acad Sci USA 100:9144–9
Lin C, Douglas W (1994) Structure-property relations and crack resistance at the bovine dentin-enamel junction. J Dent Res 73:1072–8
Lin YS, Wei CT, Olevsky EA, Meyers MA (2011) Mechanical properties and the laminate structure of Arapaima gigas scales. J Mech Behav Biomed Mater 4:1145–56
Liu WT, Zhang Y, Li GY, Miao YQ, Wu XH (2008) Structure and composition of teleost scales from snakehead Channa argus (Cantor) (Perciformes: Channidae). J Fish Biol 72:1055–67
Lopez MI, Martinez PEM, Meyers MA (2014) Organic interlamellar layers, mesolayers and mineral nanobridges: contribution to strength in abalone (Haliotis rufescence) nacre. Acta Biomater 10:2056–64
Macho GA, Jiang Y, Spears IR (2003) Enamel microstructure-a truly three-dimensional structure. J Hum Evol 45:81–90
Mann S (2000) The chemistry of form. Angew Chem-Int Ed 39:3393–406
Mayer G (2005) Rigid biological systems as models for synthetic composites. Science 310:1144–7
Mercer C, He MY, Wang R, Evans AG (2006) Mechanisms governing the inelastic deformation of cortical bone and application to trabecular bone. Acta Biomater 2:59–68
Meunier J (1981) 'Twisted plywood' structure and mineralization in the scales of a primitive living fish Amia calva. Tissue Cell 13:165–71
Meunier FJ (1984) Spatial organization and mineralization of the basal plate of elasmoid scales in osteichthyans. Am Zool 24:953
Meunier FJ, Castanet J (1982) Organisation spatiale des fibres de collagène de la plaque basale des écailles des Téléostéens. Zool Scripta 11:141–53
Meyers MA, Chen PY, Lin AYM, Seki Y (2008) Biological materials: structure and mechanical properties. Prog Mater Sci 53:1–206
Meyers MA, Lin YS, Olevsky EA, Chen PY (2012) Battle in the Amazon: arapaima versus piranha. Adv Eng Mater 14:B279–B88
Mirkhalaf M, Dastjerdi AK, Barthelat F (2014) Overcoming the brittleness of glass through bio-inspiration and micro-architecture. Nat Commun 5
Nabavi A, Capozzi A, Goroshin S, Frost DL, Barthelat F (2014) A novel method for net-shape manufacturing of metal-metal sulfide cermets. J Mater Sci 49:8095–106
Nalla RK, Kinney JH, Ritchie RO (2003) Mechanistic fracture criteria for the failure of human cortical bone. Nat Mater 2:164–8
Nalla RK, Kruzic JJ, Kinney JH, Balooch M, Ager JW, Ritchie RO (2006) Role of microstructure in the aging-related deterioration of the toughness of human cortical bone. Mater Sci Eng: C 26:1251–60
Nanci A, Ten Cate AR (2013) Ten Cate's oral histology: development, structure, and function. Elsevier, St. Louis, Mo
Nikolov S, Petrov M, Lymperakis L, Friák M, Sachs C, Fabritius H-O et al (2010) Revealing the design principles of high-performance biological composites using ab initio and multiscale simulations: the example of lobster cuticle. Adv Mater 22:519–26
Nikolov S, Petrov M, Lymperakis L, Friak M, Sachs C, Fabritius H-O, et al (2010) Revealing the design principles of high-performance biological composites using ab initio and multiscale simulations: the example of lobster cuticle. Adv Mater 22:519–526
Oxlund H, Manschot J, Viidik A (1988) The role of elastin in the mechanical-properties of skin. J Biomech 21:213–8
Peterlik H, Roschger P, Klaushofer K, Fratzl P (2006) From brittle to ductile fracture of bone. Nat Mater 5:52–5
Piekarsk K (1970) Fracture of bone. J Appl Phys 41:215–223
Poissant J, Barthelat F (2012) In situ mechanical testing of hydrated biological nanofibers using a nanoindenter transducer. Exp Mech 52:1287–95
Poundarik AA, Diab T, Sroga GE, Ural A, Boskey AL, Gundberg CM et al (2012) Dilatational band formation in bone. Proc Natl Acad Sci USA 109:19178–83

Provenzano PP, Vanderby R (2006) Collagen fibril morphology and organization: implications for force transmission in ligament and tendon. Matrix Biol 25:71–84
Purslow PP (1983) Measurement of the fracture-toughness of extensible connective tissues. J Mater Sci 18:3591–398
Puxkandl R, Zizak I, Paris O, Keckes J, Tesch W, Bernstorff S et al (2002) Viscoelastic properties of collagen: synchrotron radiation investigations and structural model. Philos Trans R Soc Lond Ser B-Biol Sci 357:191–7
Raabe D, Sachs C, Romano P (2005) The crustacean exoskeleton as an example of a structurally and mechanically graded biological nanocomposite material. Acta Mater 53:4281–92
Rabiei R, Bekah S, Barthelat F (2010) Failure mode transition in nacre and bone-like materials. Acta Biomater 6:4081–9
Rho JY, Kuhn-Spearing L, Zioupos P (1998) Mechanical properties and the hierarchical structure of bone. Med Eng Phys 20:92–102
Ridge MD, Wright V (1966) Directional effects of skin - a bio-engineering study of skin with particular reference to Langers lines. J Investig Dermatology 46:341–346
Ridge MD, Wright V (1966) The directional effects of skin: a bio-engineering study of skin with particular reference to Langer's lines*. J Investig Dermatology 46:341–6
Ritchie RO (2011) The conflicts between strength and toughness. Nat Mater 10:817–22
Ritchie RO, Kinney JH, Kruzic JJ, Nalla RK (2005) A fracture mechanics and mechanistic approach to the failure of cortical bone. Fatigue Fract Eng Mater Struct 28:345–71
Ritchie RO, Buehler MJ, Hansma P (2009) Plasticity and toughness in bone. Phys Today 62:41–7
Rousseau M, Lopez E, Stempfle P, Brendle M, Franke L, Guette A et al (2005) Multiscale structure of sheet nacre. Biomaterials 26:6254–62
Scheyer TM, Sander PM, Joyce WG, Boehme W, Witzel U (2007) A plywood structure in the shell of fossil and living soft-shelled turtles (Trionychidae) and its evolutionary implications. Org Divers Evol 7:136–44
Schonborner AA, Boivin G, Baud CA (1979) The mineralization processes in teleost fish scales. Cell Tissue Res 202:203–12
Schwiedrzik J, Raghavan R, Buerki A, LeNader V, Wolfram U, Michler J et al (2014) In situ micropillar compression reveals superior strength and ductility but an absence of damage in lamellar bone. Nat Mater 13:740–7
Seshaiya RV, Ambujabay P, Kalyani M (1963) Amino acid composition of icthylepidin from fish scales. Asp Protein Struct 343–348
Seto J, Ma Y, Davis SA, Meldrum F, Gourrier A, Kim Y-Y et al (2012) Structure-property relationships of a biological mesocrystal in the adult sea urchin spine. Proc Natl Acad Sci 109:3699–704
Shen ZL, Dodge MR, Kahn H, Ballarini R, Eppell SJ (2008) Stress-strain experiments on individual collagen fibrils. Biophys J 95:3956–63
Silver FH, Siperko LM, Seehra GP (2003) Mechanobiology of force transduction in dermal tissue. Ski Res Technol 9:3–23
Svensson RB, Herchenhan A, Starborg T, Larsen M, Kadler KE, Qvortrup K et al (2017) Evidence of structurally continuous collagen fibrils in tendons. Acta Biomater 50:293–301
Szczesny SE, Caplan JL, Pedersen P, Elliott DM (2015) Quantification of interfibrillar shear stress in aligned soft collagenous tissues via notch tension testing. Scientific Reports, vol 5
Tang Y, Ballarini R, Buehler MJ, Eppell SJ (2010) Deformation micromechanisms of collagen fibrils under uniaxial tension. J R Soc Interface 7:839–50
Taylor D, Hazenberg JG, Lee TC (2007) Living with cracks: damage and repair in human bone. Nat Mater 6:263–8
Thurner PJ, Katsamenis OL (2014) The role of nanoscale toughening mechanisms in osteoporosis. Curr Osteoporos Rep 12:351–6
Thurner PJ, Chen CG, Ionova-Martin S, Sun L, Harman A, Porter A et al (2010) Osteopontin deficiency increases bone fragility but preserves bone mass. Bone 46:1564–1573

Torres FG, Troncoso OP, Nakamatsu J, Grande CJ, Gomez CM (2008) Characterization of the nanocomposite laminate structure occurring in fish scales from Arapaima Gigas. Mater Sci Eng C-Biomim Supramol Syst 28:1276–83

Ural A, Vashishth D (2014) Hierarchical perspective of bone toughness - from molecules to fracture. Int Mater Rev 59:245–63

Uzel SGM, Buehler MJ (2011) Molecular structure, mechanical behavior and failure mechanism of the C-terminal cross-link domain in type I collagen. J Mech Behav Biomed Mater 4:153–61

Vashishth D (2007) Hierarchy of bone microdamage at multiple length scales. Int J Fatigue 29:1024–33

Vashishth D, Tanner KE, Bonfield W (2003) Experimental validation of a microcracking-based toughening mechanism for cortical bone. J Biomech 36:121–4

Vernerey FJ, Barthelat F (2010) On the mechanics of fishscale structures. Int J Solids Struct 47:2268–75

Vincent JFV, Bogatyreva OA, Bogatyrev NR, Bowyer A, Pahl AK (2006) Biomimetics: its practice and theory. J R Soc Interface 3:471–82

Wang RZ, Suo Z, Evans AG, Yao N, Aksay IA (2001) Deformation mechanisms in nacre. J Mater Res 16:2485–93

Wegst UGK, Ashby MF (2004) The mechanical efficiency of natural materials. Philos Mag 84:2167–81

Wegst UGK, Bai H, Saiz E, Tomsia AP, Ritchie RO (2015) Bioinspired structural materials. Nat Mater 14:23–36

Weiner S, Addadi L (1997) Design strategies in mineralized biological materials. J Mater Chem 7:689–702

Weiner S, Wagner HD (1998) The material bone: structure mechanical function relations. Annu Rev Mater Sci 28:271–98

Yahyazadehfar M, Arola D (2015) The role of organic proteins on the crack growth resistance of human enamel. Acta Biomater 19:33–45

Yahyazadehfar M, Bajaj D, Arola DD (2013) Hidden contributions of the enamel rods on the fracture resistance of human teeth. Acta Biomater 9:4806–14

Yahyazadehfar M, Ivancik J, Majd H, An B, Zhang D, Arola D (2014) On the mechanics of fatigue and fracture in teeth. Appl Mech Rev 66:1–19

Yang W, Chen IH, Gludovatz B, Zimmermann EA, Ritchie RO, Meyers MA (2013a) Natural flexible dermal armor. Adv Mater 25:31–48

Yang W, Gludovatz B, Zimmermann EA, Bale HA, Ritchie RO, Meyers MA (2013b) Structure and fracture resistance of alligator gar (Atractosteus spatula) armored fish scales. Acta Biomater 9:5876–89

Yang W, Sherman VR, Gludovatz B, Mackey M, Zimmermann EA, Chang EH et al (2014) Protective role of Arapaima gigas fish scales: structure and mechanical behavior. Acta Biomater 10:3599–614

Yang W, Sherman VR, Gludovatz B, Schaible E, Stewart P, Ritchie RO et al (2015) On the tear resistance of skin. Nat Commun 6:6649

Young MF (2003) Bone matrix proteins: their function, regulation, and relationship to osteoporosis. Osteoporos Int 14:S35–S42

Zhu D, Ortega CF, Motamedi R, Szewciw L, Vernerey F, Barthelat F (2012) Structure and mechanical performance of a "modern" fish scale. Adv Eng Mater 14:B185–B94

Zhu D, Szewciw L, Vernerey F, Barthelat F (2013) Puncture resistance of the scaled skin from striped bass: collective mechanisms and inspiration for new flexible armor designs. J Mech Behav Biomed Mater 24:30–40

Zimmermann EA, Gludovatz B, Schaible E, Dave NKN, Yang W, Meyers MA et al (2013) Mechanical adaptability of the Bouligand-type structure in natural dermal armour. Nat Commun 4

Zimmermann EA, Schaible E, Bale H, Barth HD, Tang SY, Reichert P et al (2011) Age-related changes in the plasticity and toughness of human cortical bone at multiple length scales. Proc Natl Acad Sci USA 108:14416–21

Zioupos P (1998) Recent developments in the study of failure of solid biomaterials and bone: 'fracture' and 'pre-fracture' toughness. Mater Sci Eng: C 6:33–40
Zioupos P, Gresle M, Winwood K (2008) Fatigue strength of human cortical bone: age, physical, and material heterogeneity effects. J Biomed Mater Res Part A 86A:627–36
Zok FW (2006) Developments in oxide fiber composites. J Am Ceram Soc 89:3309–24
Zylberberg L, Bereiterhahn J, Sire JY (1988) Cytoskeletal organization and collagen orientation in the fish scales. Cell Tissue Res 253:597–607